Scaling of charged particles produced in ultra-relativistic nuclear collisions

THESIS

SUBMITTED TO THE UNIVERSITY OF JAMMU
FOR
THE AWARD OF DEGREE
OF

DOCTOR OF PHILOSOPHY
IN
PHYSICS

BY
Zarina Banoo

UNDER THE SUPERVISION
OF
Prof. Ramni Gupta

Department of Physics
University of Jammu, Jammu
Jammu and Kashmir-180006 (India)

September, 2025

DEPARTMENT OF PHYSICS,
UNIVERSITY OF JAMMU
JAMMU–180006

CERTIFICATE

It is certified that **Ms. Zarina Banoo**, worked under my supervision and the work is worthy of consideration for the award of Ph.D. degree in Physics. It is further certified that:

1. The thesis embodies the work done by the candidate. It is original and not copied from other sources;
2. The candidate worked under my supervision for the period required under statutes;
3. The candidate has put in the required attendance in the Department of Physics, University of Jammu, Jammu during the period of research;
4. The candidate has fulfilled all the requirements of the UGC-MSP-2016 regulations;
5. The candidate has fulfilled the statutory conditions as laid down in **Section 18** of the statutes governing the degree of Doctor of Philosophy.

(**Prof. K. K. Bamzai**)
Head
Department of Physics
University of Jammu
Jammu

(**Prof. Ramni Gupta**)
Research Supervisor
Department of Physics
University of Jammu
Jammu

Plagiarism Certificate

I, **Zarina Banoo**, D/o Mr. Jaffar Ali, hereby declare that the work reported in this thesis entitled "**Scaling of charged particles produced in ultra-relativistic nuclear collisions**" has been entirely done by me under the supervision of **Prof. Ramni Gupta**, Department of Physics, University of Jammu. The work undertaken by me in this thesis is original and has not been copied from other sources without due acknowledgement. I also ascertain that no part of this thesis is presented elsewhere for the award of any degree or diploma of any University or Institution. Moreover, this thesis is having 7% degree of plagiarism as per the **DrillBit plagiarism detection software** analysis report.

Dated: **(Zarina Banoo)**

Countersigned by:

(**Prof. K. K. Bamzai**)
Head
Department of Physics
University of Jammu
Jammu

(**Prof. Ramni Gupta**)
Research Supervisor
Department of Physics
University of Jammu
Jammu

DECLARATION

I, **Zarina Banoo** D/o Mr. Jaffar Ali, hereby declare that the work reported in this thesis entitled "**Scaling of charged particles produced in ultra-relativistic nuclear collisions**," has been entirely done by me under the supervision of **Prof. Ramni Gupta**, Department of Physics, University of Jammu. The work undertaken by me in this thesis is original and has not been copied from other sources without due acknowledgements. It has not been submitted fully or partially elsewhere for the award of any degree, diploma, fellowship or other similar titles of recognition to the best of my knowledge to anybody else in any other University or Institution.

Dated: **(Zarina Banoo)**

Countersigned by:

(**Prof. K. K. Bamzai**)
Head
Department of Physics
University of Jammu
Jammu

(**Prof. Ramni Gupta**)
Research Supervisor
Department of Physics
University of Jammu
Jammu

ACKNOWLEDGMENTS

First of all, I would like to thank my **Almighty Allah**, the most merciful, the most beneficent, and the most kind, for His countless blessings, guidance, and mercy throughout this journey. It is only through His grace that I found the strength, patience, and determination to overcome challenges and bring this work to completion. I am profoundly grateful for His divine support, which has been the foundation of every step in this endeavor, and I humbly pray for His continued guidance and blessings in all my future pursuits.

I wish to express my deepest gratitude to my respected guide, **Prof. Ramni Gupta**, for her invaluable guidance, persistent support, constant encouragement, and immense care throughout my research journey. Her dedication and insightful advice have been instrumental in the successful completion of this work. Her constructive criticism and suggestions have not only refined my research but also reminded me of the broader responsibilities toward personal and community growth. I greatly appreciate the opportunities she provided to attend several national and international conferences, workshops, and schools, which significantly enriched my academic experience. Any success I achieve in my scientific career will always be indebted, in part, to her. Beyond her academic excellence, I deeply admire her unwavering commitment to fostering a collaborative and inspiring research environment that motivated me to excel. I consider myself truly fortunate to have worked under her precious guidance.

I wish to extend my sincere gratitude to **Prof. K.K. Bamzai**, Head of the Department of Physics, and **Prof. Arun Bharti**, former Head of the Department, for providing the necessary facilities and a supportive environment that greatly facilitated my research work. I am especially thankful to **Prof. Anju Bhasin**, Group Incharge of the High Energy Physics (HEP) Group, for her constant encouragement and invaluable support throughout this endeavor. My heartfelt thanks also go to **Er. Anik Gupta** for his timely assistance whenever required. I would further like to acknowledge other members of the High Energy Physics Group at the University of Jammu–**Prof. Sanjeev Singh Sambyal**, **Dr. Renu Bala**, **Dr. Rajendra Nath Patra**, **Er. Sanjay Mahajan**, and **Dr. Saroj Nayak** for creating a pleasant and collaborative atmosphere that made this journey both productive and enjoyable.

Finally, I extend my appreciation to all the teaching and non-teaching staff of the Department of Physics for their cooperation and support during the course of my research.
A special thanks goes to my friend **Mr. Nassir Mehdi Malik** for his ever-helping nature, always being there to assist me whenever I needed support, no matter the time or circumstance. His selfless dedication, willingness to share his knowledge, and positive spirit have significantly contributed to the encouraging and collaborative environment of our research group. I extend my heartfelt thanks to my fellow research colleagues **Ms. Sheetal Sharma**, **Mr. Salman Khurshid Malik**, **Mr. Vikash Sumreya**, **Mr. Randhir Singh**, **Ms. Binti Sharma**, **Mr. Fakrul Haider**, **Mr. Balwan Singh**, **Mr. Ashish Jalotra**, **Ms. Pratibha Bhaghat**, **Ms. Upasna Sharma**, **Ms. Mahima Sharma**, and **Ms. Mokshi Vaid** for creating a stimulating and enjoyable research environment. Their collaboration, encouragement, and the many moments of sharing ideas and discussions have made this journey both productive and memorable. I wish them all the very best in their future endeavors. I am also deeply grateful to my friends **Mr. Zakir Hussain**, **Mr. Hussain Mira**, **Mr. Zakir Hussain**, **Ms. Archo Fatima**, **Ms. Fatima Nissa** and **Mr. Ghulam Mustafa** for their constant support and encouragement throughout this period.
Above all, I owe my deepest gratitude to my parents, **Mr. Jaffar Ali** and **Mrs. Umbeg Kulsum**, my aunt, **Mrs. Feroz Bee**, and my sisters, **Ms. Farida Banoo** and **Ms. Maqsuma Banoo**, for their unconditional love, unwavering support, and constant encouragement, without which this work would not have been possible. Their sacrifices, guidance, and belief in me have been the cornerstone of my success, inspiring me to persevere through every challenge. A special thanks goes to my niece, **Ayman Zehra**, whose ever-cheerful smile has been a source of joy and motivation throughout this journey.

(Zarina Banoo)

Abstract

The Large Hadron Collider (LHC) serves as an experimental platform to test theoretical predictions of the Standard Model. The Standard Model is a framework for particle physics that describes, in detail, all elementary particles and their interactions through electromagnetic, strong, and weak forces, which are three of the four fundamental forces in nature. A Large Ion Collider Experiment (ALICE) is one of the major experiments at the LHC at CERN, Geneva. It focuses on collecting data from high-energy heavy-ion collisions, aiming to recreate and study a new state of nuclear matter, known as Quark-Gluon Plasma (QGP) which is believed to have existed at the beginning of the universe. Thus, investigating relativistic heavy-ion collisions with ALICE is similar to probing the early universe. QGP is a state of matter where the constituent partons (quarks and gluons) are free particles rather than being confined within hadrons where they are glued to each other through the strong force. These interactions between fundamental particles that form hadrons is explained by the theory of strong interactions, known as Quantum Chromodynamics (QCD). By analyzing heavy-ion collision data, researchers can investigate formation of QGP and its properties, such as temperature, energy density, viscosity etc..

Confirmed experimental signals of QGP formation have been observed in the data coming from the heavy-ion collisions at the Relativistic Heavy Ion Collider (RHIC) at BNL, USA and at the LHC. Experimental results from these colliders, combined with theoretical advances from various frameworks have greatly expanded our understanding of the properties of hot QCD matter. The QGP produced in these collisions behaves as a strongly coupled liquid, resembling a near-ideal Fermi liquid with the lowest specific viscosity ever measured, indicating almost no frictional resistance. Studying this newly formed matter at range of temperatures is essential to accurately characterize its properties and firmly establish the QCD theory. To achieve this goal, the LHC is designed to reach 5.5 A TeV for Pb-Pb collisions, allowing higher energy densities and temperatures conducive for the formation of QGP. It provides an opportunity to understand not only the properties of the QGP but also the mechanism of hadronization that occurs as the QGP cools and transitions from state of free quarks and gluons to hadronic matter. Direct observation of QGP is challenging due to its short lifetime (about 10 fm/c), as it rapidly thermalises and expands, forming hadron gas. Indirect methods are therefore used to identify the formation of the QGP. In addition to heavy-ion collisions, LHC also collides smaller systems such as proton-proton (*pp*) and proton-lead (*p-Pb*).

Numerous observables that can serve as evidence to qualify and quantify the creation of QGP have been proposed which can serve as a test for QCD theory. Among these fluctuations in physical measurables from the heavy-ion collisions serve as an important signal of QGP formation. Since fluctuations are inextricably linked to particle correlations, studying

fluctuations provides valuable insight into the mechanisms behind the multiparticle production in high-energy collisions and other properties, such as the initial energy density, the nature of particle interactions, and the dynamics of the system as it evolves, etc.. Specifically fluctuations in multiplicity distributions are critical for determining the properties of the QGP. Multiplicity fluctuations are sensitive to the presence of critical point in the QCD phase diagram. At the critical endpoint (CEP), where the correlation length diverges, the systems undergoing phase transition exhibits large fluctuations in various observables, such as particle multiplicity, transverse momentum, temperature, pion to kaon ratio, etc.. At CEP the system becomes scale-invariant and self-similar, like the critical opalescence in quantum electrodynamic (QED) systems and leads to significant local density fluctuations. So studying these changes is a good way to understand the type of phase transition, find the critical point on the phase diagram, grasp how particles are produced in heavy-ion collisions, and therefore learn about how the matter created in those collisions evolves over time.

The transition from QGP to a hadronic state may preserve, or "freeze in," fractal fluctuations. Thus one can also probe QGP formation and dynamics through the analysis of fractal properties in the distribution of hadrons produced in high-energy collisions and can serve as a potential signal of the QCD phase transition. Fractal structures are manifested as intermittent fluctuations in kinematic phase space that exhibit power-law scaling, a characteristic signature of self-similar cascades and a hallmark of fractal systems. Observation of multifractality–where the scaling behaviour varies across different scales–in the phase space indicates complex, non-equilibrium dynamics, further reinforcing the connection between fractal patterns and the underlying physics of the QCD phase diagram. Thus observation of self-similarity, scaling behaviour, and intermittency in final-state particle distributions suggest a deep connection between QGP phenomena and critical behaviour associated with phase transitions.

One of the effective methods for examining fluctuations in the system created in heavy-ion collisions is to carry event-by-event study of the obsevables. This approach involves measuring a particular observable for each event and then studying fluctuations in the observable across the ensemble of events. Intermittency analysis that examines patterns in the particle configurations on event-by-event basis can reveal correlations in the multiparticle production in heavy-ion collisions. Intermittency, defined as an increase in the normalized factorial moments (NFMs) with an increase in phase space resolution, is a key indicator of scale-invariant local number density fluctuations. The NFMs of the multiplicity distributions have the beauty that these contain, in integrated form the correlations of particles in the system and filter out statistical effects. These moments of the distributions of the produced particles gave first successful explanation of a high multiplicity spike event recorded

by the JACEE (Japanese-American Collaborative Emulsion Experiment) experiment. Intermittency analysis performed for the low-energy systems, in the early 1990s, were constrained due to low bin multiplicities and low resolution of the detectors. With heavy-ion collisions at ultra-relativistic energies in recent colliders such as RHIC and LHC, a large number of particles per event are produced, allowing for detailed event-by-event analysis. This gives the opportunity to investigate the scaling behaviour of NFM and allowing to analyze multiplicity fluctuations at high bin resolution.

The research work embodied in this thesis pertains to the study of local-multiplicity fluctuations in the charged particles that are produced in Xe-Xe collision at $\sqrt{s_{\rm NN}} = 5.44$ TeV, recorded with the ALICE detector at LHC. NFM of the charged particle multiplicity configurations are determined and are studied for their scaling behaviour in the contours of intermittency, to understand the multiparticle production processes and the dynamics of the system produced during collisions. The scaling behaviour of these moments and a scaling exponent (ν) are studied for various kinematic acceptance regions. Centrality and transverse momentum dependence of the observables is also studied. A study of fractal dimension $D_{\rm q}$ on the order of the moments q is also performed. The analysis is also performed for the generated charged particles in the event samples obtained using the String Melting version of the A Multi Phase Transport (AMPT) model. The work carried in this research work, for the award of Ph.D degree is compiled in six chapters, as summarized below:

- **Chapter 1**:- This chapter gives a brief introduction to the field of high energy physics. It includes a discussion on the Standard Model of particle physics, which currently offers the most comprehensive description of the elementary particles and their interactions. Following that, there is a brief discussion on the QCD phase diagram, kinematic variables, quark-gluon plasma and a few important signatures of QGP formation. Motivation of the present physics analysis and a brief overview of the thesis is also given.

- **Chapter 2**:- In this chapter, the Large Hadron Collider, ALICE experiment and its sub-detectors are briefly introduced. A description of the ALICE data taking and computing framework is also given followed by concise view of data collection and processing using central online systems. The software framework used in this work viz., the AliRoot, AliPhysics which is an extension of ROOT built on the C++ language are briefly introduced. A description of the data simulation and reconstruction techniques, including primary and secondary vertex reconstruction is also given.

- **Chapter 3**:- This chapter introduces the analysis topic and the mathematical formalism to calculate NFM. The observables studied, data sets analysed are presented

along with the event and track selection cuts. Analysis of the HIJING simulated event samples for the Xe-Xe collisions at $\sqrt{s_{\rm NN}}$ = 5.44 TeV and passed through GEANT3 simulated ALICE detector geometry is also given. A Monte-Carlo closure test is also discussed.

- **Chapter 4**:- This chapter presents the observations and results from the analysis of experimental data. The analysis details of the ALICE data for the study of local multiplicity fluctuations of the charged particles produced in Xe-Xe collision system at $\sqrt{s_{\rm NN}}$ = 5.44 TeV are given. The charged particles produced with soft transverse momentum ($p_{\rm T}$) and $|\eta| \leq 0.8$ in the most central events are mainly investigated. A centrality and $p_{\rm T}$ dependence study of scaling exponent (ν) is also done. A comparison of results with that from the Pb-Pb collision system at $\sqrt{s_{\rm NN}}$ = 2.76 TeV and Monte Carlo HIJING is also given. A study of fractal parameters $D_{\rm q}$ and $\lambda_{\rm q}$ is also presented.

- **Chapter 5**:- In this chapter intermittency analysis performed on the events generated using the string melting mode of the AMPT model is given. The scaling exponent (ν), its dependence on $p_{\rm T}$ bins and its comparison with the ν values obtained from the Pb-Pb collsions at $\sqrt{s_{\rm NN}}$ = 2.76 TeV are also discussed.

- **Chapter 6**:- Lastly in this chapter a summary of the work done and conclusions from the observations of experimental data, monte-carlo event study are given. A discussion on the outcome of the work is also given.

(Zarina Banoo)

CONTENTS

1 Introduction **1**
- 1.1 The Standard Model . . . 3
- 1.2 The Quantum Chromodynamics (QCD) . . . 7
- 1.3 The QCD Phase Diagram . . . 9
- 1.4 Heavy-ion collisions . . . 11
- 1.5 Kinematic Variable . . . 15
  - 1.5.1 Four Vector . . . 16
  - 1.5.2 Transverse Momentum (p_{T}) . . . 17
  - 1.5.3 Rapidity (y) . . . 17
  - 1.5.4 Pseudorapidity (η) . . . 18
  - 1.5.5 Center-of-mass energy . . . 19
- 1.6 Signatures of QGP and experimental probes . . . 20
  - 1.6.1 Strangeness Enhancement . . . 20
  - 1.6.2 Jet Quenching . . . 21
  - 1.6.3 Photons and dileptons . . . 22
  - 1.6.4 Anisotropic Flow . . . 23
  - 1.6.5 Fluctuations . . . 24
- 1.7 Motivation of the thesis . . . 26
- 1.8 Organisation of the thesis . . . 28

2 ALICE experimental setup and analysis software **39**
- 2.1 Introduction . . . 39
- 2.2 The Large Hadron Collider . . . 41
- 2.3 A Large Ion Collider Experiment (ALICE) . . . 44
- 2.4 Central Barrel Detectors of ALICE . . . 48
  - 2.4.1 Inner tracking system (ITS) . . . 48
  - 2.4.2 Time Projection Chamber (TPC) . . . 49
  - 2.4.3 Time-Of-Flight (TOF) . . . 51
  - 2.4.4 Transitional Radiation Detector . . . 52

2.5 Forward Detectors at ALICE . . . 53
2.5.1 V0 detector . . . 53
2.5.2 T0 detectors . . . 54
2.5.3 Zero Degree Calorimeter (ZDC) . . . 55
2.6 ALICE online operations . . . 56
2.6.1 Data Acquisition System . . . 56
2.6.2 Central Trigger Processor (CTP) . . . 56
2.6.3 High Level Trigger (HLT) . . . 57
2.6.4 The Detector Control System (DCS) . . . 58
2.6.5 The Experiment Control System (ECS) . . . 58
2.7 ALICE offline operations . . . 59
2.7.1 ALICE Grid and AliEn . . . 59
2.7.2 ROOT and AliRoot framework . . . 61

3 Analysis: methodology and hijing events 73
3.1 Methodology and Observables . . . 75
3.1.1 Intermittency and M-scaling behaviour . . . 78
3.1.2 F-scaling behaviour and scaling exponent ν . . . 79
3.1.3 Fractal parameters . . . 81
3.1.3.1 Fractal dimension . . . 82
3.1.3.2 Coefficient λ_q . . . 83
3.2 Data sets and various selection cuts . . . 84
3.2.1 ALICE experimental data . . . 85
3.2.2 HIJING Monte-Carlo events . . . 85
3.2.3 Event selection cuts . . . 86
3.2.3.1 Trigger selection . . . 86
3.2.3.2 Vertex selection . . . 87
3.2.3.3 Centrality selection . . . 88
3.2.4 Track selection . . . 89
3.3 HIJING event analysis . . . 90
3.3.1 Quality Assurance Plots . . . 91
3.3.2 Monte Carlo Closure . . . 91
3.3.3 M-scaling behaviour . . . 94
3.3.4 F-scaling and Scaling Exponent (ν) . . . 96

4 Data Analysis and Results 107
4.1 Quality Assurance (QA) Plots . . . 108
4.1.1 Event Selection . . . 108
4.1.2 Track Selection . . . 108
4.2 Observations and Results . . . 110
4.2.1 Average bin content . . . 111
4.2.2 F_q^e distributions . . . 112
4.2.3 M-scaling behaviour . . . 112
4.2.4 F-scaling and Scaling Exponent (ν) . . . 115

4.2.5 Fractal Dimension D_q . . . 117
4.2.6 Coefficient λ_q . . . 117
4.2.7 p_T bin dependence of M-scaling . . . 118
4.2.8 Dependence of Scaling exponent (ν) on p_T . . . 120
4.2.9 Dependence of D_q and λ_q on p_T bins . . . 124
4.2.10 Centrality dependence Study . . . 124
4.3 Systematic uncertainties . . . 127
4.4 Comparison of results . . . 130
4.4.1 M-scaling comparison . . . 130
4.4.2 Scaling exponent (ν) as a function of p_T . . . 131
4.4.3 Fractal parameter (D_q) as a function of q . . . 132
4.4.4 Coefficient (λ_q) as a function q . . . 133

5 The AMPT: Intermittency Analysis 139
5.1 Introduction . . . 139
5.2 A brief introduction of the AMPT . . . 140
5.2.1 HIJING initial conditions . . . 141
5.2.2 ZPC parton evolution . . . 143
5.2.3 Hadronization . . . 143
5.2.4 Hardron cascade . . . 144
5.3 The AMPT event samples . . . 145
5.4 Intermittency analysis and observations . . . 147
5.4.1 Average bin content . . . 148
5.4.2 *M-scaling* . . . 149
5.4.3 F-scaling and scaling exponent ν . . . 151
5.4.4 Dependence of ν on p_T . . . 151
5.4.5 Fractal dimension D_q . . . 154
5.4.6 Coefficient λ_q . . . 154

6 Summary and Conclusions 161

A Detector Effect Study 165
A.0.1 Tracking Efficiency Correction . . . 166
A.0.2 Statistical uncertainty calculation . . . 167

B SUPPLEMENTARY FIGURES 169
B.1 Systematic uncertainties plots . . . 169
B.1.1 Filter-Bit (FB) 32 . . . 170
B.1.1.1 Narrow Over-lapping bins . . . 170
B.1.1.2 Wider Over-lapping bins . . . 171
B.1.2 Centrality Estimation CL0 . . . 172
B.1.2.1 Narrow Over-lapping bins . . . 172
B.1.2.2 Wider Over-lapping bins . . . 173
B.1.3 Primary Vetex cut $|Vz| \leq 8$ cm . . . 174
B.1.3.1 Narrow Over-lapping bins . . . 174

B.1.3.2 Wider Over-lapping bins 175
B.1.4 Primary Vetex cut $|Vz| \leq 12$ cm 176
B.1.4.1 Narrow Over-lapping bins 176
B.1.4.2 Wider Over-lapping bins 177
B.1.5 TPC clusters cut (TPCNcls ≤ 80) 178
B.1.5.1 Narrow Over-lapping bins 178
B.1.5.2 Wider Over-lapping bins 179
B.1.6 ITS clusters (ITSNcls ≤ 3) 180
B.1.6.1 Narrow Over-lapping bins 180
B.1.6.2 Wider Over-lapping bins 181

C Service Work **183**

D List of Publications/ Presentations **187**

E Reference **209**

List of Figures

1.1 Elementary particles and fundamental interactions as per the Standard Model of particle physics [4]. . . . 3

1.2 Schematics of (a) electromagnetic interaction between two charged particles and (b) strong interaction via gluon-mediated color charge exchange (c) strong interaction between two quarks. . . . 8

1.3 The coupling constant (α_s (Q^2)) as a function of different energy scales (Q) via various processes. The order of QCD Perturbation Theory used to extract α_s (Q^2) is indicated in brackets. The theoretical calculation of α_s is given by $\alpha_s(M_Z)$ [18]. . . . 9

1.4 A schematic of the QCD phase diagram is shown as a function of temperature (T) and baryochemical potential (μ_B). The solid black line indicates the chemical freeze-out, while the dashed orange line depicts the chiral/deconfinement transition. Both end at the critical point, which is connected to the $\mu = 0$ axis by a cross-over around T $\approx$ 170 MeV. The ground state of nuclear matter is at T = 0 MeV and $\mu = \mu_0$. At high chemical potential and low temperature, a phase of colour superconductivity occurs. The dashed black lines indicate the estimated properties of the medium created by various experiments [24]. . . . 11

1.5 Systematic representation of the various stages of the relativistic heavy-ion collisions. Figure from Ref. [29] . . . 12

1.6 Visualization of the spacetime evolution of the system created in relativistic heavy-ion collisions. Figure from Ref. [25]. . . . 13

1.7 Left: Two heavy ions approaching each other before their collision with the impact parameter b. Right: An illustration of a heavy-ion collision where participant nucleons collide with nucleons of the other nucleus and spectators are almost unaffected. (Figure is taken from [33].) . . . 15

1.8 Cartoon showing the correlation of the final state charged particle multiplicity with impact parameter and number of participants. (Figure is taken from [34].) . . . 15

1.9 Strange and anti-strange quarks produced by the gluon fusion mechanism ($gg \rightarrow s\bar{s}$). 21
1.10 Strange and anti-strange quarks are produced by the quark-antiquark combination ($q\bar{q} \rightarrow s\bar{s}$). 21
1.11 A cartoon showing jet quenching in central A-A collisions [43]. 22
1.12 Photon production through the (a) quark-antiquark annihilation ($q + \bar{q} = \gamma + g$) and (b) Compton scattering ($q + g = \gamma + \bar{q}$). 23
1.13 A semi-central heavy ion collision is shown where the almond-shaped participant zone is shown in red, and the spectator zone in blue. Arrows represent pressure gradients. The reaction plane corresponds to the xz plane. (Figure taken from [55]. 25

2.1 Schematic diagram of the Large Hadron Collider complex at CERN depicting the accelerators, beam lines, and a selection of major detector experiments.The ALICE detector is marked with a closed yellow circle and is situated at Interaction Point 2 (IP2). Figure is taken from [25]. 43
2.2 Schematic layout of the ALICE experiment during LHC Run 2, showing the central barrel detectors (ITS, TPC, TRD, TOF, EMCAL, etc.) within the L3 solenoid, the forward detectors (V0, T0, ZDC, FMD, PMD, AD), and the muon spectrometer. Different sub-detectors are indicated by numbers. Source [22] 46
2.3 Diagram of the ALICE Inner Tracking System (ITS) showing its layered structure designed for high-precision vertexing and tracking [27]. 48
2.4 Layout of Time Projection Chamber (TPC) detector in the ALICE experiment at LHC [32]. 50
2.5 Schematic cross-section of the ALICE central barrel detector pendicular to the LHC beam direction showing sectors of TRD [39]. 53
2.6 Time alignment condition on V0A and V0C [42]. 54
2.7 The HLT system is integrated into the data-flow architecture of the ALICE experiment, in which the DAQ replicates the raw data from the detector and sends an identical copy to the HLT system [54]. 58
2.8 A scheme of AliRoot data processing framework [40] of ALICE experiment. 60

3.1 A pictorial representation of binning in the two-dimensional (η, ϕ) phase space. Two different scenarios are shown with the number of bins set to M = 6 and 10 in each direction. Figure illustrate the increasing resolution of the bins in the phase space. As M increases, the bin sizes become smaller. 76
3.2 Pictorial representation of binning and the distribution of particles in an event mapped onto the (η, ϕ) phase space partitioned with M = 4 bins along each dimension. 77
3.3 The cofficient λ_q as a function of order of the moment q shows distinct behaviours for the systems, one-phase, two-phase and a system with no intermittency [48]. 84

3.4 V0M amplitude distribution measured in Xe-Xe collisions recorded using ALICE at LHC, are divided in various multiplicity classes. The distribution is fitted using the Gluaber model function, represented by the red line(Figure Ref. [57]). 89
3.5 HIJING (LHC17j7): (a) V_z distribution and (b) Centrality distribution for the most central HIJING event samples. 92
3.6 HIJING (LHC17j7): Transverse momentum (p_T) distribution (b) Multiplicity distributions (c) pseudorapidity (η) distributions and (d) azimuthal angle (ϕ) distributions of generated and reconstructed charged particle tracks in Xe-Xe collisions simulated using the HIJING model at $\sqrt{s_{NN}} = 5.44$ TeV. A case of $0.4 \leq p_T \leq 1.0$ GeV/c interval is shown. 93
3.7 HIJING (LHC17j7) : Two dimensional tracking efficiency maps in (η, ϕ) phase space for four p_T bins, in case of $M = 40$ for the 0-5% central events in $|\eta| \leq 0.8$ region. 94
3.8 HIJING (LHC17j7): F_2 versus $\ln M^2$plot for generated and reconstructed events showing closure test for the charged particles in p_T bins $0.4 \leq p_T \leq 0.6$ GeV/c, $0.4 \leq p_T \leq 1.0$ GeV/c, $0.4 \leq p_T \leq 1.5$ GeV/c and $0.4 \leq p_T \leq 2.0$ GeV/c. The bottom panels display the ratio of $F_q^{rec}(M)$ to $F_q^{gen}(M)$. . 95
3.9 HIJING (LHC17j7): $\ln F_q$ vs $\ln M^2$ plots for (a) Reconstructed and (b) Generated charged particles in the p_T bin $0.4 \leq p_T \leq 1.0$ GeV/c with FB-768 96
3.10 HIJING (LHC17j7): *F-scaling* plot for the (a) Reconstructed and (b) Generated charged particles in the p_T bin $0.4 \leq p_T \leq 1.0$ GeV/c (FB-768). . . 96
3.11 HIJING (LHC17j7): $\ln \beta_q$ versus $\ln(q-1)$ for the (a) Reconstructed and (b) Generated event samples. The slope ν is extracted for the p_T interval $0.4 \leq p_T \leq 1.0$ GeV/c (FB-768). 97

4.1 (a) Primary vertex distribution of selected events and (b) the centrality distribution of the most central (i.e., 0-5%) Xe–Xe collision events at $\sqrt{s_{NN}} =$ 5.44 TeV. 109
4.2 The charged particle multiplicity distributions in the kinematic acceptance with $|\eta| \leq 0.8$ and $0 \leq \phi \leq 2\pi$ recorded by ALICE detector at LHC during RUN 2 for (a) wide p_T bins and (b) narrow p_T bins. 109
4.3 (a) Pseudorapidity (η) and (b) azimuthal angle (ϕ) distributions of the charged particles produced in wide p_T bins ($0.4 \leq p_T \leq 1.0$ GeV/c, $0.4 \leq p_T \leq 1.5$ and $0.4 \leq p_T \leq 2.0$ GeV/c), as recorded by ALICE in Xe–Xe collisions at $\sqrt{s_{NN}} = 5.44$ TeV. 110
4.4 (a) Pseudorapidity (η) and (b) azimuthal angle (ϕ) distributions of the charged particles in narrow p_T bins ($0.4 \leq p_T \leq 0.6$ GeV/c, $0.5 \leq p_T \leq 0.8$ GeV/c and $0.6 \leq p_T \leq 1.0$ GeV/c) produced in Xe–Xe collisions at $\sqrt{s_{NN}} = 5.44$ TeV. 110
4.5 Log-log plot of the average bin content $\langle n_i \rangle$ as a function of M^2 for (a) wide p_T bins and (b) narrow p_T bins. 111

4.6 F_q^e distributions (q = 2, 3, 4 and 5) determined for the charged particles produced in the p_T bin $0.4 \leq p_T \leq 1.0$ GeV/c having (η, ϕ) phase space partitioned with M = 10. 113
4.7 F_q^e distributions (q = 2, 3, 4 and 5), determined for the charged particles in the $0.4 \leq p_T \leq 1.0$ GeV/c bin, with (η, ϕ) phase space partitioned in 25 bins (M = 25) along each dimension. This figure and Fig. 4.6 shows how event factorial moment distributions behave with change in phase space binning and order of the moments. 114
4.8 *M-scaling* plot for $q = 2, 3, 4$ and 5 for all M values in the p_T bin $0.4 \leq p_T \leq 1.0$ GeV/c for 0-5% central events. 114
4.9 (a) Plot of $\ln F_q$ versus $\ln M^2$ (*M-scaling*) for only high-M values, showing a linear behaviour (b) Dependence of the intermittency indices φ_q on the order q is shown. In both figures lines connecting the data points are to guide the eye. 115
4.10 F-scaling plot for $q = 2, 3, 4$ and 5 for all M values in the p_T bin $0.4 \leq p_T \leq 1.0$ GeV/c. 116
4.11 (a) F-scaling with straight line fits and (b) $\ln \beta_q$ vs $\ln(q-1)$ plot with line fit that gives a slope termed as the scaling exponent (ν), in case of the p_T bin $0.4 \leq p_T \leq 1.0$ GeV/c. 116
4.12 D_q vs q plot for q = 2, 3, 4 and 5 for the charged particles produced in the p_T bin $0.4 \leq p_T \leq 1.0$ GeV/c from the 0-5% central Xe–Xe collision events. 117
4.13 λ_q vs q plot for the charged particles produced in the p_T bin $0.4 \leq p_T \leq 1.0$ GeV/c for 0-5% central Xe–Xe collision events. 118
4.14 $\ln F_q(M)$ vs. $\ln M^2$ plots (M-scaling) for $q = 2, 3, 4$, and 5 for charged particles produced in narrow p_T bins in the mid-rapidity region of the most central Xe–Xe events recorded using ALICE. 119
4.15 $\ln F_q(M)$ vs. $\ln M^2$ plots (M-scaling) in case of $q = 2, 3, 4$, and 5, for the charged particles produced in wide p_T bins in the mid-rapidity region of the most central Xe–Xe events recorded using ALICE. 120
4.16 (a), (c), (e) $\ln F_q$ vs $\ln F_2$ and (b), (d), (f) $\ln \beta_q$ vs $\ln(q-1)$ plot for the charged particles produced in the narrow p_T bins $0.4 \leq p_T \leq 0.6$ GeV/c , $0.5 \leq p_T \leq 0.8$ GeV/c and $0.6 \leq p_T \leq 1.0$ GeV/c for the most central Xe–Xe events at $\sqrt{s_{NN}}$ = 5.44 TeV. 121
4.17 (a), (c) $\ln F_q$ vs $\ln F_2$ and (b), (d) $\ln \beta_q$ vs $\ln(q-1)$ plots for the charged particles produced in the p_T bins $0.4 \leq p_T \leq 1.5$ GeV/c and $0.4 \leq p_T \leq 2.0$ GeV/c. 122
4.18 Scaling exponent (ν) as a function of p_T interval for the (a) narrow p_T bins ($0.4 \leq p_T \leq 0.6$ GeV/c , $0.5 \leq p_T \leq 0.8$ GeV/c and $0.6 \leq p_T \leq 1.0$ GeV/c) (b) wider p_T bins ($0.4 \leq p_T \leq 1.0$ GeV/c, $0.4 \leq p_T \leq 1.5$ GeV/c and $0.4 \leq p_T \leq 2.0$ GeV/c) for the most central Xe–Xe collision events at $\sqrt{s_{NN}}$ = 5.44 TeV. Theoretically predicted average [2] value of ν and the one predicted by the SCR model [5, 6] are also shown. Horizontal lines on the markers show the p_T intervals, with filled boxes depicting systematic uncertainty, whereas the vertical bars represent statistical uncertainty. . . 123

4.19 (a) D_q versus q and (b) λ_q versus q, across various p_T bin interval for the charged particles produced in the central Xe–Xe collision events. The vertical error bar show the fitting errors. 124
4.20 *M-scaling* and *F-scaling* for the charged particles produced in the $0.4 \leq p_T \leq 1.0$ GeV/c transverse momentum bin for various centralities. 126
4.21 $\ln\beta_q$ versus $\ln(q-1)$ plots for the charged particles with $0.4 \leq p_T \leq 1.0$ GeV/c, $|\eta| \leq 0.8$ and $0 \leq \phi \leq 2\pi$ in the centrality bins (a) 5-10%, (b) 10-20%, (c) 20-30% and (d) 30-40%. Lines joining the markers are the linear fits to the data that are used to extract the scaling exponents ν. 127
4.22 The scaling exponent ν as a function of collision centrality for Xe–Xe collision events in the two p_T intervals $0.4 \leq p_T \leq 0.6$ GeV/c and $0.4 \leq p_T \leq 1.0$ GeV/c. 128
4.23 Relative Uncertainties in the value of scaling exponent ν across various transverse momentum bins. (a) $0.5 \leq p_T \leq 0.8$ GeV/c and (b) $0.6 \leq p_T \leq 1.0$ GeV/c, (c) $0.4 \leq p_T \leq 0.6$ GeV/c, (d) $0.4 \leq p_T \leq 1.0$ GeV/c, (e) $0.4 \leq p_T \leq 1.5$ GeV/c and (f) $0.4 \leq p_T \leq 2.0$ GeV/c 129
4.24 Comparison of $\ln F_q$ versus $\ln M^2$ plot for the charged particles produced in the Xe–Xe collision at $\sqrt{s_{NN}} = 5.44$ TeV (this thesis) with that in the Pb–Pb collision at $\sqrt{s_{NN}} = 2.76$ TeV and HIJING Xe–Xe data ($0.4 \leq p_T \leq 1.0$ GeV/c). 131
4.25 Comparison of the scaling exponent (ν) versus p_T bin plot for charged particles produced in the Xe–Xe collision at $\sqrt{s_{NN}} = 5.44$ TeV (this thesis) with that of charged particles produced in Pb–Pb collision at $\sqrt{s_{NN}} = 2.76$ TeV [7]. 132
4.26 Fractal dimension D_q as a function of the order of the moment q. Plots are for the charged particles produced in the $0.4 \leq p_T \leq 1.0$ GeV/c bin, measured in central Xe–Xe collision at $\sqrt{s_{NN}} = 5.44$ TeV (this thesis) and central Pb–Pb collision at $\sqrt{s_{NN}} = 2.76$ TeV [7]. Results from experiment are compared with the baseline Toy model [8] behaviour. 133
4.27 λ_q versus q: A comparative study. 134

5.1 Schematic overview of the two primary AMPT configurations: the default (DF) mode (left) and the string-melting (SM) mode (right). 141
5.2 Pseudorapidity density distributions of charged particles generated using the SM AMPT at different centrality ranges compared with that of the ALICE data [29]. 145
5.3 Normalized charged-particle density distribution as a function of number of participants from AMPT (SM) events. Data points from ALICE [29] are also shown for comparison. 146
5.4 Events from Xe–Xe central collisions at $\sqrt{s_{NN}} = 5.44$ TeV analyzed using the string-melting (SM) AMPT model. Pseudorapidity (η) and azimuthal angle (ϕ) distributions of the generated charged particles (protons, kaons, and pions) within $|\eta| \leq 0.8$ and $0 \leq \phi \leq 2\pi$ for the p_T bin are shown. . . 147
5.5 Multiplicity distribution plot of charged particles in Xe–Xe collisions at $\sqrt{s_{NN}} = 5.44$ TeV with the SM AMPT model across different p_T intervals. 148
5.6 log-log plot of the average charged particle bin multiplicity for the p_T bins in the SM AMPT model as a function of number of bins. 149

5.7 *(M-scaling)* log-log plots of $F_q(M)$, (q = 2, 3, 4 and 5) as a function of the number of cells (M^2) for the p_T bins (a) $0.4 \leq p_T \leq 0.6$ GeV/c, (b) $0.4 \leq p_T \leq 1.0$ GeV/c, (c) $0.4 \leq p_T \leq 2.0$ GeV/c, (d) $0.6 \leq p_T \leq 0.8$ GeV/c, (e) $0.6 \leq p_T \leq 1.0$ GeV/c and (f) $0.6 \leq p_T \leq 2.0$ GeV/c. 150
5.8 *(F-scaling)* log-log plots of (F_q), (q = 3, 4, 5) as a function of F_2 for the p_T bins (a) $0.4 \leq p_T \leq 0.6$ GeV/c, (b) $0.4 \leq p_T \leq 1.0$ GeV/c, (c) $0.4 \leq p_T \leq 2.0$ GeV/c, (d) $0.6 \leq p_T \leq 0.8$ GeV/c, (e) $0.6 \leq p_T \leq 1.0$ GeV/c and (f) $0.6 \leq p_T \leq 2.0$ GeV/c. Lines joining the data points are the straight line fits to obtain β_q (the slope). 152
5.9 Plot for $\ln\beta_q$ vs $\ln(q-1)$ from the various p_T intervals. The lines joining the markers represent the fits used to extract the slope "ν", referred to as the scaling exponent. Error bars denote the fitting uncertainties in the β_q values. 153
5.10 Scaling exponent (ν) as a function of p_T intervals and its comparison with the results from Pb-Pb system at $\sqrt{s_{NN}}$ = 2.76 TeV [31] for the same p_T bins. Horizontal bars on both sides of the markers are to show the p_T bins with marker at the center of the bin. Vertical error bars are the fitting errors. 153
5.11 Intermittency indices (φ_q) for q = 2, 3, 4 and 5 as a function of q in various p_T bins is shown. Lines joining the data points are to guide the eye. . . . 155
5.12 D_q as function of q from various p_T intervals are shown. Lines joining the data markers are to guide the eye. 155
5.13 λ_q as a function of order of moments (q) for the SM AMPT events for different p_T bins. Experimental value of λ_q from ALICE (This Thesis) are also shown. 156

B.1 Plots illustrating (left to right): (i) $\ln F_q(M)$ versus $\ln M^2$ (M-scaling), (ii) $\ln F_q(M)$ versus $\ln F_2(M)$ (F-scaling), and (iii) $\ln\beta_q$ versus $\ln(q-1)$ for charged particles in the narrow p_T intervals (a) $0.4 \leq p_T \leq 1.0$ GeV/c, (b) $0.4 \leq p_T \leq 1.5$ GeV/c, and (c) $0.4 \leq p_T \leq 2.0$ GeV/c, using Filter Bit 32. 170
B.2 Plots illustrating (left to right): (i) $\ln F_q(M)$ versus $\ln M^2$ (M-scaling), (ii) $\ln F_q(M)$ versus $\ln F_2(M)$ (F-scaling), and (iii) $\ln\beta_q$ versus $\ln(q-1)$ for charged particles in the wide p_T intervals (a) $0.4 \leq p_T \leq 1.0$ GeV/c, (b) $0.4 \leq p_T \leq 1.5$ GeV/c, and (c) $0.4 \leq p_T \leq 2.0$ GeV/c, using filter bit 32. . 171
B.3 Plots illustrating (left to right): (i) $\ln F_q(M)$ versus $\ln M^2$ (M-scaling), (ii) $\ln F_q(M)$ versus $\ln F_2(M)$ (F-scaling), and (iii) $\ln\beta_q$ versus $\ln(q-1)$ for charged particles in the narrow p_T intervals (a) $0.4 \leq p_T \leq 0.6$ GeV/c, (b) $0.5 \leq p_T \leq 0.8$ GeV/c, and (c) $0.6 \leq p_T \leq 1.0$ GeV/c, with the centrality estimator CL0. 172
B.4 Plots illustrating (left to right): (i) $\ln F_q(M)$ versus $\ln M^2$ (M-scaling), (ii) $\ln F_q(M)$ versus $\ln F_2(M)$ (F-scaling), and (iii) $\ln\beta_q$ versus $\ln(q-1)$ for charged particles in the wide p_T intervals (a) $0.4 \leq p_T \leq 1.0$ GeV/c, (b) $0.4 \leq p_T \leq 1.5$ GeV/c, and (c) $0.4 \leq p_T \leq 2.0$ GeV/c, with the centrality estimator CL0. 173

B.5 Plots illustrating (left to right): (i) $\ln F_q(M)$ versus $\ln M^2$ (M-scaling), (ii) $\ln F_q(M)$ versus $\ln F_2(M)$ (F-scaling), and (iii) $\ln \beta_q$ versus $\ln(q-1)$ for charged particles in the narrow p_T intervals (a) $0.4 \leq p_T \leq 0.6$ GeV/c, (b) $0.5 \leq p_T \leq 0.8$ GeV/c, and (c) $0.6 \leq p_T \leq 1.0$ GeV/c, with the vertex cut $|V_z| \leq 8$ cm. 174
B.6 Plots illustrating (left to right): (i) $\ln F_q(M)$ versus $\ln M^2$ (M-scaling), (ii) $\ln F_q(M)$ versus $\ln F_2(M)$ (F-scaling), and (iii) $\ln \beta_q$ versus $\ln(q-1)$ for charged particles in the wide p_T intervals (a) $0.4 \leq p_T \leq 1.0$ GeV/c, (b) $0.4 \leq p_T \leq 1.5$ GeV/c, and (c) $0.4 \leq p_T \leq 2.0$ GeV/c, with the vertex cut $|V_z| \leq 8$ cm. 175
B.7 Plots illustrating (left to right): (i) $\ln F_q(M)$ versus $\ln M^2$ (M-scaling), (ii) $\ln F_q(M)$ versus $\ln F_2(M)$ (F-scaling), and (iii) $\ln \beta_q$ versus $\ln(q-1)$ for charged particles in the narrow p_T intervals (a) $0.4 \leq p_T \leq 0.6$ GeV/c, (b) $0.5 \leq p_T \leq 0.8$ GeV/c, and (c) $0.6 \leq p_T \leq 1.0$ GeV/c, with the vertex cut $|V_z| \leq 12$ cm. 176
B.8 Plots illustrating (left to right): (i) $\ln F_q(M)$ versus $\ln M^2$ (M-scaling), (ii) $\ln F_q(M)$ versus $\ln F_2(M)$ (F-scaling), and (iii) $\ln \beta_q$ versus $\ln(q-1)$ for charged particles in the wide p_T intervals (a) $0.4 \leq p_T \leq 1.0$ GeV/c, (b) $0.4 \leq p_T \leq 1.5$ GeV/c, and (c) $0.4 \leq p_T \leq 2.0$ GeV/c, with the vertex cut $|V_z| \leq 12$ cm. 177
B.9 Plots illustrating (left to right): (i) $\ln F_q(M)$ versus $\ln M^2$ (M-scaling), (ii) $\ln F_q(M)$ versus $\ln F_2(M)$ (F-scaling), and (iii) $\ln \beta_q$ versus $\ln(q-1)$ for charged particles in the narrow p_T intervals (a) $0.4 \leq p_T \leq 0.6$ GeV/c and (b) $0.6 \leq p_T \leq 1.0$ GeV/c, with the ITS cluster cut TPCNcls ≤ 80. 178
B.10 Plots illustrating (left to right): (i) $\ln F_q(M)$ versus $\ln M^2$ (M-scaling), (ii) $\ln F_q(M)$ versus $\ln F_2(M)$ (F-scaling), and (iii) $\ln \beta_q$ versus $\ln(q-1)$ for charged particles in the wide p_T intervals (a) $0.4 \leq p_T \leq 1.0$ GeV/c, (b) $0.4 \leq p_T \leq 1.5$ GeV/c, and (c) $0.4 \leq p_T \leq 2.0$ GeV/c, with the ITS cluster cut TPCNcls ≤ 80. 179
B.11 Plots illustrating (left to right): (i) $\ln F_q(M)$ versus $\ln M^2$ (M-scaling), (ii) $\ln F_q(M)$ versus $\ln F_2(M)$ (F-scaling), and (iii) $\ln \beta_q$ versus $\ln(q-1)$ for charged particles in the narrow p_T intervals (a) $0.4 \leq p_T \leq 0.6$ GeV/c and (b) $0.6 \leq p_T \leq 1.0$ GeV/c, with the ITS cluster cut ITSNcls ≤ 3. 180
B.12 Plots illustrating (left to right): (i) $\ln F_q(M)$ versus $\ln M^2$ (M-scaling), (ii) $\ln F_q(M)$ versus $\ln F_2(M)$ (F-scaling), and (iii) $\ln \beta_q$ versus $\ln(q-1)$ for charged particles in the wide p_T intervals (a) $0.4 \leq p_T \leq 1.0$ GeV/c, (b) $0.4 \leq p_T \leq 1.5$ GeV/c, and (c) $0.4 \leq p_T \leq 2.0$ GeV/c, with the ITS cluster cut TPCNcls ≤ 3. 181

List of Tables

1.1 Classification of quarks and antiquarks [3, 6]. Q, U, D, C, S, T, B represent charge, upness, downness, charmness, strangeness, topness, and beauty quantum numbers. . . . 4

1.2 Families of leptons and antileptons [3, 6]. The symbols Q, L_e, L_μ, and L_τ denotes the electric charge and the corresponding lepton numbers of the electron, muon, and tau particles, respectively. . . . 5

1.3 The four fundamental interactions of nature. . . . 6

2.1 Summary of LHC collision systems, center-of-mass energies, and integrated luminosities across different run periods. . . . 45

3.1 Details of experimental dataset analyzed in this work. . . . 85

3.2 Details of Monte-Carlo (HIJING) from ALICE production. . . . 86

3.3 List of the kinematic cuts used for the track selection. . . . 90

4.1 Scaling exponent (ν) from the experimental transverse momentum bins across a range below 2.0 GeV/c. . . . 123

4.2 Cuts varied for the estimation of systematic uncertainties. . . . 128

5.1 Extracted values of the scaling exponent (ν) for charged particles in different p_{T} intervals. . . . 151

CHAPTER 1

INTRODUCTION

In any field of science, a strong working relationship between theorists and experimentalists is essential for expanding our knowledge. The role of an experimentalist is to determine which of these theories is correct, whereas theorists focus primarily on imagining how the world may be. Even if the "glory" is undoubtedly most of the time received for theoretical work, the key to success is a collaborative effort by both experimentalists and theorists. An excellent example is the study of elementary particles, which explores the idea that the world's matter is composed of smaller, more fundamental particles. Theoretical and experimental work in high-energy physics, including work on accelerator science and technology, has assisted in discovering such basic elements of matter [1]. In order to investigate the basics of matter and, consequently, the nature of fundamental interactions, the high-energy collision experiments are performed at big accelerator facilities. On the theoretical side, according to studies based on Lattice Quantum Chromodynamics (QCD), at extremely high temperature and energy density, ordinary nuclear matter undergoes a

phase transition. The matter in the hadronic state transitions into a quark-gluon plasma (QGP), where quarks and gluons exist freely in a deconfined state. This state is believed to have existed for only a few microseconds at the very early stages of the Universe. In the laboratory, the ultra-relativistic heavy-ion collisions produce a very hot and dense nuclear matter, providing a possible environment to create the QGP state. These experiments are performed at big accelerator facilities to study the properties of QGP, to test the QCD predictions, and to learn about the fundamentals of matter.

An important aspect of studying heavy-ion collision, particularly at the Large Hadron Collider (LHC) operated by the European Organization for Nuclear Research (CERN) in Geneva–the world's largest and most powerful particle accelerator–is to understand the production mechanism of the particles in the these collisions. From exhaustive studies in the field, both theoretical and experimental, it has been established that matter is composed of quarks and leptons, whose dynamics are governed fundamentally by gravity, electromagnetism, and the weak and strong nuclear forces. Among these, gravity is the weakest of the four fundamental interactions and yet extends throughout all of space time. Charged particles participate in electromagnetic interactions, which are governed by Quantum Electrodynamics (QED). The weak interaction is responsible for beta decay and several other nuclear processes, whereas the strong force binds the constituents of the atomic nucleus together. The theory describing weak interactions is called Quantum Flavour Dynamics (QFD). Among the four fundamental interactions, gravity is the weakest, whereas the strong interaction exhibits the greatest strength. A model known as the Standard Model, provides a successful basic understanding of elementary particle physics and describes the interactions among them[1, 3] without including gravitational force.

In the following sections, relativistic heavy-ion collisions, some important kinematic measurable signatures of the hot and dense nuclear matter (the QGP), and the widely accepted model explaining the characteristics of matter and the fundamental interactions between its constituents and the Standard Model, are discussed.

1.1 The Standard Model

The Standard Model (SM) is the most successful framework in particle physics, providing a detailed understanding of the fundamental particles and their interactions – namely, the weak, electromagnetic, and the strong force. Weak and electromagnetic force are also combinely known as electroweak force [3]. In SM all elementary particles are defined by their mass and a collection of quantum numbers, such as charge, spin, baryon and lepton quantum number etc. Fig. 1.1 provides an overview of the elementary particles and the fundamental interactions described by the Standard Model.

Based on their intrinsic spin, elementary particles are grouped into two categories: integer

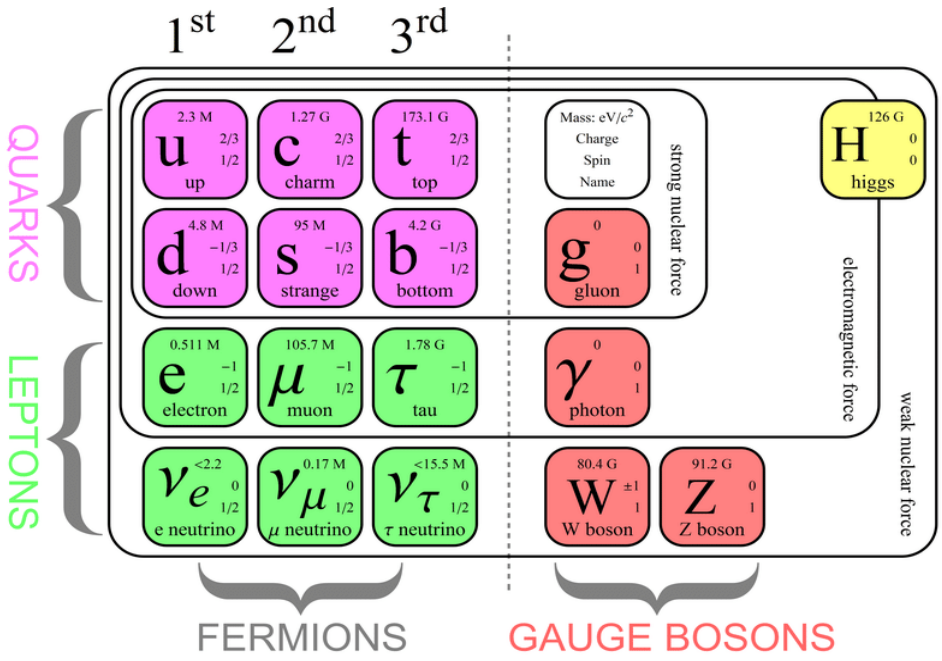

Figure 1.1: Elementary particles and fundamental interactions as per the Standard Model of particle physics [4].

spin and half-integer spin particles. The fundamental particles with half-integer $(\frac{1}{2})$ spin are known as fermions that obey Fermi-Dirac statistics and are subject to the Pauli's exclusion principle [5]. Whereas particles with integral spin are known as bosons, which obey the Bose-Einstein statistics. The fermions are further classified into two groups: quarks, which participate in both electromagnetic and strong interactions, and leptons, which interact only through electroweak forces. The quarks participate in strong interactions as they carry color charges (red, green, and blue) and fractional electrical charges of $+\frac{2}{3}|e|$

or $-\frac{1}{3}|e|$. The quarks exist in 6 different flavors: u (up), d (down), s (strange) , c (charm), b (bottom), and t (top) and are classified into three generations. The up and down quarks are part of the first generation, strange and charm quarks are part of the second generation, charm and bottom quarks belong to the third generation [6]. Quarks in the second and third generations are unstable and decay through the weak interaction into quarks of the earlier generations. The only stable generation is the first one (up and down) [5], the most prevalent quarks in the universe with invariant masses of around 2.2 and 4.7 MeV, respectively. The classification of quarks, along with their mass, charge, and quantum numbers is given in Table 1.1.

Leptons are also grouped into three generations, each comprising a charged lepton and its

Generation	Quark, Anti-quark	Mass	Q	U	D	C	S	T	Baryon No. (B).
1st	u, $\bar{u}$	2.2^{+5}_{-4} MeV/c^2	$\pm\frac{2}{3}$	±1	0	0	0	0	$\pm\frac{1}{3}$
	d, $\bar{d}$	4.7^{+5}_{-4} MeV/c^2	$\mp\frac{1}{3}$	0	∓1	0	0	0	$\pm\frac{1}{3}$
2nd	c, $\bar{c}$	1.275^{+5}_{-4} GeV/c^2	$\pm\frac{2}{3}$	0	0	±1	0	0	$\pm\frac{1}{3}$
	s, $\bar{s}$	95^{+5}_{-4} MeV/c^2	$\mp\frac{1}{3}$	0	0	0	∓1	0	$\pm\frac{1}{3}$
3rd	t, $\bar{t}$	$173^{\pm4}$ GeV/c^2	$\pm\frac{2}{3}$	0	0	0	0	±1	$\pm\frac{1}{3}$
	b, $\bar{b}$	$4.18^{+0.04}_{-0.03}$ GeV/c^2	$\mp\frac{1}{3}$	0	0	0	0	∓1	$\pm\frac{1}{3}$

Table 1.1: Classification of quarks and antiquarks [3, 6]. Q, U, D, C, S, T, B represent charge, upness, downness, charmness, strangeness, topness, and beauty quantum numbers.

associated neutral neutrino. The first-generation lepton, the electron (e), carries a negative unit charge, while the higher-generation leptons, the muon (μ) and tau (τ), are heavier counterparts of the electron [6]. The neutral leptons denoted by ν in Table 1.2 are referred to as neutrinos. The muon (μ) and tauon (τ) are unstable and decay spontaneously into electrons, neutrinos, and other particles. The muon has a characteristic lifetime of 2.2×10^{-6} s, whereas the tau lepton lives much shorter, around 2.9×10^{-13} s. In 1956,

experiments provided the first direct evidence of neutrinos as separate particles. Neutrinos do not decay; instead, they transform between six distinct flavors. The three generations of leptons are distinguished by their masses, electric charges, and unique sets of quantum numbers. Here, Q denotes electric charge, while L_e, L_μ, and L_τ correspond to electron, muon, and tau lepton numbers, respectively as summarized in Table 1.2. All quarks and leptons have corresponding antiparticles that possess same mass and spin, but opposite electric charge and quantum numbers.

Bosons, have integer spin values and are not subject to the Pauli's Exclusion Princi-

Generation	Lepton / Antilepton	Q	L_e	L_μ	L_τ	Mass
1st	e, $\bar{e}$	∓ 1	± 1	0	0	0.511 MeV/c^2
	ν_e, $\bar{\nu}_e$	0	± 1	0	0	2 eV/c^2
2nd	μ, $\bar{\mu}$	∓ 1	0	± 1	0	105 MeV/c^2
	ν_μ, $\bar{\nu}_\mu$	0	0	± 1	0	0.19 MeV/c^2
3rd	τ, $\bar{\tau}$	∓ 1	0	0	± 1	1.73 GeV/c^2
	ν_τ, $\bar{\nu}_\tau$	0	0	0	± 1	18.2 MeV/c^2

Table 1.2: Families of leptons and antileptons [3, 6]. The symbols Q, L_e, L_μ, and L_τ denotes the electric charge and the corresponding lepton numbers of the electron, muon, and tau particles, respectively.

ple. The fundamental forces in the Standard Model framework are each mediated by the exchange of an integral spin gauge boson between interacting particles [7]. The weak nuclear force is mediated by the $W^\pm$ and Z^0 bosons. The electromagnetic force is described by Quantum Electrodynamics (QED) theory, with the photon (γ) mediating the interaction between charged particles. Lastly, the strong nuclear force is mediated by the gluon (g), which governs the interactions between particles carrying a color charge and is responsible for binding quarks into hadrons. The recently discovered Higgs boson (H) [8, 9] is also a part of the Standard Model, which is responsible for elementary particle masses [10, 11]. The Higgs boson, unlike the γ, g, Z, and $W^\pm$ bosons, has spin zero and is a scalar boson.

Fig. 1.1 displays the bosons of the Standard Model, categorized into gauge bosons and the scalar Higgs boson.

The Standard Model describes the known elementary particles and their fundamental interactions, based on gauge theory with an underlying gauge group structure [6] as

$$SU(3) \times SU(2) \times U(1)$$

The SU(3) group is associated with the strong interactions, representing the rotations in space of the three color charges of QCD. Where, the $SU(2) \times U(1)$ gauge symmetry group forms the theoretical foundation for electroweak unification [12]. Using the Higgs mechanism, the $SU(2) \times U(1)$ group spontaneously breaks down into SU(2) and U(1) groups underlying weak and electromagnetic interactions, producing three massive W^+, W^-, and Z^0 bosons and massless photon γ respectively [13]. This Higgs mechanism is considered responsible for giving mass to the elementary particles and the majority of known matter in the universe.

According to our current understanding, the dynamics of all matter is governed by the four types of fundamental interactions: electromagnetic, strong, weak, and gravitational (Table 1.3) [14, 15]. The electromagnetic interactions are responsible for almost all extra-

Interaction	Effective Coupling	Mediator Boson	Range	Spin/Parity
Strong	1	8 Gluons (G)	10^{-15}	1^-
Electromagnetic	10^{-2}	Photons (γ)	∞	1^-
Weak	10^{-7}	$W^{\pm}$, Z^0	10^{-18}	$1^-, 1^+$
Gravitational	10^{-39}	graviton (g)	∞	2^-

Table 1.3: The four fundamental interactions of nature.

nuclear physics events, particularly the bound states of electrons with nuclei, i.e., atoms and molecules, as well as intermolecular forces in liquids and solids. Strong interactions binds quarks into composite particles like protons and neutrons, and it provides the residual force that holds nuclei together. The weak interaction mediates β-decay, a fundamental nuclear process wherein an unstable nucleus undergoes transformation through the emission of

electrons (or positrons) and neutrinos. Gravitational interactions occur between all particle kinds [6]. Despite being dominant on a cosmic scale, gravity is by far the weakest of the fundamental interactions in particle physics experiments and not a part of the Standard Model.

1.2 The Quantum Chromodynamics (QCD)

Quantum Chromodynamics is a non-Abelian quantum field theory which describes the strong nuclear force governing interactions between quarks and gluons. Quarks and gluons are also known as partons. According to QCD, each quark may be characterized by three color charges, red, green, and blue, and a hadron made out of quarks is always colorless. There are a total of six color charges in the strong interactions, with each quark carrying one of the three colors $red(r)$, $green(g)$ or $blue(b)$ and antiquark carrying the corresponding anticolor ($\bar{r}$, $\bar{g}$, $\bar{b}$). A hadron consists of either three quarks or a quark-antiquark pair. Gluons mediate quark-quark interactions and carry one color and one anti-color, implying a total of 9 color combinations as [3].

$$r\bar{g}, r\bar{b}, b\bar{g}, b\bar{r}, g\bar{b}, g\bar{r}, \frac{1}{\sqrt{3}}\sqrt{(r\bar{r}-b\bar{b})}, \frac{1}{\sqrt{6}}\sqrt{(r\bar{r}+b\bar{b}-2g\bar{g})}, \frac{1}{\sqrt{3}}\sqrt{(r\bar{r}+g\bar{g}+2b\bar{b})}$$

However, only 8 active states of the gluons remain in these 9 combinations since

$$\frac{1}{\sqrt{3}}\sqrt{(r\bar{r}+g\bar{g}+2b\bar{b})}$$

is a colorless singlet. The force between quarks is not influenced by the color of the gluons involved in the interaction. Fig.1.2(a) and Fig.1.2(b) illustrates an electromagnetic interaction between two charges via one-photon exchange and a blue quark interacting with a green quark via the exchange of a green-antiblue gluon. Quarks can also interact with gluons [3], as shown in Fig. 1.2(c).

QCD is a non-Abelian gauge field theory, where the Lagrangian is invariant under local SU(3) transformations [13, 16]. The QCD Lagrangian density can be expressed as:

$$L_{QCD} = \sum_f q_f^k (i\gamma_\mu D_\mu^{kl} - m_f \delta_{kl}) q_f^l - \frac{1}{4} G_{\nu\mu}^a G_a^{\nu\mu} \tag{1.1}$$

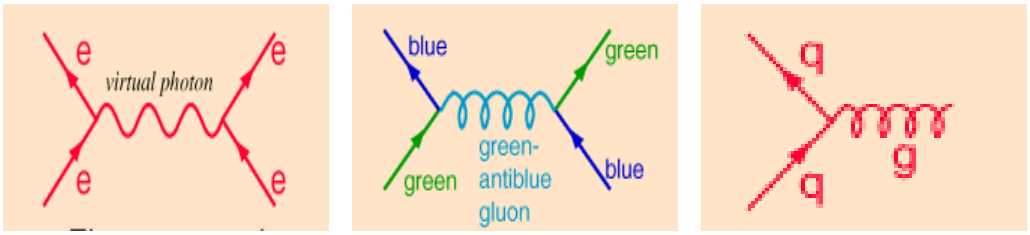

(a) (b) (c)

Figure 1.2: Schematics of (a) electromagnetic interaction between two charged particles and (b) strong interaction via gluon-mediated color charge exchange (c) strong interaction between two quarks.

where q_l^f is a quark-field with flavours f, color charge l, and mass m_f, and the sum runs over the six quark flavours (up, down, strange, charm, beauty, and top). The covariant derivative D_μ^{kl} introduces the interaction between quarks and gluons, and it is written as [13].

$$D_\mu^{kl} = \partial^\mu \delta_{kl} - ig_s \frac{\lambda_{kl}^a}{2} A_a^\mu \tag{1.2}$$

Here, A_a^μ are the gluon fields corresponding to eight color states, and λ_{kl}^a are the Gell-Mann matrices. The constant g_s quantifies the intensity of the interaction, and it is related to the strong coupling constant α_s as $g_s = 4\alpha_s$. The kinematics and dynamics of the gluons are described by the second term of Eq.(1.1), and $G_{\mu\nu}^a$ is expanded as

$$G_{\mu\nu}^a = \partial_\mu A_\nu^a - \partial_\nu A_\mu^a + g_s f^{abc} A_\mu^b A_\nu^c, \tag{1.3}$$

where f^{abc} corresponds to the structure constants of the SU(3) Lie algebra. Because the SU(3) group is non-Abelian, the structure constants are not null, and vertices between three and four gluons are possible in addition to vertices between a quark, an antiquark, and a gluon. Even though gluons are massless particles, the presence of gluon self-interactions implies that the color force is a short-range interaction. The peculiar properties of the strong interaction can be understood by investigating the relationship between the strong coupling constant α_s and the interaction's energy scale. The evolution of the value of α_s as

a function of the squared transferred momentum Q^2 is defined as:

$$\alpha_s(Q^2) = \frac{\alpha_s \mu^2}{1 + \frac{\alpha_s \mu^2}{12\pi}(33 - 2n_f) ln(\frac{Q^2}{\mu^2})} \tag{1.4}$$

Where n_f denotes the number of quark flavors and μ is the mass scale of the renormalization. The α_s evolution described by Eq.(1.4) is confirmed by experimental measurements as summarised in Fig. 1.3. It is evident from the figure that the coupling strength increases

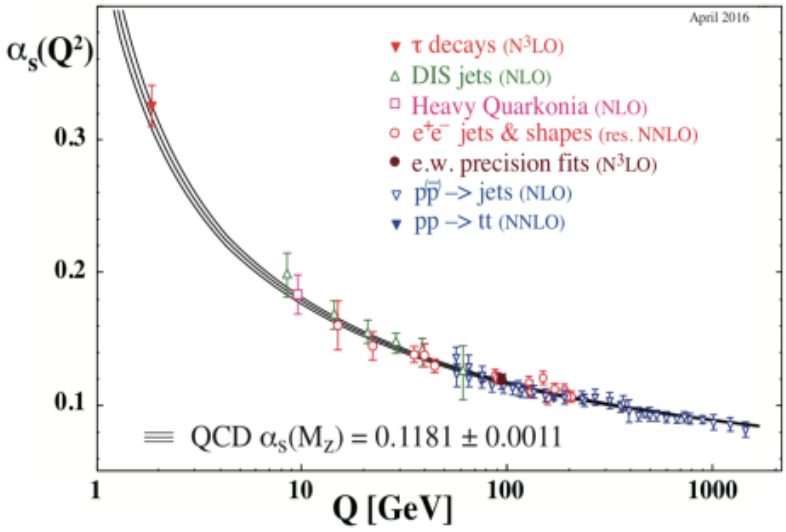

Figure 1.3: The coupling constant (α_s (Q^2)) as a function of different energy scales (Q) via various processes. The order of QCD Perturbation Theory used to extract α_s (Q^2) is indicated in brackets. The theoretical calculation of α_s is given by $\alpha_s(M_Z)$ [18].

as momentum transfer (Q) decreases, implying a large probed length scale [19]. This phenomenon is related to the so-called *confinement* property, which states that no isolated color object can be found in nature. The coupling decreases as Q increases, implying a small probed length scale. In the limit, when coupling tends to zero, the quarks and gluons behave as free particle, and this property is called *asymptotic freedom*. The formation of quark-gluon plasma (QGP) is a manifestation of this property of the strong interactions.

1.3 The QCD Phase Diagram

Asymptotic freedom leads directly to the idea that QCD matter transforms into the QGP, a system of deconfined quarks and gluons at high enough temperatures and densities. Since

quarks and gluons are no longer restricted as hadronic matter in this phase, where chiral symmetry is restored, they are the relevant degrees of freedom characterising the system's dynamics. To understand this transition into a deconfined state of matter, a phase diagram of QCD matter is studied as a function of baryochemical potential (μ_B) and temperature (T) [20]. Similar to how water can exist as a solid, liquid, or gas depending on temperature and pressure, it is proposed that QCD matter exists in various phases. A schema showing a possible QCD phase diagram in μ_B and T plane is shown in Fig.1.4. The baryon chemical potential (μ_B) quantifies the net baryon density, defined as the imbalance between baryon and antibaryon number densities. The region of the diagram where QCD matter exists in a gaseous state of confined hadrons within the relevant T and μ_B ranges is shown by the lower left portion of Fig.1.4, labelled as "hadron gas". As the temperature approaches zero ($T \rightarrow 0$ MeV) and the baryon chemical potential μ_B increases, the phase labeled "Nuclear Matter" in Fig. 1.4 emerges at $\mu_B \approx 950$ MeV. As μ_B rises above the nuclear matter regime in this low-temperature range, a transition into a gaseous phase of degenerate neutrons occurs, conditions similar to those found in neutron star cores. It is predicted that, the separating distance between neutrons decreases for larger μ_B values, and gas of free-roaming quarks forms and enters a color superconducting regime [21].

The lattice QCD calculations have shown that at vanishing baryochemical potential (i.e. $\mu_B \approx 0$ MeV), the hadronic system experiences a smooth transition [22] into the QGP phase when T rises to a high enough temperature. It is believed that the phase transition is first order around this temperature range for increasing values of μ_B, indicating the presence of a critical point in it's vicinity. Lattice QCD calculations become more difficult for non-zero μ_B. Recent QCD predictions suggest that the phase transition temperature for $\mu_B = 0$ MeV, called the critical temperature, is approximately $T_c = 156$ MeV [23]. Despite different techniques developed recently for real finite chemical potential and extensive experimental efforts, it is yet to determine whether crossover exists on the whole border of the QGP and hadron gas phases.

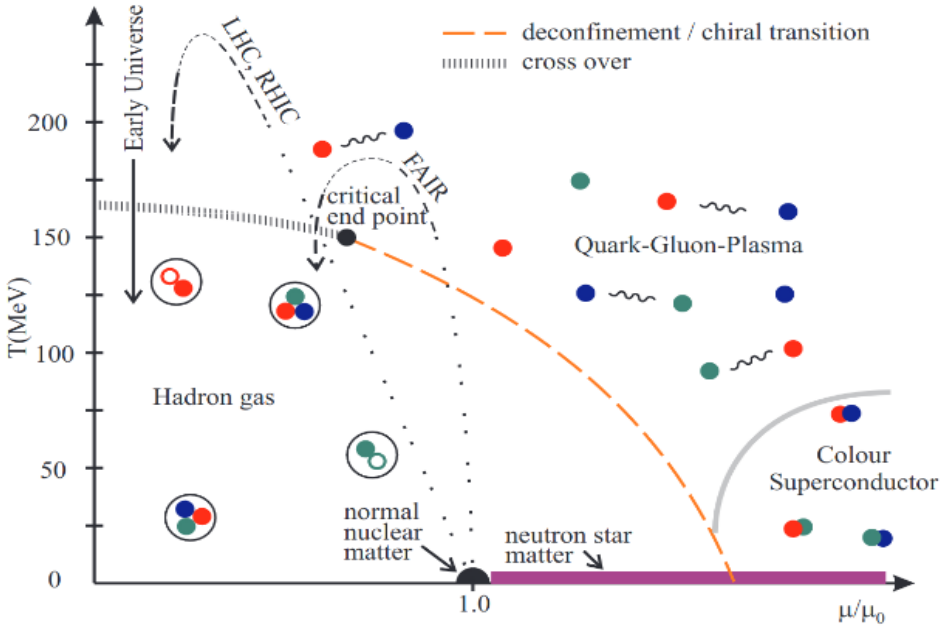

Figure 1.4: A schematic of the QCD phase diagram is shown as a function of temperature (T) and baryochemical potential (μ_B). The solid black line indicates the chemical freeze-out, while the dashed orange line depicts the chiral/deconfinement transition. Both end at the critical point, which is connected to the $\mu = 0$ axis by a cross-over around T $\approx$ 170 MeV. The ground state of nuclear matter is at T = 0 MeV and $\mu = \mu_0$. At high chemical potential and low temperature, a phase of colour superconductivity occurs. The dashed black lines indicate the estimated properties of the medium created by various experiments [24].

1.4 Heavy-ion collisions

Relativistic heavy-ion collisions is a versatile tool for creating the conditions needed to create QGP and thus to investigate various aspects of the QCD Phase Diagram. The main experiments where high-energy heavy-ion collisions are currently studied are the Brookhaven National Laboratory's Relativistic Heavy Ion Collider (RHIC) and the European Organisation for Nuclear Research's Large Hadron Collider (LHC) [25]. The centre-of-mass energy per nucleon pair achievable for Au−Au collisions at the RHIC and Pb−Pb collisions at the LHC are $\sqrt{s_{\mathrm{NN}}}$ = 5.04 GeV and 5.36 TeV respectively [26]. The study of heavy-ion collisions provides a unique window into the extreme conditions of temperature and energy density that existed microseconds after the Big Bang [27]. Studying the evolution of heavy-ion collisions help scientists unravel the mysteries of the early universe, understand the behaviour of nuclear matter under extreme conditions, and explore the phase diagram

of QCD. In a heavy-ion collision two relativistically accelerated heavy nuclei are longitudinally Lorentz contracted and are made to collide with each other. A schematic representation of the various stages of the relativistic heavy-ion collision is shown in Fig.1.5 and the space-time evolution after the collision is shown in Fig.1.6. At time t = 0, the two Lorentz contracted nuclei collide, depositing a significant amount of energy in a small volume in a very short time. If the energy density of the system produced by the collision is very high, a deconfined state of partons is formed after the collision. It is initially in a non-equilibrium state. As the system expands, the partons interact amongst themselves and the system approaches local thermal equilibrium. The local equilibrium occurs on a time scale of 1 fm/c [28]. Such a deconfined state of quarks and gluons in local equilibrium constitutes the quark-gluon plasma (QGP), wherein they exhibit nearly free motion. The system starts

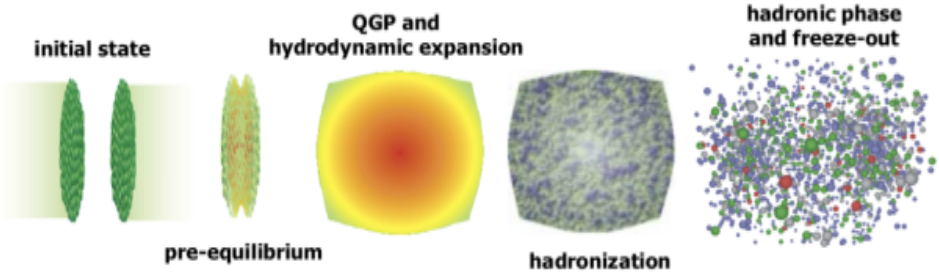

Figure 1.5: Systematic representation of the various stages of the relativistic heavy-ion collisions. Figure from Ref. [29]

expanding due to the pressure gradient and gradually cools down. After QGP's lifetime $\tau \approx 10$ fm/c [30], when the temperature reaches a critical value (T_c), the system's energy density falls below a critical density$\approx$ 1GeV/fm^3, and the quarks and gluons recombine to form colour-neutral hadrons (mesons and baryons). The process of hadron formation is known as hadronization. During the initial stages of this hadronization, hadrons and free partons are expected to coexist; however, over time, these parts disappear, leaving the system with only hadron gas. As the system keeps expanding, at temperature $T = T_{ch}$, the probability of inelastic interactions among the hadrons is almost zero. This temperature ($T = T_{ch}$) is called the chemical freeze-out temperature. This is the phase where the stable particle ratios get frozen with the elastic collisions still going on. When the mean free

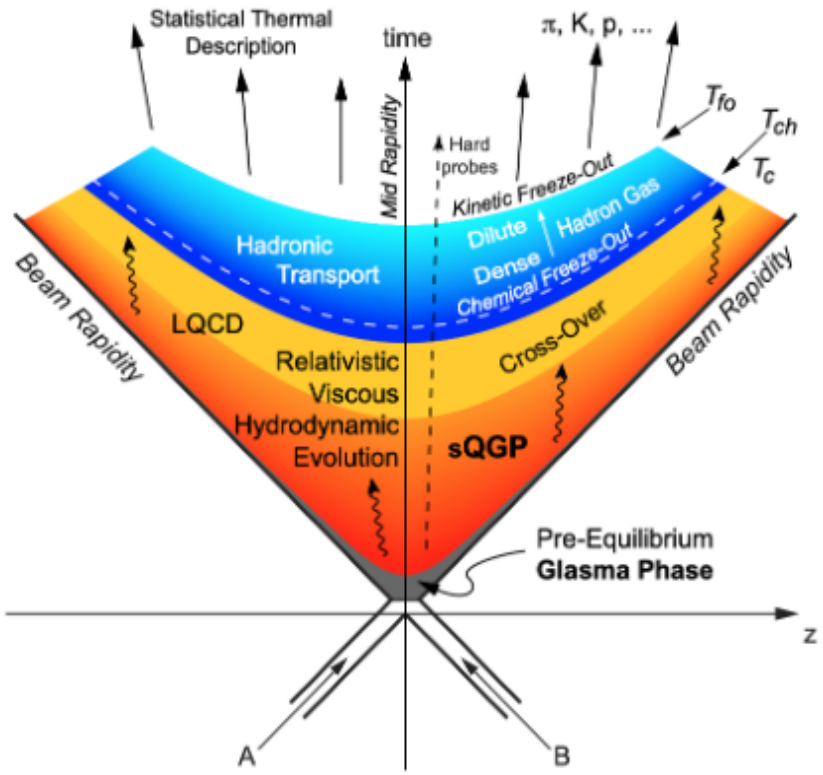

Figure 1.6: Visualization of the spacetime evolution of the system created in relativistic heavy-ion collisions. Figure from Ref. [25].

path becomes sufficiently large, elastic collisions among hadrons stop, leading to kinetic or thermal freeze-out. The temperature at this point is referred to as the thermal/kinetic freeze-out temperature (T_{fo}). This is the phase where transverse momentum spectral shape of particles get frozen, and the system can no longer maintain thermal equilibrium. Finally, all the hadrons fly towards the detector after the freeze-out.

Experimental detectors record characteristics like momenta, energy, velocity etc. of the particles, providing crucial information about the collision dynamics. By studying various observables obtained from the measurables of these produced particles, experimentalists deduce the QGP formation and its properties. However, if the system created in a heavy-ion collision does not meet the requirements of high temperature and high energy density so as to form QGP, in that case, another scenario of space-time evolution might also be feasible, shown on the left side of Fig. 1.5 In that case, the system is characterized by purely hadronic degrees of freedom, with a pre-hadronic phase forming rapidly post-collision. As

the hadron gas freezes the hadrons come out of the system and are detected by detectors.

Centrality of the collisions

The impact parameter (b), representing the perpendicular offset between the centers of two colliding nuclei at the instant of collision, dictates the extent and geometry of the nuclear overlap region (Fig. 1.7). In the overlap region, nucleons of one nucleus interact with those from the other nucleus termed as participants, establishing the number of participants (N_{part}). In contrast, the nucleons outside the overlap region move away from each other in the beam direction and are referred to as spectators. The geometrical properties of this overlap region in heavy-ion collision are characterized by the impact parameter (b), the number of participants (N_{part}), and the number of binary nucleon-nucleon collisions (N_{coll}). A vanishing impact parameter ($b \approx 0$) results in the most central collision [31]. As a result, the collision's centrality decreases as the impact parameters increase. However on the other side, collision with the impact parameter ($b \approx 2R$), where R is the radius of the nucleus, are associated with the most peripheral collisions [32]. Because of the small typical number of participants, the properties of these collisions are more like single-nucleon collisions than central heavy-ion collisions.

In heavy-ion collisions, centrality is determined by the percentile of the total cross-section for hadronic interactions. Selecting the centrality and determining the number of participants and spectators is very crucial because they are required to normalize the other measured observables before comparing them to other collision system, such as smaller collision systems of proton-lead (p-Pb) and proton-proton (pp). In heavy-ion collisions, these initial geometric quantities b, $N_{\rm part}$ and $N_{\rm coll}$ are not directly determined from experiments. Centrality of a collision can be found using the correlation between centrality and the number of charged particles in the collision's final state or by measuring the number of outside particles in the collision. The initial approach relies on choosing a geometrical model for the hadronic processes, whereas the latter utilizes measurements of the spectator nucleons' energy in the forward calorimeters/detectors.

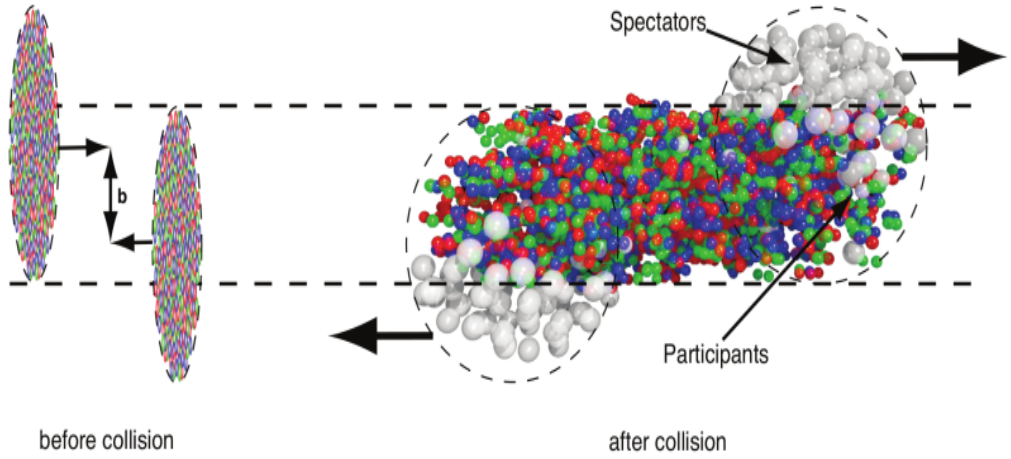

Figure 1.7: Left: Two heavy ions approaching each other before their collision with the impact parameter b. Right: An illustration of a heavy-ion collision where participant nucleons collide with nucleons of the other nucleus and spectators are almost unaffected. (Figure is taken from [33].)

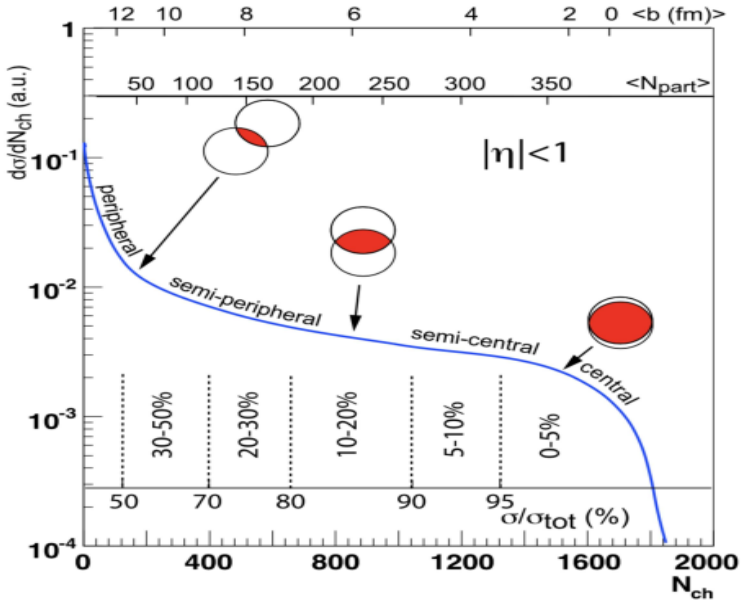

Figure 1.8: Cartoon showing the correlation of the final state charged particle multiplicity with impact parameter and number of participants. (Figure is taken from [34].)

1.5 Kinematic Variable

In high-energy physics and relativistic heavy-ion collision experiments, it is convenient to use kinematic variables that transform in simple and predictable ways under Lorentz trans-

formations. Quantities such as rapidity (y), pseudorapidity (η), and transverse momentum (p_T) are preferred because of their well-defined behaviour under changes of reference frame. Here in this section the definition of such variables to set the language of particle collisions at relativistic energies are introduced.

1.5.1 Four Vector

In special relativity, a four-vector represents a mathematical construct that unifies the time coordinate t with its three-dimensional spatial coordinates (x,y,z) of an event into a four-dimensional vector. The four-vector is expressed as (ct,x,y,z) [1]. In four-vector notation, the spacetime coordinates of a point x are written as:

$$x^{\mu} = (ct,x,y,z). \tag{1.5}$$

where c represents the speed of light, t corresponds to the temporal coordinate and (x,y,z) correspond to the spatial coordinates in Euclidean space. The index μ takes values from 0 to 3, where $x^0 = ct$ serves as the temporal component, while $x^1 = x$, $x^2 = y$, and $x^3 = z$ constitute the spatial components. The multiplication of the time coordinate by c ensures that all components have consistent units of length, as required in Minkowski spacetime. The four-momentum p is constructed analogously to the four-position, with its contravariant components p^{μ} given by

$$p^{\mu} = (p^0,p^1,p^2,p^3) = (E,\mathbf{p}) = (E,p_x,p_y,p_z). \tag{1.6}$$

where E is the total energy of the particle, and p_x,p_y,p_z are the components of the three-momentum vector $\mathbf{p}$. The index μ ranges from 0 to 3, with $p^0 = \frac{E}{c}$ as the temporal component and $p^1 = p_x$, $p^2 = p_y$, $p^3 = p_z$ as the spatial components. This normalization by c in the temporal component p^0 ensures dimensional consistency, as the quantity E/c possesses the same physical dimensions (momentum) as the spatial components p^x,p^y,p^z.

1.5.2 Transverse Momentum (p_T)

The transverse momentum (p_T) represents the momentum component perpendicular to the beam direction. For a particle with momentum components (p_x, p_y, p_z) in a coordinate system aligned with the beam axis ($\hat{z}$), the transverse momentum is defined as:

$$p_T = \sqrt{{p_x}^2 + {p_y}^2} \tag{1.7}$$

The transverse momentum remains invariant under lorentz transformation along the beam-line (z-axis) [1]. Besides, p_T = 0 for the beams before the collision; all of the p_T in the final state particles are generated dynamically in the collision.

1.5.3 Rapidity (y)

Rapidity (y) is a kinematic variable used in high-energy physics to describe the relativistic motion of the particles, particularly in heavy-ion collisions where particle velocities approach the speed of light. Unlike velocity, rapidity is additive under Lorentz transformations along the direction of motion making it a powerful tool for analyzing particle kinematics in relativistic regimes. In the non-relativistic limit, where the momentum of the particle (p_z) is equivalent or smaller than its mass (m_0), y approximates the particle's velocity.

In the laboratory frame, the rapidity y of a particle is defined as:

$$y = \frac{1}{2} \ln \left(\frac{E + p_z}{E - p_z} \right), \tag{1.8}$$

where E is the total energy of the particle, and p_z is the component of its momentum along the z-axis.

In a Lorentz frame F' boosted with velocity v along the z-axis relative to the lab frame F, the particle's rapidity y' is given by:

$$y' = \frac{1}{2} \ln \left(\frac{E' + p'_z}{E' - p'_z} \right), \tag{1.9}$$

where E' and p'_z represent the particle's energy and longitudinal momentum components in the boosted frame. The additivity of rapidity under Lorentz transformations imply that if the boosted frame moves with a rapidity y_{boost}, the relationship between the rapidities in the two frames is:

$$y' = y - y_{\text{boost}}. \tag{1.10}$$

This additive behaviour makes rapidity an ideal variable for analyzing particle production in different reference frames, particularly in collider experiments where boosts along the beam axis are common.

1.5.4 Pseudorapidity (η)

The rapidity is hard to measure for highly relativistic particles. In many experiments, measuring a particle's longitudinal momentum component (p_z) may be challenging or impractical. In such cases, where the particle identification is difficult, a variable called pseudorapidity (η) [3], which is easier to calculate than rapidity, can be defined based on the polar angle (θ) at which the particle is detected with respect to the beam axis. This is defined as;

$$\eta = \frac{1}{2} ln \left(\frac{p + p_z}{p - p_z} \right) \tag{1.11}$$

For highly relativistic particles, p_z = pcosθ, thus equation Eq.(1.11) become

$$\eta = \frac{1}{2} ln \left(\frac{p + pcos\theta}{p - pcos\theta} \right) \tag{1.12}$$

$$\eta = -ln \left(tan(\frac{\theta}{2}) \right) \tag{1.13}$$

where θ represents the polar angle between the beam axis and the particle's momentum vector **p**. Rapidity variable (y) can also be written in terms of pseudorapidity variable η

as:

$$y = \frac{1}{2}\ln\left[\frac{\sqrt{p_T^2\cosh^2\eta - (mc)^2} + p_T\sinh\eta}{\sqrt{p_T^2\cosh^2\eta - (mc)^2} - p_T\sinh\eta}\right] \tag{1.14}$$

Or the pseudorapidity variable η in terms of the rapidity variable (y) is;

$$\eta = \frac{1}{2}ln\frac{\sqrt{{m_T}^2cosh^2(y) - (mc)^2} + m_T sinh(y)}{\sqrt{{m_T}^2cosh^2(y) - (mc)^2} - m_T sinh(y)} \tag{1.15}$$

Here, m is the rest mass of the particle, and the transverse mass m_T is given by $m_T^2 = p_T^2 + m^2$, using natural units where $c = 1$. Pseudorapidity is particularly useful in experimental contexts because it is related to rapidity (y) in the limit of high energies, where p >> m or E >> m (the particle's energy is much larger than its rest mass). In this regime, rapidity and pseudorapidity converge so that

$$y \approx \eta \tag{1.16}$$

1.5.5 Center-of-mass energy

In a two-body collision system, the arriving particles' center-of-mass energy is represented by the square of their combined four-momentum. This quantity is Lorentz invariant and is typically denoted by the Mandelstam variable ("s") [58], which is defined as:

$$s = (\mathbf{p}_1 + \mathbf{p}_2)^2 = (E_1 + E_2)^2 - (\vec{p}_1 + \vec{p}_2)^2 = (E_1 + E_2)^2 \tag{1.17}$$

E_1 and E_2 represents their energies and $(\vec{p}_1)$ and $(\vec{p}_2)$ are the momentum vector of incoming particles, respectively. In the center-of-mass frame, the total momentum of the colliding beams is zero, so $(\vec{p}_1)$ = - $(\vec{p}_2)$ because the masses of the particles are identical. As a result, the center-of-mass energy s is expressed as:

$$s = E_1 + E_2 = 2E \tag{1.18}$$

For example, in the context of heavy-ion collisions such as at the LHC, Xenon (Xe) nuclei are accelerated to an energy of 2720 GeV per nucleon. This results in a total centre-of-mass energy of 2 $\times$ 2720 GeV = 5440 GeV = 5.44 TeV for each pair of colliding nucleons. Thus the estimation of the total center-of-mass energy involved in the most central (head-on, b=0) Xe–Xe collisions (with 129 as mass of Xe nucleus) is given by: 2 $\times$ 2720 GeV $\times$ 129 nucleons, which equals 7.00 $\times$ 10^5 GeV. This calculation shows that an immense energy concentration occurs within a femtoscale volume during head-on collisions.

1.6 Signatures of QGP and experimental probes

The short-lived and extremely high-temperature nature of the QGP formed in the heavy-ion collisions make it challenging to measure its existence directly. However, the creation of a deconfined state of quarks and gluons in relativistic heavy ion collisions has been established based on various experimental observables serving as potential signatures of the QGP. Some characteristic experimental signatures of QGP are presented below.

1.6.1 Strangeness Enhancement

Elementary particles that include one or more strange quarks are known as strange particles. The threshold energy required for the production of strange hadrons is about 400 MeV, whereas for anti-strange quarks, the threshold is much smaller. In 1982, Rafelski and Muller proposed strangeness enhancement as a signature of QGP formation [35]. Strangeness enhancement refers to the increased production of hadrons containing strange quarks in nucleus-nucleus collisions compared to proton-proton collisions. In hadronic reactions, the production of particles containing strange quarks is normally suppressed due to the large mass of s-quark ($m_s = 170 MeV/c^2$) relative to u and d quark masses [36]. A pair $s\bar{s}$ can be produced either by gluon fusion ($gg \rightarrow s\bar{s}$) as shown in Fig. 1.9 or by the contribution of light quarks ($q\bar{q} \rightarrow s\bar{s}$) as shown in Fig. 1.10 [39]. The u and d quarks are expected to be rich in the initial phase of QGP and are expected to follow Pauli principle, which suppresses the production of $u\bar{u}$ and $d\bar{d}$ pair and thus favours the formation of heavier

quarks [40]. The first evidence of strangeness signature of QGP formation was presented by Super Proton Synchrotron (SPS) CERN-NA35 collaboration [37]. Later, the STAR experiment at RHIC provided additional evidence in favour of this result [38]. These experiments reveal an increase in the production of particles containing two or more strange quarks and/or antiquarks.

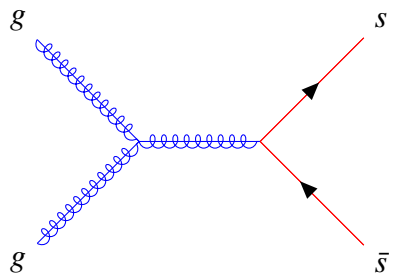

Figure 1.9: Strange and anti-strange quarks produced by the gluon fusion mechanism ($gg \rightarrow s\bar{s}$).

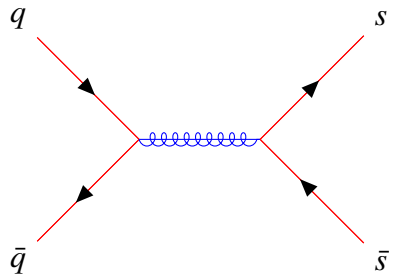

Figure 1.10: Strange and anti-strange quarks are produced by the quark-antiquark combination ($q\bar{q} \rightarrow s\bar{s}$).

1.6.2 Jet Quenching

The early-stage partons of the colliding hadrons undergo elastic $(2 \rightarrow 2)$ or inelastic $(2 \rightarrow 2+X)$ scattering, resulting in the production of two or more partons in the final state. The outgoing partons with large momentum travel in the opposite direction and lose energy by radiating gluons and splitting into quark-antiquark pairs [41, 42, 43]. The QCD radiation probability drives such a parton branching evolution and then breaks up into a collection of final state hadrons. This collimated shower of hadrons produced from the fragmentation of an outgoing parton is called a "**jet**". Jet measurements in heavy-ion collisions serve as a powerful probe for studying the properties of the hot and dense medium created during

these high-energy interactions. The outgoing parton loses energy as it moves through the medium, leading to the attenuation or even disappearance of the hadron shower. The phenomenon of energy loss is known as "**jet** − **quenching**," and the amount of energy loss (ΔE) depends on particle and plasma properties. This energy loss gives fundamental information about the medium formed by the collision.

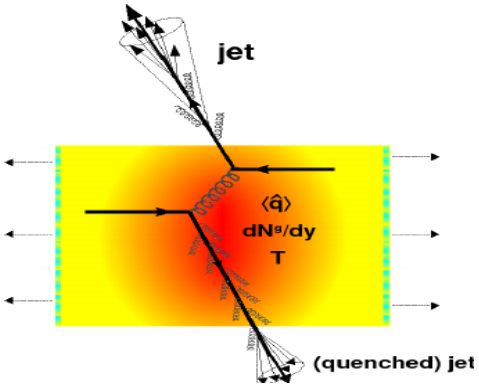

Figure 1.11: A cartoon showing jet quenching in central A-A collisions [43].

Fig. 1.11 depicts the possibile jet quenching in head-on nucleus-nucleus collisions caused by the hard scattering of two incoming quarks. One parton travels directly into the vacuum and hadronizes by emitting a few gluons, while another parton passes through the dense medium created by the collision and experiences energy loss, and eventually fragments into a quenched jet [41]. In high energy physics, Jet was first observed in 2008 in an experiment performed at BNL's RHIC experiment in US [44]. Jet quenching has also been observed in the experiments like ALICE, ATLAS, CMS, perfomed at LHC CERN [45].

1.6.3 Photons and dileptons

The electromagnetic probes photons and leptons originate from every phase of the expanding fireball, whereas hadrons are generated from the freeze-out surface following severe rescattering. In comparison to the typical system size $(\approx 10 fm)$, the electromagnetic probes have a long mean free path. Furthermore, because they are electromagnetic in nature, they interact weakly, allowing them to escape and reach the detectors with minimal interaction with the medium created by heavy-ion collisions. As a result, they convey undistorted information about the early stages of deconfined state of matter [41]. Con-

sequently, photons and dileptons - specifically electron-positron (e^+e^-) pairs and muon-antimuon ($\mu^+\mu^-$) pairs - emerge as particularly powerful probes for examining the early-time dynamics of heavy-ion collisions.

Photons are studied to obtain important information, such as the temperature of the plasma, evolution of the system size [42, 46, 47, 48], momentum anisotropy of the initial partons [49, 50] etc. Dileptons are considered as the most reliable observables of the QGP formation as well the medium modification of vector meson [51]. Photons can be produced via differnt processes in heavy-ion collision, some of the dominating processes for direct photon production are compton scattering, quark-antiquark annihilation.

Figure 1.12: Photon production through the (a) quark-antiquark annihilation ($q+\bar{q}=\gamma+g$) and (b) Compton scattering ($q+g=\gamma+\bar{q}$).

1.6.4 Anisotropic Flow

When two nuclei collide in a semi-central or peripheral collision, the participant zone resembles an anisotropic almond. The beam axis and the impact parameter vector lie within the reaction plane, which coincides with the symmetry plane of the almond-shaped overlap region formed by the colliding nuclei. The initial spatial anisotropy of the participant zone transforms into a hot and dense medium with anisotropic pressure gradients. Pressure gradients in the reaction plane are larger than gradients pointing outside the plane. Thus, the medium near the reaction plane experiences stronger pushing, resulting in larger momenta for particles in this region compared to those in the out-of-plane direction. Comparing observed azimuthal anisotropy to hydrodynamic model predictions allows for analysis of QGP properties such as shear viscosity to entropy density ratio (η/s) and bulk viscosity to

entropy density ratio (ζ/s). Experimentally, the azimuthal yield distribution of produced particle can be expressed in terms of Fourier expansion [52] as

$$E\frac{d^3N}{dp^3} = \frac{1}{2\pi}\frac{d^2N}{p_T dp_T dy}(1+2\sum_{n=1}^{\infty} v_n cos[n(\phi-\Psi_n)]) \tag{1.19}$$

where, p is momentum, p_T is transverse momentum, E is energy, y is rapidity, ϕ is azimuthal angle (section 1.5), and Ψ_n is the n^{th} harmonic symmetry plane. Since the angle of the reaction plane cannot be observed directly, it is estimated experimentally for each harmonic separately using the measured azimuthal anisotropy. The estimation of the reaction plane is also known as the participant plane. The Fourier coefficients can be determined from the following expression.

$$v_n(p_T, y) = < cos[n(\phi-\Psi_n)] > \tag{1.20}$$

Fourier coefficient analysis, combined with hydrodynamic predictions, constrains medium transport coefficients as well as event-by-event fluctuations in the initial collision geometry. The second-order Fourier coefficient, v_2, commonly referred to as elliptic flow [53], characterizes the azimuthal anisotropy of particle distribution arising from the almond-shaped initial geometry. For non-central collisions, the observed particle anisotropy is overwhelmingly influenced by elliptic flow (v_2). The third-order coefficient v_3, known as triangular flow, is primarily determined by initial-state fluctuations [54].

1.6.5 Fluctuations

The study of fluctuations is vital to characterize any physical system and it's properties, such as QGP created in the heavy-ion collisions at ultra-relativistic energies. Fluctuations are predicted to be large at the critical point of QCD phase diagram, and this makes the study of fluctuation more challenging and intresting [56] as it is still elusive and one of the main goals of present investigations in the field.

In general fluctuations are of two types viz statistical and non-statistical fluctuations. The fluctuations that result due to a finite number of particles in a given event are known

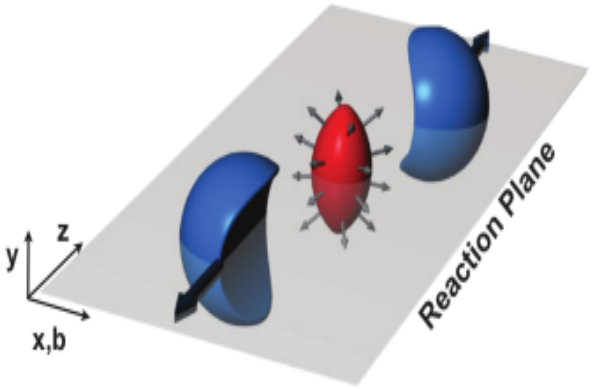

Figure 1.13: A semi-central heavy ion collision is shown where the almond-shaped participant zone is shown in red, and the spectator zone in blue. Arrows represent pressure gradients. The reaction plane corresponds to the xz plane. (Figure taken from [55].

as statistical fluctuations. Whereas non-statistical fluctuations are further of two types, dynamical and geometrical fluctuations. The first type of fluctuations are present at all stages of the collision and do not change from event-to-event. This type of fluctuation contains intresting physics related with collisions, that includes time evolution of fluctuations at various stages of the collision, hydrodynamic expansion, hadronization and freeze-out [2] etc. The second type of fluctuation vary on event-by-event basis and arise when the impact parameter of the sample of events are different, and causes an intrinsic variation in particle multiplicity from one event to another. By selecting events of a particular type of class (e.g central, peripheral etc), these fluctuations can be reduced .

Fluctuations offer crucial insight into the dynamics of the processes involved in collisions [57]. Enhanced fluctuations in observables like particle multiplicity and transverse momentum are especially important because they can reflect changes in the medium's equation of state. The fluctuations in the observables become more pronounced during phase transition, such as hadron gas to QGP transition if there is critical point. At that point, in particular, the correlation length diverges, and generates a larger fluctuation signal. Thus, various event properties including multiplicity, net charge, and mean transverse momentum ($\langle p_T \rangle$) can be used to study these fluctuations. However, these measurements not only pertain to the characteristics of physical processes but are also impacted by statistical fluctuations, which is suggestive of the limitations associated with the intrinsic prop-

erties of data collection and detectors. Thus, the necessary condition for accurate analysis is a lot of data to avoid statistical noise and show the true character of those fluctuations.

The Beam Energy Scan (BES) program at RHIC, experiments at the LHC and future facilities, aim to map out these fluctuations across different energies in order to better comprehend the QCD phase diagram and identify potential critical points. These studies will assist to bridge the gap between experimental observables and theoretical models, enhancing our understanding of the behaviour of strongly interacting matter under severe conditions.

1.7 Motivation of the thesis

In this thesis the local multiplicity fluctuations in the charged particle production in the high-enegy heavy-ion collisions are studied to learn about multiparticle production mechanism. In a heavy-ion collision, an event is defined as a single interaction between two heavy nuclei at extremely high energies. These collisions, such as those involving lead (Pb) or xenon (Xe) nuclei at ultra-relativistic energies, produce a number of particles in each event, making it possible to study relevant physical quantities on an event-by-event basis. The NA49 collaboration has carried out pioneering experimental studies of event-by-event fluctuations [59] analyzing fluctuations in the kaon-to-pion ratio and transverse momentum. Similarly, experiments conducted at the RHIC and CERN have made available large amount of high multiplicity data which can unravel the mysteries of matter formed at high energy and density. In these experiments, event-by-event fluctuations in temperature, mean transverse momentum, particle multiplicity, and particle ratios are considered [53, 56] highly significant for understanding the evolution of the of the different stages of the formation of QGP and its freeze-out to the hadronic phase.

The dynamics of the initial process as have a significant impact on the final particle distributions produced in relativistic heavy-ion collisions [60]. As a result, multiplicity distributions play an important role in obtaining first-hand information on the multiparticle production mechanism in these collisions. As per lattice QCD, the phase transition

from the hadronic to QGP state will occur at critical temperature T_c and vanishing baryonic chemical potential (μ_B) [62, 63]. This phase transition induces significant density fluctuations, which lead to the formation of hot spots and result in substantial multiplicity fluctuations. Multiplicity fluctuations are, therefore, highly sensitive to the presence of the critical point T_c, in the QCD phase transition diagram [64], making them valuable observables for probing the nature of the phase transition. Therefore, studying these fluctuations is essential for understanding the phase transition processes in relativistic nuclear interactions and for gaining deeper insights into the fundamental properties of matter under such extreme conditions. [61].

Intermittency methodology is used to study non-statistical density fluctuations in particles produced in ALICE data and generated in AMPT model events. ALICE (A Large Ion Collider Experiment) at the LHC is one of the specialized detectors designed to investigate the physics of ultra-relativistic heavy-ion collisions, particularly focusing on the QGP. A few of its primary goals is to better understand the properties of QGP, such as its temperature, energy density, and viscosity, as well as to investigate how quarks and gluons, the fundamental constituents of hadrons, behave when freed from confinement in nuclear matter. Intermittency focuses on the calculation of normalized factorial moments, which measures fluctuations in particle density across different spatial or momentum scales. The power-law behaviour of these moments as the number of bins increases is what is called intermittency [2, 65], revealing self-similar or scale-invariant fluctuations with presence of underlying fractal-like structures in the system. Intermittency study of data may give signal of order of the phase transition and quantify fluctuations in particle densities. The early investigations of intermittency at low energies faced significant challenges, such as low bin multiplicities, which made it difficult to draw definitive conclusions about critical phenomena such as the location of the critical point, the order of the phase transition, the nature of multiplicity fluctuations, or clear signals of quark-gluon plasma (QGP) formation [65]. However, the recent advances in collider experiments, which currently generate data with high charged particle densities per bin, restored interest in applying intermittency analysis to a wider range of systems and collision energies on event-by-event basis. This

increased availability of high-quality data has improved the reliability and sensitivity of intermittency studies, allowing for a more in-depth investigation of multiparticle production processes and the underlying mechanisms governing these complex phenomena [66].

Over the last decade, the NA49 and NA61/SHINE experiments have performed intermittency analyses on a variety of heavy-ion systems ranging in size and collision energy [67, 68, 69, 70]. The STAR experiment at the RHIC reported the first measurement of intermittency in Au-Au collisions over a broad range of collision energies, from $\sqrt{s_{\rm NN}}$ =7.7 to 200 GeV [66]. Observations and results reported from these experiments motivate to further look into high energy data such as at LHC to have precise and accurate information on the particle production behaviour.

By studying local multiplicity fluctuations in the charged particle distributions from ALICE data on the event-by-event basis, using the intermittency analysis technique, the aim is to gain deeper insights into the nature of the phase transition, the location of the critical point in the QCD phase diagram, and the processes responsible for particle production in heavy-ion collisions, the answers to which are yet not available.

1.8 Organisation of the thesis

In this work the charged particles produced during the Xe-Xe collisions at $\sqrt{s_{\rm NN}}$ = 5.44 TeV are investigated for their scaling properties using the intermittency methodology. In this Chapter 1 provides a general introduction to the Standard Model and QCD, followed by a brief discussion of heavy-ion collisions, QGP, its signatures and physics problem was discussed. Chapter 2 provides an overview of the CERN-LHC accelerator system, the ALICE experiment, various subdetectors and a brief description of software used for analysis is given. In Chapter 3 a detailed analysis methodology to investigate local multiplicity fluctuations using the normalized factorial moments is given. The observations and results from the HIJING simulated events are also given in this chapter. Chapter 4 discusses the observations and results from ALICE experimental data analysis. In Chapter 5, results from the analysis performed on the event samples from String Melting

mode of the AMPT model are presented. Finally, Chapter 6 gives a brief overview of the work reported in this thesis and conclusions of the work.

BIBLIOGRAPHY

[1] C. Wong, "Introduction To High-Energy Heavy-Ion Collisions," World Scientific publishing company, 1944.

[2] X. Cao and H. Liu, "Impact of the phase transition on quark-gluon plasma with an extremely strong magnetic field in holographic QCD," Phys. Rev. D **111**, no.2, 026008 (2025) [arXiv:2408.00467 [hep-th]].

[3] D. H. Perkins, "Introduction to high-energy physics," (4th ed. Cambridge Univ. Press, Cambridge, 2000).

[4] Jovanovic, O., "Possible Structure of the Electron and the Up Quark," ResearchGate, available at https://www.researchgate.net/publication/381551014_Possible_Structure_of_the_Electron_and_the_Up_Quark.

[5] W. Pauli, "The Connection Between Spin and Statistics," Phys. Rev. **58**, 716-722 (1940)

[6] D. J. Griffiths. "Introduction to Elementary Particles ". Wiley VCH. (2008).

[7] F. Halzen and A. D. Martin. "Quarks and Leptons: An Introductory Course in Modern Particle Physics". Wiley and Sons, Inc. (1991).

[8] G. Aad *et al.* [ATLAS], "Observation of a new particle in the search for the Standard Model Higgs boson with the ATLAS detector at the LHC," Phys. Lett. B **716**, 1-29 (2012) [arXiv:1207.7214 [hep-ex]].

[9] S. Chatrchyan *et al.* [CMS], "Observation of a New Boson at a Mass of 125 GeV with the CMS Experiment at the LHC," Phys. Lett. B **716**, 30-61 (2012) [arXiv:1207.7235 [hep-ex]].

[10] F. Englert and R. Brout, "Broken Symmetry and the Mass of Gauge Vector Mesons," Phys. Rev. Lett. **13**, 321-323 (1964)

[11] P. W. Higgs, "Broken Symmetries and the Masses of Gauge Bosons," Phys. Rev. Lett. **13**, 508-509 (1964)

[12] M. D. Schwartz, "Quantum Field Theory and the Standard Model," Cambridge University Press, 2014, ISBN 978-1-107-03473-0, 978-1-107-03473-0

[13] M. E. Peskin and D. V. Schroeder, "An Introduction to quantum field theory," Addison-Wesley, 1995, ISBN 978-0-201-50397-5, 978-0-429-50355-9, 978-0-429-49417-8

[14] H. K. Quang and X. Y. Pham, "Elementary particles and their interactions: concepts and phenomena," (Springer, 1998).

[15] F. Halzen and A. D. Martin, "Quarks and Leptons: An Introductory Course in Modern Physics," (WILEY-India, 2008).

[16] K. Melnikov, "Lectures on QCD for hadron colliders," CERN Yellow Rep. School Proc. **3**, 37-82 (2018)

[17] Exchange Particles–HyperPhysics, 2020. Available at: http://www.hsc.edu.kw/student/materials/Physics/website/hyperphysics%20modified/hbase/particles/expar.html

[18] P. Zyla et al., Particle Data Group Collaboration, "Review of Particle Physics,"PTEP 2020 no. 8, (2020) 083C01.

[19] K. G. Wilson, "Confinement of Quarks," Phys. Rev. D **10**, 2445-2459 (1974)

[20] J. N. Guenther, "Overview of the QCD phase diagram: Recent progress from the lattice," Eur. Phys. J. A **57**, no.4, 136 (2021) [arXiv:2010.15503 [hep-lat]].

[21] K. Rajagopal and F. Wilczek. "The Condensed Matter of QCD ". At the Frontier of Particle Physics: Handbook of QCD (2001), pp. 2061-2151.

[22] Y. Aoki, G. Endrodi, Z. Fodor, S. D. Katz and K. K. Szabo, "The Order of the quantum chromodynamics transition predicted by the standard model of particle physics," Nature **443** (2006), 675-678 [arXiv:hep-lat/0611014 [hep-lat]].

[23] J. N. Guenther, "Overview of the QCD phase diagram: Recent progress from the lattice,"Eur. Phys. J. A **57** (2021) no.4, 136 [arXiv:2010.15503 [hep-lat]].

[24] B. Betz, "Jet Propagation and Mach-Cone Formation in (3+1)-dimensional Ideal Hydrodynamics," [arXiv:0910.4114 [nucl-th]].

[25] J. D. Bjorken, "Highly Relativistic Nucleus-Nucleus Collisions: The Central Rapidity Region," Phys. Rev. D **27**, 140-151 (1983)

[26] BRAHMS Collaboration, I. C. Arsene et al., "Nuclear stopping and rapidity loss in Au+Au collisions at 62.4 GeV,"Phys. Lett. B 677 (2009) 267-271, arXiv:0901.0872 [nucl-ex].

[27] H. Satz, " Statistical Mechanics of Quarks and Hadrons. Proceedings of an International Symposium Held at the University of Bielefeld, F.R.Germany, August 24-31, 1980. North-Holland, 1981,".

[28] W. Florkowski, "Phenomenology of Ultra-Relativistic Heavy-Ion Collisions," Technical Design Report ALICE. Geneva: World Scientific, 2010.

[29] L. McLerran, "Theoretical Concepts for Ultra-Relativistic Heavy Ion Collisions, in Meeting of the Division of Particles and Fields of the American Physical Society "(DPF 2009), **11**, 2009 [0911.2987]. xvii, 8

[30] K. Aamodt et al. “Two-pion Bose-Einstein correlations in central PbâĂŞPb collisions at $\sqrt{s_{NN}}$ = 2.76 TeV ”. In: Phys. Lett. B 696 (2011), pp. 328-337. arXiv: 1012.4035 [nucl-ex].

[31] “Inclusive J/ψ production in Pb-Pb collisions at $\sqrt{s_{NN}}$ = 5.02 TeV with ALICE ”.

[32] O. V. Rueda, et al., CERN-THESIS-2022-290, “Study of the production of , K and p in pp collisions at s=13 TeV as a function of the Transverse Spherocity and the Relative Transverse Activity.”

[33] R. Snellings, “Collective Expansion at the LHC: selected ALICE anisotropic flow measurements,”J. Phys. G **41** (2014) no.12, 124007 [arXiv:1408.2532Wilson:1974 [nucl-ex]].

[34] M. L. Miller, K. Reygers, S. J. Sanders and P. Steinberg, “Glauber Modeling in High-Energy Nuclear Collisions,”Ann. Rev. Nucl. Part Sci. 57,no1 (2007):205-243.

[35] B. Abelev *et al.* [ALICE], “Centrality determination of Pb-Pb collisions at $\sqrt{s_{NN}}$ = 2.76 TeV with ALICE,”Phys. Rev. C **88** (2013) no.4, 044909 [arXiv:1301.4361 [nucl-ex]].

[36] C. Alt *et al.* [NA49], “Pion and kaon production in central Pb + Pb collisions at 20-A and 30-A-GeV: Evidence for the onset of deconfinement,”Phys. Rev. C **77** (2008), 024903 [arXiv:0710.0118 [nucl-ex]].

[37] J. Eschke [NA35], “Strangeness enhancement in sulphur - nucleus collisions at 200-GeV/N,” Acta Phys. Hung. A **4**, 105-116 (1996) [arXiv:hep-ph/9609242 [hep-ph]].

[38] B. I. Abelev *et al.* [STAR], “Enhanced strange baryon production in Au + Au collisions compared to p + p at s(NN)**(1/2) = 200-GeV,” Phys. Rev. C **77**, 044908 (2008) [arXiv:0705.2511 [nucl-ex]].

[39] J. Rafelski and B. Muller, “Strangeness Production in the Quark - Gluon Plasma,”Phys. Rev. Lett. **48** (1982), 1066 [erratum: Phys. Rev. Lett. **56** (1986), 2334]

[40] M. A. Stephanov, K. Rajagopal, E. V. Shuryak, "Signatures of the Tricritical Point in QCD,"Phys. Rev. Lett. **81**, (1998) 4816.

[41] S. Sarkar, H. Satz and B. Sinha, "The physics of the quark-gluon plasma,"Lect. Notes Phys. **785** (2010), pp.1-369 doi:10.1007/978-3-642-02286-9

[42] S. A. Bass, B. Muller and D. K. Srivastava, Phys. Rev. C **66**, 061902 (2002).

[43] R. S. Bhalerao, "Relativistic heavy-ion collisions," [arXiv:1404.3294 [nucl-th]].

[44] M. Gyulassy and L. McLerran, "New forms of QCD matter discovered at RHIC," Nucl. Phys. A **750**, 30-63 (2005) [arXiv:nucl-th/0405013 [nucl-th]].

[45] B. Muller, J. Schukraft and B. Wyslouch, "First Results from Pb+Pb collisions at the LHC," Ann. Rev. Nucl. Part. Sci. **62**, 361-386 (2012) [arXiv:1202.3233 [hep-ex]].

[46] S. A. Bass, B. Muller and D. K. Srivastava, "Probing the evolution of heavy-ion collisions using direct photon interferometry,"Phys. Rev. Lett. **93**, 162301 (2004).

[47] S. A. Bass, B. Muller and D. K. Srivastava, "Jet-Triggered Back-Scattering Photons for Quark Gluon Plasma Tomography,"Phys. Rev. Lett. **90**, 082301 (2009).

[48] T. Renk, S. A. Bass and D. K. Srivastava, "Dynamics of the Landau–Pomeranchuk–Migdal effect in Au + Au collisions at $\sqrt{s} = 200\,A\,GeV$,"Phys. Lett. B 632, (2006).

[49] R. Chatterjee, E. Frodermann, U. Heinz and D. K. Srivastava, "Elliptic Flow of Thermal Photons in Relativistic Nuclear Collisions,"Phys. Rev. Lett. **96**, 202302 (2006).

[50] U. Heinz, R. Chatterjee, E. Frodermann, C. Gale D. K. Srivastava, Nuclr. Phys. A **783**, 379 (2007).

[51] K. Kajantie, J. Kapusta, L. McLerran and A. Mekijan, "Dilepton emission and the QCD phase transition in ultrarelativistic nuclear collisions,"Phys. Rev. D **34**, 2746 (1986).

[52] S. Voloshin and Y. Zhang, "Flow study in relativistic nuclear collisions by Fourier expansion of Azimuthal particle distributions," Z. Phys. C **70**, 665-672 (1996) [arXiv:hep-ph/9407282 [hep-ph]].

[53] K. Aamodt *et al.* [ALICE], "Elliptic flow of charged particles in Pb-Pb collisions at 2.76 TeV," Phys. Rev. Lett. **105**, 252302 (2010) [arXiv:1011.3914 [nucl-ex]].

[54] R. S. Bhalerao and J. Y. Ollitrault, "Eccentricity fluctuations and elliptic flow at RHIC," Phys. Lett. B **641**, 260-264 (2006) [arXiv:nucl-th/0607009 [nucl-th]].

[55] R. Snellings, "Elliptic Flow: A Brief Review," New J. Phys. **13**, 055008 (2011) [arXiv:1102.3010 [nucl-ex]].

[56] J. D. Bjorken, "Asymptotic Sum Rules at Infinite Momentum," Phys. Rev. **179**, 1547-1553 (1969)

[57] M. A. Stephanov, K. Rajagopal and E. V. Shuryak, "Event-by-event fluctuations in heavy ion collisions and the QCD critical point," Phys. Rev. D **60**, 114028 (1999) [arXiv:hep-ph/9903292 [hep-ph]].

[58] M. E. Peskin and D. V.Schroeder, "An Introduction to Quantum Field Theory,"Westview Press, 1995.

[59] R. C. Hwa and C. B. Yang "Local multiplicity fluctuations as a signature of critical hadronization in heavy-ion collisions at TeV energies ", *Phys. Rev. C* 85 **(2012)** 044914.

[60] S. Gavin and G. Moschelli, "Fluctuation Probes of Early-Time Correlations in Nuclear Collisions," Phys. Rev. C **85**, 014905 (2012) [arXiv:1107.3317 [nucl-th]].

[61] L. Van Hove, "Hadronization Model for Quark - Gluon Plasma in Ultrarelativistic Collisions," Z. Phys. C **27**, 135 (1985)

[62] V. Koch, "Correlations and fluctuations: status and perspectives," J. Phys. G **35**, 104030 (2008)

[63] K. Aamodt *et al.* [ALICE], "Centrality dependence of the charged-particle multiplicity density at mid-rapidity in Pb-Pb collisions at $\sqrt{s_{NN}} = 2.76$ TeV," Phys. Rev. Lett. **106**, 032301 (2011) [arXiv:1012.1657 [nucl-ex]].

[64] Z. w. Lin, S. Pal, C. M. Ko, B. A. Li and B. Zhang, "Charged particle rapidity distributions at relativistic energies," Phys. Rev. C **64**, 011902 (2001) [arXiv:nucl-th/0011059 [nucl-th]].

[65] E. A. De Wolf, I. M. Dremin and W. Kittel, "Scaling laws for density correlations and fluctuations in multiparticle dynamics," Phys. Rept. **270**, 1-141 (1996) [arXiv:hep-ph/9508325 [hep-ph]].

[66] M. Abdulhamid *et al.* [STAR], "Energy dependence of intermittency for charged hadrons in Au+Au collisions at RHIC," Phys. Lett. B **845**, 138165 (2023) [arXiv:2301.11062 [nucl-ex]].

[67] M. Maćkowiak-Pawłowska [NA61/SHINE], "Fluctuations and correlations in nucleus-nucleus collisions observed by NA61/SHINE at CERN SPS energies," PoS **CPOD2021**, 028 (2022) [arXiv:2111.05042 [nucl-ex]].

[68] T. Anticic *et al.* [NA49], "Search for the QCD critical point in nuclear collisions at the CERN SPS," Phys. Rev. C **81**, 064907 (2010) [arXiv:0912.4198 [nucl-ex]].

[69] T. Anticic *et al.* [NA49], "Critical fluctuations of the proton density in A+A collisions at 158*A* GeV," Eur. Phys. J. C **75**, no.12, 587 (2015) [arXiv:1208.5292 [nucl-ex]].

[70] H. Adhikary *et al.* [NA61/SHINE], "Search for the critical point of strongly-interacting matter in ^{40}Ar + ^{45}Sc collisions at 150A Ge V /c using scaled factorial moments of protons," Eur. Phys. J. C **83**, no.9, 881 (2023) [arXiv:2305.07557 [nucl-ex]].

CHAPTER 2

ALICE EXPERIMENTAL SETUP AND ANALYSIS SOFTWARE

2.1 Introduction

During the last century, many efforts have been made both theoretically and experimently to investigate the internal structure of matter and the interactions among its constituent particles. Sir Ernest Rutherford through his renowned gold foil experiment, in which he directed a beam of alpha particles at a thin gold sheet, discovered the atomic nucleus, thereby establishing the fundamental principles of nuclear physics. Experiments conducted in the 1920s and 1930s provided more information about the substructure of atomic nucleus. A positively charged subatomic particle named as proton was suggested and identified by Rutherford and later, in 1932, his student James Chadwick discovered a neutral subatomic particle of the nucleus, that is named as neutron [1].

Due to the extremely small size of the nucleus, it was a big challenge for physicists to

study the substructure of the atomic nucleus. Louis de Broglie came up with an incredible idea that proved to be solution to this issue. He proposed that all matter exhibits wave properties. As more energy is imparted to a particle, its momentum (p) increases, thereby reducing the wavelength (λ) of its associated matter-wave, as described by the equation $\lambda = \frac{\hbar}{p}$. With each additional increase in particle's momentum, the wave-length decreases more and more, making it feasible to investigate progressively smaller building blocks of matter using energetic particles. Based on this approach, machines known as accelerators were designed and developed. Experiments at these accelerators revealed that protons and neutrons are not elementary particles, but are instead composed of smaller constituents [1]. Today, it is also known today that the fundamental constituents of these nucleons are quarks and gluons that interact strongly with each other. To further investigate these strongly interacting particles, large particle accelerators have been built. First among these was at the Lawrence Laboratory in Berkeley, USA and the other at the Brookhaven National Laboratory (BNL) in New York, USA, with energy of the bombarding nuclei reaching up to 14 GeV per nucleon. The beam energies upto 158 A GeV were achieved by the Super Proton Synchrotron (SPS) accelerator facility at CERN [2] in Geneva.

When an accelerated projectile strikes a stationary target, it is called a fixed-target experiment, while in a collider experiment, collisions take place between two beams of accelerated particles aimed at each other. This head-on collision of two beams in a collider provides a much greater energy for the system compared to the fixed target collision. The first heavy-ion collider experiment was carried out at the BNL's Relativistic Heavy Ion Collider (RHIC) [3], where two accelerated Au–Au beams collided at a maximum centre of mass energy of 200 GeV per nucleon pair [3]. With increased energy and larger system that can give precise measurements of various physics observables, the Large Hadron Collider (LHC) was built at CERN. At present it is the world's largest heavy-ion accelerator. At LHC, an ultra-relativistic heavy-ion collision at an unprecedented energy in the TeV (tera electron volt) range produces a large number of particles, making precise measurement of the various parameters of these emitted particles possible. Particle detector systems are installed around the interaction points of the LHC to achieve various physics

objectives. ALICE (A Large Ion Collider Experiment) [4] is one of the major experimental setup installed at the LHC. To study different physics observables that can comprehend the properties of particles and system of hot and dense matter created in the heavy-ion collision experiment. A variety of sub-detectors are installed within the ALICE experiment. Each detector has a unique method of identifying properties of particles of varied nature. A brief overview of the LHC and a few detector in the ALICE experiment is presented below.

2.2 The Large Hadron Collider

The Large Hadron Collider [6] at the European Organization for Nuclear Research (CERN), which started its operation in 2009, is presently the largest and the most powerful hadron collider ever built in terms of collision energy and luminosity. The project proposal for constructing an accelerator on the scale of the LHC was initiated in 1984 and received approval in 1994. Construction of the current underground tunnel commenced in 2001, after the LEP collider was dismantled [7]. The LHC, with a circumference of 26.7 km and at a depth of 45-170 m from the earth's surface, is located underground across Swiss-French border [8]. It is designed to collide two particle beams moving in opposing directions. It is a synchrotron which consists of superconducting magnets and other structures that boost and accelerate two counter-rotating beams in separate parallel beam pipes at speeds close to the speed of light. In each beam pipe, particles travel around the accelerator ring multiple times before colliding at some fixed points termed as interaction point (IP).

Fig. 2.1 shows a schematic view of the LHC facility and depicts the acceleration chain of particles (for both protons and heavy-ions). The accelerators in this chain [9, 10] function sequentially, each one increasing the beam particles energy before transferring them to the subsequent machine. Initially, the Linear Accelerator 4 (Linac4) accelerates negative hydrogen ions from proton beam source to 160 MeV before injecting these into the Proton Synchrotron Booster (PSB). The injection process into the PSB includes a stripping stage that removes the two electrons from each H^- ion, converting them into protons. Protons

are then accelerated to 2 GeV and prepared for injection into the Proton Synchrotron (PS), where they are further accelerated up to 25 GeV. Thereafter, the energy is elevated to 450 GeV by injection into the Super Proton Synchrotron (SPS) [11, 12]. Lead or xenon ions, on the other hand, are prepared from a source of vaporised lead (Pb) or xenon (Xe) and enter LINAC3, where they are accelerated in the Low Energy Ion Ring (LEIR) before following the same route as that of proton for further acceleration.

Once the particle beams are accelerated these are injected into one of two beam pipes that run in opposite directions (one in clockwise and one in anticlockwise) around the main LHC ring, colliding at four major interaction points. At these locations around the ring, the seven main detector experiments collect data: ALICE [4], CMS [14], ATLAS [13], LHCb [15], LHCf [16], TOTEM [17], and MoEDAL [18]. The four main experiments, Compact Muon Solenoid (CMS), A Large Heavy Ion Collider Experiment (ALICE), LHC beauty (LHCb) and A Toroidal LHC Apparatus (ATLAS) are set-up around the four interaction points, located at IP1, IP2, IP5, and IP8, which are spaced at different positions along the LHC ring. CMS and ATLAS are the general-purpose particle physics detectors which were instrumental in the discovery of the Higgs boson [20], one of the biggest discoveries at the LHC. The primary focus of the LHCb experiment is the study of particles containing bottom (b) quarks and their decays, providing crucial insight into matter-antimatter asymmetry. The ALICE is built to investigate strongly interacting matter (the Quark-Gluon Plasma (QGP)) at extremely high temperatures and densities. LHCf (LHC forward) and TOTEM (TOTal cross section, Elastic scattering, and diffraction dissociation Measurement) are among the smallest-scale experiments at the LHC, focusing on specialized measurements. The MoEDAL is also a small detector system which uses detectors near LHCb in the cavern to search for highly ionizing particles, magnetic monopoles and other exotic new physics signatures [18].

The first collisions at LHC were that of protons at 900 GeV center-of-mass energy on September 10, 2008 and later after an year in November 2009 it become the powerful accelerator, colliding protons at 1.18 TeV energy per proton beam. In March 2010, the first *pp* collisions at $\sqrt{s_{\mathrm{NN}}} = 7$ TeV were achieved, followed by the first Pb–Pb collisions at

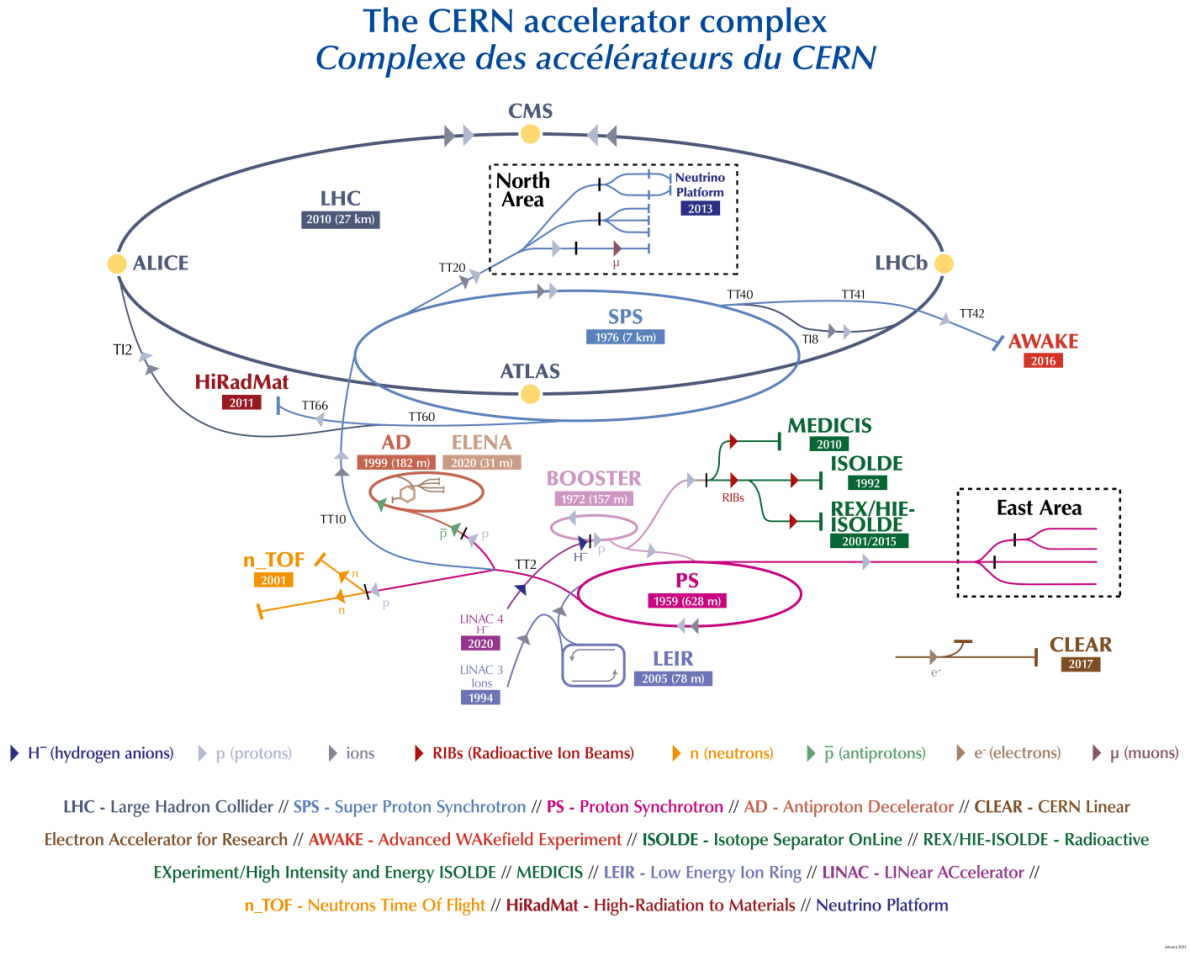

Figure 2.1: Schematic diagram of the Large Hadron Collider complex at CERN depicting the accelerators, beam lines, and a selection of major detector experiments.The ALICE detector is marked with a closed yellow circle and is situated at Interaction Point 2 (IP2). Figure is taken from [25].

$\sqrt{s_{\mathrm{NN}}}$ = 2.76 TeV in November. The integrated luminosity delivered by the LHC reached approximately 48 pb^{-1} in proton-proton collisions at $\sqrt{s_{\mathrm{NN}}} = 7$ TeV and about 10 μb^{-1} Pb–Pb collisions at $\sqrt{s_{\mathrm{NN}}} = 2.76$ TeV. With same beam energy for both Pb–Pb and *pp*, in 2011 LHC's luminosity improved to approximately 5.61 fb^{-1} for *pp* and approximately 166 μb^{-1} for Pb–Pb collisions. The 2012 run period set a new milestone, as the Large Hadron Collider achieved "proton-proton collisions reaching a center-of-mass energy of 8 TeV. By the end of the *pp* program in December 2012, the integrated luminosity reached $\approx$ 23.3 fb^{-1}, with $\approx$ 10 μb^{-1} recorded in the ALICE experiment [19, 21].

In September 2012, a pilot p–Pb run at 5.02 TeV was carried out, followed by a longer run in February 2013 with a luminosity of 31.2 nb^{-1}. The LHC RUN 1 programme concluded with a very short *pp* run at 2.76 TeV, followed by the begining of the first long shutdown (LS1) until the end of 2014. During the long shutdown (LS1), both the LHC accelerator complex and several of its main detectors were significantly upgraded. Following the upgrades, the LHC commenced its second run (RUN 2) in April 2015; this operational period continued until October 2018. During this run, the ALICE experiment recorded collisions at higher energies, with $\sqrt{s_{\mathrm{NN}}} = 13$TeV for *pp*, 8.16TeV for p–Pb, and 5.02 TeV for Pb–Pb systems. Additionally, the LHC conducted a brief xenon-xenon (Xe-Xe) collision run at $\sqrt{s_{\mathrm{NN}}} = 5.44$ In addition, On 5$^{\mathrm{th}}$ July, 2022 [6], the LHC began Run 3 operations achieving the highest energy proton-proton collisions at $\sqrt{s_{\mathrm{NN}}}$ = 13.6 TeV after more than three years of upgrading during long shutdown 2 (LS2). A summary of this information is given in Table 2.1.

2.3 A Large Ion Collider Experiment (ALICE)

ALICE [4], one of the four major experiments at the LHC, is located at Point 2 of the accelerator tunnel near the Swiss-French border in the St. Genis-Pouilly commune. ALICE is capable of studying different collision systems. The primary focus of ALICE is to investigate lead-lead (Pb–Pb) collisions, to study the properties of QGP. It is also equipped to record and analyze data from other collision configurations, including proton-lead (p–Pb)

Run Phase	Year	Collision system	Centre-of-Mass Energy [TeV]	Int. Luminosity
RUN 1	2008	p–p	0.9	–
	2009	p–p	1.18	6.8 μb^{-1}
	2010	p–p, Pb–Pb	7.0, 2.76	48 pb^{-1}, 10 μb^{-1}
	2011	p–p, Pb–Pb	7.0, 2.76	5.61 fb^{-1}, 166 μb^{-1}
	2012	p–p, p–Pb (pilot)	8.0, 5.02	23.3 fb^{-1},
RUN 2	2013	p–Pb / p–p	5.02 / 2.76	31.2 nb^{-1},
	2015–2017	p–p, p–Pb	13.0, 8.16	150 fb^{-1}, 25 nb^{-1}
	2015–2018	Pb–Pb	5.02	1 nb^{-1}
	2017	Xe–Xe	5.44	0.3 μb^{-1}
RUN 3	2022	p–p	13.6	39.7 fb^{-1}

Table 2.1: Summary of LHC collision systems, center-of-mass energies, and integrated luminosities across different run periods.

and proton-proton (*pp*) collisions. Studying different collision systems allows physicists to explore a range of energy densities and conditions. While heavy-ion collisions are particularly interesting for creating extreme conditions akin to the early universe, the proton-proton and proton-lead collisions provide a baseline for comparison and help researchers to understand the baseline properties of the colliding particles.

The ALICE experiment at CERN is a big international collaboration which involves around 1800 researchers and professionals including scientists, engineers, technicians, and graduate students from around the 178 institutes representing 41 countries. The ALICE detector has approximate dimensions of 16 m in length, 16 m in width, and 26 m in height, resulting in a total volume of $16 \times 16 \times 26$ m^3 with a weight of approximately 10,000 tons. The large size of the detector accommodates various sub-detectors and instruments positioned around the collision point to capture and to measure various parameters of the particles produced during the heavy-ion collisions. A detailed schematic of the ALICE detector's layout from the RUN 2 period, highlighting its key components, is provided in Fig. 2.2

The ALICE detector is composed of two primary sections: a central barrel and a forward muon spectrometer. The central barrel OF ALICE covers the pseudorapidity range of $-0.9 \leq \eta \leq 0.9$ over the full azimuth, whereas the forward muon spectrometer covers the pseudorapidity range of $2.5 \leq \eta \leq 4.0$. The central barrel contains multiple sub-detectors

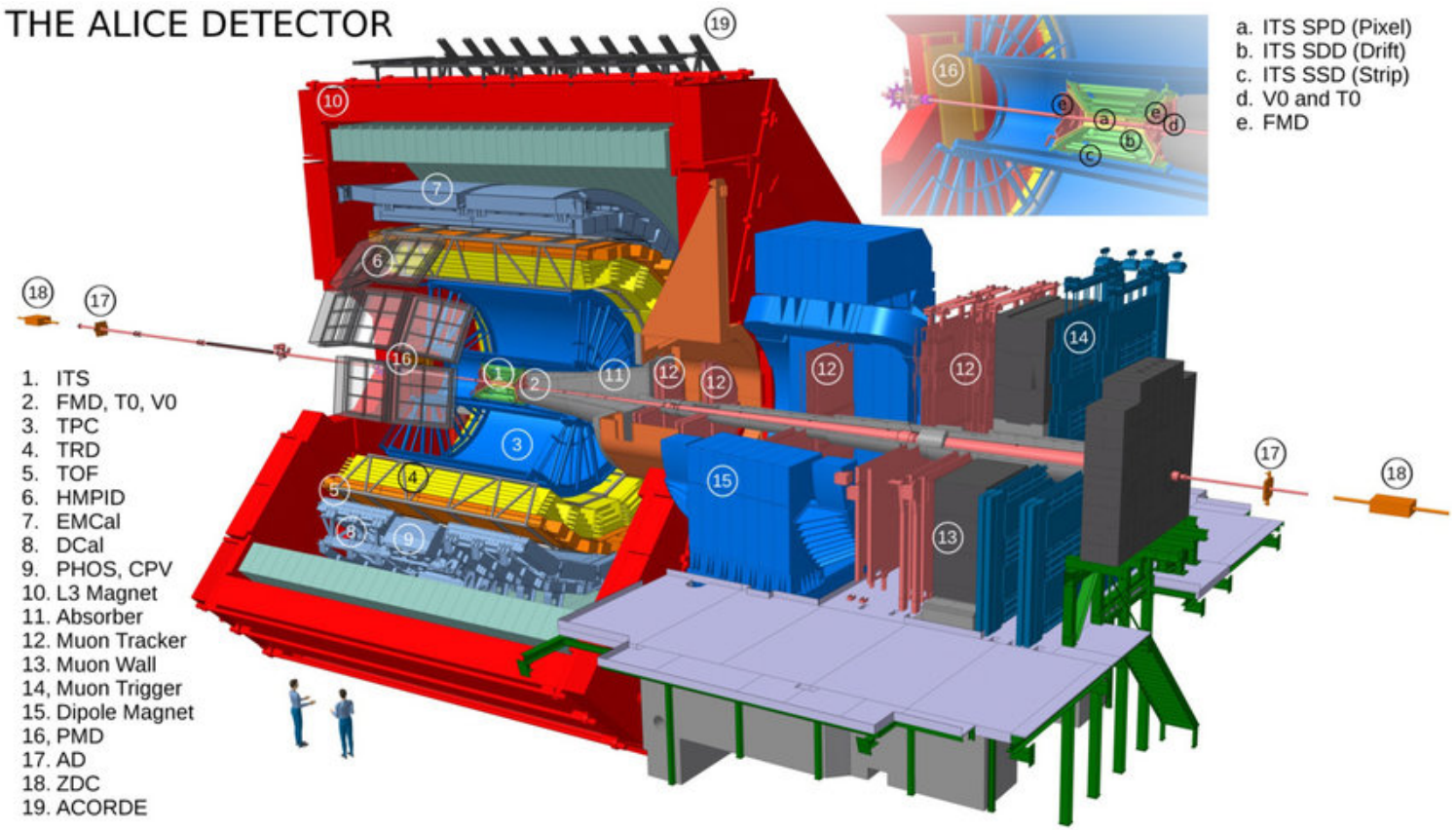

Figure 2.2: Schematic layout of the ALICE experiment during LHC Run 2, showing the central barrel detectors (ITS, TPC, TRD, TOF, EMCAL, etc.) within the L3 solenoid, the forward detectors (V0, T0, ZDC, FMD, PMD, AD), and the muon spectrometer. Different sub-detectors are indicated by numbers. Source [22]

.

with specialized roles in tracking charged particles, identifying different species, and generating trigger signals. The central part of the ALICE detector is designed to measure a wide range of particles, including electrons, hadrons (such as protons and pions), and photons. This central barrel is positioned directly around the collision point and is composed of multiple specialized sub-detectors arranged in concentric layers. A 0.5 T magnetic field is created by a solenoid magnet surrounding the Central Barrel detectors, bending the trajectories of charged particles. This allows ALICE to determine momenta and distinguish between particles with opposite charges. The Inner Tracking System (ITS) forms the innermost layer of the Central Barrel, with the Time Projection Chamber (TPC) surrounding it in the next outward layer. These detectors are dedicated to determine primary and secondary vertices as well as tracking low-momentum particles. Outside the TPC, the Transition Radiation Detector (TRD) is positioned specifically for electron identification. The TRD plays a crucial role in distinguishing electrons from the other charged particles by taking advantage of the transition radiation phenomenon. The Time of Flight (TOF) detector provides particle identification by measuring the flight time of particles, enabling it to distinguish between species such as pions, kaons, and protons. Additionally, there are two single-armed detectors: an array of RHIC counters optimised for High Momentum Particle Identification (HMPID) and the Photon Spectrometer (PHOS).

The muon spectrometer, installed in forward section OF THE ALICE, focuses on muon tracking and identification. This upgrade enhanced the ALICE experiment's coverage in Run 2, making it possible to detect particles emitted at more extreme angles relative to the collision point [4]. In addition to the forward muon spectrometer, several other detectors of small dimensions in RUN 2 operations of LHC, such as V0, T0, Zero Degree Calorimeters (ZDC), Photon Multiplicity Detector (PMD), Forward Multiplicity Detector (FMD) are located at forward and backward rapidity region. An array of scintillators (ACORDE) is mounted on top of the L3 magnet and is used to trigger muons emitted by cosmic rays, which can be used for alignment and cosmic-ray measurement. A brief overview of a few of these detectors is given below.

2.4 Central Barrel Detectors of ALICE

The central barrel contains multiple sub-detectors with specialized roles in tracking charged particles, identifying different species, and generating trigger signals.

2.4.1 Inner tracking system (ITS)

The Inner Tracking System (ITS) in RUN 1 and RUN 2 of LHC operation is a semiconductor detector system positioned closest to the interaction point in the ALICE experiment, extending radially from 3.9 cm to 43.0 cm along the z-axis. With a cylindrical geometry, this detector covers the pseudorapidity range $-0.9 \leq \eta \leq 0.9$. A layout of the ITS detector is shown in Fig. 2.3. It is composed of three primary detector subsystems, all of which are configured with two layers each [5]. The three subsystems are:

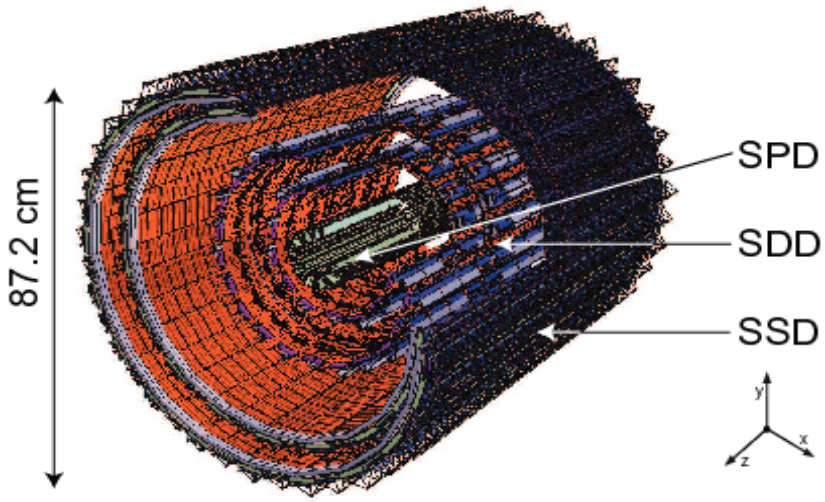

Figure 2.3: Diagram of the ALICE Inner Tracking System (ITS) showing its layered structure designed for high-precision vertexing and tracking [27].

- **Silicon Pixel Detectors (SPD)**: The ITS innermost layers are composed of Silicon Pixel Detectors. These detectors use pixel technology, providing fine spatial resolution. The extreme fine segmentation of the SPD allows it to operate in regions with very high track density, up to 50 tracks per square centimeter which makes it particularly suitable for measuring events with high particle multiplicities. Therefore, it is utilized to trigger high-multiplicity events.

- **Silicon Drift Detectors (SDD)**: The two middle layers of the ITS are built using Silicon Drift Detector technology. SDDs are designed to achieve accurate position measurements and are effective for tracking particles in regions of moderate density. They contribute to enhancing tracking coverage at larger radial distances from the beam pipe.

- **Silicon Strip Detectors (SSD)**: The ITS's external layers are equipped with Silicon Strip Detectors. Strip detectors are suitable for tracking particles in the regions with low particle density but over a larger area. SSDs extend the coverage to even larger radial distances, enhancing the tracking capabilities of particles with lower momenta.

ITS in the ALICE experiment identifies both primary and secondary vertices in heavy-ion collisions [28, 29, 30]. It also plays an important role in enhancing the momentum resolution of tracks reconstructed with the other central-barrel detectors. It serves as a stand-alone tracking detector for particles with low transverse momenta that do not reach the TPC in particular pions with momenta below 200 MeV/c.

2.4.2 Time Projection Chamber (TPC)

The Time Projection Chamber in the central barrel is the main ALICE tracking device. The TPC, like the ITS, measures charged particle momentum, identifies them, and determines interaction vertex [28, 31]. The TPC covers the pseudorapidity region $\mid \eta \mid \leq 0.9$ and the azimuthal acceptance of 360°. The schematic layout of the TPC detector is shown in Fig. 2.4. The TPC has a cylindrical shape, with an internal radius of about 85 cm, an external radius of around 247 cm, and a length of approximately 510 cm, resulting in a total active volume of approximately 88 m^3. As of right now, this is the largest TPC ever installed in any experiment. The active volume is split into two drift regions by the central electrode, positioned at the axial centre and biased to 100 kV. The active volume was filled with a mixture of Ne:CO_2:N_2 (Run 1) combination (90:10:5), except in 2017, during RUN 2 when Neon was replaced by argon. The maximum event rate that the TPC can support is limited by the maximum drift time of approximately 90 μs, which is generated

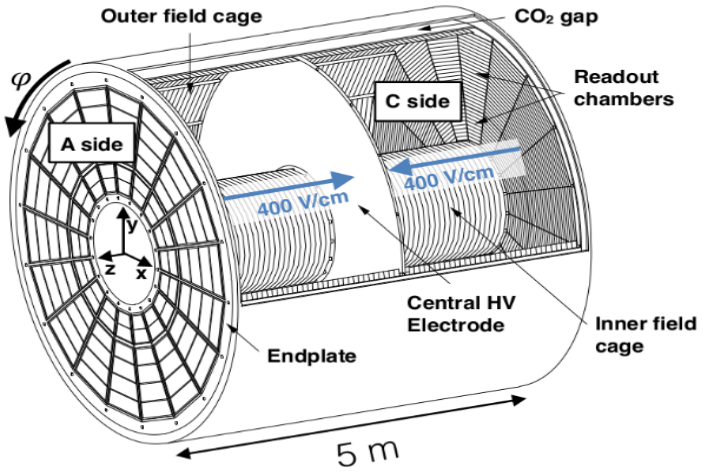

Figure 2.4: Layout of Time Projection Chamber (TPC) detector in the ALICE experiment at LHC [32].

by the electron drift velocity of 2.7 cm/s over 250 cm. Multi-Wire Proportional Chamber (MWPC) based readout chambers are mounted in 18 trapezoidal sectors at both ends of the TPC. As charged particles move within the gas volume, they cause ionization of gas molecules, generating electrons that drift through the chamber. As electrons reach the MWPC at the end plates, an electron avalanche occurs, which travels to the cathode pads on the readout plane. The pad coordinates provide the charged particle's position in the radial (r) and azimuthal (ϕ) directions. The z coordinate, where a constant drift velocity is assumed, is obtained by measuring the time taken to cross the chamber. This achieves a position resolution of 1100 (800) μm in the r,ϕ direction and 1250 (1100) μm in the z direction for tracks with inner (outer) radii. These values represent the precision with which the TPC can determine the positions of the charged particle tracks in the radial and longitudinal (z) direction. The transverse momentum (p_{T}) of the charged particles is extracted from the curvature of its track in the magnetic field [66]. The momentum resolution, expressed as a percentage, characterizes how well the TPC can determine the transverse momentum of a particle, reaching approximately 0.7% for p_{T} below 1 GeV/c and increasing to nearly 6.5% at p_{T} close to 10 GeV/c.

Particle Identification and track reconstruction

The TPC in the ALICE experiment is capable of reconstructing primary tracks across a large momentum range, spanning approximately $p_{\mathrm{T}} \approx 0.1 - 100, \mathrm{GeV}/c$, with an efficiency greater than 90% within this range. The efficiency here refers to the ability of the TPC to reconstruct and identify charged particle tracks successfully. The ITS and TPC can measure charged particle momentum with a resolution of more than 1% for low p_{T} and 20% for $p_{\mathrm{T}} \approx 100$ GeV/c by observing the deflection in the magnetic field [34]. The charge collected in the readout pads is used to evaluate the energy loss of the charged particles as they traverse the gas-filled volume of the TPC. The TPC measures particle momentum and energy loss at the same time which helps to distinguish different charged particle species in the low momentum range.

2.4.3 Time-Of-Flight (TOF)

The primary role of the Time-of-Flight detector is particle identification in the intermediate momentum range [35]. The detector consists of a large array of Multigap Resistive Plate Chambers (MRPCs), providing full coverage in azimuth (ϕ) and within the pseudorapidity interval $|\eta| \leq 0.9$, and is located 370-399 cm from the beam axis. Each TOF module is built as a 10-gap double-stack MRPC strip. This indicates a specific design with multiple gaps and a double-stack configuration. Any ionisation caused by a charged particle moving through a chamber will cause signals to be seen on the pick-up electrodes through the gas avalanche process.

Time resolution refers to the detector's ability to precisely measure the time of flight of particles which for TOF module in ALICE is stated to be approximately 40 ps. That means the detector can distinguish events with a time difference as small as 40 ps. The overall TOF resolution is stated to be around 60-80 ps for tracks with a momentum of 1 GeV/c in Pb-Pb collisions [36]. In contrast, for proton-proton events, the TOF resolution is around 100 ps. The slightly larger resolution in proton-proton events is attributed to a larger uncertainty in the determination of t_0, the event start time, (the moment when the particle is created at the interaction point).

The TOF detector provides particle identification with capability of providing a separation between protons and kaons with more than 3 standard deviations (3σ) [37] up to a momentum of p $\approx$ 4 GeV/c. While, for kaons and pions, the TOF detector is effective in distinguishing them up to around p $\approx$ 2.5 GeV/c, with a separation of about 2.5 standard deviations (2.5σ). Particle identification is carried out by measuring the time of flight of particles from the collision point to the TOF detector. The start time t_0 is determined using the T0 detector. The effectiveness of particle identification depends on the matching efficiency between TPC tracks and TOF hits, which rapidly falls to zero for tracks with momentum less than 0.7 GeV/c due to energy loss effects. However, for high transverse momenta (p_{T}), the identification efficiency reaches approximately 70%.

2.4.4 Transitional Radiation Detector

The Transition Radiation Detector (TRD) plays an essential role in identifying electrons with transverse momentum (p_{T}) $\geq$ 1 GeV/c [38]. This is achieved by detecting the transition radiation emitted by charged particles as they pass through the detector. The TRD can enhance the reconstruction of light and heavy vector mesons because of its ability to identify $e^{\pm}$. The TRD reconstructs a set of space points with good spatial resolution (approximately 600μm), allowing for longer tracks outside the TPC and improving overall track momentum resolution. Fig. 2.5 depicts the geometry of the TRD in the ALICE central barrel. The TRD detector surrounds the TPC, having an inner diameter of 290 cm and an outer diameter of 368 cm with respect to the beam axis [4]. The TRD is made up of 540 modules arranged into 18 sectors, (or super-modules), with a multi-wire proportional chamber and a radiator with a thickness of 4.8 cm in each module. It covers the entire azimuth in the mid-rapidity region (-0.84 < η < 0.84) and has a fast response time, enabling it to trigger on charged particles. This detector is effective for particles with a Lorentz factor γ greater than 1000, indicating good electron/pion separation for momenta $1 \leq p_{\mathrm{T}} \leq 100\ GeV/c$.

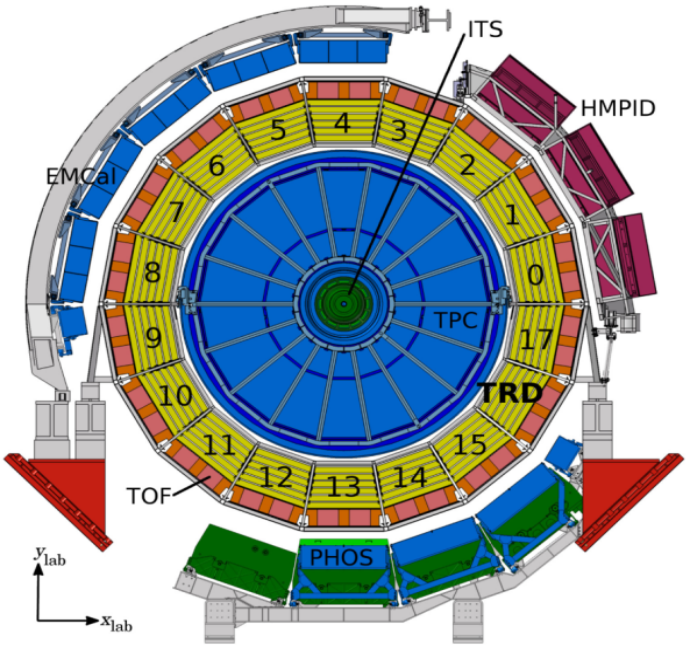

Figure 2.5: Schematic cross-section of the ALICE central barrel detector pendicular to the LHC beam direction showing sectors of TRD [39].

2.5 Forward Detectors at ALICE

The forward detectors in the ALICE experiment are specialized subsystems positioned at small angles relative to the beam axis, corresponding to the forward rapidity regions. Their primary purpose is to provide essential information about global event characteristics such as event triggering, multiplicity, centrality, and the position of the primary vertex. They also contribute in luminosity measurements.The main forward-detector systems in ALICE during RUN 2 consist of the Vertex (V0) and Timing (T0) detectors, Zero Degree Calorimeter (ZDC), Photon Multiplicity Detector (PMD), Forward Multiplicity Detector (FMD), and the ACORDE Diffractive (AD) detector. A couple of these are briefly discussed below.

2.5.1 V0 detector

The V0 detector is primarily used for triggering and for rejecting background events originating from beam-gas interactions. It is made up of two arrays, each with 32 counters. These counters are made of scintillator (Scintillators are materials that emit light when

charged particles pass through them.) material with embedded Wave Length Shifting fibers. The two arrays are placed asymmetrically on each side of the Interaction Point (IP) as shown in Fig. 2.6). One array is installed in the forward direction and is called VZERO-A (V0-A), and the other installed in the backward direction is called VZERO-C (V0-C). The V0-A array is located at a distance of 330 cm from the IP and it covers a pseudorapidity range of $2.8 > \eta > 5.1$ [40, 41]. The V0C array is positioned 90 cm from the IP and covers a pseudorapidity range of approximately $-3.7 < \eta < -1.7$ (Fig. 2.6).

The time resolution of this detector is about 1ns. By measuring the time-of-flight dif-

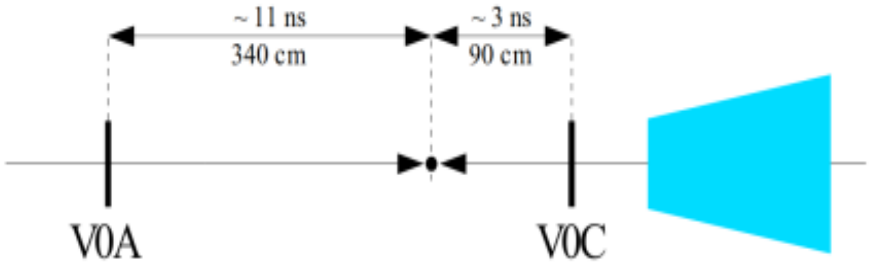

Figure 2.6: Time alignment condition on V0A and V0C [42].

ferences between V0A and V0C, the system can filter out background events associated with beam-gas interactions. It offers a Minimum-Bias trigger (MB) for the central barrel detectors. The V0 system, by measuring the energy deposition in its two discs, provides a means to gauge the centrality of the heavy-ion collisions and contributes to the overall characterization of the collision events. The total energy recorded by the V0 system correlates directly with the number of primary particles produced in the collision.

2.5.2 T0 detectors

The T0 detector consists of two arrays of quartz Cherenkov counters [4]. The two arrays are strategically positioned with the IP in-between them. The array located on side-A is known to as T0A, whereas the array located on side-C is referred to as T0C. The T0A and TOC are positioned at a distance of 3.6 meters and 70 centimeters repectively from the IP and thus covers a range of $4.5 < \eta < 5$ and $3.3 > \eta > 2.9$ respectively. The detector supplies fast signals to the ALICE Level-0 (L0) trigger system. With a time resolution of

50 ps, this detector can accurately determine the vertex position to within ± 1.5 cm. It also possesses a great ability to reject beam-gas interaction events.

2.5.3 Zero Degree Calorimeter (ZDC)

The Zero Degree Calorimeter (ZDC) [43] detector includes six quartz-fibre sampling calorimeters: two electromagnetic calorimeters (ZEM), two hadronic calorimeters for the detection of neutrons (ZN) and two for the detection of protons (ZP). The ZN and ZP calorimeters lie opposite to each other at a distance of approximately 112.5 meters from the interaction point. The ZP calorimeters are located outside the vacuum tubes. They are located on the side where positive particles are deflected by the LHC magnets. On the other hand, the ZN calorimeters are installed between the two beam vacuum tubes. The electromagnetic calorimeters are positioned on either side of the vacuum tube, approximately 7 meters from the IP, in the opposite direction relative to the muon arm detector. The muon arm is a forward spectrometer designed to detect and identify muons, which are produced in the forward rapidity region. It is installed on the C-side of the ALICE experiment, covering the pseudorapidity range $-4.0 < \eta < -2.5$. Its position defines the reference direction for the placement of other forward detectors such as the ZEM, helping in asymmetric detector layout [40].

ZDC covers the pseudorapidity range $4.8 < \eta < 5.7$ and is used to determine event centrality in Pb-Pb and p-Pb collisions by measuring the energy deposited by spectator nucleons, which emerge at zero degrees relative to the beam direction and do not participate in the collision. The ZEMs measure the energy deposited by photons and π^0 decays in the forward rapidity to resolve ambiguities in centrality determination caused by nuclear fragments that remain in the beam vacuum tubes and are not collected by hadronic calorimeters [43]. By using the ZDC for time measurements, background events resulting from main bunch collisions with satellite bunches during Pb-Pb data tracking can be rejected.

2.6 ALICE online operations

ALICE has central online systems that are used to control data-taking activities. The detector can operate independently, which is known as a standalone mode. Standalone mode is used to perform commissioning, calibration, and debugging activities. During the collection of physics data, detectors are assembled into "partitions" that can operate simultaneously and independently after receiving trigger inputs. The management of the data collection activities during the RUN 2 of LHC operations is carried out by five central web systems [41, 44, 45, 46, 47]. A brief introduction to these is given below.

2.6.1 Data Acquisition System

The Data Acquisition system (DAQ), is responsible for configuring the various detectors during data collection. Its primary role is to control the transfer of data from the detector electronics to permanent storage. It includes two types of interfaces: the TRiGger (TRG) system and the High-Level Trigger (HLT) system [48]. It permits the detector hardware to function from a central interface and thus provides overall supervision for the experimental equipment and ensures safe operation under beam conditions. The Experiment Control System (ECS) oversees and synchronizes all DAQ, TRG, and central system operations. The Local Data Concentrators (LDCs) retrieve events from the optical Dedicated Data Lines (DDLs), compile the data into sub-events, and then sends them to the Global Data Collectors (GDCs) [49]. The GDCs first place the data into temporary Transient Data Storage (TDS), after which it is moved to the Permanent Data Storage (PDS).

2.6.2 Central Trigger Processor (CTP)

The primary function of ALICE Trigger system during LHC Run 1 and Run 2 was to distribute trigger decisions and clock signals to the various ALICE subdetectors. Its architecture is organized around two major components: the CTP and the HLT [50, 51]. Each detector's CTP is made up of 24 Local Trigger Units (LTUs). The CTP is responsible for receiving signals from the various subdetectors and deciding whether to trigger data

readout based on predefined criteria. Whereas the LTUs receive signals directly from their respective subdetectors and perform local processing tasks. The LTUs provide input to the CTP regarding the status and activity of their associated subdetector.

During the first two LHC runs (Run1 and Run2), the CTP operated using a four-level trigger logic. The triggers are referred to as LM, L0, L1, and L2. The four trigger levels have varying latencies: The LM trigger has a latency of 650 ns, which serves as a wake-up trigger sent exclusively to the TRD. L0 has a latency of 900 ns, L1 has a latency of 6.5 μs, and L2 has a latency of 88 μs [52]. After the L2 trigger, the event is saved, and the CTP output is routed to the LTUs of each detector. The LTUs link the CTP to the Front End Electronics (FEE) of individual detectors. Additionally, they can emulate the CTP protocol, enabling subdetectors to operate independently from the rest of the ALICE detector. The output is shifted to the detector's front-end electronics via Low Voltage Differential Signalling (LVDS) cables and optical fibers. More details on the trigger system can be found in [52]

2.6.3 High Level Trigger (HLT)

A High Level Trigger (HLT) system in ALICE was developed to enable on-line data processing at full input rate and efficient data rate reduction. Fig. 2.7 shows how the HLT is integrated into the ALICE experiment's data flow. Raw data from the detector front-end is sent by optical fibers to the DAQ system, where ReadOut Receiver Cards (D-RORCs) read and send a copy to the HLT [53]. The HLT-RORCs receive data and interface with the processing nodes via the PCI bus. They are also equipped with an FPGA co-processor to efficiently handle complex pattern recognition tasks involving large datasets.

At a higher level, processed data from several detector sectors is combined and evaluated to reconstruct entire events and make trigger decisions. The HLT sends its outputs, such as trigger decisions, subevent maps, and compressed data, back to the DAQ, which helps decrease the total data rate.

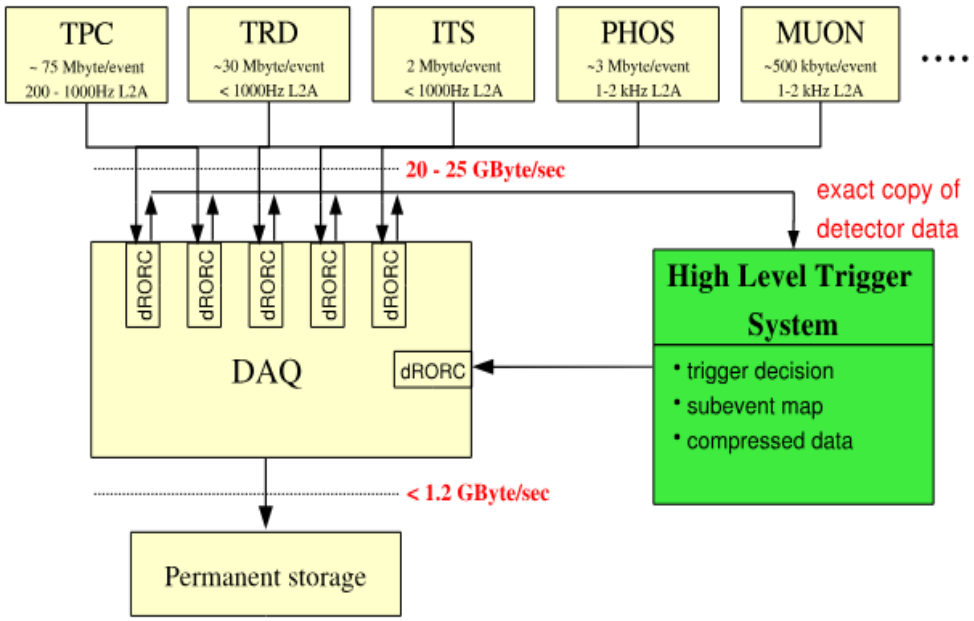

Figure 2.7: The HLT system is integrated into the data-flow architecture of the ALICE experiment, in which the DAQ replicates the raw data from the detector and sends an identical copy to the HLT system [54].

2.6.4 The Detector Control System (DCS)

The Detector Control System (DCS) provides optimal operating conditions for the experiment's data collection, resulting in the best possible results. The DCS is fundamentally responsible for guaranteeing the safe and dependable functioning of the ALICE experiment. It enables remote control and monitoring of all experimental equipment in carven via a special set of operator panels, allowing the ALICE experiment data collection to be managed and controlled from the ALICE Control Room (ACR). The DCS controls channel availability and constantly supervises the parameters necessary for high-quality physics data analysis. It can handle a variety of operating modes and allows each sub-detector, or any component of it, to operate independently and concurrently.

2.6.5 The Experiment Control System (ECS)

The ALICE experiment adjusts its operation using the Experimental Control System based on the LHC beam state (on/off) and beam type (heavy-ion or proton). The ECS adjusts ALICE operations in accordance with the current state of the LHC. It provides a framework en-

abling different teams to work simultaneously on separate detector groups without mutual interference. This is achieved by dividing the experiment into sections known as partitions. Tasks within each partition are coordinated and synchronized by the ECS. It addresses all of the correlations that occur between distinct activity domains [55]. The activity domains are managed by online systems with their own standards, methodologies, and tools, which can operate independently. The online systems operate independently, interacting with the ECS only to exchange control commands and status updates. The ECS communicates with all 'online systems' through the Finite-State Machine interfaces (FSM). Each detector performs calibration and configuration steps, particularly for the Front-End ReadOut (FERO). The ECS allows these procedures to be performed simultaneously across several detectors inside a partition [55].

2.7 ALICE offline operations

The raw data collected from the detectors must be processed before it can be converted into events for further analysis. This section outlines the offline data processing and analysis tools employed in ALICE data handling. ALICE offline analysis is done using AliRoot [59, 60] software platform based on the ROOT [61, 62] framework. A large section of the high-energy physics experimental community, including ALICE uses scientific software ROOT as analysis framework. The volume of the data collected by ALICE is huge and is stored in the various computing facilities using GRID network technology.

2.7.1 ALICE Grid and AliEn

Because of the massive and unprecedented volume of data collected at the LHC, processing and data storage resources are spread over numerous computing centers [57]. For this, a worldwide distributed computing project was started in 2000, which successfully established the dispersed computing infrastructure required for processing and storage of data in the LHC experimental program. The ALICE Environment (AliEn) architecture was designed to offer ALICE experiments users with transparent access to globally distributed

computing resources across the Grid. The Grid allows the project's partner institutions to distribute their computing resources. The ALICE Grid divides its computing resources into multiple Tiers, designed according to the MONARC (Models of Network Analysis at Regional Centers for the LHC Experiments) model. Responsibilities of these Tiers are:

- Tier-0 at CERN handles the initial recording and secure preservation of the raw data generated by the experiments.
- A second copy of the data is made available to the big external Tier 1 centers with responsibility to duplicate the event.
- Regional Tier 2 centers take part in Monte Carlo simulations and assist in to prepare files for solo users to analyze.

The AliEn environment ensures that ALICE users can access the Grid middleware. ALICE users can access data, send analytical jobs and simulations, and monitor them through the AliEn User Interface, in particular. Fig.2.8 depicts a schematic representation of the ALICE offline framework where AliEn comprises of AliRoot, the analysis framework ROOT integrated with ALICE experiment specific classes and functions [58].

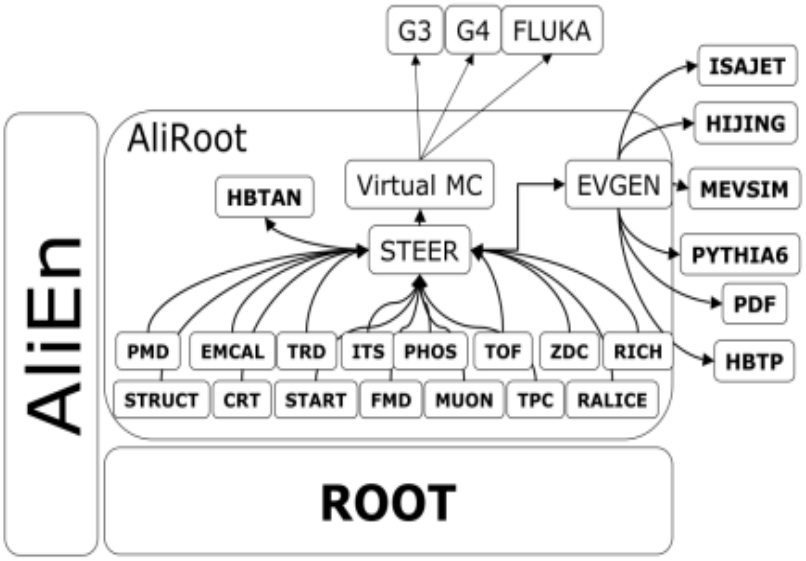

Figure 2.8: A scheme of AliRoot data processing framework [40] of ALICE experiment.

2.7.2 ROOT and AliRoot framework

ALICE project relies on the ROOT analysis framework [61]. ROOT is primarily written in C++, but it also offers interfaces for other languages like Python and R. ROOT was developed at CERN to handle and analyze large data from the heavy-ion collisions efficiently. In addition to its extensive data management and storage features, ROOT includes a comprehensive range of mathematical and statistical analytical tools. AliRoot [59, 60] is a modified version of ROOT [62] designed exclusively for the ALICE experiment's simulation, reconstruction requirements [63] and analysis related classes and functions.

Simulation

A simulation is a computer-generated representation of an experiment. The high-energy collision experiments are heavily reliant on simulations of experiment and simulated collision events. To optimise physics data for detector efficiency and acceptance constraints, simulated event samples are used. A simulated collision event is typically described using two elements: the event generator and the transport code. Event generators generate particles and events with average behaviours identical to those found in real data by applying the theoretical ideas of collision dynamics. Many event generators use a variety of theories and physical procedures to produce events that are as close to known real data as possible. Outputs from the event generator are subsequently fed into the transport models as input. Transport models such as GEANT [64, 65], replicates the behaviour of detectors and attempts to approximate as closely as possible the amount and properties of particles gathered by the experiments.

Data Reconstruction

When a charged particle traverses the sensitive volume of a detector, it leaves behind a signal (called a "digit") corresponding to energy deposition. These signals are recorded along with their spatial coordinates and represent the raw data of the experiment. The process of transforming this raw data into meaningful physical quantities, such as particle

trajectories and identities, is called reconstruction. Reconstruction is a crucial step that enables the transition from detector-level signals to physics-level observables. The first step in reconstruction is clustering, where adjacent digits are grouped to form clusters. These clusters indicate the locations where particles passed through the detector. The center-of-gravity of these clusters provide a reconstructed point, giving an estimate of the actual particle trajectory within the detector [66]. These reconstructed points from various sub-detectors are then linked to form tracks, which contain kinematic information (such as momentum and charge) and enable the identification of particle species (if applicable). The complete output of the reconstruction process is stored in a structured format known as Event Summary Data (ESD). For physics analysis, a more compact data format called Analysis Object Data (AOD) is used in ALICE.

In ALICE, the reconstruction of raw data begins with detector-specific calibration followed by clustering. This process is executed independently for each detector. For instance, in tracking detectors such as the ITS and TPC , clusters are formed by grouping nearby digitized signals. The energy deposited by clusters in calorimeters are also saved within the ESDs [67]. The reconstruction begins with estimating the primary interaction vertex from SPD-generated tracklets. A tracklet is constructed by correlating clusters from the two SPD layers that point back to a common origin [68], and the vertex position is obtained from the point where most of these tracklets converge.

ALICE uses a three-iteration track reconstruction procedure in the central barrel region that relies on the Kalman filter algorithm [28]. This method allows simultaneous track finding and fitting by locally updating track parameters while propagating through the detector.

- **First iteration:** Track finding begins at the outer radius of the TPC, where seed tracks are created using pairs of clusters. These seeds are projected inward, and clusters are progressively added to refine the tracks. The tracks are then extrapolated to the ITS, using the preliminary vertex from the SPD [69].

- **Second iteration:** Tracks are propagated outward from the SPD vertex back through the TPC using clusters identified in the first step. At this stage, energy loss informa-

tion is incorporated to aid in particle identification. The refined tracks are subsequently matced with energy deposits in the surrounding outer detectors, including the TRD, TOF, HMPID, EMCAL, and PHOS.

- **Third iteration:** The tracks are refitted inward again using updated cluster associations. The final result is a set of refined tracks called global tracks, which offer improved estimates of particle kinematics [69]. These are used to recalculate the interaction vertex with greater precision.

By combining precise spatial information from multiple detectors and using advanced tracking algorithms, the ALICE reconstruction framework builts the events and a big pool of data. Analysis of this data for various physics studies helps to understand the dynamics of heavy-ion collisions, system formed and its properties.

ESD and AOD files

Once reconstruction is complete, the raw data are archived in files called Event Summary Data (ESD) files. These ESD files contain detailed reconstructed information from all sub-detectors, which includes trigger information, collision vertex measurements, and individual particle track data from various sub-detectors. However, because of their larger size, the ESD files are heavy for local analysis. To minimize file size and boost analysis, the ESD objects are processed further to generate Analysis Object Data (AOD) files. AOD files contain only the information required for physics analysis, resulting in much smaller file sizes than their corresponding ESD objects. Physics analysis can be performed using either ESD or AOD format, depending on the specific requirements.

In this work the data recorded using ALICE detector in Run 2 of LHC operations and simulated events for the similar conditions of the experiment are analyszed. In the following chapters the analysis methodology, is given followed by discussion on the observations and results from the analysis of simulated events and experimental data using AliPhysics version "*vAN-20200510-1*"and ROOT [*6.26/04*] within the AliEn analysis environment is given.

BIBLIOGRAPHY

[1] M. Beech, "The Large Hadron Collider. Unraveling the Mysteries of the Universe," Springer, ISBN 978-1-4419-5667-5, (2010).

[2] CERN, *The SPS Physics Programme*, CERN Report OPEN-99-049, 1999. Available at: https://cds.cern.ch/record/397571/files/open-99-049.pdf.

[3] J. Adams *et al.* [STAR], "Identified particle distributions in pp and Au+Au collisions at s(NN)**(1/2) = 200 GeV," Phys. Rev. Lett. **92**, 112301 (2004) doi:10.1103/PhysRevLett.92.112301 [arXiv:nucl-ex/0310004 [nucl-ex]].

[4] K. Aamodt *et al.* [ALICE], "The ALICE experiment at the CERN LHC," JINST **3**, S08002 (2008).

[5] B. B. Abelev *et al.* [ALICE], "Performance of the ALICE Experiment at the CERN LHC," Int. J. Mod. Phys. A **29**, 1430044 (2014). [arXiv:1402.4476 [nucl-ex]].

[6] L. Evans and P. Bryant, "LHC Machine, The CERN large hadron collider: accelerator and experiments," *JINST*, **3**, S08001, 2008.

[7] CERN, "Large Electron-Positron Collider (LEP)," https://home.cern/science/accelerators/large-electron-positron-collider.

[8] CERN, "LEP Design Report," http://cds.cern.ch/record/102083.

[9] K. Schindl, "The injector chain for the LHC," 9th LEP Performance Workshop, CERN-PS-99-018-DI.

[10] A. Beuret, A. Blas, J. Borburgh, H. Burkhardt, C. Carli, M. Chanel, T. Fowler, M. Gourber-Pace, S. Hancock and C. E. Hill, *et al.* "The LHC Lead Ion Injector Chain," 9th European Particle Accelerator Conference, EPAC-2004-TUPLT011.

[11] R. Garoby, "Upgrade Issues for the CERN Accelerator Complex," Conf. Proc. C **0806233**, fryagm01 EPAC08-FRYAGM01 (2008).

[12] CERN, "The CERN accelerator complex," http://public-archive.web.cern.ch/public-archive/en/research/AccelComplex-en.html.

[13] G. Aad *et al.* [ATLAS], "The ATLAS Experiment at the CERN Large Hadron Collider," JINST **3**, S08003 (2008).

[14] S. Chatrchyan *et al.* [CMS], "The CMS Experiment at the CERN LHC," JINST **3**, S08004 (2008).

[15] A. A. Alves, Jr. *et al.* [LHCb], "The LHCb Detector at the LHC," JINST **3**, S08005 (2008).

[16] A. Tiberio [LHCf],"The LHCf experiment at the Large Hadron Collider: status and prospects," PoS **ICRC2023**, 444 (2023).

[17] G. Anelli *et al.* [TOTEM], "The TOTEM experiment at the CERN Large Hadron Collider," JINST **3**, S08007 (2008).

[18] J. Pinfold *et al.* [MoEDAL], "Technical Design Report of the MoEDAL Experiment," CERN-LHCC-2009-006.

[19] [ALICE], "ALICE luminosity determination for pp collisions at $\sqrt{s} = 8$ TeV," ALICE-PUBLIC-2017-002.

[20] S. Chatrchyan *et al.* [CMS], "Observation of a New Boson at a Mass of 125 GeV with the CMS Experiment at the LHC," Phys. Lett. B **716**, 30-61 (2012) [arXiv:1207.7235 [hep-ex]].

[21] M. Hostettler and G. Papotti, "Luminosity Lifetime at the LHC in 2012 Proton Physics Operation".

[22] ALICE Collaboration, "Components of the ALICE detector in its Run 2 configuration," https://www.researchgate.net/figure/Components-of-the-ALICE-detector-in-its-Run-2-configuration-4_fig1_382247236, 2023.

[23] G. Aad *et al.* [ATLAS], "Observation of a new particle in the search for the Standard Model Higgs boson with the ATLAS detector at the LHC," Phys. Lett. B **716**, 1-29 (2012) [arXiv:1207.7214 [hep-ex]].

[24] S. Chatrchyan *et al.* [CMS], "Observation of a New Boson at a Mass of 125 GeV with the CMS Experiment at the LHC," Phys. Lett. B **716**, 30-61 (2012) [arXiv:1207.7235 [hep-ex]].

[25] CERN, "The CERN accelerator complex: Operation and configuration," http://cds.cern.ch/record/2636343/files.

[26] E. Botta [ALICE], "Particle identification performance at ALICE," [arXiv:1709.00288 [nucl-ex]].

[27] K. Aamodt *et al.* [ALICE], "Alignment of the ALICE Inner Tracking System with cosmic-ray tracks," JINST **5**, P03003 (2010) [arXiv:1001.0502 [physics.ins-det]].

[28] R. Fruhwirth, "Application of Kalman filtering to track and vertex fitting," Nucl. Instrum. Meth. A **262**, 444-450 (1987).

[29] Y. Belikov *et al.* [ALICE], "Kalman Filtering Application for Track Recognition and Reconstruction in ALICE Tracking System," ALICE-INT-1997-24.

[30] G. Dellacasa *et al.* [ALICE], "ALICE: Technical design report of the inner tracking system (ITS)," CERN-LHCC-99-12.

[31] G. Dellacasa *et al.* [ALICE], "ALICE: Technical design report of the time projection chamber," CERN-OPEN-2000-183.

[32] J. Alme, Y. Andres, H. Appelshauser, S. Bablok, N. Bialas, R. Bolgen, U. Bonnes, R. Bramm, P. Braun-Munzinger and R. Campagnolo, *et al.* "The ALICE TPC, a large 3-dimensional tracking device with fast readout for ultra-high multiplicity events," Nucl. Instrum. Meth. A **622**, 316-367 (2010) [arXiv:1001.1950 [physics.ins-det]].

[33] I. Belikov [ALICE], "Event reconstruction and particle identification in the ALICE experiment at the LHC," EPJ Web Conf. **70**, 00029 (2014).

[34] C. Lippmann [ALICE TPC], "The Time Projection Chamber for the ALICE Experiment," [arXiv:0809.5133 [nucl-ex]].

[35] P. Cortese *et al.* [ALICE], "ALICE: Addendum to the technical design report of the time of flight system (TOF)," CERN-LHCC-2002-016.

[36] A. Akindinov, A. Alici, A. Agostinelli, P. Antonioli, S. Arcelli, M. Basile, F. Bellini, G. Cara Romeo, L. Cifarelli and F. Cindolo, *et al.* "Performance of the ALICE Time-Of-Flight detector at the LHC," Eur. Phys. J. Plus **128**, 44 (2013).

[37] G. Dellacasa *et al.* [ALICE], "ALICE technical design report of the time-of-flight system (TOF)," CERN-LHCC-2000-012.

[38] A. Andronic and J. P. Wessels, "Transition Radiation Detectors," Nucl. Instrum. Meth. A **666**, 130-147 (2012) [arXiv:1111.4188 [physics.ins-det]].

[39] S. Acharya *et al.* [ALICE], "The ALICE Transition Radiation Detector: construction, operation, and performance," Nucl. Instrum. Meth. A **881**, 88-127 (2018) [arXiv:1709.02743 [physics.ins-det]].

[40] F. Carminati *et al.* [ALICE], "ALICE: Physics performance report, volume I," J. Phys. G **30**, 1517-1763 (2004).

[41] E. Abbas *et al.* [ALICE], "Performance of the ALICE VZERO system," JINST **8**, P10016 (2013) [arXiv:1306.3130 [nucl-ex]].

[42] P. Cortese *et al.* [ALICE], "ALICE technical design report on forward detectors: FMD, T0 and V0," CERN-LHCC-2004-025.

[43] G. Dellacasa *et al.* [ALICE], "ALICE technical design report of the zero degree calorimeter (ZDC)," CERN-LHCC-99-05.

[44] B. B. Abelev *et al.* [ALICE], "Performance of the ALICE Experiment at the CERN LHC," Int. J. Mod. Phys. A **29**, 1430044 (2014) [arXiv:1402.4476 [nucl-ex]].

[45] G. Herrera-Corral [ALICE], "A new detector array for diffractive physics in ALICE at the LHC," AIP Conf. Proc. **1350**, no.1, 176-179 (2011).

[46] J. Allen, C. Bernard, O. Bourrion, M. Chala, M. Del Franio, O. Driga, F. Fichera, N. Giudice, A. Grimaldi and P. Laloux, *et al.* "ALICE DCal: An Addendum to the EMCal Technical Design Report Di-Jet and Hadron-Jet correlation measurements in ALICE," CERN-LHCC-2010-011.

[47] C. Finck [ALICE Muon Spectrometer], "The muon spectrometer of the ALICE," J. Phys. Conf. Ser. **50**, 397-401 (2006).

[48] F. Carena *et al.* [ALICE], "The ALICE data acquisition system," Nucl. Instrum. Meth. A **741**, 130-162 (2014).

[49] A. Holba *et al.* [ALICE], "ALICE Data Acquisition System Program of \& Work," ALICE-INT-1995-03.

[50] ALICE Collaboration, "ALICE trigger data-acquisition high-level trigger and control system: Technical Design Report," CERN/LHCC 2003/062 (2004), https://edms.cern.ch/document/456354/2.

[51] F. Bergsma et al., CERN ALICE DAQ Group, "ALICE DAQ and ECS users guide," ALICE Internal Note ALICE-INT-2005-015, https://edms.cern.ch/record/960457.

[52] M. Krivda, "The ALICE trigger electronics," Topical Workshop on Electronics for Particle Physics, (2007).

[53] M. Richter, T. Alt, S. Bablok, C. Cheshkov, P. T. Hille, V. Lindenstruth, G. Øvrebekk, M. Ploskon, S. Popescu and D. Röhrich, *et al.* "High Level Trigger applications for the ALICE experiment," IEEE Trans. Nucl. Sci. **55**, 133-138 (2008).

[54] M. Richter, "Development and Integration of on-line Data Analysis for the ALICE Experiment," CERN-THESIS-2009-189.

[55] F. Carena, W. Carena, S. Chapeland, R. Divia, J. C. Marin, K. Schossmaier, C. Soos, P. Vande Vyvre and A. Vascotto, "The ALICE experiment control system," Conf. Proc. C **051010**, MO4A.3-7O (2005).

[56] P. Chochula et al., "The ALICE detector control system," 2009 16th IEEE-NPSS Real Time Conference, Beijing, China, 2009, pp. 346-350, https://doi:10.1109/RTC.2009.5322159.

[57] CERN Courier, "The ALICE Computing Project," https://cerncourier.com/a/the-alice-computing-project/.

[58] A. Gheata [ALICE], "ALICE analysis framework," PoS **ACAT08**, 028 (2008).

[59] R. Brun, P. Buncic, F. Carminati, A. Morsch, F. Rademakers, and K. Safarik, "Computing in ALICE," Nucl. Instrum. Meth. A **502**, 339–346 (2003). https://doi.org/10.1016/S0168-9002(03)00440-6.

[60] K. Aamodt *et al.* [ALICE], "Alignment of the ALICE Inner Tracking System with cosmic-ray tracks," JINST **5**, P03003 (2010) [arXiv:1001.0502 [physics.ins-det]].

[61] ROOT Data Analysis Framework, https://root.cern/.

[62] CERN, "ROOT Data Analysis Framework," CERN-Brochure-2017-002-Eng (2017). https://cds.cern.ch/record/2255762.

[63] ALICE Collaboration, *ALICE Offline Webpage*, http://aliceinfo.cern.ch/Offline/.

[64] S. Agostinelli *et al.* [GEANT4], "GEANT4 - A Simulation Toolkit," Nucl. Instrum. Meth. A **506**, 250-303 (2003).

[65] R. Brun, R. Hagelberg, M. Hansroul and J. C. Lassalle, "Geant: Simulation Program for Particle Physics Experiments. User Guide and Reference Manual," CERN-DD-78-2-REV.

[66] I. Belikov [ALICE], "Event reconstruction and particle identification in the ALICE experiment at the LHC," EPJ Web Conf. **70**, 00029 (2014).

[67] E. Bruna, A. Dainese, M. Masera, and F. Prino, "Vertex reconstruction for proton-proton collisions in ALICE," CERN-ALICE-INT-2009-018 (2009). https://cds.cern.ch/record/1225497.

[68] D. Elia, J. Grosse-Oetringhaus, M. Nicassio, and T. Virgili, "The pixel detector based tracklet reconstruction algorithm in ALICE," CERN-ALICE-INT-2009-021 (2009), https://cds.cern.ch/record/1225500.

[69] M. Arslandok, E. Hellbar, M. Ivanov, R. H. Münzer and J. Wiechula, "Track Reconstruction in a High-Density Environment with ALICE," Particles **5**, no.1, 84-95 (2022) [arXiv:2203.10325 [physics.ins-det]].

CHAPTER 3

ANALYSIS: METHODOLOGY AND HIJING EVENTS

The primary objective of high-energy nuclear collisions is to create and analyze the behaviour of hot and dense nuclear matter. Recent ongoing experiments like STAR at RHIC, CMS, ATLAS and ALICE at LHC yielded an extensive amount of data revealing the creation of Quark-Gluon Plasma (QGP). As system formed in the high-energy collisions cools, the QGP transitions to the hadronic phase. To determine order of this transition and to search for the location of the critical point in the nuclear matter phase diagram are among some of the main objectives of the searches in this fields [1]. Examining event-by-event fluctuations of global observables is a valuable tool for comprehending QGP to hadronic phase transition and understanding the fundamental dynamics of multiparticle production in heavy-ion collisions. Since fluctuation observables are inherently related to particle correlations thus, studying fluctuations can shed light on the mechanism underlying the production of particles in a relativistic nuclear collision [2].

A. Bialas and R. Peschanski successfully explained the high multiplicity spike observed

in the eta distribution of Japanese-American Collaborative Emulsion Experiment (JACEE) event in 1986 using scaled factorial moments in one-dimensional space [3]. After that, there was a surge of interest in this analytical technique for understanding multiparticle production dynamics in the field by many experimental groups for different systems [4, 5, 6]. It was hypothesized that if the produced particle spectra from high-energy collisions exhibits intermittent behaviour, it would result in spikes in the rapidity distribution. These spikes, which are clusters of particles in small rapidity intervals, appear as high-density peaks of dynamical origin in the phase space distribution of individual events [2, 7]. Analyzing particle distributions using factorial moments is inspired by intermittency studies in turbulence phenomenon in fluids, where irregular, large fluctuations occur in the system near phase transition.

The power-law behaviour of the normalised factorial moments in the decreasing bin sizes, known as *intermittency* was proposed as a signal of QGP formation [2] and self-similarity in particle production processes. A fundamental characteristic of the system undergoing phase transition is that it exhibits fluctuations across all scales. Numerous experimental studies using factorial moments have revealed intermittent patterns in various types of interactions, such as nucleus-nucleus [8, 9, 10, 11], hadron-nucleus [12, 13], muon-hadron [14, 15], and e^+e^- [16, 17, 18] interactions. However, none of these studies reported any observation of signal of a phase transition. Recently the scaling properties of the normalized factorial moments of multiplicity fluctuations in the data from LHC [19] are proposed to be investigated. Dependence of these moments on resolution signifies genuine dynamic fluctuations. Infact the ability to filter out Poissonian noise [2] from the signal makes normalized factorial moment analysis, a candidate for investigating fluctuation behaviour of various systems in nature.

In low-energy collision experiments particle multiplicities were quite low to support binning of the phase space into small bin sizes. However, at LHC, the average collision contains multiple parton interactions resulting in very high multiplicities that even small bins in the phase space contain some particles. At these energies, tight kinematic cuts can be applied while still retaining enough particles in small (p_{T}) bins, making it feasi-

ble to investigate scaling behaviour across different bin sizes in the chosen phase space. Performing intermittency analysis for the LHC data overrides the limitations of low energy experiments and promises to reveal an important information about the dynamics of multiparticle production at extreme conditions of temperature and energy [20].

A model that gives insight into the phase transition processes is the Ising model [21]. Intermittency in the Ising model has been studied through analytical and numerical approaches [22, 23], revealing an anomalous fractal dimension (d_q) of 1/8, regardless of the order of the moment (q). This has led to speculation that intermittency might exhibit monofractal characteristics in QCD second-order phase transitions [24]. However, various interactions, such as those in heavy-ion collisions, exhibit multifractal behaviour [25]. With decreasing phase-space bins, within the Ginzburg-Landau second-order formalism the anomalous fractal dimension varies rather than remaining constant. Investigations into the fractal characteristics of the system, to understand the fractal nature of the system of quarks and gluons created in heavy-ion collisions can be carried.

In this chapter, a two-dimensional intermittency analysis methodology as proposed in [26], for examining fluctuations in multiplicity distributions using normalized factorial moments is presented. The data sets and the various selection cuts on the events and tracks are also discussed. Observations and results from the analysis of the Monte Carlo HIJING [27] events from the central production of the ALICE experiment for Xe–Xe collisions at $\sqrt{s_{\mathrm{NN}}} = 5.44$ TeV are also given in this chapter.

3.1 Methodology and Observables

The methodology for event-by-event two dimensional intermittency analysis as proposed in [26] is performed on the data sets (section 3.2) is;

The (η, ϕ) phase space of an event is divided into a square lattice with $M_\eta \times M_\phi$ bins, M_η and M_ϕ being the number of bins along η and ϕ dimension respectively. This is graphically illustrated in Fig. 3.1. The binning is show for two cases one with $M = 6$ and another with $M = 10$ ($M_\eta = M_\phi = M$(say)). M defines the number of bins that takes positive integer values

and is varied from a minimum value $M_{\rm min}$ to a maximum value $M_{\rm max}$. These values are constrained by the detector resolution, charged particle density, and the acceptance region. Particles in an event in the selected kinematic phase space are mapped onto this (η,ϕ) matrix partitioned into M^2 bins (see Fig. 3.1 and Fig. 3.2). The number of particles that fall in each bin determines its bin multiplicity $(n_{\rm m})$ also termed as bin content. Because each event is unique, this mapping results in distinct configurations for each M and every event. The normalized factorial moments of an $e^{\rm th}$ event as a function of M is then defined as [28],

$$F_{\rm q}^{\rm e}(M) = \frac{f_{\rm q}^{\rm e}(M)}{[f_{\rm 1}^{\rm e}(M)]^q}. \tag{3.1}$$

where,

$$f_{\rm q}^{\rm e}(M) = \left[\langle n_{\rm m}(n_{\rm m}-1)\cdots(n_{\rm m}-q+1)\rangle\right]_{\rm e}. \tag{3.2}$$

Here q is the order of the moment and it takes positive integer values ≥ 2 such that in

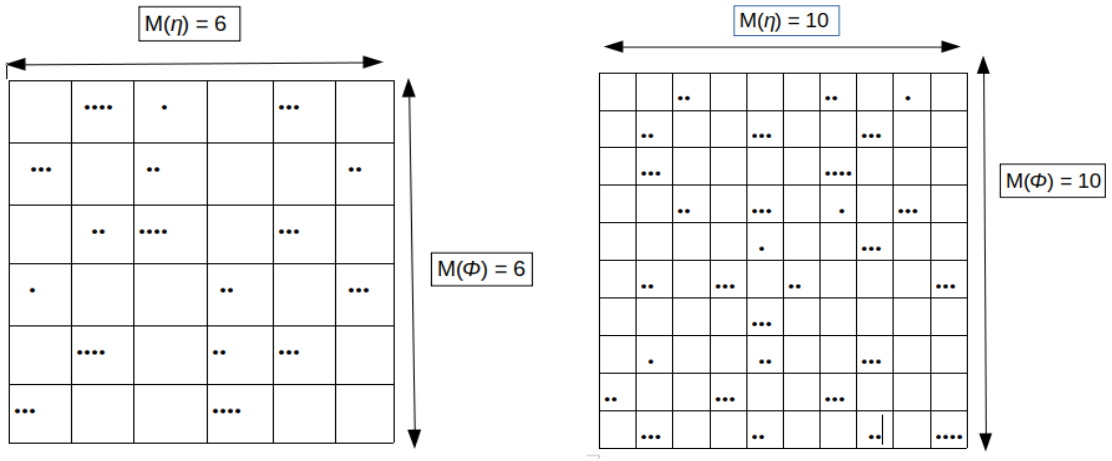

(a) (b)

Figure 3.1: A pictorial representation of binning in the two-dimensional (η,ϕ) phase space. Two different scenarios are shown with the number of bins set to M = 6 and 10 in each direction. Figure illustrate the increasing resolution of the bins in the phase space. As M increases, the bin sizes become smaller.

Eq. (3.2) only bins with $n_{\rm m} \geq q$ are considered. $n_{\rm m}$ represents the bin multiplicity of the $m^{\rm th}$ bin for an event partitioned into M^2 bins. <...> is the averaging over bins and is

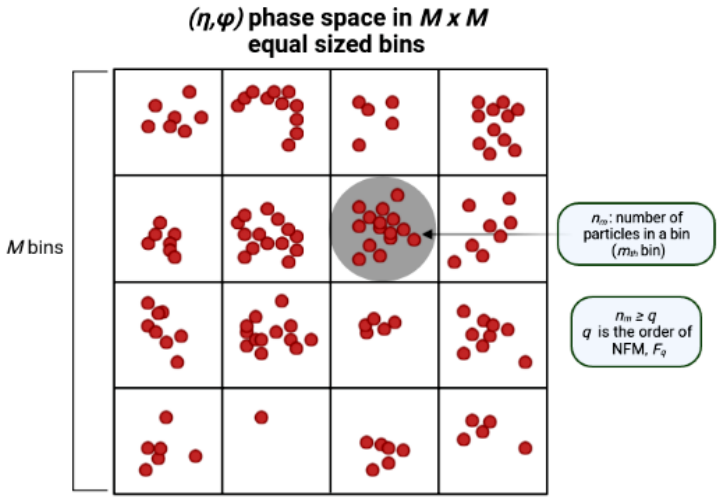

Figure 3.2: Pictorial representation of binning and the distribution of particles in an event mapped onto the (η, ϕ) phase space partitioned with M = 4 bins along each dimension.

referred to as the horizontal average, in a practice that considers different events as being vertically stacked. More explicitly Eq. (3.2) can be rewritten as

$$f_{\mathrm{q}}^{\mathrm{e}}(M) = \left[\frac{1}{M^2}\sum_{m=1}^{M^2} n_{\mathrm{m}}(n_{\mathrm{m}}-1)\ldots(n_{\mathrm{m}}-q+1)\right]_{\mathrm{e}}. \tag{3.3}$$

Accordingly $f_1^{\mathrm{e}}(M)$ in the denominator of Eq.(3.1) is just the average bin multiplicity $< n_{\mathrm{m}} >$ of an e^{th} event, such that

$$[f_1^{\mathrm{e}}(M)]^{\mathrm{q}} = \left(\frac{1}{M^2}\sum_{m=1}^{M^2} n_{\mathrm{m}}\right)_{\mathrm{e}}^{\mathrm{q}} = (< n_{\mathrm{m}} >)_{\mathrm{e}}^{\mathrm{q}}. \tag{3.4}$$

The $F_{\mathrm{q}}^{\mathrm{e}}(M)$ in Eq.(3.1) defines the normalized factorial moments of the spatial fluctuations of particles in an e^{th} event, which in expanded form is;

$$F_{\mathrm{q}}^{\mathrm{e}}(M) = \frac{\left[\frac{1}{M^2}\sum_{m=1}^{M^2} n_{\mathrm{m}}(n_{\mathrm{m}}-1)\cdots(n_{\mathrm{m}}-q+1)\right]_{\mathrm{e}}}{\left[\frac{1}{M^2}\sum_{m=1}^{M^2} n_{\mathrm{m}}\right]_{\mathrm{e}}^{q}}. \tag{3.5}$$

The normalized factorial moments $F_{\mathrm{q}}(M)$ for a sample of "N" events, also termed as vertically average horizontal moments, are then defined as;

$$F_{\mathrm{q}}(M) = \frac{1}{N}\sum_{e=1}^{\mathrm{N}} F_{\mathrm{q}}^{\mathrm{e}}(M). \tag{3.6}$$

In expanded form, it is

$$F_{\mathrm{q}}(M) = \frac{\frac{1}{N}\sum_{e=1}^{N} f_{\mathrm{q}}^{\mathrm{e}}(M)}{\frac{1}{N}\sum_{e=1}^{N}[f_1^{\mathrm{e}}(M)]^{\mathrm{q}}} = \frac{\frac{1}{N}\sum_{e=1}^{N}\left[\frac{1}{M^2}\sum_{m=1}^{M^2} n_m(n_m-1)\ldots(n_m-q+1))\right]_e}{\frac{1}{N}\sum_{e=1}^{N}\left[\left(\frac{1}{M^2}\sum_{m=1}^{M^2} n_m\right)\right]_e^{\mathrm{q}}}. \tag{3.7}$$

Normalized factorial moments as defined in above equation filter statistical noise (due to the finite multiplicity per event). $F_{\mathrm{q}}(M)$ = 1 if the multiplicity distribution is pure Poissonian. Thus F_{q} moments enable the detection of dynamical multiplicity fluctuations from bin-to-bin, such as the development of new scales or the presence of an "intermittent" background, characterized by cascading fluctuations at multiple scales. Hwa and Yang [26] proposed that the charged particles produced in heavy-ion collisions at LHC, where the particle number densities per bin are very high, must be investigated using NFM to study their scaling behaviour [29], as it can give vital information about various characteristics of the system. These studies have potential to reveal the hidden characteristics of systems at high energy density and may provide answers to questions still under vigrous scientific investigations such as the location of the critical point, particle production mechanism, order of the phase transition etc.

3.1.1 Intermittency and M-scaling behaviour

The behaviour of normalized factorial moments $F_{\mathrm{q}}(M)$ also known as scaled factorial moments can be investigated for their dependence on the number of bins (M for one-dimensional case and M^2 for two-dimensional case). As the number of bins determine the phase space resolution, this dependence is known as *resolution scaling*. For the q^{th} order normalized factorial moments (NFM) exhibiting a *power-law* behaviour with the size

of the bins (δ) or number of bins (M) (with $\delta \propto \frac{1}{M}$), as;

$$F_{\mathrm{q}}(\delta) \propto \frac{1}{\delta^{\varphi_{\mathrm{q}}}} \tag{3.8}$$

or

$$F_{\mathrm{q}}(M) \propto M^{\varphi_{\mathrm{q}}}, \tag{3.9}$$

is termed as intermittency [25, 26]. For the d-dimensional phase-space, it can be written as

$$F_{\mathrm{q}}(M^{\mathrm{d}}) \propto \left(M^{\mathrm{d}}\right)^{\varphi_{\mathrm{q}}}, \tag{3.10}$$

where d is the dimension of the phase space. The scaling index, φ_{q}, is called the intermittency index and it characterizes the strength of the intermittency [30, 31]. Presence of intermittency in a system that is observation of behaviour as defined in Eq.(3.10) indicates the scale invariance of particle number density. In other words the statistical properties of the particle distributions remain consistent across different scales. This scaling behaviour is also known as *M-scaling*. This is also a feature of systems having self-similar nature or the fractal nature. Conversely, any deviation from this behaviour would indicate the absence of self-similarity and also that of the fractal nature. In effect, the study of *M-scaling* behaviour gives insight into the nature of the underlying physical processes in a system under study thereby helping to identify non-trivial dynamics. Presence of strict linear dependence of the normalized factorial moments on M is expected to be shown by the systems near critical point and exhibiting large multiplicity fluctuations.

3.1.2 F-scaling behaviour and scaling exponent ν

With Ginzburg-Landau (GL) formalism for second-order phase transition, it is observed [32] that $F_{\mathrm{q}}(M)$ moments follow a power-law behaviour

$$F_{\mathrm{q}}(M) \propto F_2(M)^{\beta_{\mathrm{q}}}. \tag{3.11}$$

This dependence of the q^{th} order NFM ($F_q(M)$) for q > 2 on the second order NFM ($F_2(M)$) is called the order scaling or simply termed as *F-scaling*. Here β_q, the exponent is observed to be related to the order of the moments (q) through relation

$$\beta_q = (q-1)^{\nu}, \tag{3.12}$$

where ν is called the *scaling exponent* which is a dimensionless parameter [33] and characterizes the system being studied. This *scaling* (Eq. 3.11) is independent of the M-scaling behaviour of Eq.(3.9).

The scaling behaviour as in Eq.(3.11) has been experimentally verified for the optical systems at the lasing threshold [34] and is also observed for Pb-Pb collisions at LHC energies [35]. With formalism for second-order phase transition using Ginzburg-Landau theory, the average value of ν is found to be 1.304 [32]. Cao, Gao, and Hwa in [36] examined the two-dimensional Ising model and found that the dimensionless parameter ν is function of temperature. For temperatures below critical temperature (T_c), where T_c =$2J/k_B$ (Ising parameters), the average value of ν is approximately 1.3. Larger values of ν correspond to temperatures below the critical temperature T_c. Therefore it is suggested that the systems where temperature cannot be directly measured, *calculating ν can serve as a valuable parameter for characterizing the system's thermodynamic properties* [36]. This is particularly relevant in heavy-ion collisions, where temperature is not an experimentally controlled variable. Thus determining ν can provide an insight into the temperature relative to the theoretical critical temperature expressed in terms of the Ising model parameters.
The Successive Contraction and Randomization (SCR) model, introduced in [19], simulates the conditions that may be existing during transformation of the quark-gluon plasma (QGP) into hadronic matter state near the phase transition. It alternates two processes: contractions, where confinement forces redistribute quarks and anti-quarks in dense regions in the form of hadrons, and randomization, where thermal diffusion randomly distributes quarks and anti-quarks in less dense regions . This mechanism models the dynamics of the phase transition, yielding a scaling exponent $\nu \approx 1.41$. These studies encourage to determine ν to characterize phase transition dynamics in heavy-ion collisions at the LHC.

A universal property of critical phenomena is the presence of clusters of all sizes, which do not have a characteristic scale. Thus the scaling properties of the system can be investigated in search of critical fluctuations or critical point. The scaling exponent (ν) becomes one of the key parameters that characterizes these properties and provides valuable information about the dynamics of the system [32]. The beauty of ν lies in its dimensionless nature, making it a universal parameter that quantifies fluctuations in the spatial patterns of the particles produced in high-energy collision events, providing a clear measure of the underlying dynamics.

3.1.3 Fractal parameters

There is a property of turbulent fluids in which vortices of varying sizes alternate in such a way that they form self-similar structures. These vortices do not always fill the entire volume, but rather form intermittent patterns in the regions of laminar flow [26]. This property is represented by a power-law variation of the vortex-distribution moments based on their size. The self-similarity of vortices establishes a direct relationship between intermittency and fractality. *Fractals* are self-similar objects, meaning the same structure repeats itself across different scales of magnification with non-integral dimensions [37]. Fractals are inherently complex structures [38] and their appearance in particle distributions point to underlying correlations and intricate dynamics.

Fractal dimensions are non-integer extensions of ordinary topological dimensionality. In two or higher-dimensional spaces, fractals can be categorized as either self-similar or self-affine, depending on the scales used. A measure following a power-law relationship with decreasing resolution of the measurement is a characteristic of a fractal object. If this power-law holds when the phase space is divided equally in all directions, the fractal is termed as self-similar, indicating isotropic number density fluctuations. In case the power-law holds when the phase space is partitioned unequally in various directions, the fractal is known as self-affine, corresponding to non-isotropic fluctuations. Further fractal systems can be broadly categorized into monofractals and multifractals, each representing different level of structural complexity [37, 39, 40]. A monofractal system is defined by a

single, consistent scaling property throughout its entire structure, with one fractal dimension that effectively captures its complexity. This uniformity makes monofractals relatively straightforward to analyze. Multifractal systems, on the other hand, are more complex, as different regions within the structure have different scaling properties. Heavy-ion collisions produce complex particle distributions. The investigation of the underlying scaling behaviours and self-similar properties in these systems help to know about the nature of the complexity of these system. The behaviour of two fractal parameters, discussed below, has been investigated in the present work.

3.1.3.1 Fractal dimension

The intermittency indices φ_q (Eq. 3.10) and the anamalous fractal dimension (d_{q}) are related through the relation

$$d_{\mathrm{q}} = \frac{\varphi_{\mathrm{q}}}{(q-1)}. \tag{3.13}$$

also the anomalous fractal dimension (d_{q}) is realted to the generalised dimension (D_{q}) as:

$$d_{\mathrm{q}} = D_{\mathrm{T}} - D_{\mathrm{q}}. \tag{3.14}$$

In this equation D_{T} refers to the ordinary topological dimension which is 1 for one dimensional analysis and 2 for two dimensional analysis [41, 42, 43]. D_{q} is the generalized (or Renyi) fractal dimension. In the present work two-dimensional analysis is performed for that, the ordinary topological dimension is 2 and therefore Eq.(3.14) can be written as:

$$D_{\mathrm{q}} = 2 - \frac{\varphi_{\mathrm{q}}}{(q-1)}. \tag{3.15}$$

A distinct characterization of fractality is revealed based on how D_{q} depends on the moment order q. A study of D_{q}'s dependence on q provides information about the nature of the system under study. If the generalised fractal dimension D_{q} varies with the order of the moment q, it indicates the presence of *multifractality* [44] and the corresponding system is known as multifractal system. Whereas, system is *monofractal* if D_{q} is independent of q.

In [43], a simple multifractal one-parameter model is used to investigate how multiple fractal distributions affect the intermittency signal. This model enables the simulation of random combinations of different fractal distributions within a single event. The key finding of this study is that the intermittency signal weakens as the number of fractal sources within a single event increases. In other words, the intermittency signal becomes less distinct as more fractal sources are combined. That is multiple fractal sources tend to dilute the characteristic fluctuations making intermittency signal less pronounced. Intermittency studies for data from various experiments, such as e^+e^- two-jet collisions [17] and $^{16}\mathrm{O}+^{197}$ Au collisions from the WA80 experiment [45] have been performed. The most pronounced signals appear in e^+e^- two-jet data, while the weakest are seen in central $^{16}\mathrm{O}+^{197}$ Au collisions, likely due to the superposition of numerous independent subprocesses. These observations suggest a possible decrease in intermittency with increasing multiplicity, potentially resulting from fractal superposition effects. However, further measurements were suggested [43] to be taken before drawing definitive conclusions.

3.1.3.2 Coefficient λ_q

Using φ_q one can further examine the structure of the distinct phases within self-similar multiparticle system created in high energy collisions [46, 47]. Bialas and Zalewski in [48] proposed that the observed intermittent behaviour of the particles produced during ultra-relativistic collisions, expressed with coefficient λ_q, can give information about the thermal or non-thermal nature of the system undergoing transition. The intermittency index φ_q is mathematically related to the coefficient λ_q [49, 50] as:

$$\lambda_q = \frac{(\varphi_q + 1)}{q} \tag{3.16}$$

A dependence of λ_q on q (Fig. 3.3) can be studied to look for whether two phases coexist in nature. λ_q is minimum at $q = q_c$ in case of non-thermal phase transition. In case q_c exists, then $q \geq q_c$ and $q \leq q_c$ corresponds to different nature of the system. The region where $q \leq q_c$, the system appears to be dominated by multiple fluctuations containing no more than q_c particles in a single bin. This region is characterized by a "liquid-like" phase,

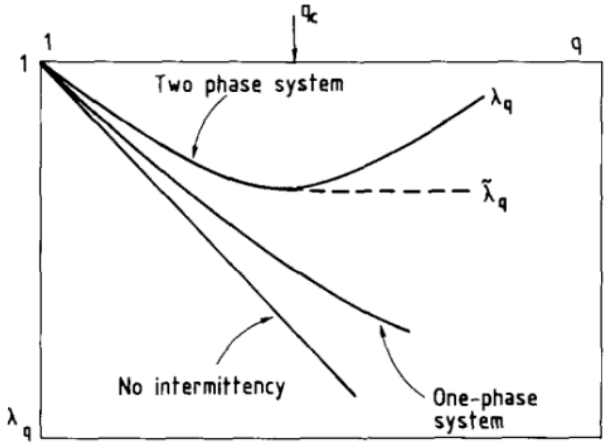

(a)

Figure 3.3: The cofficient λ_q as a function of order of the moment q shows distinct behaviours for the systems, one-phase, two-phase and a system with no intermittency [48].

where these small fluctuations dominate the overall behaviour. On the other hand the region where $q \geq q_c$, the system is dominated by rarely occurring large fluctuations [48] resembling a "dust-like" phase made up of a small number of high-density "grains". Higher-order moments, which are less sensitive to small fluctuations, emphasize the dust phase by highlighting the larger, denser fluctuations.

In this thesis the two scaling-behaviours of NFM ($F_q(M)$) (The M-scaling and the F-scaling) are studied. The scaling exponent's (ν) dependence on the transverse momentum (p_T), dependence of D_q and λ_q on q is also investigated for the soft charged particles recorded by ALICE experiment at LHC and the ones generated by the HIJING event generator, AMPT model in the midrapidity region.

3.2 Data sets and various selection cuts

This section gives details of the data sets, selection cuts used to filter good events and tracks for the analysis.

System	Energy	Production	Runs	Year	Statistics
Xe-Xe	5.44 TeV	LHC17n Full production, pass 1, ALIROOT-7526	280234, 280235	2017	4.49M

Table 3.1: Details of experimental dataset analyzed in this work.

3.2.1 ALICE experimental data

In October 2017 during RUN 2, ALICE experiment participated in a short run in which Xenon ^{129}Xe nuclei were accelerated in the LHC to collide at a centre-of-mass energy of 5.44 TeV per nucleon pair. The data with stable beams lasted for about six hours, during which ALICE collected about 2 million minimum bias triggered events. The recorded luminosity was $3 \times 10^{-25} cm^{-2} s^{-1}$, and the detected hadronic interaction rate was around 80-150 Hz. The solenoidal magnet of the ALICE apparatus was set to operate at a low field strength of 0.2 Tesla.

Present analysis uses the AOD production corresponding to pass1 reconstruction of LHC17n data [51]. The details of this dataset are given in Table 3.1. Both runs were validated by the Quality Assurance, as has been reported in [52]. The ALICE central quality assurance selects these two runs as "good" runs. The details on the reconstruction of tracks can be found in [51]. The soft charged particles with transverse momentum $\leq$ 2.0 GeV/c produced in these Xe-Xe collisions at $\sqrt{s_{\rm NN}}$ = 5.44 TeV are analyzed.

3.2.2 HIJING Monte-Carlo events

In high-energy physics experiments, simulation studies are a crucial tool for replicating experimental conditions and interpreting results in terms of known physics. These simulations, commonly known as Monte Carlo productions, are generated using sophisticated event generators that simulate particle collisions under controlled conditions. ALICE experiments relies on these simulations to closely replicate the complex environment created by ultra-relativistic heavy-ion collisions. A key component of this process is the use of GEANT3 [53], a detector simulation toolkit specifically designed to model the passage of

System	Energy	Anchored MC Production	Runs	Year	Statistics
Xe-Xe	5.44 TeV	LHC17j7_3 General-purpose, Monte Carlo production for Xe-Xe (LHC17n)	280234, 280235	2017	3.18M

Table 3.2: Details of Monte-Carlo (HIJING) from ALICE production.

particles through detectors. GEANT3 enables the precise implementation of the ALICE detector geometry, ensuring that every detail of the experimental setup is accurately reproduced in the simulation. Monte Carlo (MC) production events from the HIJING event generator [54] for Xe-Xe collisions at a center-of-mass energy of $\sqrt{s_{\rm NN}}$ = 5.44 TeV (Table. 3.2) are analyzed for determining the detector efficiencies and to understand the experimental results in terms of known physics of the HIJING event generator. These MC event samples are taken from the runs anchored to LHC17n pass1. This production from HIJING event generator named as LHC17j7_3 are the minimum biased events with conditions similar to that in the experimental run conditions of LHC17n pass1.

3.2.3 Event selection cuts

The event selection criteria used for the analysis to identify pertinent events are covered in this section. The standard event selection in the analysis includes basic trigger criteria, quality of primary vertex reconstruction with TPC and ITS detectors and centrality of the events.

3.2.3.1 Trigger selection

Due to ALICE's high collision rate, a trigger system is used to select relevant data segments containing the physics information of interest, which are then stored for analysis. The selection of triggers is based on the events that meet the analysis requirements and interests. Events for present analysis are selected using the minimum-bias (MB) trigger AliVEvent: : kINT7 in the AliPhysics ALICE data analysis framework. As the name in-

dicates, the minimum bias trigger selects inelastic events with a minimal bias. In ALICE, V0 is made up of two arrays of 32 scintillator detectors, located on either side of the interaction point, covering the entire azimuthal angle in the pseudorapidity regions $2.8 < \eta < 5.1$ (V0A) and $-3.7 < \eta < -1.7$ (V0C). The minimum bias trigger selection (kINT7 trigger) requires a hit on both sides of the V0 detector to confirm the occurrence of a collision. More details regarding the use of these triggers are available in [55].

3.2.3.2 Vertex selection

The "Vertex Z" position is the point in the z-axis at which the two beams collide. Depending on the system under study, a single event can be characterised as the collision of two heavy-ions or two protons. For each event, a primary interaction vertex is identified which typically extend a few inches along the z-axis or perpendicular to the beam direction. In this analysis, the vertex is identified using global tracks from the TPC and ITS. To ensure a successfully reconstructed primary interaction vertex, certain criteria are implemented. First, this is accomplished by necessitating the presence of at least one track that contributes to the determination of the primary vertex. Furthermore, a limitation is imposed on the maximum allowed distance of the reconstructed primary vertex from the nominal interaction point, which is situated at the centre of the experiment, along the z direction (beam's direction) [56]. This selection criterion is essential because it changes the geometrical acceptance of charged particle tracks in subdetectors depending on the z-position of the vertex. At the nominal interaction point (z = 0), the geometrical acceptance of the central barrel detectors symmetrically covers pseudorapidity. However, as the distance from the nominal centre increases, the acceptance varies asymmetrically, expanding on one side and contracting on the other side of the experiment. Thus by setting the range of the primary Z-vertex restricted to ± 10 cm (i.e., $|V_z| \leq 10$ cm), it ensures a uniform tracking acceptance both in the Inner Tracking System (ITS) and in the Time Projection Chamber (TPC) within the central pseudo-rapidity region $|\eta| < 0.8$. This standardized acceptance ensures consistent and reliable tracking of particles across these detector systems.

3.2.3.3 Centrality selection

Centrality is an important concept that quantifies the extent of overlap between the two colliding nuclei in the heavy-ion collisions, and is directly related to the energy density, particle production, and other key properties of the quark-gluon plasma (QGP). Centrality is used to classify collisions as either "central" (where the nuclei collide head-on with significant overlap) or "peripheral" (where the nuclei collide with only a small overlap). An accurate determination of centrality is essential for effectively comparing ALICE measurements with both theoretical models and results from other experiments [57]. Centrality is typically expressed as a percentile of the total hadronic cross-section, indicating the degree of overlap between nuclei, with more central collisions corresponding to higher overlap and larger particle production.

In heavy-ion collisions, events are selected based on the signal amplitudes from the two scintillator arrays referred to as V0. which measures the combined amplitudes of V0A and V0C. These amplitudes indicate the ionization energy collected by the detectors and are presented as percentiles of the selected events. The ALICE V0 detector, which consists of V0A on the A-side and V0M on the C-side of the experiment is used as the centrality estimator. The VZERO detector signals are known as V0 amplitude, and is proportional to the number of charged particle multiplicity. This is used to classify the events in centrality intervals. The V0 amplitude measures the sum of V0A and V0C amplitudes. These amplitudes correspond to the ionization energy deposited in the detectors and are expressed as percentiles of selected events. Minimum bias events are categorized into various multiplicity classes based on the total charge deposited in the V0M detector, as shown in Fig. 3.4 [58]. In the figure various centrality classes are shown based on centrality percentile for example the 0-5% centrality class refers to the top 5% of the collision distribution, representing the most central or highest amplitude collisions, characterized by the greatest sum of amplitudes. Similarly, other centrality classes, such as 5-10%, 10-20%, 20-30% and 30-40% etc, correspond to progressively less central collisions, as the sum of amplitudes decreases. Each class represents a different level of interaction intensity, with central collisions having more participating nucleons and peripheral collisions having

fewer, thereby affecting the overall characteristics and outcomes of the collisions.

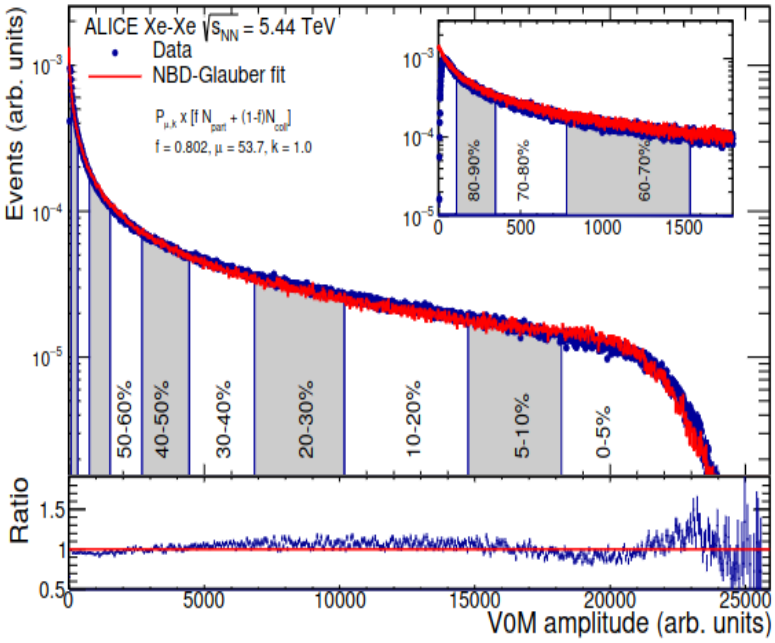

Figure 3.4: V0M amplitude distribution measured in Xe-Xe collisions recorded using ALICE at LHC, are divided in various multiplicity classes. The distribution is fitted using the Gluaber model function, represented by the red line(Figure Ref. [57]).

3.2.4 Track selection

The TPC and the ITS are the two primary tracking detectors in the central barrel of the ALICE, as outlined in Chapter 2. To choose primary charged particles that come from the primary interaction vertex are obatained by applying track selection criteria. Track selection criteria are used to reduce spurious trajectories that are not associated with physical particles, minimising contamination from secondary particles and increasing tracking efficiency. To ensure that the physics analysis includes only primary tracks, several quality standards must be met. Charged particle tracks reconstructed within the ITS and the TPC are analysed for the physics study. For this various track selection cuts are defined. It is required that a track has a signal in at least one layer of the Silicon Pixel Detector (SPD), maintain a maximum chi-square per cluster value of 36 from the fitting of ITS clusters, and satisfies specific requirements regarding the distance of closest approach (DCA) to the primary vertex. To reduce the likelihood of split tracks caused, running conditions yield-

Table 3.3: List of the kinematic cuts used for the track selection.

Pseudorapidity (η) range	$-0.8 \leq \eta \leq +0.8)$
Azimuthal angle (ϕ) range	$0 \leq \phi \leq 2\pi$
Wide p_{T} intervals (GeV/c)	$0.4 \leq p_{\mathrm{T}} \leq 1.0$ $0.4 \leq p_{\mathrm{T}} \leq 1.5$ $0.4 \leq p_{\mathrm{T}} \leq 2.0$
Narrow p_{T} intervals (GeV/c)	$0.4 \leq p_{\mathrm{T}} \leq 0.6$ $0.5 \leq p_{\mathrm{T}} \leq 0.8$ $0.6 \leq p_{\mathrm{T}} \leq 1.0$

ing large hit occupancy in the TPC, a p_{T}-dependent cut of the minimum number of TPC clusters per track, TPCNcls ≤ 70, is implemented. Furthermore, for all charged particles, different narrow and wide transverse momentum ranges are studied.

Tracks that correspond to normal global tracks marked with both ITS+TPC reconstructed tracks named as Filterbit 768, also known as hybrid tracks are selected for analysis. Further charged particle tracks produced within the mid-rapidity region $-0.8 \leq \eta \leq +0.8$ and covering the entire azimuthal range ($0 \leq \phi \leq 2\pi$) with low transverse momentum region ($p_{\mathrm{T}} < 2.0$ GeV/c) are considered. Table. 3.3 tabulates the list of the kinematics cuts used for selection of tracks.

3.3 HIJING event analysis

The HIJING (Heavy Ion Jet INteraction Generator) model is a sophisticated Monte Carlo event generator specifically designed to simulate high-energy heavy-ion collisions. HIJING provides a comprehensive framework for modelling the early stages of these collisions by focusing on the complex interactions between the colliding nuclei, as well as the subsequent production of particles. The model incorporates both hard processes, like the perturbative QCD jet production, and soft processes, such as nuclear remnant interactions and multiple parton scattering, resulting in a dual approach to capture collision dynamics, multiple parton scattering and gluon radiation. HIJING is particularly effective at simulating the formation of a dense medium, the QGP, as well as particle production at a variety of speeds and transverse momenta. By providing a detailed simulation of high-energy events,

HIJING enables researchers to investigate the mechanisms of particle production, energy deposition, and collision system evolution, contributing to a better understanding of the physics governing the heavy-ion collisions. More technical details related to HIJING are available in [54, 59]. Event samples (section 3.2.2) from HIJING Monte Carlo are analyzed for the intermittency study (given in section 3.1).

3.3.1 Quality Assurance Plots

Event and track selection as given in section. 3.2.3 and 3.2.4 are applied on the HIJING event samples. Events are selected based on their primary vertex positions being within $\pm$ 10cm from the center of the detector along the beam direction (i.e., $|V_z| < 10$ cm). This is varied to determine systematic uncertainities (section 4.3). The distribution of the primary vertex z-coordinate V_z for selected HIJING events is given in Fig.3.5(a) which shows a symmetrical distribution of events across $V_z = 0$. A total of 3.18M minimum bias most central (0-5% centrality) events from the HIJING are analysed. The centrality distribution of the events (0-5%) is shown in Fig.3.5(b). The other distributions of the charged particle track in one of the p_T bin ($0.4 \leq p_T \leq 1.0$ GeV/c) are given in Fig. 3.6. Both generated and reconstructed distributions are shown. The observed difference between the reconstructed and generated tracks may be attributed to the detector efficiency effects.

3.3.2 Monte Carlo Closure

The detector efficiency calculations are done first using Monte Carlo simulations with HIJING events after event and track selection cuts. All charged particle tracks generated using HIJING are termed as generated tracks. These tracks are passed through the detector geometry simulated with GEANT 3 and after passing the detector's track selection criteria, tracks that originate from a primary particle are termed as reconstructed primary tracks. The ratio of number of reconstructed tracks to the number of generated tracks defines the efficiency of the detector (Appendix A.0.1). For the intermittency analysis in the (η, ϕ) phase space, efficiencies are calculated on a bin-by-bin basis for each value of M. The two-dimensional efficiency maps for all M values for each p_T bin are obtained. As example, for

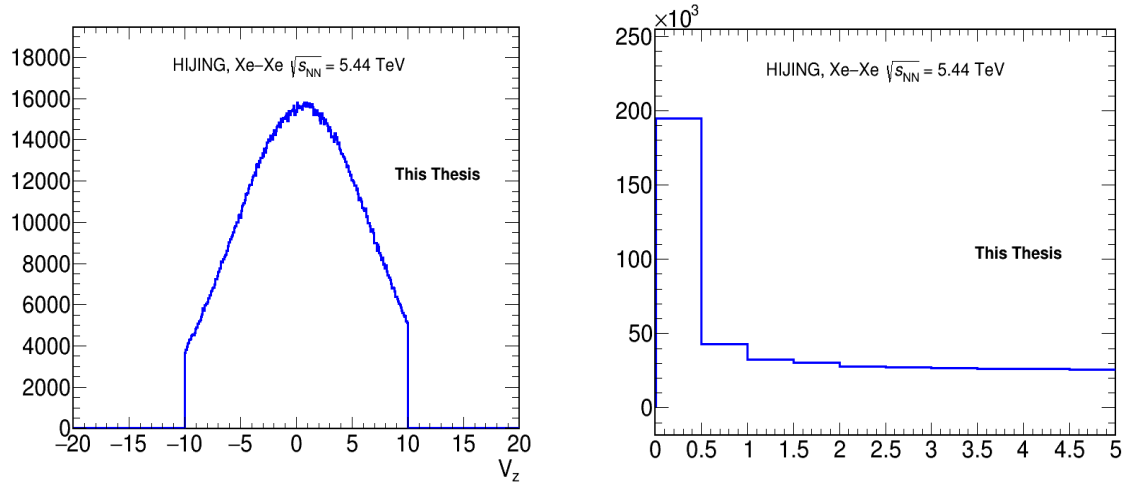

(a) (b)

Figure 3.5: HIJING (LHC17j7): (a) V_z distribution and (b) Centrality distribution for the most central HIJING event samples.

tracks generated in four different p_{T} bins the efficiency maps in (η, ϕ) space with $M = 40$ are shown in Fig. 3.7 . Monte Carlo closure test for NFM is performed for NFM using such efficiency maps is further described below.

The normalised factorial moments from the reconstructed HIJING tracks are corrected using correction factors, that is the efficiency of the bin defined for each M, to determine $F_{\mathrm{q}}^{\mathrm{corr}}$ (Eq.(A.6)). These corrected moments are compared with the normalized factorial moments determined for the generated HIJING tracks ($F_{\mathrm{q}}^{\mathrm{gen}}$) and reconstructed tracks ($F_{\mathrm{q}}^{\mathrm{rec}}$). For $q = 2$, it is observed that the corrected NFM, (F_2^{corr}) are identical to the uncorrected NFM, (F_2^{rec}) indicating that efficiency corrections do not affect the values of reconstructed tracks. In addition, it is observed [60] that when efficiencies are uniform in the kinematical acceptance region and therefore $F_{\mathrm{q}}^{rec}(M) \approx F_{\mathrm{q}}^{corr}$. The ALICE detector in the acceptance region under investigation has nearly Gaussian efficiencies with no sharp discontinuities and thus normalised factorial moments are robust against detector efficiencies. Because of this $F_{\mathrm{q}}(M)$ for $q = 2$, 3, 4 and 5 are not corrected for detector efficiencies in the experimental data analysis (chapter 4). In the various transverse momentum intervals, it is also observed that the ratio $F_{\mathrm{q}}^{\mathrm{rec}}(M)/F_{\mathrm{q}}^{\mathrm{gen}}(M)$ is close to 1 for all M values except in case of very high M values, where a slight deviation of the ratio from 1 (lower panel of Fig. 3.7) is

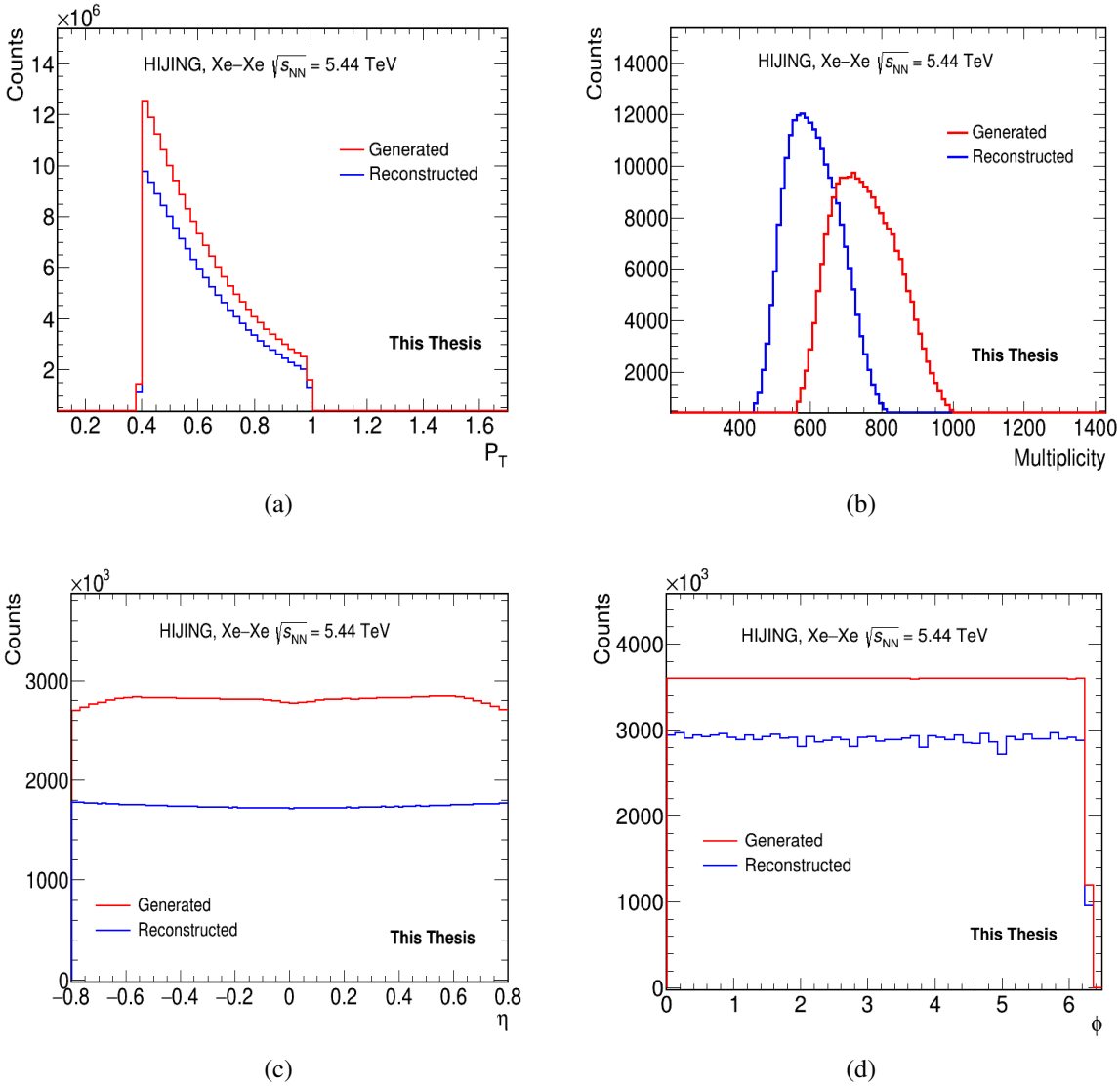

Figure 3.6: HIJING (LHC17j7): Transverse momentum (p_{T}) distribution (b) Multiplicity distributions (c) pseudorapidity (η) distributions and (d) azimuthal angle (ϕ) distributions of generated and reconstructed charged particle tracks in Xe-Xe collisions simulated using the HIJING model at $\sqrt{s_{\mathrm{NN}}}$ = 5.44 TeV. A case of $0.4 \leq p_{\mathrm{T}} \leq 1.0$ GeV/c interval is shown.

seen. A non-closure of $\lesssim 2\%$ at higher M for the normalized factorial moment for $q = 2$, is probably an effect due to coarse p_{T} resolution at large M. This non-closure at high M is observed (Fig.3.8) to decrease as p_{T} bin width increases. For each p_{T} bin, the maximum M value (M_{max}), is determined as the point where the Monte Carlo closure of at least 98% is achieved for $q = 2$.

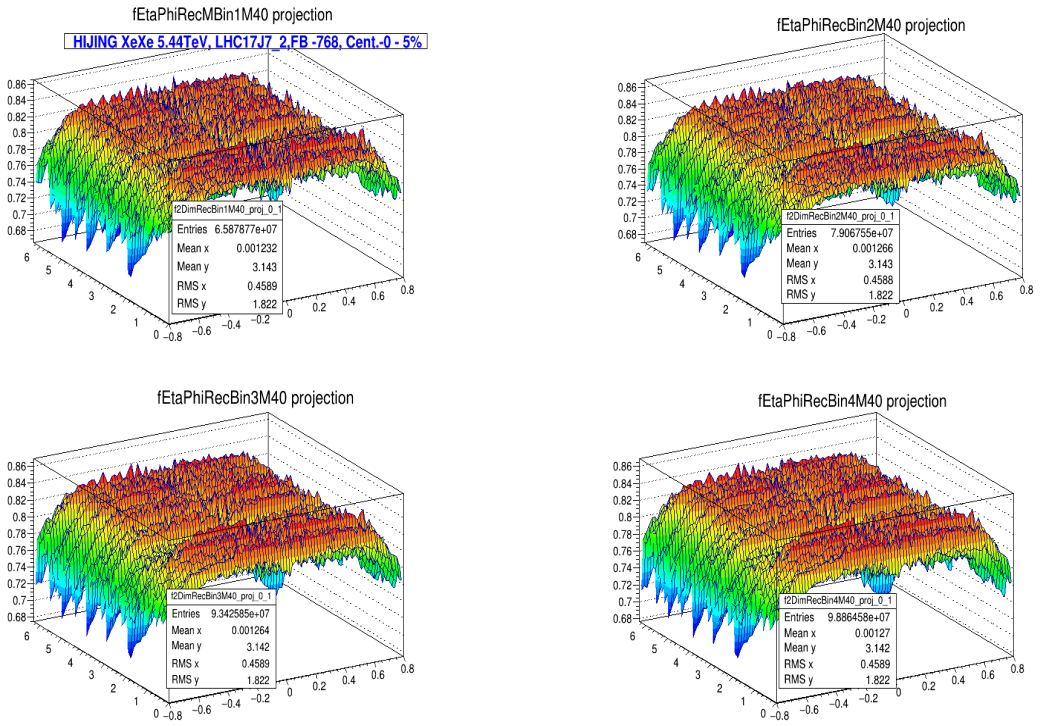

Figure 3.7: HIJING (LHC17j7) : Two dimensional tracking efficiency maps in (η, ϕ) phase space for four p_{T} bins, in case of $M = 40$ for the 0-5% central events in $|\eta| \leq 0.8$ region.

3.3.3 *M*-scaling behaviour

The M-scaling behaviour of the spatial configurations of the generated charged particles is studied as discribed in section 3.1.1. The normalised factorial moments, calculated for generated and reconstructed tracks of the event samples. The log-log plots of $F_{\mathrm{q}}(M)$ versus M^2 from the reconstructed and generated tracks in $0.4 \leq p_{\mathrm{T}} \leq 1.0$ p_{T} interval are shown in Fig. 3.9(a) and Fig. 3.9(b) respectively. In both cases for all q values it is observed that $\ln F_{\mathrm{q}}$ vs $\ln M^2$ plots are flat for the low values of M when the bin sizes are big. As $\ln M^2$ goes above 8, where non closure is above 2% there is deviation of $\ln F_{\mathrm{q}}(M)$ with respect to straight line behaviour. This is more pronounced for $q = 4$ and $q = 5$. These fluctuations in $F_{\mathrm{q}}(M)$ values at high M are more because of statistical reasons since there are less number of bins with bin multiplicity greater than or equal to 4 and 5. The generated tracks do not show any dependence of $\ln F_{\mathrm{q}}(M)$ on $\ln M^2$ even at high M but have high statistical uncertainties. While the scaling behaviour is consistent, the statistical limitations at higher M values affect the precise conclusions. Similar observations are made from the study of

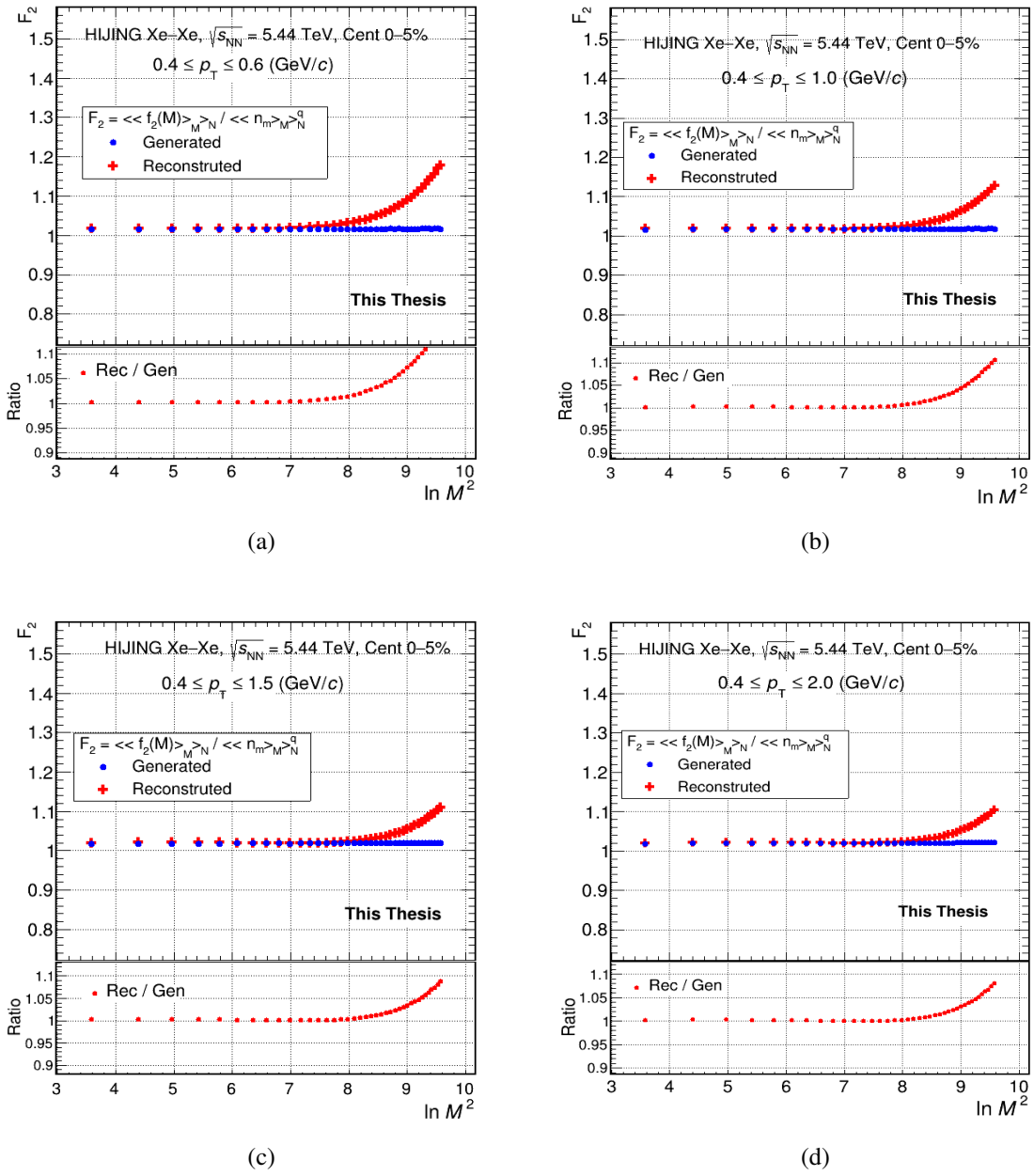

Figure 3.8: HIJING (LHC17j7): F_2 versus lnM^2plot for generated and reconstructed events showing closure test for the charged particles in p_{T} bins $0.4 \leq p_{\mathrm{T}} \leq 0.6$ GeV/c, $0.4 \leq p_{\mathrm{T}} \leq 1.0$ GeV/c, $0.4 \leq p_{\mathrm{T}} \leq 1.5$ GeV/c and $0.4 \leq p_{\mathrm{T}} \leq 2.0$ GeV/c. The bottom panels display the ratio of $F_{\mathrm{q}}^{rec}(M)$ to $F_{\mathrm{q}}^{gen}(M)$.

other transverse momentum intervals. From the present observations *M-scaling* is broadly seen to be absent in the HIJING and this further indicates that there are no self-similar spatial fluctuations in the HIJING event generation. Because of large error bars on $F_{\mathrm{q}}(M)$ at high M for all q, φ_q the intermittency indices are not determined.

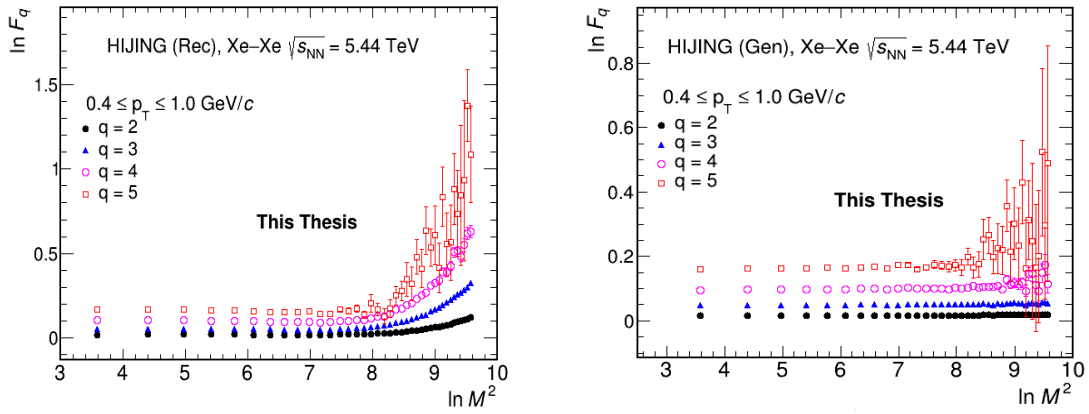

(a) Reconstructed (b) Generated

Figure 3.9: HIJING (LHC17j7): $\ln F_{\mathrm{q}}$ vs $\ln M^2$ plots for (a) Reconstructed and (b) Generated charged particles in the p_{T} bin $0.4 \leq p_{\mathrm{T}} \leq 1.0$ GeV/c with FB-768

3.3.4 *F*-scaling and Scaling Exponent (ν)

As discussed in section 3.1.2, even in the absence of the *M-scaling*, *F-scaling* may be present; thus, the $\ln F_{\mathrm{q}}(M)$ vs $\ln F_2(M)$ plots are drawn for the high M values as shown in Fig.3.10, for the p_{T} bin $0.4 \leq p_{\mathrm{T}} \leq 1.0$ GeV/c. In case of reconstructed tracks a weak power-law dependence of $\ln F_{\mathrm{q}}(M)$ on $\ln F_2(M)$ is observed and fitting is performed in the M region, which has at least 98% closure. At higher orders, q = 4 and q = 5, significant fluctuations and statistical uncertainties on $F_{\mathrm{q}}(M)$ are seen. A straight line fit is performed

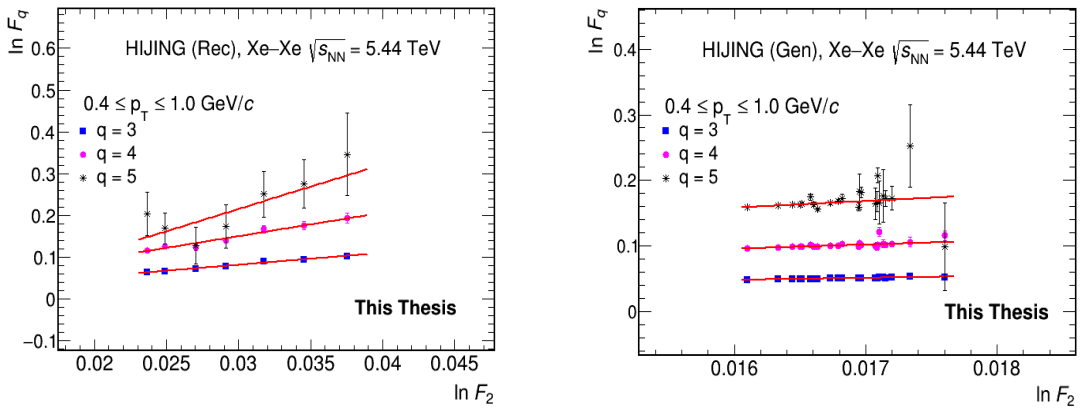

(a) Reconstructed (b) Generated

Figure 3.10: HIJING (LHC17j7): *F-scaling* plot for the (a) Reconstructed and (b) Generated charged particles in the p_{T} bin $0.4 \leq p_{\mathrm{T}} \leq 1.0$ GeV/c (FB-768).

on these plots to obtained the β_{q} values for q =3, 4 and 5. The $\ln\beta_{\mathrm{q}}$ versus ln $(q-1)$

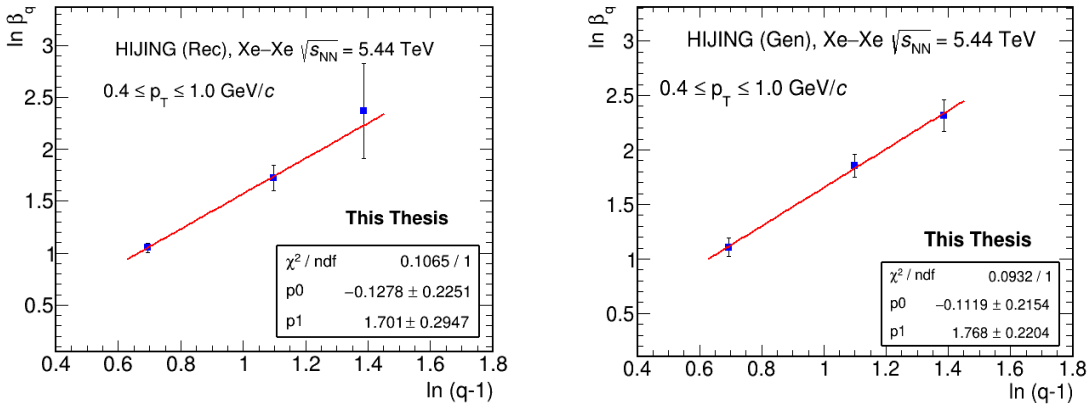

(a) Reconstructed (b) Generated

Figure 3.11: HIJING (LHC17j7): $\ln\beta_q$ versus $\ln(q-1)$ for the (a) Reconstructed and (b) Generated event samples. The slope ν is extracted for the p_T interval $0.4 \leq p_T \leq 1.0$ GeV/c (FB-768).

plot, shown in Fig.3.11(a) and Fig.3.11(b) gives a scaling exponent, ν =1.70 $\pm$ 0.29 and ν = 1.77 $\pm$ 0.22 for the reconstructed and generated tracks respectively. The scaling exponent ν is significantly greater than 1.304, a value predicted for the second-order phase transition formalism, using Ginzburg-Landau theory. Similar studies are performed for the other p_T bins as in the case of this p_T bin. The average value of scaling exponent is found to be $\gtrsim$ 1.7 from the HIJING event analysis.

Since HIJING does not have physics of self-similar particle generation and that of the phase transition, thus these values of ν obtained here and the corresponding scaling behaviours can be treated as baseline behaviour of the NFM in case of multiparticle production in the heavy-ion collision physics. These results are significant to understand the experimental data so as to build up our knowledge on the multiparticle production. Analysis performed for the experimental data, is presented in the next chapter.

BIBLIOGRAPHY

[1] W. Kittel and E. A. De Wolf, "Soft multihadron dynamics," World Scientific Publishers, Singapore, (2005).

[2] A. Bialas and R. Peschanski, "Moments of rapidity distributions as a measure of short-range fluctuations in high-energy collisions," Nucl. Phys. B **273**, (1986) 703.

[3] T. H. Burnett, S. Dake, M. Fuki, J. C. Gregory, T. Hayashi, R. Holynski, J. Iwai, W. V. Jones, A. Jurak and J. J. Lord, *et al.* "Extremely High Multiplicities in High-Energy Nucleus Nucleus Collisions," Phys. Rev. Lett. **50**, (1983) 2062-2065.

[4] I. V. Ajinenko *et al.* [EHS/NA22], "Intermittency Patterns in pi+ p and K+ p Collisions at 250-GeV/c," Phys. Lett. B **222**, (1989) 306 .

[5] T. Akesson *et al.* [HELIOS Emulsion], "A Search for multiplicity fluctuations in high-energy nucleus-nucleus collisions," Phys. Lett. B **252**, (1990) 303-310 .

[6] D. Ghosh, P. Ghosh and A. Ghosh, "Intermittency and correlations in O-16 + Ag / Br interactions at 2.1-GeV/nucleon," Phys. Rev. C **49**, (1994) 3219-3223.

[7] A. Bialas and R. B. Peschanski, "Intermittency in Multiparticle Production at High-Energy," Nucl. Phys. B **308**, (1988) 857-867.

[8] D. Ghosh, M. Lahiri, S. Das, K. Purkait, B. Biswas, J. Roychoudhury, R. Chatterjee, A. K. Jafry and A. Deb, "Fluctuation study of pionisation in ultrarelativistic nucleus nucleus interaction," Z. Phys. C **71**, (1996) 243-249.

[9] D. Ghosh, A. Deb, R. Chattopadhyay, S. Sarkar, A. K. Jafry, M. Lahiri, S. Das, K. Purkait, B. Biswas and J. Roychoudhury, "Evidence of multifractal nature of target-evaporated slow particles produced in ultrarelativistic heavy ion interactions," Phys. Rev. C **58**, (1998) 3553-3559.

[10] D. Ghosh, A. Deb, S. Bhattacharyya, J. Ghosh, R. Das and S. Mukherjee, "Evidence of intermittent type fluctuation of target residue in relativistic nuclear collisions at a few GeV/n," Int. J. Mod. Phys. E **12**, (2003) 407-419 .

[11] D. Ghosh, A. Deb, S. Bhattacharyya, J. Ghosh and R. Sarkar, "Evidence of self-affine target fragmentation process in relativistic nuclear collision at a few GeV/n," J. Phys. G **29**, (2003) 983-992.

[12] R. Holynski, A. Jurak, A. Olszewski, B. Wilczynska, H. Wilczynski, W. Wolter, B. Wosiek, L. M. Barbier, V. W. Jones and O. E. Pruet, *et al.* "Evidence for Intermittent Patterns of Fluctuations in Particle Production in High-Energy Interactions in Nuclear Emulsion," Phys. Rev. Lett. **62**, (1989) 733-736 .

[13] R. Holynski, A. Jurak, A. Olszewski, M. Szarska, A. Trzupek, B. Wilczynska, H. Wilczynski, W. Wolter, B. Wosiek and K. Wozniak, *et al.* "One-dimensional and Two-dimensional Analysis of the Factorial Moments in 200-GeV/nucleon P, ^{16}O and ^{32}S Interactions With Ag / Br Nuclei," Phys. Rev. C **40**, (1989) R2449-R2453 .

[14] I. Derado, G. Jancso, N. Schmitz and P. Stopa, "Investigation of Intermittency in Muon - Proton Scattering at 280-GeV," Z. Phys. C **47**, (1990) 23-30 .

[15] S. S. Wang, J. Zhang, Y. X. Ye, C. G. Xiao and Y. Zhong, "Intermittency exponents in p-p collisions at 400-GeV/c," Phys. Rev. D **49**, (1994) 5785-5788.

[16] A. De Angelis, "Study of intermittency in hadronic Z0 decays," Mod. Phys. Lett. A **5**, (1990) 2395-2402.

[17] B. Buschbeck, P. Lipa and R. B. Peschanski, "Signal for Intermittency in e^+e^- Reactions Obtained From Negative Binomial Fits," Phys. Lett. B **215**, (1988) 788-791.

[18] W. Braunschweig *et al.* [TASSO], "Study of Intermittency in Electron - Positron Annihilation Into Hadrons," Phys. Lett. B **231**, (1989) 548-556.

[19] R. C. Hwa and C. B. Yang, "Observable Properties of Quark-Hadron Phase Transition at the Large Hadron Collider," Acta Phys. Polon. B **48**, (2017) 23, [arXiv:1601.04671 [nucl-th]].

[20] P. Bartalini, E. L. Berger, B. Blok, G. Calucci, R. Corke, M. Diehl, Y. Dokshitzer, L. Fano, L. Frankfurt and J. R. Gaunt, *et al.* "Multi-Parton Interactions at the LHC," [arXiv:1111.0469 [hep-ph]].

[21] L. Reichl, "A modern course in statistical physics," American Journal of Physics 67, 12 (1999).

[22] H. Satz, "Intermittency and Critical Behavior," Nucl. Phys. B **326**, (1989) 613-618 .

[23] B. Bambah, J. Fingberg and H. Satz, "The Onset of Intermittent Behavior in the Ising Model," Nucl. Phys. B **332**, (1990) 629-640.

[24] A. Bialas and R. C. Hwa, "Intermittency parameters as a possible signal for quark - gluon plasma formation," Phys. Lett. B **253**, (1991) 436-438.

[25] E. A. De Wolf, I. M. Dremin and W. Kittel, "Scaling laws for density correlations and fluctuations in multiparticle dynamics," Phys. Rept. **270**, (1996) 1-141, [arXiv:hep-ph/9508325 [hep-ph]].

[26] R. C. Hwa and C. B. Yang, "Local Multiplicity Fluctuations as a Signature of Critical Hadronization at LHC," Phys. Rev. C **85** 044914 (2012), arXiv:1111.6651 [nucl-th].

[27] ALICE Collaboration, "General-purpose Monte Carlo production (LHC17n) for Xe–Xe Collisions at $\sqrt{s_{\rm NN}} = 5.44$ TeV, HIJING,". https://alimonitor.cern.ch/job_events.jsp?timesel=0&owner=aliprod&filter_run=280234:

280235&filter_jobtype=Xe-Xe%2C+5.44+TeV%2C+General-purpose+Monte+Carlo+production+for+Xe-Xe+%28LHC17n%29%2C+with+updated+SPDSparseDead%2C+HIJING%2C+extra+statistics%2C+ALIROOT-7531

[28] R. Sharma and R. Gupta, "Scaling Properties of Multiplicity Fluctuations in the AMPT Model," Adv. High Energy Phys. **2018**, (2018) 6283801, [arXiv:1806.10854 [hep-ph]].

[29] K. Aamodt *et al.* [ALICE], "Charged-particle multiplicity density at mid-rapidity in central Pb-Pb collisions at $\sqrt{s_{NN}} = 2.76$ TeV," Phys. Rev. Lett. **105**, (2010) 252301,

[30] R. C. Hwa, "Quark-Gluon Plasma 2," R.C. Hwa Ed., p 749, World Scientific Publishers, Singapore, (1995).

[31] R. C. Hwa, "Recognizing Critical Behavior amidst Minijets at the Large Hadron Collider," Adv. High Energy Phys. **2015**, (2015) 526908, [arXiv:1411.6083 [nucl-ex]].

[32] R. C. Hwa and M. T. Nazirov, "Intermittency in second order phase transition," Phys. Rev. Lett. **69**, (1992) 741-744.

[33] R. C. Hwa and J. c. Pan, "Intermittency in the Ginzburg-Landau theory," Phys. Lett. B **297**, (1992) 35-38.

[34] M. R. Young, Y. Qu, S. Singh and R. C. Hwa, "Scaling behaviour of photon number fluctuations at laser threshold," Opt. Commun. **105**, 325 (1994).

[35] S. Sharma *et al.* [ALICE], "Local Multiplicity Fluctuations in Pb−Pb Collisions at $\sqrt{s_{\rm NN}}$ = 2.76 TeV with ALICE at the LHC," Springer Proc. Phys. **304**, (2024) 860-862 , [arXiv:2307.14407 [nucl-ex]].

[36] Z. Cao, Y. Gao and R. C. Hwa, "Scaling properties of hadron production in the Ising model for quark - hadron phase transition," Z. Phys. C **72**, (1996) 661-670, [arXiv:nucl-th/9601011 [nucl-th]].

[37] Benoit. B. Mandelbrot, "The Fractal Geometry of Nature," W.H. Freeman and Company, New York, (1982).

[38] R. C. Hwa, "Fractal Measures in Multiparticle Production," Phys. Rev. D **41** (1990) 1456.

[39] S. Ahmad and M. A. Ahmad, "A comparative study of multifractal moments in relativistic heavy-ion collisions," J. Phys. G **32**, 1279-1293 (2006).

[40] G. Bhoumik, A. Deb, S. Bhattacharyya and D. Ghosh, "Comparative Multi Fractal De-trended Fluctuation Analysis of heavy ion interactions at a few GeV to a few hundred GeV," [arXiv:1603.04663 [hep-ex]].

[41] E. K. Sarkisian, L. K. Gelovani, and G. G. Taran, "Fractality in central collisions of C-12 nuclei with Ne and Cu nuclei at 4.5-A/GeV/c," Phys. Atom. Nucl. **56** (1993) 832-840 .

[42] E. K. Sarkisian, L. K. Gelovani and G. G. Taran, "Fractality and fluctuations in charged particle pseudorapidity distributions in central C (Ne, Cu) collisions at 4.5-A/GeV/c," Phys. Lett. B **302**, (1993) 331-335.

[43] P. Lipa and B. Buschbeck, "From strong to weak intermittency," Phys. Lett. B **223**, (1989) 465-469.

[44] R. Gupta and S. K. Malik, "Intermittency study of charged particles generated in Pb-Pb collisions at $\sqrt{s_{\rm NN}}$= 2.76 TeV using EPOS3," Adv. High Energy Phys. **2020**, (2020) 5073042, [erratum: Adv. High Energy Phys. **2020**, 7319894 (2020)]. [arXiv:1911.13111 [hep-ex]].

[45] R. Albrecht *et al.* [WA80], Phys. Lett. B **221**, (1989) 427-431.

[46] T. C. Halsey, M. H. Jensen, L. P. Kadanoff, I. Procaccia, and B. I. Shraiman, "Fractal measures and their singularities: The characterization of strange sets," Phys. Rev. A **33** (1986) 1141-1151 .

[47] G. Paladin and A. Vulpiani, "Anomalous scaling laws in multifractal objects," 156 no. 4, (1987) 147-225 .

[48] A. Bialas and K. Zalewski, "Phase Structure of Selfsimilar Multiparticle Systems and Experimental Determination of Intermittency Parameters," Phys. Lett. B **238**, (1990) 413-416.

[49] R. B. Peschanski, "On the Existence of a Nonthermal Phase Transition in Multiparticle Production," Nucl. Phys. B **327**, (1989) 144-156.

[50] R. B. Peschanski, "Intermittency in particle collisions," Int. J. Mod. Phys. A **6**, (1991) 3681-3722.

[51] ALICE Collaboration. *MonALISA tutorial*. ALICE Analysis Tutorial. Available at: https://alice-doc.github.io/alice-analysis-tutorial/analysis/monalisa.html.

[52] ALICE Collaboration, *ALICE Run Configuration Monitor*, https://alimonitor.cern.ch/configuration/index.jsp.

[53] R. Brun, F. Bruyant, and A. C. McPherson, "GEANT: Detector Description and Simulation Tool," CERN, Geneva, Tech. Rep. CERN-DD/EE/84-1, 1987, updated through 1994. [Online]. Available: https://cds.cern.ch/record/1082634.

[54] M. Gyulassy and X. N. Wang, "HIJING 1.0: A Monte Carlo program for parton and particle production in high-energy hadronic and nuclear collisions," Comput. Phys. Commun. **83**, (1994) 307, [arXiv:nucl-th/9502021 [nucl-th]].

[55] CERN Web, 2017, "DPG ALICE,".

[56] B. B. Abelev *et al.* [ALICE], "Performance of the ALICE Experiment at the CERN LHC," Int. J. Mod. Phys. A **29**, (2014) 1430044, [arXiv:1402.4476 [nucl-ex]].

[57] [ALICE], "Centrality determination using the Glauber model in Xe-Xe collisions at $\sqrt{s_{\mathrm{NN}}} = 5.44$ TeV," ALICE-PUBLIC-2018-003.

[58] S. Acharya *et al.* [ALICE], "Centrality and pseudorapidity dependence of the charged-particle multiplicity density in Xe–Xe collisions at $\sqrt{s_{\mathrm{NN}}}$ =5.44TeV," Phys. Lett. B **790**, (2019) 35-48, [arXiv:1805.04432 [nucl-ex]].

[59] X. N. Wang and M. Gyulassy, "HIJING: A Monte Carlo model for multiple jet production in p p, p A and A A collisions," Phys. Rev. D **44**, (1991) 3501-3516 .

[60] S. Sharma, S. K. Malik, Z. Banoo and R. Gupta, "Normalized factorial moments of spatial distributions of particles in high multiplicity events: A Toy model study," Nucl. Phys. A **1053**, (2025) 122963, [arXiv:2309.07712 [hep-ph]].

CHAPTER 4

DATA ANALYSIS AND RESULTS

The analysis of experimental data for fluctuation studies is an essential tool for probing the underlying dynamics of high-energy nuclear collisions at the macroscopic level. The strongly interacting matter created in the heavy-ion collisions show hydrodynamic evolution with minimum viscosity and flow properties at low p_{T} region. However, the location of QCD critical point in the nuclear matter phase diagram is still elusive with predictions for it to be at T $\approx$ 156 MeV. Various observables especially the higher order moments and cumulant moments are being extensively investigated by various experimental groups with no success. Search for the critical end point (CEP) and the order of the phase transition of hadron-quark and quark-hadron phase transition are among some of the main goals of both experimental and theoretical studies in the field. At LHC energies a crossover transition is predicted where the critical fluctuations may or may not exist for the system having passed through a critical point. In this chapter, a detailed analysis of event-by-event multiplicity fluctuations of charged particle production, utilizing data recorded by the ALICE detector

at the Large Hadron Collider (LHC) is presented. The analysis is performed on Xe–Xe collision data at a center-of-mass energy per nucleon pair of 5.44TeV, collected during Run2 of LHC operations. The intermittency methodology as discussed in chapter 3 is used as a principal analytical method to characterize fluctuations in the charged particle production in these collisions. Sections below describe the event and track selection plots followed by the observations and results from the analysis.

4.1 Quality Assurance (QA) Plots

The data recorded during Run 2 of LHC is analyzed here. Details on the beam energy, number of events, production name, run numbers etc are given in section 3.2.1. The event selection cuts are applied on the data available in the AOD file format to get events of interest followed by the track selection cuts to obtain charged tracks.

4.1.1 Event Selection

Events with a kINT7 trigger and with primary vertex reconstructed from ITS+TPC tracks having at least one track with $|V_z| \leq 10$ cm are selected for analysis. By setting the range of the primary Z-vertex restricted to ± 10 cm, a uniform tracking acceptance both in the ITS and in the TPC, within the central pseudorapidity region $|\eta| \leq 0.8$ is ensured. The V_z distribution obtained after the application of event selection cut is shown in Fig. 4.1(a). Followed by this, a centrality selection cut is applied on the selected events. Most central events of 0-5% centrality are taken for default analysis. Fig. 4.1(b) shows the centrality distribution of the selected events.

4.1.2 Track Selection

The track selection cuts are applied to choose primary charged particles originating from the primary interaction vertex. The track selection cuts as detailed in section 3.2.4, are also applied for experimental data track selection. The kinematic cuts further applied on the tracks are listed in Table 3.3. The analysis has been performed on the charged particles

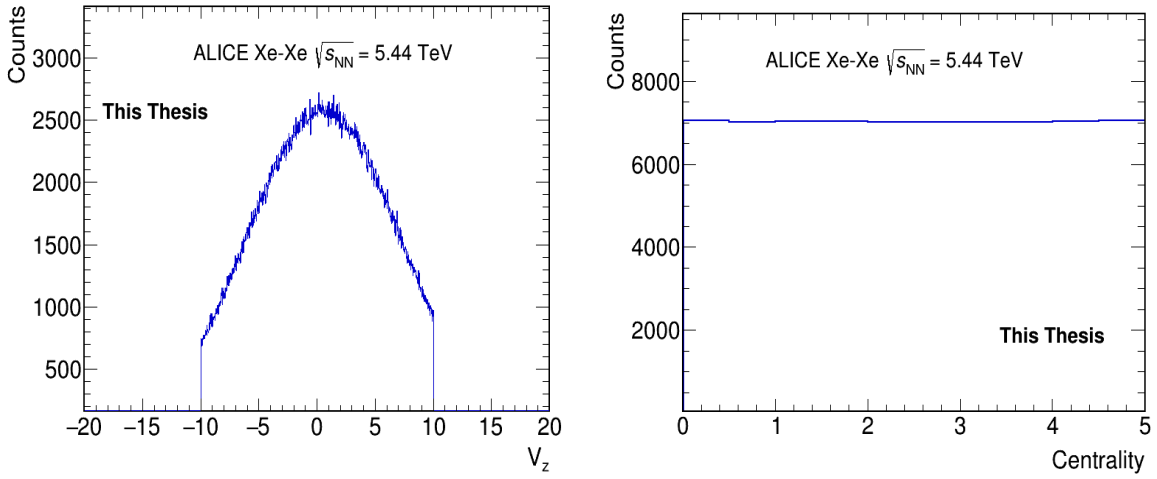

(a) (b)

Figure 4.1: (a) Primary vertex distribution of selected events and (b) the centrality distribution of the most central (i.e., 0-5%) Xe–Xe collision events at $\sqrt{s_{\rm NN}}$ = 5.44 TeV.

in the various transverse momentum intervals with $p_{\rm T} \leq 2.0$ GeV/c, to ensure uniform tracking efficiency. Figure 4.2(a) and Figure 4.2(b) show the multiplicity distributions of the selected charged particle tracks in narrow and wide $p_{\rm T}$ bins respectively and their η and ϕ distributions are given in Fig. 4.3 and Fig. 4.4.

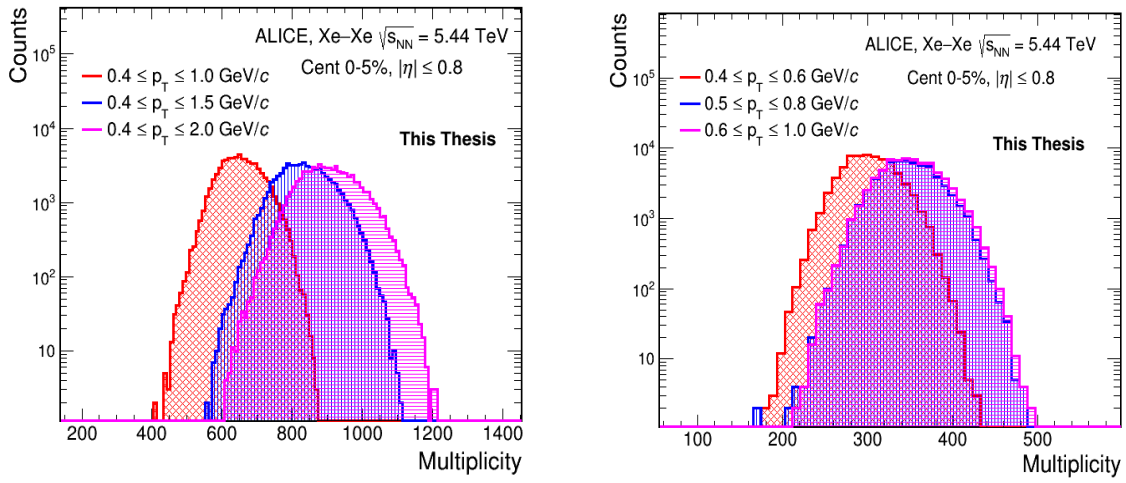

(a) (b)

Figure 4.2: The charged particle multiplicity distributions in the kinematic acceptance with $|\eta| \leq 0.8$ and $0 \leq \phi \leq 2\pi$ recorded by ALICE detector at LHC during RUN 2 for (a) wide $p_{\rm T}$ bins and (b) narrow $p_{\rm T}$ bins.

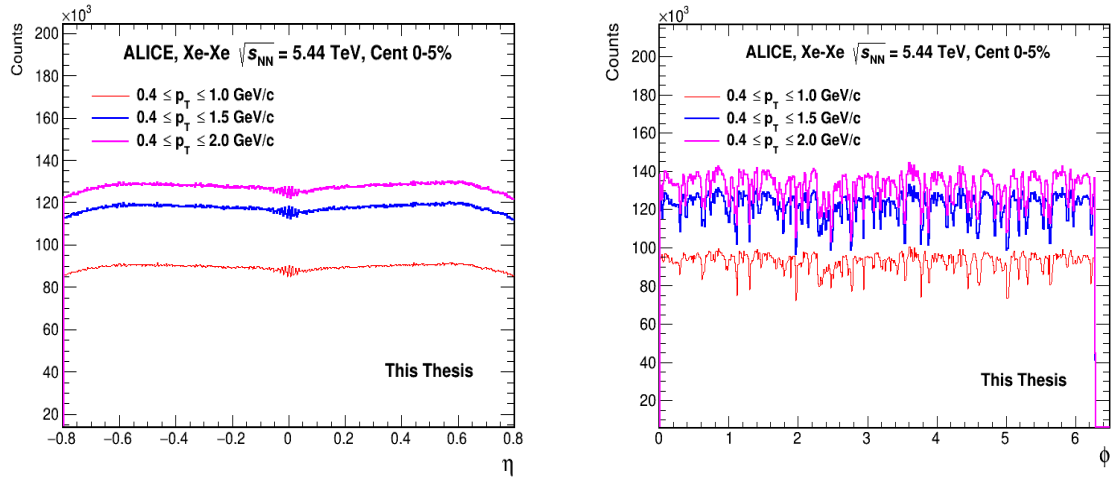

(a) (b)

Figure 4.3: (a) Pseudorapidity (η) and (b) azimuthal angle (ϕ) distributions of the charged particles produced in wide p_{T} bins ($0.4 \leq p_{\mathrm{T}} \leq 1.0$ GeV/c, $0.4 \leq p_{\mathrm{T}} \leq 1.5$ and $0.4 \leq p_{\mathrm{T}} \leq 2.0$ GeV/c), as recorded by ALICE in Xe–Xe collisions at $\sqrt{s_{\mathrm{NN}}} = 5.44$ TeV.

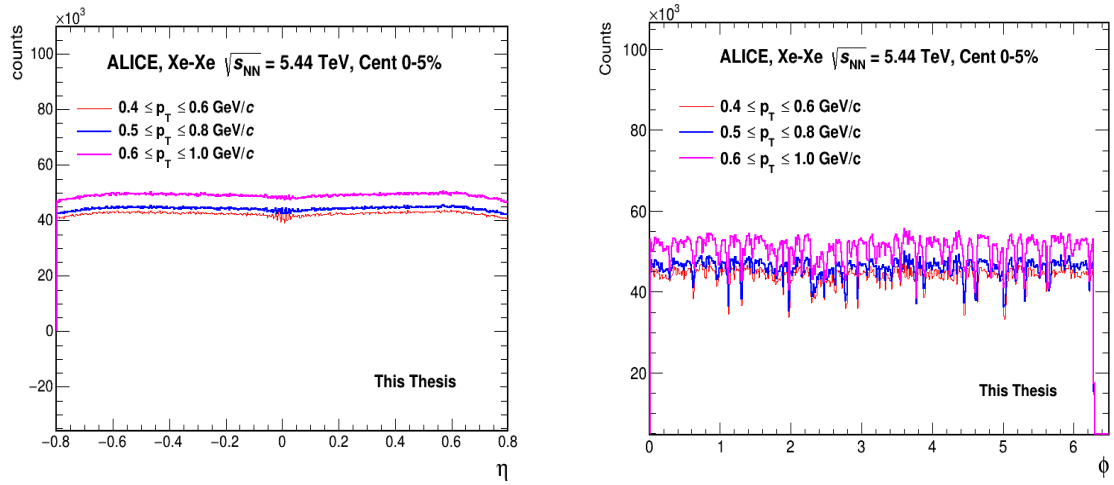

(a) (b)

Figure 4.4: (a) Pseudorapidity (η) and (b) azimuthal angle (ϕ) distributions of the charged particles in narrow p_{T} bins ($0.4 \leq p_{\mathrm{T}} \leq 0.6$ GeV/c, $0.5 \leq p_{\mathrm{T}} \leq 0.8$ GeV/c and $0.6 \leq p_{\mathrm{T}} \leq 1.0$ GeV/c) produced in Xe–Xe collisions at $\sqrt{s_{\mathrm{NN}}} = 5.44$ TeV.

4.2 Observations and Results

In this section observations and results from the analysis of experimental data (section 3.2.1) are discussed.

4.2.1 Average bin content

The charged particles produced in the acceptance region ($\eta \leq 0.8$ and $0 \leq \phi \leq 2\pi$) of an event are mapped onto the two-dimensional (η, ϕ) phase space divided into M^2 bins. The bin multiplicity (n_{m}), the number of particles that enter each bin, depends on dynamics of the particle production. Thus the distribution of bin-multiplicity, for an M, is function of dynamics of the particle production processes. The average bin content plots as function of increasing M^2 for the wide p_{T} and narrow p_{T} bins are shown in Fig. 4.5(a) and Fig. 4.5(b) respectively. For all p_{T} bins, it is observed that the average bin content decreases trivially as M increases. The detector resolution limits the upper bound of M and minimum value of M where M_{min} = 6 and maximum M_{max} = 123, is taken in this analysis. The average bin content $<n_{\mathrm{i}}>$ is defined as

$$< n_{\mathrm{i}} >= \frac{1}{N} \sum_{i=1}^{N} \left(\frac{1}{M^2} \sum_{m=1}^{M^2} n_m \right)_i . \tag{4.1}$$

Wide p_{T} bins have large value of the average bin content in comparison to small width p_{T} bins.

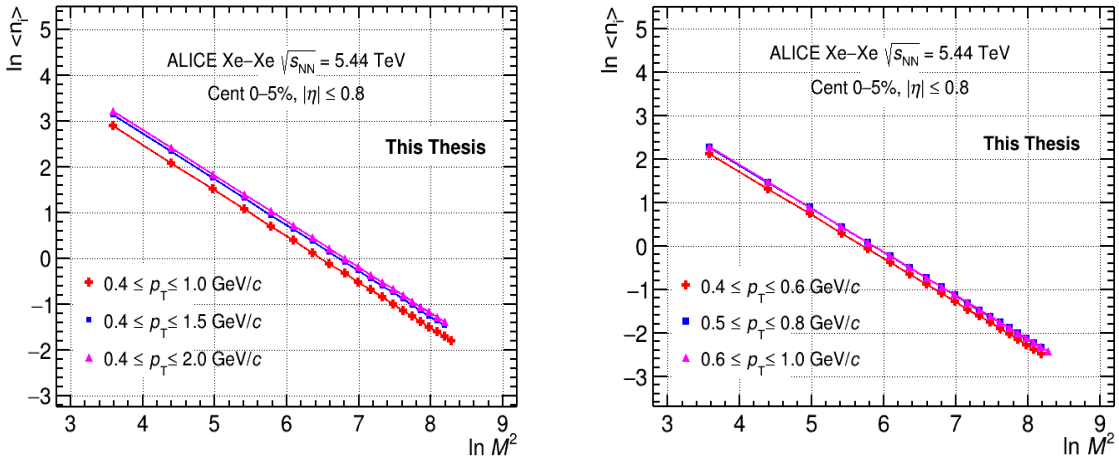

Figure 4.5: Log-log plot of the average bin content $\langle n_i \rangle$ as a function of M^2 for (a) wide p_{T} bins and (b) narrow p_{T} bins.

4.2.2 F_q^e distributions

To study the scaling behaviour of the normalized factorial moments (NFM) $F_q(M)$, for an event sample of N events, first the factorial moments are determined for each bin in an event. To get event factorial moments ($f_q^e(M)$) is calculated for an M (F_q^e) as defined in Eq. 3.2. The normalized event factorial moment distributions corresponding to each q value are shown in Fig. 4.6 and Fig. 4.7 for two cases of phase space partitioning: M = 10 and M = 25 respectively. These distributions quantify bin-to-bin fluctuations in particle multiplicity within the (η, ϕ) phase space across the event samples, for $q = 2, 3, 4$ and 5. Figures correspond to the transverse momentum bin $0.4 \leq p_T \leq 1.0$ GeV/c only. It is observed that with the increase in moment order q, the width of the distributions also increases indicating stronger deviations from gaussian behaviour. As the resolution of phase space increases, this deviation increases. In particular, for the higher q values, the distributions exhibit only a few prominent peaks in the values of F_q^e, reflecting enhanced fluctuations in some events only.

The increase in the width of the F_q^e distribution with the order of the moments q, imply significant fluctuations in the spatial distributions of the particles multiplicities across events. This broadening is primarily attributed to the empty bin effect, which becomes prominent when the phase space is partitioned in sufficiently small bins such that the average multiplicity per bin falls well below the moment order q. At higher q and higher M, there are not many events with particles in the bins. Thus, higher order moments at small bin sizes reflect statistical properties of only a small subset of the full event sample. Similar patterns of F_q^e(M) are observed across all p_T bins. This behaviour shows that higher-order moments are particularly sensitive to nonlinear dynamics and multiparticle correlations in particle production processes.

4.2.3 M-scaling behaviour

The scaling behaviour of the factorial moments is an important parameter to characterize the dynamics of the systems under study. As described in Chapter 3, the normalized factorial moments (F_q) are determined for $q = 2, 3, 4$, and 5. Fig. 4.8 shows the log-log plot

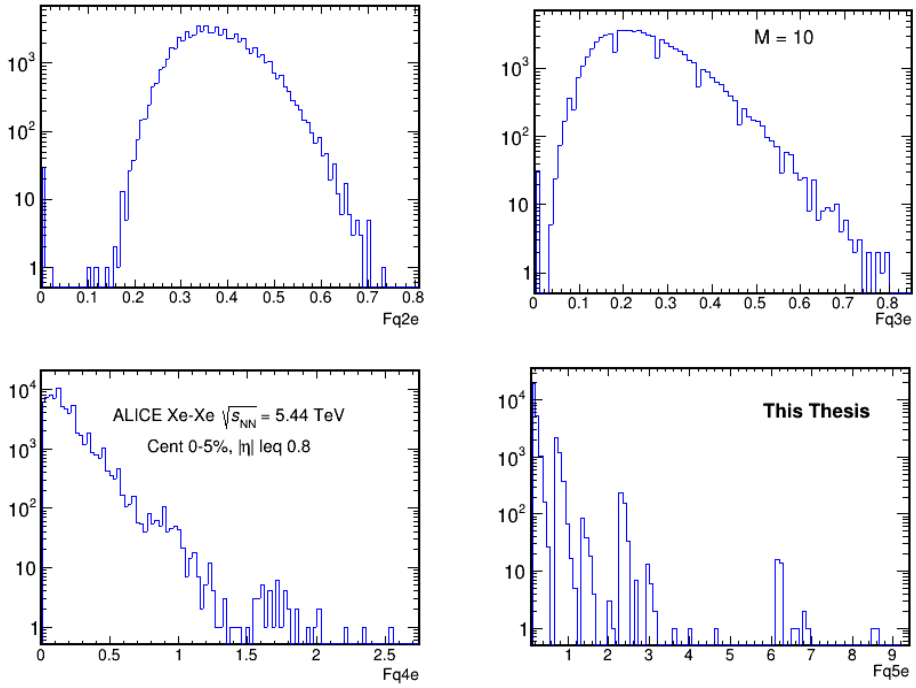

Figure 4.6: F_q^e distributions (q = 2, 3, 4 and 5) determined for the charged particles produced in the p_T bin $0.4 \leq p_T \leq 1.0$ GeV/c having (η, ϕ) phase space partitioned with M = 10.

of $F_q(M)$ versus $\ln M^2$ in the p_T bin $0.4 \leq p_T \leq 1.0$ GeV/c, for the charged particles produced in Xe–Xe collisions at $\sqrt{s_{NN}}$ = 5.44 TeV. It is observed that, for all q, $F_q(M)$ increase with increase in the number of bins (M^2) indicating a uniform monotonic relationship between $\ln F_q$ and $\ln M^2$. It is also observed that $F_{q+1}(M) > F_q(M)$ for all M values. The power-law growth of $F_q(M)$ with M^2 shows multiple linear regions for all q values. These observations indicate the presence of intermittency signal and hence the presence of local multiplicity fluctuations in the charged particle production. The error bars on the markers are the statistical + systematic uncertainties calculated using quadrative rule. Statistical uncertainties are determined using the sub-sampling method as discussed in section A.0.2. Systematic uncertainties estimation is given in section 4.3 and Appendix.

Fig. 4.9(a) shows the $\ln F_q(M)$ versus $\ln M^2$ plots, corresponding to high M values with at least 98% Monte Carlo closure. In this region of the plots, straight line fits are performed which yield the intermittency indices φ_q. The dependence of φ_q on the order q for the transverse momentum bin $0.4 \leq p_T \leq 1.0$ GeV/c, within 0-5% centrality is presented in Fig. 4.9(b). It is observed that φ_q increase with q, indicating that the higher order fluc-

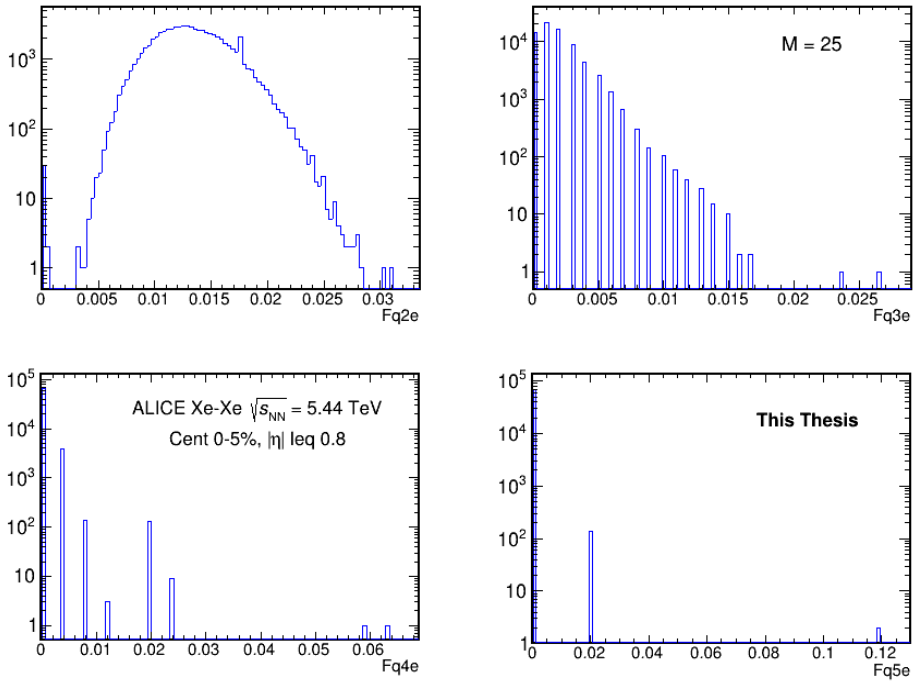

Figure 4.7: F_q^e distributions (q = 2, 3, 4 and 5), determined for the charged particles in the $0.4 \leq p_T \leq 1.0$ GeV/c bin, with (η, ϕ) phase space partitioned in 25 bins (M = 25) along each dimension. This figure and Fig. 4.6 shows how event factorial moment distributions behave with change in phase space binning and order of the moments.

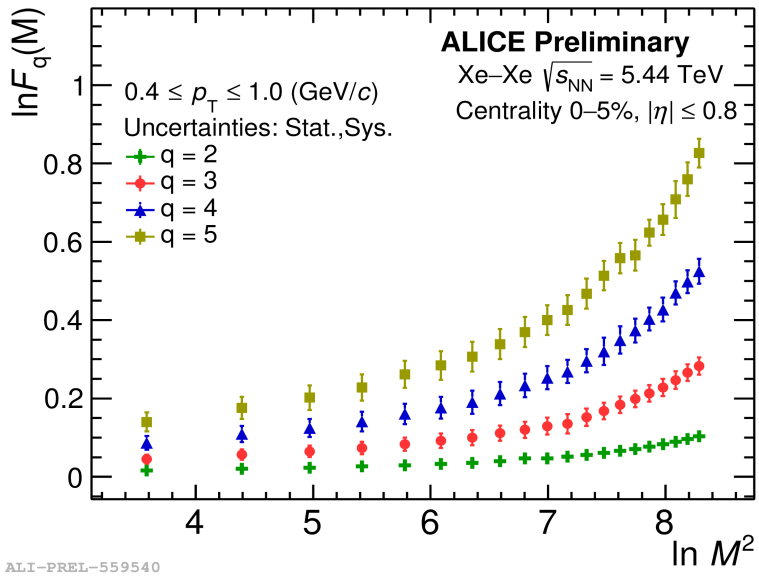

Figure 4.8: *M-scaling* plot for q = 2, 3, 4 and 5 for all M values in the p_T bin $0.4 \leq p_T \leq 1.0$ GeV/c for 0-5% central events.

tuations become more pronounced as q increases. The increasing trend of φ_q with q shows the presence of non statistical fluctuations in the data. Further, the observed M-scaling

behaviour suggests self-similar patterns in the underlying particle production mechanism in the data.

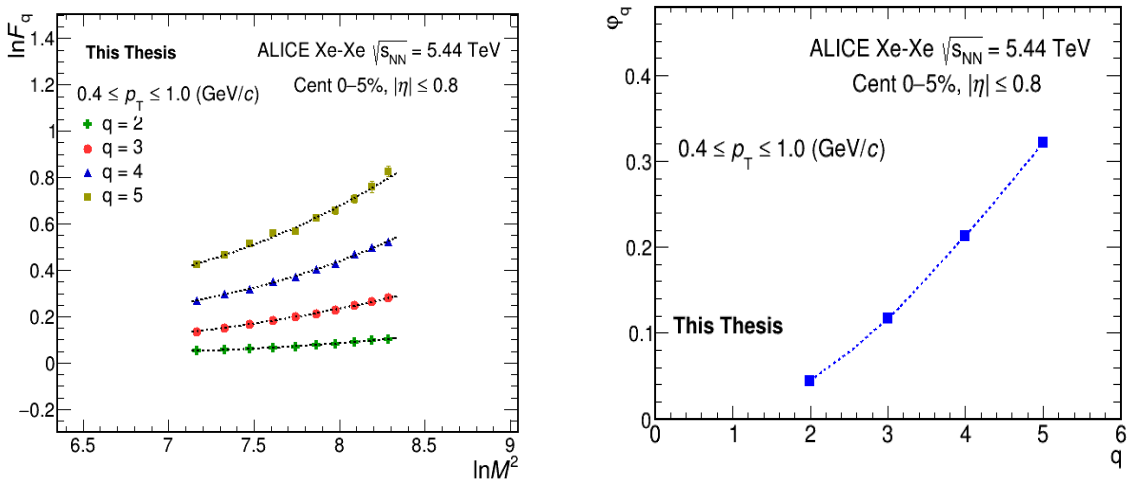

(a) (b)

Figure 4.9: (a) Plot of $\ln F_q$ versus $\ln M^2$ (*M-scaling*) for only high-M values, showing a linear behaviour (b) Dependence of the intermittency indices φ_q on the order q is shown. In both figures lines connecting the data points are to guide the eye.

4.2.4 F-scaling and Scaling Exponent (ν)

The second scaling behaviour studied is the *F-scaling*, that is dependence of $\ln F_q$ on the $\ln F_2$ for $q > 2$. Fig. 4.10 shows the $\ln F_q(M)$ versus $\ln F_2$(M) plots for all M values (M_{min} to M_{max}) for the charged particles in the transverse momentum interval $0.4 \leq p_T \leq 1.0$ GeV/c. A power-law growth of $\ln F_q(M)$ with $\ln F_2$(M) is observed for the whole range of M-values. Similar observations are made for the other transverse momentum bins as well. For high M region corresponding to high resolution binning in the phase space, the F-scaling behaviour is shown in Fig. 4.11(a). A strict linear behaviour of $\ln F_q(M)$ with $\ln F_2$(M) shows the presence of good order scaling in the data. On these plots, line fits are performed to yield β_3, β_4 and β_5. The lines joining the data points in the figure are straight line fits. The values of $\ln \beta_q$ plotted against $\ln(q-1)$ are shown in Fig. 4.11(b). A straight line fit to this plot gives slope called the scaling exponent (ν). ν

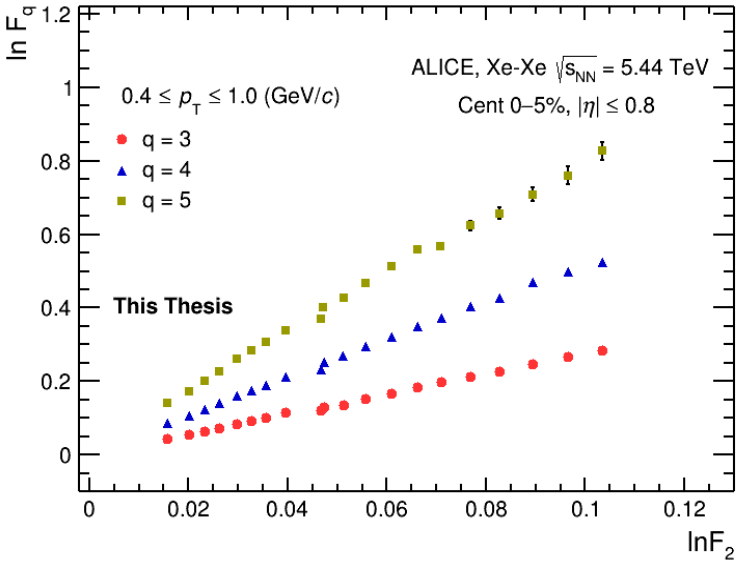

Figure 4.10: F-scaling plot for q = 2, 3, 4 and 5 for all M values in the p_{T} bin $0.4 \leq p_T \leq 1.0$ GeV/c.

being independent of q and M is a dimensionless parameter and characterizes the system under study. The scaling exponents obtained from different p_{T} intervals are given in Table 4.1. The average value of ν so obtained from different p_{T} intervals is 1.41 ± 0.03. This value of ν is consistent with the predictions from model [4] with critical fluctuations as expected near the QCD critical point.

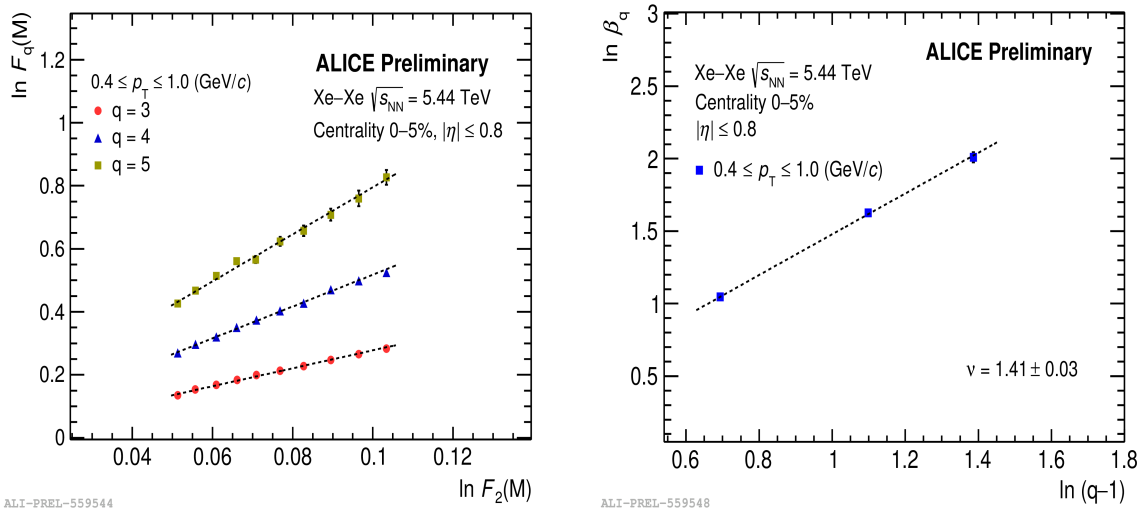

(a) (b)

Figure 4.11: (a) F-scaling with straight line fits and (b) $\ln\beta_{\mathrm{q}}$ vs $\ln(q-1)$ plot with line fit that gives a slope termed as the scaling exponent (ν), in case of the p_{T} bin $0.4 \leq p_{\mathrm{T}} \leq 1.0$ GeV/c.

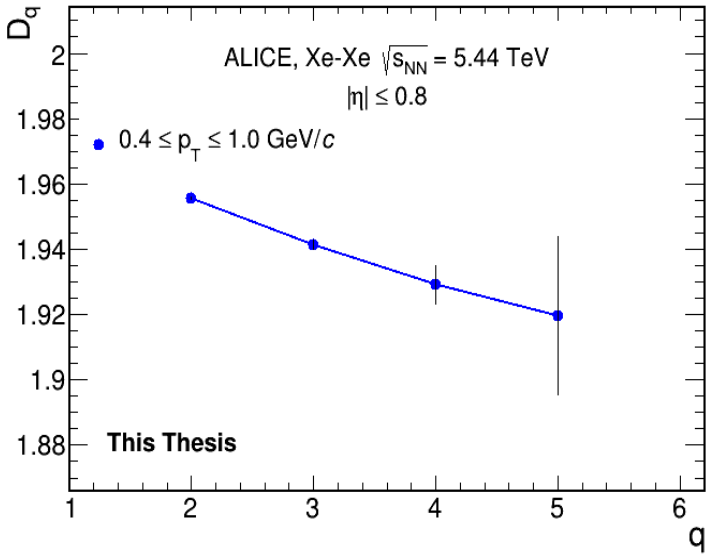

Figure 4.12: D_q vs q plot for q = 2, 3, 4 and 5 for the charged particles produced in the p_T bin $0.4 \leq p_T \leq 1.0$ GeV/c from the 0-5% central Xe–Xe collision events.

4.2.5 Fractal Dimension D_q

The normalised factorial moments $F_q(M)$ for q = 2, 3, 4 and 5 are observed to follow a power-law dependence on the number of bins (M^2), which is indicative of the self-similarity in particle multiplicity fluctuations. This behaviour is known feature of the systems with fractal characteristics. In the context of multifractal analysis, this scaling behaviour is quantified by the fractal dimension D_q which is related to the intermittency index φ_q through Eq.3.15. Using intermittency indices φ_q for q = 2, 3, 4, and 5, D_q are calculated. Fig. 4.12 shows the D_q versus q plot for the charged particles produced in the midrapidity region of the p_T bin $0.4 \leq p_T \leq 1.0$ GeV/c. A decrease in D_q values with increase in q is observed, a feature of multifractal behaviour that is observed to be present in the experimental data. Similar observations are made for other p_T bins as well.

4.2.6 Coefficient λ_q

If there is a non-thermal phase transition, theoretical models predict that λ_q should exhibit a minimum at some $q = q_c$. The coefficient λ_q as defined in Eq.3.16 is calculated and plots of λ_q as function of q, for q = 2, 3, 4, and 5 are drawn, as shown in Fig. 4.13 for the charged particles in the transverse momentum bin $0.4 \leq p_T \leq 1.0$ GeV/c and within

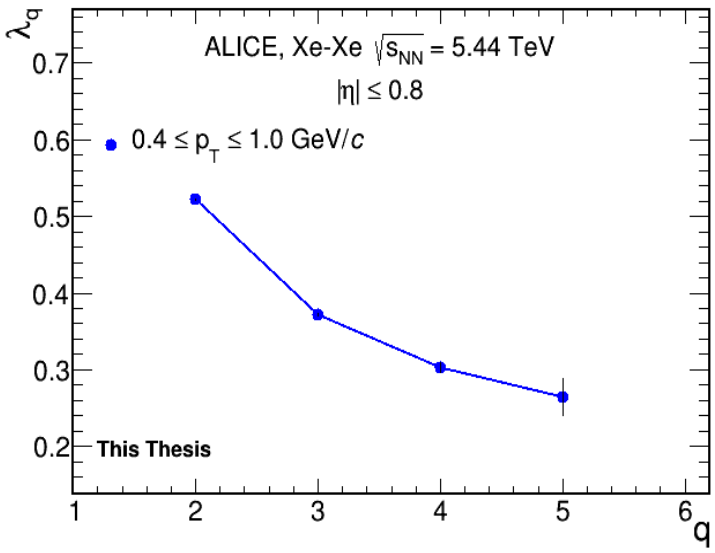

Figure 4.13: λ_q vs q plot for the charged particles produced in the p_T bin $0.4 \leq p_T \leq 1.0$ GeV/c for 0-5% central Xe–Xe collision events.

$|\eta| \leq 0.8$ and full azimuthal coverage $0 \leq \phi \leq 2\pi$. Figure shows no distinct minima for λ_q at any q value from 2 to 5. For $q \geq 5$, there are large statistical uncertainties and this limits conclusive evidence on presence of non-thermal phase transition. Nevertheless, λ_q is a valuable tool and may give a definitive insight into the thermal behaviour if further investigations are carried with large event statistics, improved detector resolution and a broader q-range coverage.

4.2.7 p_T bin dependence of M-scaling

The p_T bin dependence of the M-scaling is studied across narrow and wide p_T intervals (Table 3.3). Fig. 4.14 and Fig. 4.15 show these plots, that is $\ln F_q$ versus $\ln M^2$ for $q = 2, 3, 4$ and 5. For every p_T bin investigated, a power-law scaling is observed with no strict single linearity. In other words $F_q(M)$ increases with an increase in M values for all q = 2, 3, 4 and 5. This suggests that as resolution of the bins increases, there are more fluctuations in the charged particle number density in the (η, ϕ) phase space. Significant fluctuations are particularly evident at higher M values in the narrow p_T bins, mainly for the higher order (q = 5) moment. As M increases, the average number of tracks per bin decreases. If there are not many events in which the number of tracks within each bin is greater than

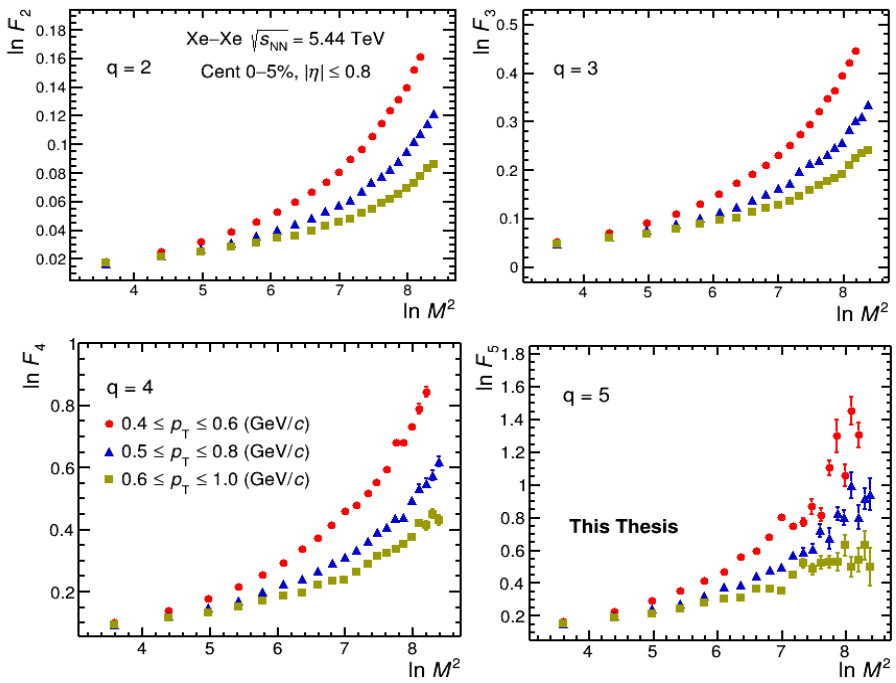

Figure 4.14: $\ln F_q(M)$ vs. $\ln M^2$ plots (M-scaling) for $q = 2, 3, 4$, and 5 for charged particles produced in narrow p_T bins in the mid-rapidity region of the most central Xe–Xe events recorded using ALICE.

the order of the moment ($n_i > q$), then $F_q(M)$ becomes statistically unstable, resulting in increased fluctuation in the measured high-order moments. These fluctuations are more in the p_T bin $0.6 \leq p_T \leq 1.0$ GeV/c than the other two narrow p_T bins as it has low average bin multiplicity in comparison to the other two bins and not many events with $n_m \geq q$ for $q = 5$. Low multiplicity increases statistical weight of fluctuations, thereby enhancing the observed intermittency signal at high resolution. On the other hand, these statistical fluctuations in the higher M region for wide p_T bin intervals are small as compared to the narrow p_T intervals. This difference is attributed to the increase in particle count within the phase space as the width of the p_T bin increases. For all transverse momentum intervals multiple linear regions are observed in the $\ln F_q(M)$ versus $\ln M^2$ plots and thus absence of strict linear behaviour. However a linear behaviour of $\ln F_q(M)$ with $\ln M^2$ in high M region is observed, which is a region of high resolution of bins in the phase space and thus suggest presence of intermittency.

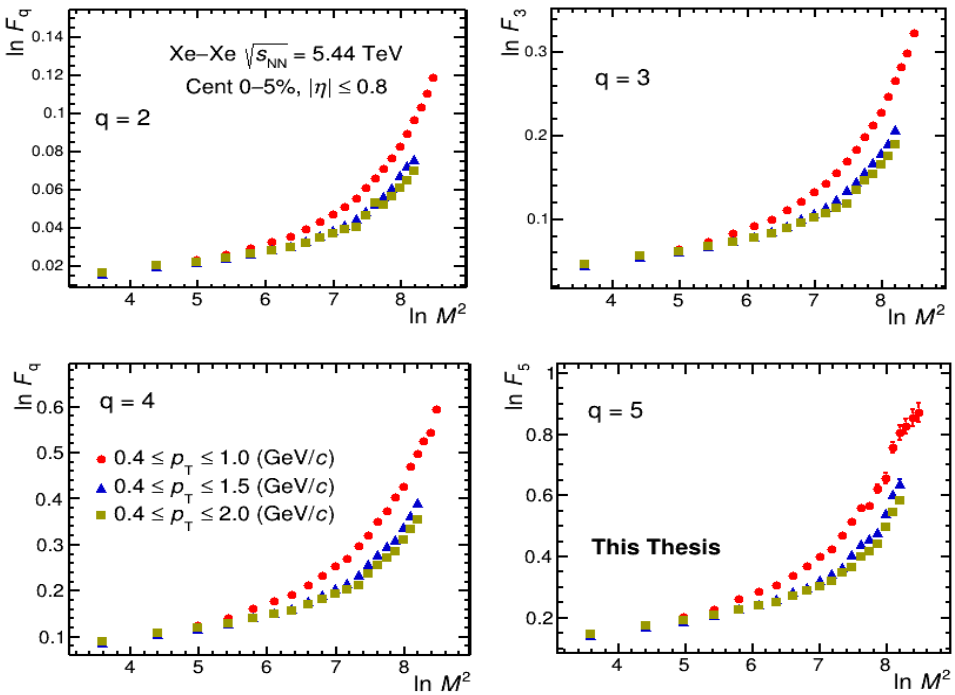

Figure 4.15: $\ln F_q(M)$ vs. $\ln M^2$ plots (M-scaling) in case of $q = 2, 3, 4$, and 5, for the charged particles produced in wide p_{T} bins in the mid-rapidity region of the most central Xe–Xe events recorded using ALICE.

4.2.8 Dependence of Scaling exponent (ν) on p_{T}

To investigate the dependence of the scaling exponent ν on the transverse momentum (p_{T}) and p_{T} bin width, narrow and wide p_{T} intervals with different bin widths are studied. Fig. 4.16 shows the $\ln F_{\mathrm{q}}$ vs $\ln F_2$ and $\ln \beta_{\mathrm{q}}$ versus $\ln(q-1)$ plots for the narrow p_{T} bins ($0.4 \leq p_{\mathrm{T}} \leq 0.6$ GeV/c , $0.5 \leq p_{\mathrm{T}} \leq 0.8$ GeV/c and $0.6 \leq p_{\mathrm{T}} \leq 1.0$ GeV/c). Similarly Fig. 4.17 shows the F-scaling plots for the two wide p_{T} bins ($0.4 \leq p_{\mathrm{T}} \leq 1.5$ GeV/c and $0.4 \leq p_{\mathrm{T}} \leq 2.0$ GeV/c). It is observed that the *F-scaling* plots do not show smooth linear behaviour in case of narrow p_{T} bins with large error bars. This behaviour is likely due to lower average bin content in the small p_{T} intervals which gives statistical fluctuations in the factorial moments values. The ν values obtained from the straight line fit to $\ln \beta_{\mathrm{q}}$ versus $\ln(q-1)$ plots for the different transverse momentum intervals are tabulated in the Table 4.1.

Fig. 4.18 shows the variation of ν as a function of the central value of the p_{T} bins for both narrow and wide transverse momentum bins. For both cases, the horizontal bars and

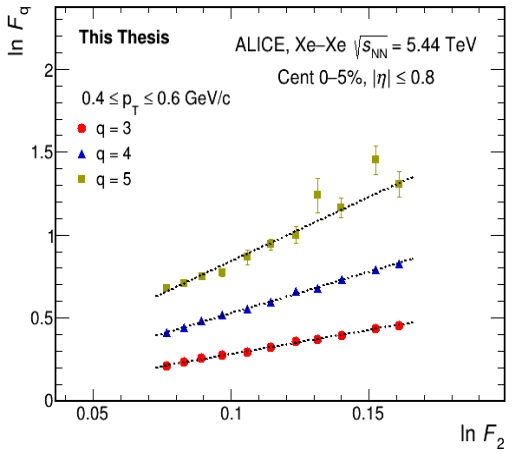

(a)

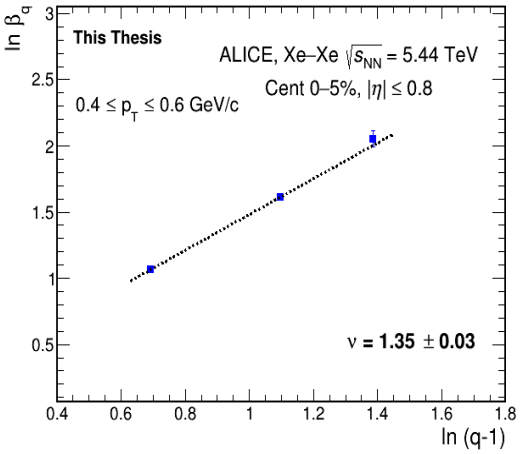

(b)

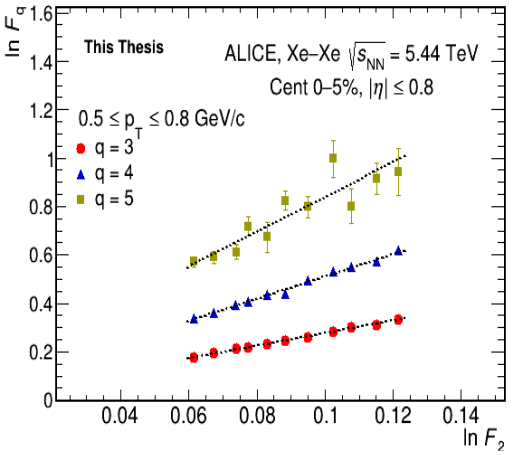

(c)

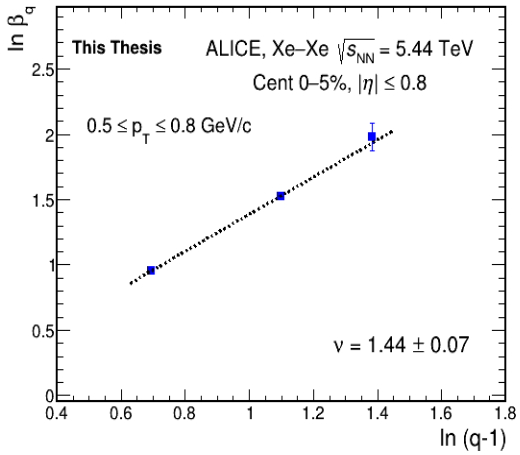

(d)

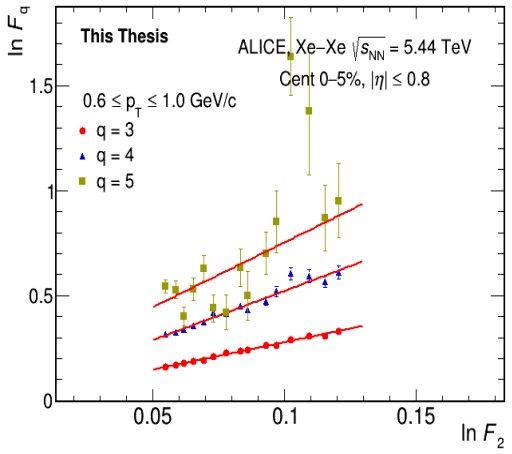

(e)

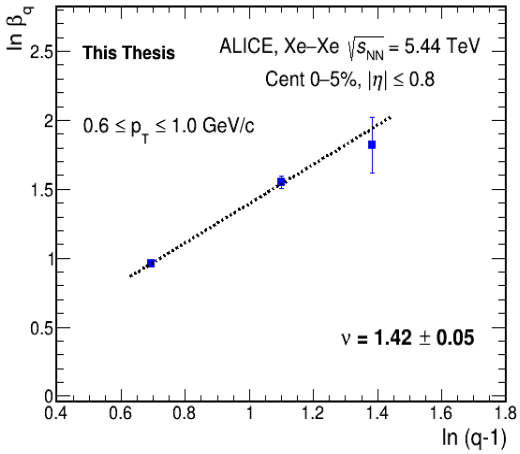

(f)

Figure 4.16: (a), (c), (e) $\ln F_q$ vs $\ln F_2$ and (b), (d), (f) $\ln \beta_q$ vs $\ln(q-1)$ plot for the charged particles produced in the narrow p_T bins $0.4 \leq p_T \leq 0.6$ GeV/c , $0.5 \leq p_T \leq 0.8$ GeV/c and $0.6 \leq p_T \leq 1.0$ GeV/c for the most central Xe–Xe events at $\sqrt{s_{NN}} = 5.44$ TeV.

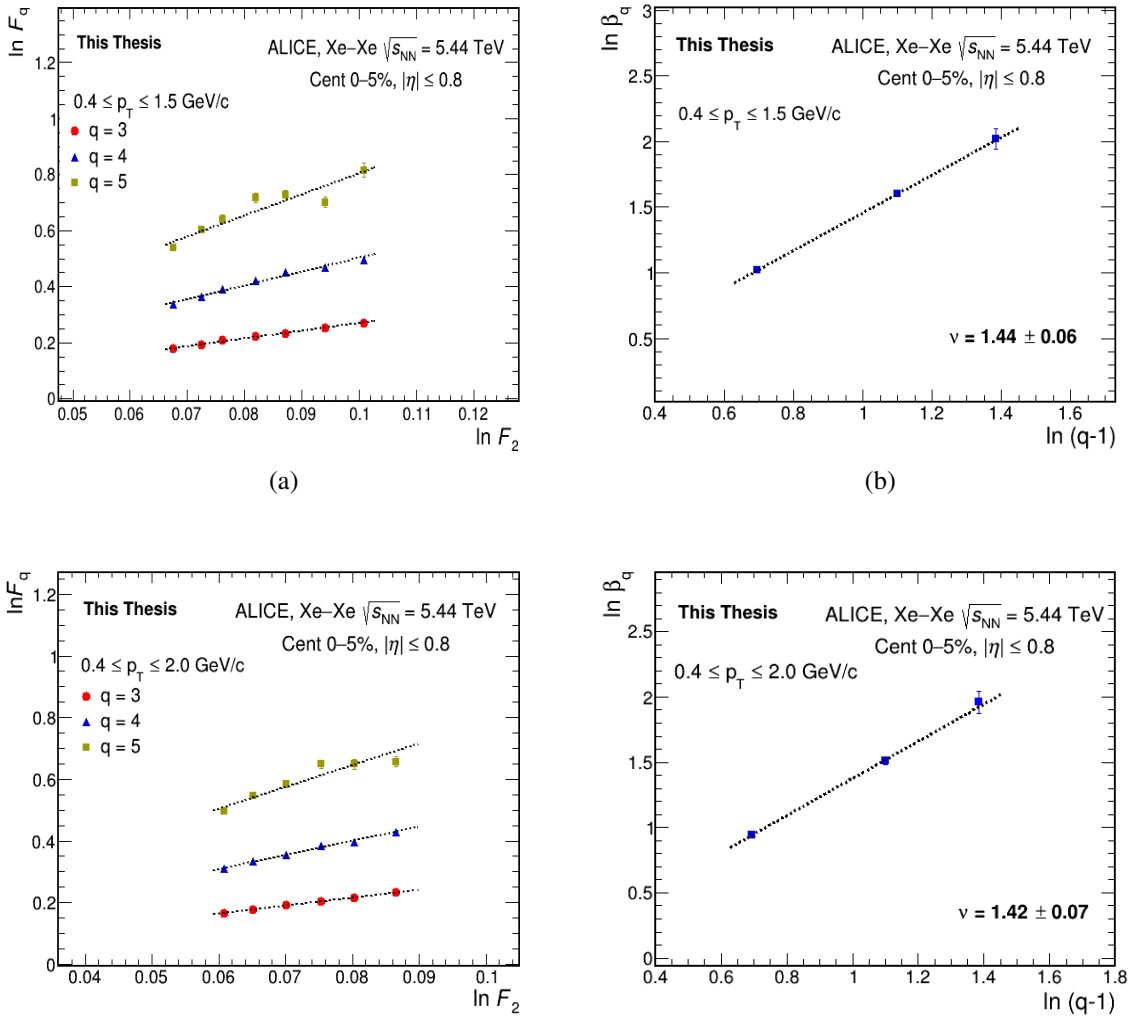

Figure 4.17: (a), (c) $\ln F_q$ vs $\ln F_2$ and (b), (d) $\ln \beta_q$ vs $\ln(q-1)$ plots for the charged particles produced in the p_T bins $0.4 \leq p_T \leq 1.5$ GeV/c and $0.4 \leq p_T \leq 2.0$ GeV/c.

the vertical error bars show the width of the p_T bin with a marker in the centre of the bin and fitting error on $\ln \beta_q$ vs. $\ln(q-1)$ plots respectively. However, the shaded boxes shows the systematic uncertainties. It can be observed from the given figure that, within the systematic uncertainties, the scaling exponent ν remains independent of p_T and p_T bin width in the soft transverse momentum region. The extracted values of ν are also found to be close to the average value predicted by the Ginzburg-Landau (GL) formalism for second-order phase transition[1, 2, 3] and the SCR model with critical fluctuations [4].

p_{T} intervals (GeV/c)	Scaling exponent (ν)
$0.4 \leq p_{\mathrm{T}} \leq 0.6$	1.35 ± 0.03
$0.5 \leq p_{\mathrm{T}} \leq 0.8$	1.44 ± 0.07
$0.6 \leq p_{\mathrm{T}} \leq 1.0$	1.42 ± 0.05
$0.4 \leq p_{\mathrm{T}} \leq 1.0$	1.40 ± 0.04
$0.4 \leq p_{\mathrm{T}} \leq 1.5$	1.44 ± 0.06
$0.5 \leq p_{\mathrm{T}} \leq 2.0$	1.42 ± 0.07

Table 4.1: Scaling exponent (ν) from the experimental transverse momentum bins across a range below 2.0 GeV/c.

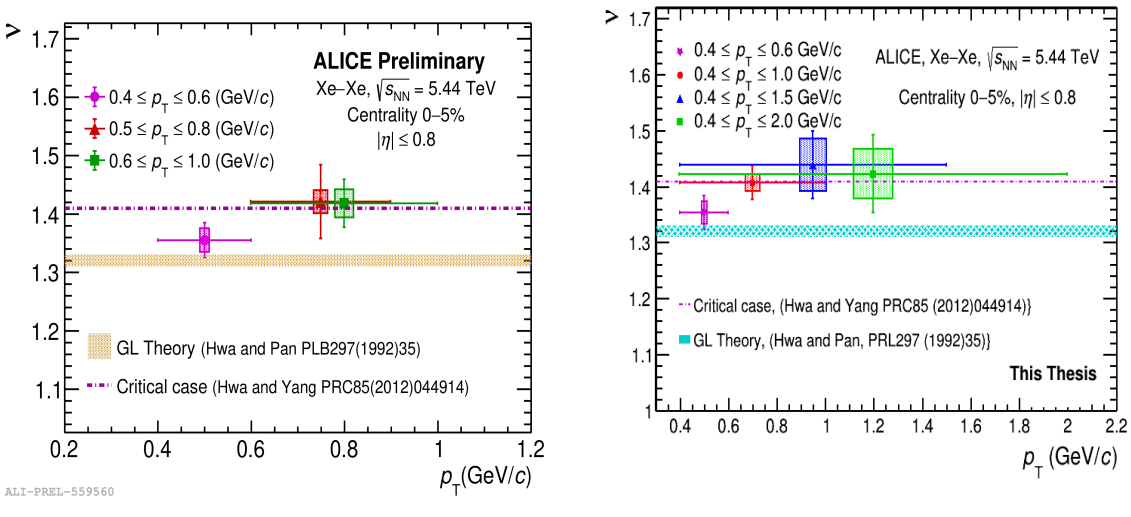

(a) (b)

Figure 4.18: Scaling exponent (ν) as a function of p_{T} interval for the (a) narrow p_{T} bins ($0.4 \leq p_{\mathrm{T}} \leq 0.6$ GeV/c , $0.5 \leq p_{\mathrm{T}} \leq 0.8$ GeV/c and $0.6 \leq p_{\mathrm{T}} \leq 1.0$ GeV/c) (b) wider p_{T} bins ($0.4 \leq p_{\mathrm{T}} \leq 1.0$ GeV/c, $0.4 \leq p_{\mathrm{T}} \leq 1.5$ GeV/c and $0.4 \leq p_{\mathrm{T}} \leq 2.0$ GeV/c) for the most central Xe–Xe collision events at $\sqrt{s_{\mathrm{NN}}}$ = 5.44 TeV. Theoretically predicted average [2] value of ν and the one predicted by the SCR model [5, 6] are also shown. Horizontal lines on the markers show the p_{T} intervals, with filled boxes depicting systematic uncertainty, whereas the vertical bars represent statistical uncertainty.

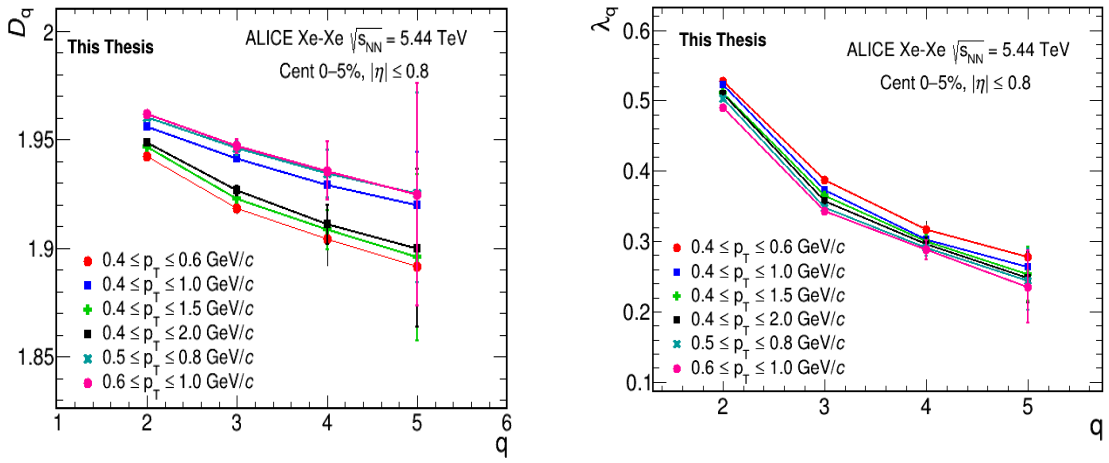

(a) (b)

Figure 4.19: (a) D_q versus q and (b) λ_q versus q, across various p_T bin interval for the charged particles produced in the central Xe–Xe collision events. The vertical error bar show the fitting errors.

4.2.9 Dependence of D_q and λ_q on p_T bins

For the various p_T intervals, Fig. 4.19(a) shows D_q as a function of the moment order q = 2, 3, 4 and 5. For all cases, D_q is observed to decrease with increasing q reflecting the multifractal nature of the multiplicity fluctuations in the central Xe–Xe collisions recorded by the ALICE experiment. Fig. 4.19(b) shows the dependence of the coefficient λ_q on the order of the moments for the same p_T intervals. λ_q is seen to decrease monotonically with increasing q, and no distinct minima is observed in any p_T bin in the range q = 2 to 5. This suggests that the system exhibits a single phase structure, rather than undergoing a non-thermal phase transition. In both figures, the vertical error bars are the fitting errors associated with the extraction of φ_q. The consistent behaviour of both D_q and λ_q as a function of the order parameter q across different transverse momentum (p_T) bins suggests that particle production dynamics is multifractal in nature within the soft p_T region.

4.2.10 Centrality dependence Study

A centrality dependence study of the scaling exponent has been performed for the centrality classes 0-5%, 5-10%, 10-20%, 20-30%, and 30-40% in Xe–Xe collisions. Fig. 4.20

shows the *M-scaling* and *F-scaling* plots for the charged particles produced in these various centrality bins within the transverse momentum range $0.4 \leq p_{\mathrm{T}} \leq 1.0$ GeV/c. A power-law increase in the $\ln F_{\mathrm{q}}(M)$ with $\ln M^2$ is observed across all centrality classes and thus the observation of intermittency (M-scaling). There is decrease in particle multiplicity in more peripheral collisions, resulting in noticeable decrease in the average bin content, reflecting a less dense particle environment. As a result, the quantitative differences among the F_{q}(M) values for different q become more pronounced with decreasing centrality. All centralities follow the F-scaling behaviour as well. On the F-scaling plots, the straight line fits are performed in the high-M region for q = 3, 4 and 5 as shown in Fig. 4.20.

The $\ln \beta_{\mathrm{q}}$ versus $\ln(q-1)$ plot for these centrality bins are given in Fig. 4.21. The scaling exponent (ν) so obtained from these line fits as function of centrality are plotted (Fig. 4.22). Figure also include results from similar exercise performed for the charged particles produced in the narrow p_{T} bin $0.4 \leq p_{\mathrm{T}} \leq 0.6$ GeV/c. It is observed that, within statistical and systematic uncertainties, the scaling exponent ν remains independent of centrality. Moreover, the extracted values of ν are found to be close to the theoretical predictions from the Ginzburg-Landau (GL) formalism for the second-order phase transition [2] and the SCR (Successive Contraction and Randomization) model [4], which accounts for critical fluctuations in the complex systems. The results are consistent across all centrality classes for both the p_{T} bins shown in Fig. 4.22. The extracted values of the scaling exponent ν, which are observed to cluster around the value 1.4 across the centralities and the p_{T} bins, provide important insight into the underlying particle production dynamics in heavy-ion collisions.

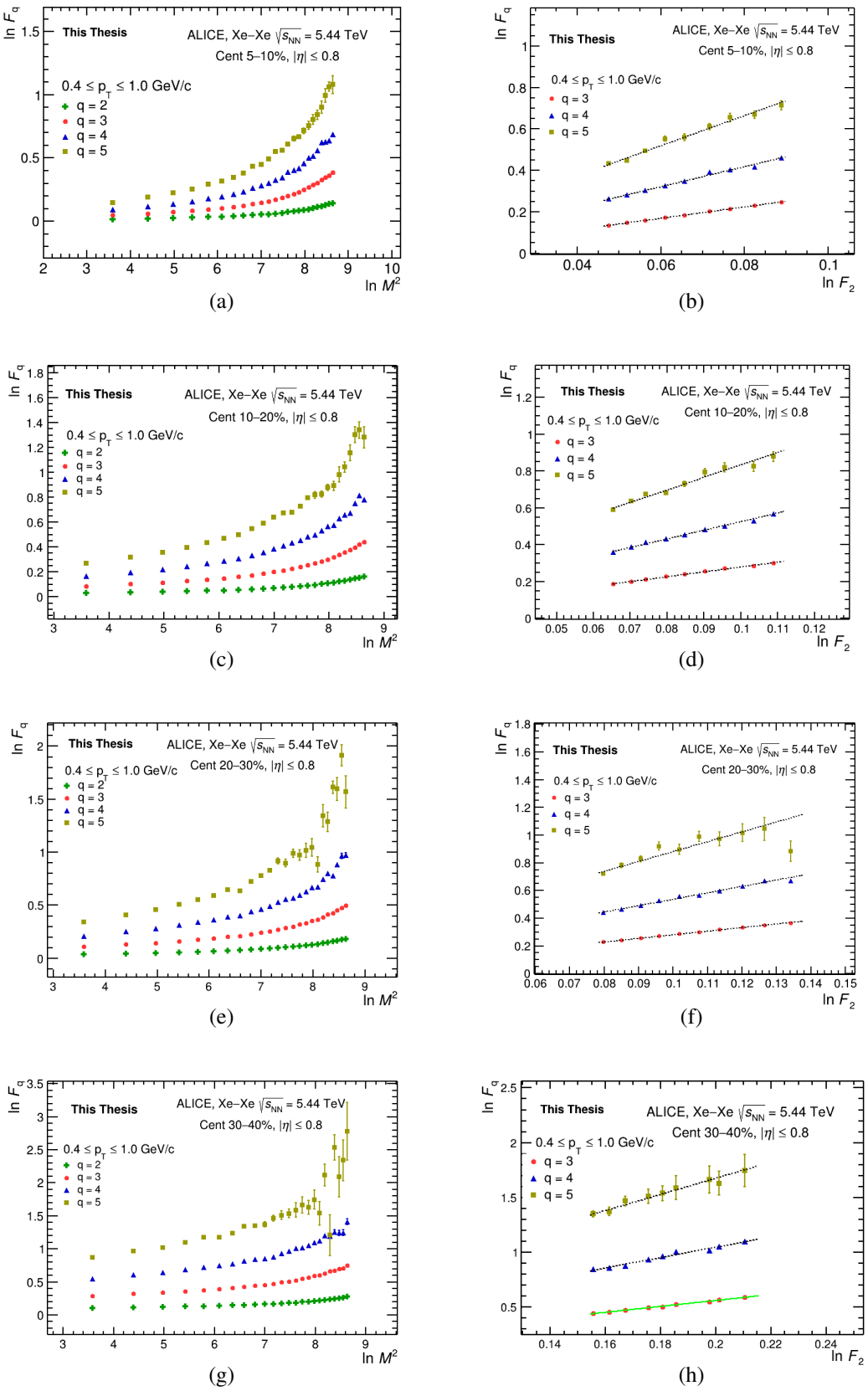

Figure 4.20: *M-scaling* and *F-scaling* for the charged particles produced in the $0.4 \leq p_T \leq 1.0$ GeV/c transverse momentum bin for various centralities.

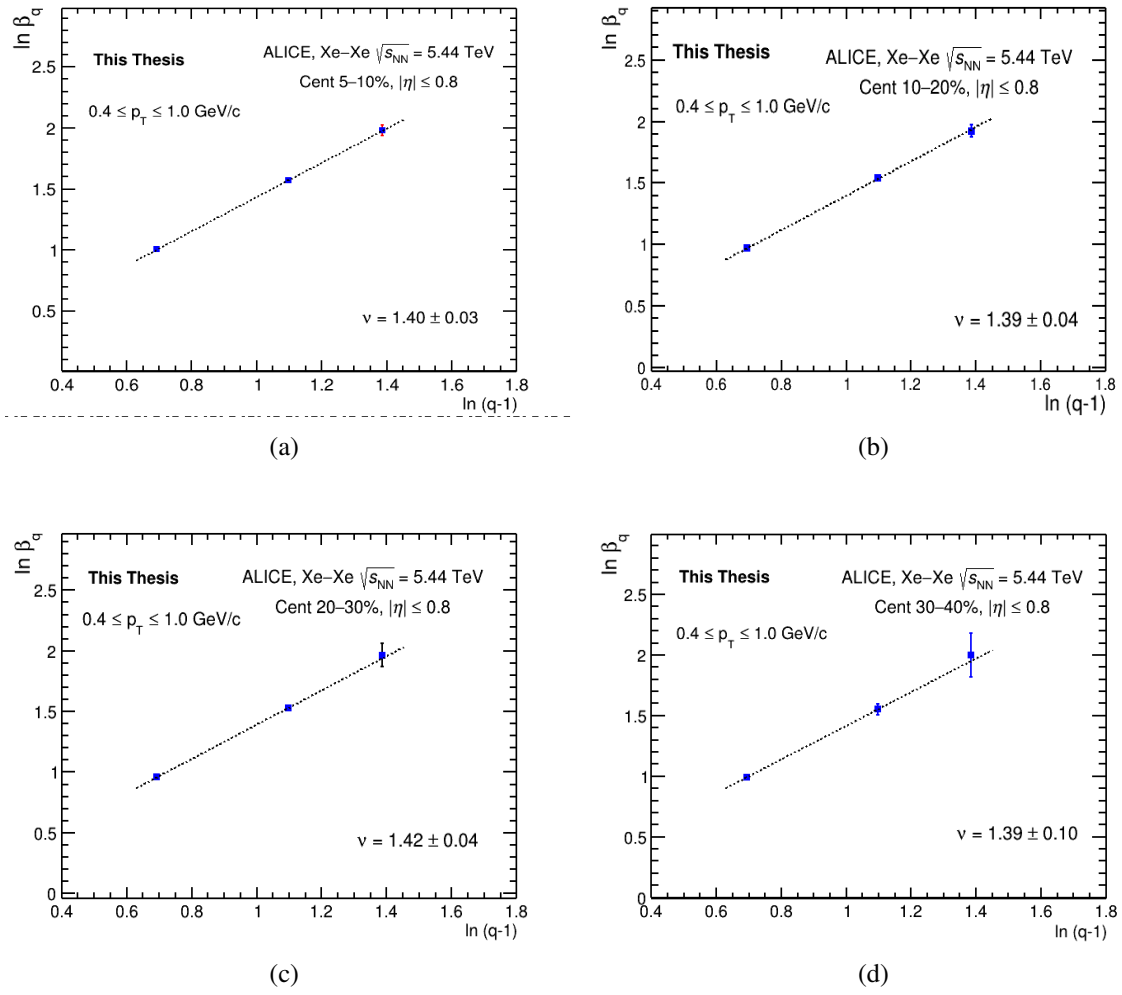

Figure 4.21: $\ln\beta_q$ versus $\ln(q-1)$ plots for the charged particles with $0.4 \leq p_T \leq 1.0$ GeV/c, $|\eta| \leq 0.8$ and $0 \leq \phi \leq 2\pi$ in the centrality bins (a) 5-10%, (b) 10-20%, (c) 20-30% and (d) 30-40%. Lines joining the markers are the linear fits to the data that are used to extract the scaling exponents ν.

4.3 Systematic uncertainties

Systematic uncertainties account for potential biases arising from the experimental setup, detector calibration, or analysis methods. Unlike statistical uncertainties these can have a consistent impact on the results and must be quantified in order to provide a complete understanding of measurement reliability. Therefore, these uncertainties must be carefully identified, quantified and reported. Different experimental conditions may produce results with varying uncertainties. Incorporating these uncertainties in the measured observables allow for more accurate and comprehensive comparisons of the data and results across

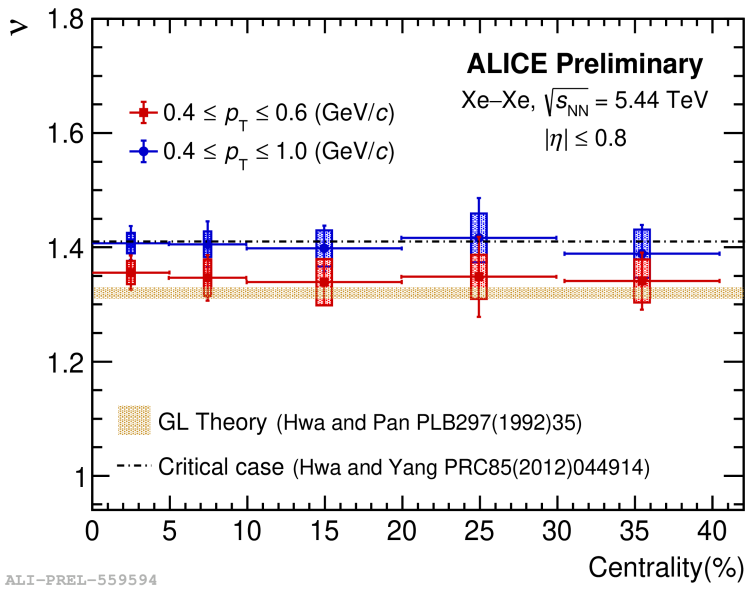

Figure 4.22: The scaling exponent ν as a function of collision centrality for Xe–Xe collision events in the two p_T intervals $0.4 \leq p_T \leq 0.6$ GeV/c and $0.4 \leq p_T \leq 1.0$ GeV/c.

Table 4.2: Cuts varied for the estimation of systematic uncertainties.

cut name	Default	Varied
Filter-Bit	768	32
$\|Vz\|$	$\pm$ 10cm	$\pm$ 8cm, $\pm$ 12cm
Centrality Estimator	VOM	CLO
TPCNcls	70	80
ITSNcls	2	3

different experiments and model predictions. It also enables the identification of possible sources of discrepancy and ensures robustness of any conclusions drawn from the analysis.

The systematic uncertainties which arise due to event and track selection criteria are determined. Systematic uncertainties due to event selection cuts are assessed by varying the method of centrality determination, and changing the cut on the position of the primary vertex along the beam direction $|V_z|$. As such for the first one the centrality estimation cut is changed to CL0 instead of default multiplicity measurement in the VZERO detector (V0M). The systematic uncertainty from different primary vertex cut is studied by changing the cuts from $|Vz| \leq 10$ cm to $|Vz| \leq 8$ cm and $|Vz| \leq 12$ cm. Systematics arising because of track selection criteria are determined by varying the filter bit cut from hybrid (bit 768) mode to a global selection (bit 32), varying number of TPC

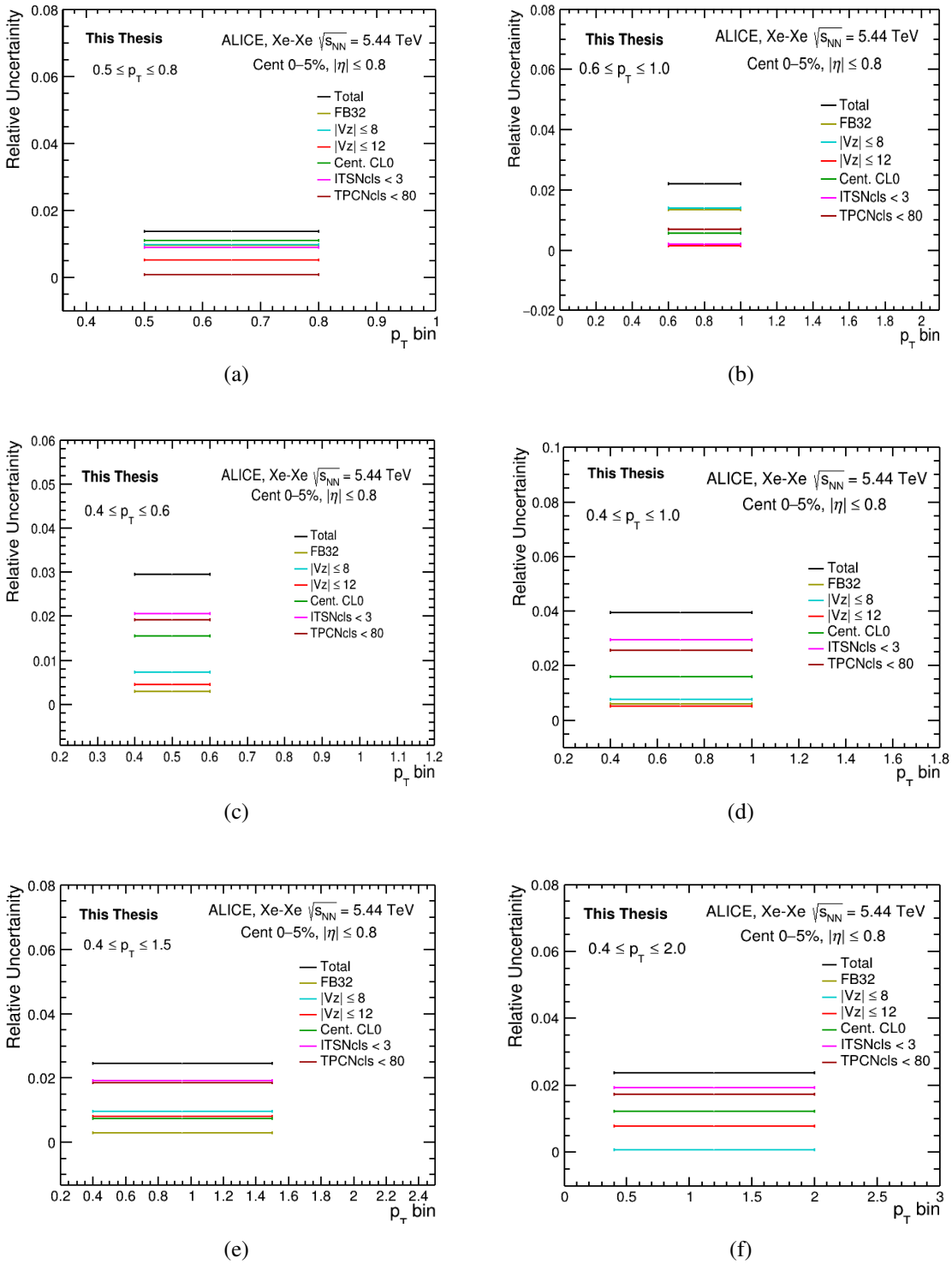

Figure 4.23: Relative Uncertainties in the value of scaling exponent ν across various transverse momentum bins. (a) $0.5 \leq p_{\mathrm{T}} \leq 0.8$ GeV/c and (b) $0.6 \leq p_{\mathrm{T}} \leq 1.0$ GeV/c, (c) $0.4 \leq p_{\mathrm{T}} \leq 0.6$ GeV/c, (d) $0.4 \leq p_{\mathrm{T}} \leq 1.0$ GeV/c, (e) $0.4 \leq p_{\mathrm{T}} \leq 1.5$ GeV/c and (f) $0.4 \leq p_{\mathrm{T}} \leq 2.0$ GeV/c

.

clusters (70 replaced by 80), and changing number of ITS clusters (2 replaced by 3). The total systematic uncertainty on the scaling exponent ν was calculated by taking the quadrature sum of the contributions from these individual sources (summarized in Table 4.2). The relative uncertainty on scaling exponent ν as a function of transverse momentum bins, $0.5 \leq p_{\mathrm{T}} \leq 0.8$ GeV/c, $0.6 \leq p_{\mathrm{T}} \leq 1.0$ GeV/c, $0.4 \leq p_{\mathrm{T}} \leq 0.6$ GeV/c, $0.4 \leq p_{\mathrm{T}} \leq 1.0$ GeV/c, $0.4 \leq p_{\mathrm{T}} \leq 1.5$ GeV/c and $0.4 \leq p_{\mathrm{T}} \leq 2.0$ GeV/c are shown in Fig. 4.23. For individual plots of various observables to estimate systematic uncertainties on ν please refer to Appendix B.1

4.4 Comparison of results

Results from data analysis of Xe–Xe collisions at $\sqrt{s_{\mathrm{NN}}}$ = 5.44 TeV are compared with that from Pb–Pb collisions at $\sqrt{s_{\mathrm{NN}}}$ = 2.76 TeV. The two systems, while differing in size and beam energy, provide a valuable opportunity to examine the system-size and energy dependence of key observables related to multiplicity fluctuations that is, intermittency and scaling behaviour.

4.4.1 M-scaling comparison

To assess the universality and system size dependence of intermittency and scaling behaviour, a comparison of results from Xe–Xe collisions at $\sqrt{s_{\mathrm{NN}}}$ = 5.44 TeV with those from Pb–Pb collisions at $\sqrt{s_{\mathrm{NN}}}$ = 2.76 TeV, as well as with the HIJING model simulations is done. This comparison focuses on the behaviour of $F_{\mathrm{q}}(M)$ as function of increasing phase-space resolution. Both datasets from the experiment show a power-law growth of $\ln F_{\mathrm{q}}$ with $\ln M^2$ for all values of q as is shown in Fig. 4.24 that is M-scaling is exhibited by both datasets. While Xe–Xe and Pb–Pb data show strong M-scaling behaviour, HIJING fails to reproduce it. HIJING event results significantly underestimate the data at high q and high M.

This underlines models inability to account for the scale invariant fluctuations present in the ALICE data. Data from the two colliding systems (Pb–Pb and Xe–Xe) show similar

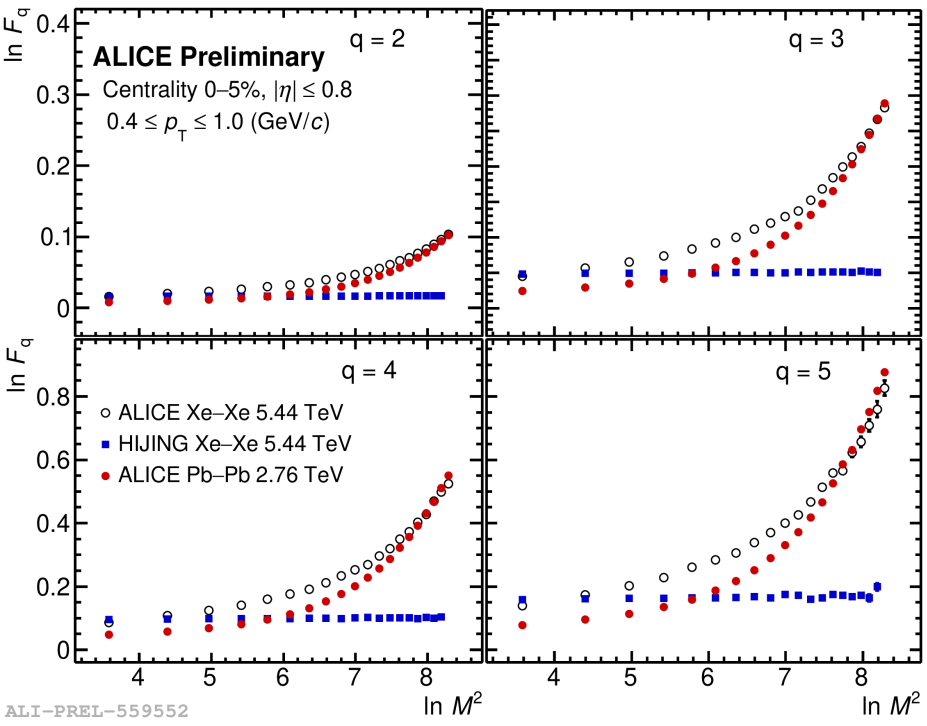

Figure 4.24: Comparison of $\ln F_q$ versus $\ln M^2$ plot for the charged particles produced in the Xe–Xe collision at $\sqrt{s_{NN}}$ = 5.44 TeV (this thesis) with that in the Pb–Pb collision at $\sqrt{s_{NN}}$ = 2.76 TeV and HIJING Xe–Xe data ($0.4 \leq p_T \leq 1.0$ GeV/c).

qualitative nature with a small quantitative difference at low M values. As M increases this difference is observed to decrease and a similar behaviour of the results from the two systems at different energies indicate that the multiparticle production in the nature is same especially at fine phase space scales. These findings reinforce the interpretation that multiparticle production in collisions exhibits intermittency and multifractal features that are not there in the HIJING model. These findings emphasize the need to update and modify the models.

4.4.2 Scaling exponent (ν) as a function of p_T

To investigate the system size and energy dependence of the scaling exponent ν, the observations from Xe–Xe and Pb–Pb collisions are compared and presented in Fig. 4.25. The value of scaling exponents obtained from central Xe–Xe collisions at $\sqrt{s_{NN}}$ = 5.44 TeV and the central Pb–Pb collisions at $\sqrt{s_{NN}}$ = 2.76 TeV, for the p_T bins $0.4 \leq p_T \leq 0.6$ GeV/c , $0.4 \leq p_T \leq 1.0$ GeV/c, $0.4 \leq p_T \leq 1.5$ GeV/c and $0.4 \leq p_T \leq 2.0$ GeV/c are shown in

the plot in Fig. 4.25. It is observed that ν values obtained from the two different experimental datasets are very close within uncertainties. The horizontal bars correspond to the width of each p_{T} bin. The shaded boxes depict the systematic uncertainties derived from the variations in the selection cuts, as discussed in the previous section. The vertical lines depict the fitting error. The scaling exponent values from the two system, for the various p_T bins analyzed, are very close within the errors and are consistent with theory and model based predictions [2, 3, 5, 6]. The scaling exponent are thus observed to be independent of the p_{T} bin and the p_{T} bin width and across the colliding systems. This figure presents a comprehensive comparison of experimental data with theoretical predictions.

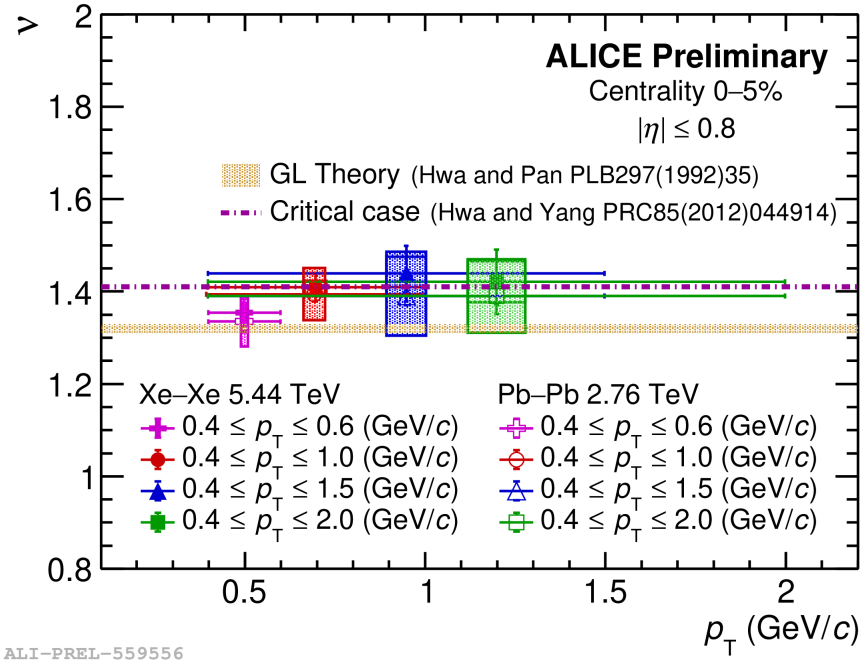

Figure 4.25: Comparison of the scaling exponent (ν) versus p_{T} bin plot for charged particles produced in the Xe–Xe collision at $\sqrt{s_{\mathrm{NN}}}$ = 5.44 TeV (this thesis) with that of charged particles produced in Pb–Pb collision at $\sqrt{s_{\mathrm{NN}}}$ = 2.76 TeV [7].

4.4.3 Fractal parameter (D_{q}) as a function of q

D_{q} behaviour with q extracted from central Xe–Xe and Pb–Pb collisions is compared and also contrasted with a Toy Model baseline trend to assess the role of underlying dynamics in generating complex scaling features. Fig. 4.26 shows the variation of the fractal dimension D_{q} as a function of the order of the moment q for the above said cases. For the two

experimental data sets from ALICE, D_q is observed to decrease with increasing q, indicating a multifractal character in the particle production process. However, results from the Toy-Model events show a markedly different trend. The Toy Model [8] events exhibit a constant D_q as a function q, a characteristic of monofractal behaviour. This quantitative difference between the real data and the baseline simulated events suggests that the multifractality observed in the experimental data arises from underlying dynamical correlations which are absent in uncorrelated particle emission models.

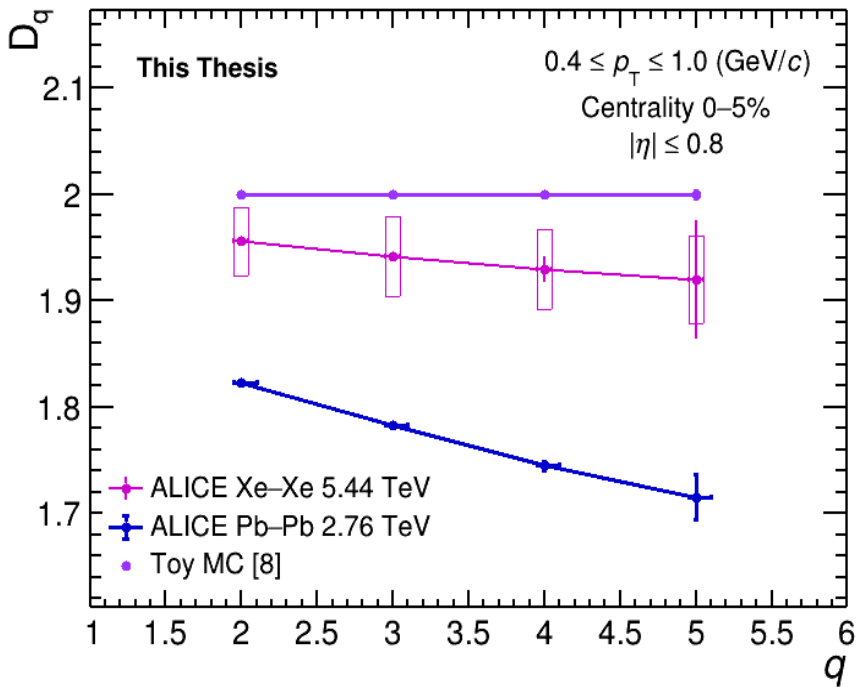

Figure 4.26: Fractal dimension D_q as a function of the order of the moment q. Plots are for the charged particles produced in the $0.4 \le p_T \le 1.0$ GeV/c bin, measured in central Xe–Xe collision at $\sqrt{s_{NN}}$ = 5.44 TeV (this thesis) and central Pb–Pb collision at $\sqrt{s_{NN}}$ = 2.76 TeV [7]. Results from experiment are compared with the baseline Toy model [8] behaviour.

4.4.4 Coefficient (λ_q) as a function q

Results on the trends of λ_q with increasing moment order q from Xe–Xe collision data are compared with Pb–Pb collision data as well as low-energy experiments. Fig. 4.27 shows λ_q versus q plot for the charged particles produced in the p_T bin $0.4 \le p_T \le 1.0$ GeV/c in the central Xe–Xe collisions at $\sqrt{s_{NN}}$ = 5.44 TeV and the central Pb–Pb collisions at

$\sqrt{s_{\rm NN}}$ = 2.76 TeV. A similar dependence of $\lambda_{\rm q}$ on q is observed to be there in both datasets from ALICE experiment. $\lambda_{\rm q}$ is observed to decreases monotonically with an increase in q values but with quantitative differences. No distinct minima is seen for $\lambda_{\rm q}$ at any q, for q upto 5. The absence of a minima may attributed to the limited range of q studied

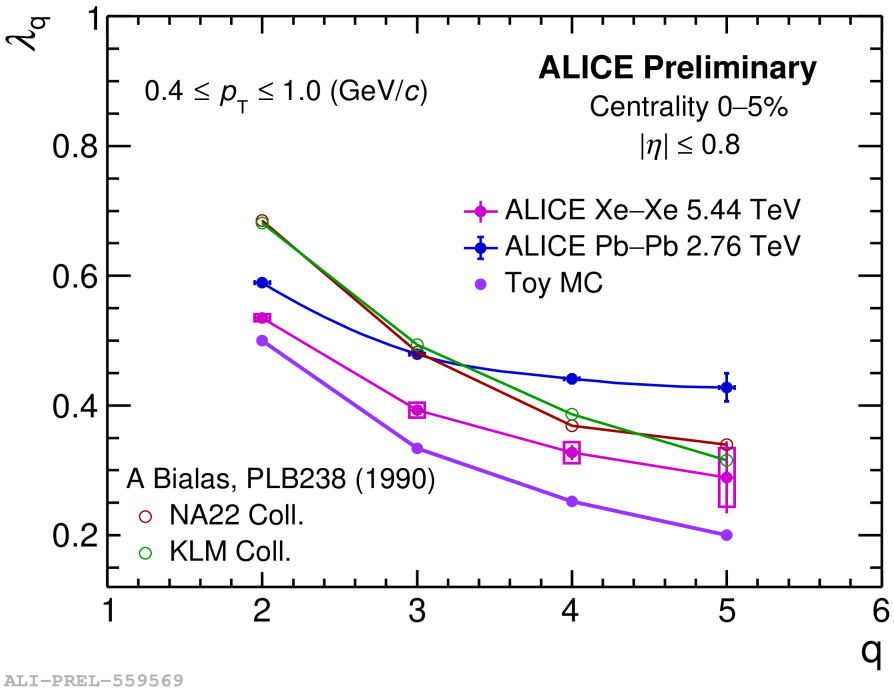

Figure 4.27: $\lambda_{\rm q}$ versus q: A comparative study.

and to statistical uncertainties, particularly at higher moment orders. A more definitive analysis would require extending the calculations beyond $q = 5$. However, this demands a significantly large data set, to ensure statistical reliability in the absence of which it is difficult to make concrete conclusions from this study on $\lambda_{\rm q}$ coefficient except that none of these experiments see two phase system.

This chapter presents a detailed intermittency analysis of charged particle production in the central Xe–Xe collisions at $\sqrt{s_{\rm NN}}$ = 5.44 TeV, using experimental data from the ALICE experiment. The results are compared with data from Pb–Pb collisions at $\sqrt{s_{\rm NN}}$ = 2.76 TeV, as well as with baseline expectations from the HIJING event generator, Toy model and with theoretical models. The normalized factorial moments of the soft charged particles produced within the pseudorapidity window $\eta \leq 0.8$ and full azimuthal coverage $0 \leq \phi \leq 2\pi$

are determined. The NFM's exhibit power-law increase with the number of bins (M^2) for q = 2, 3, 4 and 5 giving evidence for the presence of intermittency and non-statistical multiplicity fluctuations in the data. This monotonic behaviour between $\ln F_{\mathrm{q}}$ and $\ln M^2$ signals the presence of self-similar scale invariant fluctuations. The decreasing trend of the fractal dimension D_{q} with increasing q further shows that the system produced in the collisions has multifractal structure. A comparative study with Pb–Pb collisions at $\sqrt{s_{\mathrm{NN}}}$ = 2.76 TeV reveals qualitatively similar scaling behaviour with quantitative differences at lower M values that diminish at finer resolution. This indicates a common underlying particle production mechanism exhibited by both collision systems created in the experiment despite differences in system size and collision energy. On the other hand, intermittency and multifractal nature of particle generation is absent in HIJING. This observation signals that the physics behind particle interactions in high-energy collisions has factors or processes that are still not understood or not implemented in this event generator. This highlights the need for models to incorporate critical dynamics or collective behaviour beyond independent particle emission so as to explain what is observed in the real data.

The scaling exponent ν extracted from the F-scaling in this thesis, across various p_T bins, is found to be consistent across different p_T bins and agrees well with theoretical predictions from the Ginzburg-Landau formalism and Successive Contraction and Randomization model, suggesting the presence of features of critical behaviour in the particle production dynamics in real data. The centrality dependence study shows that while the magnitude of factorial moments $F_{\mathrm{q}}(M)$ varies with centrality, primarily due to decreasing particle multiplicity in more peripheral events, the scaling behaviour is qualitatively same thereby the scaling exponent (ν) remains approximately constant across all centrality classes. In fact it is the scaling behaviour which is of significance and not the quantitative measure of the NFMs ($F_{\mathrm{q}}(M)$). Thus the observed scaling behaviour is robust and universal, and a strong candidate that must further investigated to characterize fluctuations and to understand system created at high energies and different collision systems.

BIBLIOGRAPHY

[1] R. C. Hwa and J. c. Pan, "Intermittency in the Ginzburg-Landau theory," Phys. Lett. B **297**, (1992) 35-38.

[2] R. C. Hwa and M. T. Nazirov, "Intermittency in second order phase transition," Phys. Rev. Lett. **69**, (1992) 741-744.

[3] R. C. Hwa, "Scaling exponent of multiplicity fluctuation in phase transition," Phys. Rev. D **47**, (1993) 2773-2781.

[4] R. C. Hwa and C. B. Yang, "Observable Properties of Quark-Hadron Phase Transition at the Large Hadron Collider," Acta Phys. Polon. B **48**, (2017) 23, [arXiv:1601.04671 [nucl-th]].

[5] R. C. Hwa, "Recognizing Critical behaviour amidst Minijets at the Large Hadron Collider," Adv. High Energy Phys. **2015**, (2015) 526908, [arXiv:1411.6083 [nucl-ex]].

[6] R. C. Hwa and C. B. Yang, "Local Multiplicity Fluctuations as a Signature of Critical Hadronization at LHC," Phys. Rev. C **85** 044914 (2012), arXiv:1111.6651 [nucl-th].

[7] S. Sharma and R. Gupta [ALICE collaboration], "A study of fluctuations in the mul-

tiparticle production at ultra-relativistic high energy collisions," Ph.D. thesis, CERN, 2025.

[8] S. Sharma, S. K. Malik, Z. Banoo and R. Gupta, "Normalized factorial moments of spatial distributions of particles in high multiplicity events: A Toy model study," Nucl. Phys. A **1053**, (2025) 122963, [arXiv:2309.07712 [hep-ph]].

[9] A. Bialas and K. Zalewski, "Phase Structure of Selfsimilar Multiparticle Systems and Experimental Determination of Intermittency Parameters," Phys. Lett. B 238 (1990) 413âĂŞ416.

CHAPTER 5

THE AMPT: INTERMITTENCY ANALYSIS

5.1 Introduction

The field of particle physics is quite challenging when it comes to conduct experiments with the aim to uncover the underlying physics of heavy-ion collisions. In the field numerous theoretical questions persist, due to various inherent factors such as the non-perturbative behaviour of QCD in the strong coupling regime, the intricate dynamics of multi-particle production and evolution during the heavy-ion collisions. To gain an insight into these phenomena, a diverse array of theories and concepts have been developed and implemented as Monte-Carlo codes. A variety of theoretical models are there in high energy physics each with distinct physical characteristics and based on different principles. However, no single model is capable of providing a complete description of all the experimental findings. As more and more experimental data is collected and analyzed, the requirement for more accurate and predictive theories grows with the abandonment of less suitable ones.

The Monte-Carlo codes, or theoretical calculations, for modeling these collisions can be categorized in various ways. There are a number of Monte Carlo codes which are based on principles and theories, such as lattice QCD and perturbative QCD models, while many others rely on phenomenological assumptions, approximations, and adjustments based on experimental data. Further there are models which focus on collective phenomena, such as thermal. [1, 2] and hydro [3] models, while others address microscopic phenomena, such as parton scattering, jet quenching, and string fragmentation. The classification scheme of these models may be done on various aspects like there are hydrodynamic expansion models, hadronization models, and hadron cascade models [4, 5] etc. There are some models that use different principles and theories at different stages and they are referred to as hybrid codes as these offer a diverse array of approaches. These hybrid models are more useful for creating a realistic picture of the various stages of a nuclear collision and can simulate collisions more accurately [6, 7] near to the experimental data. The A Multi Phase Transport (AMPT) model comes in the category of hybrid models [7] that has been used to investigate the key signatures of QGP formation in heavy-ion collisions. This chapter presents the details of the intermittency analysis for soft charged particles produced in the midrapidity region of Xe–Xe collisions at $\sqrt{s_{\rm NN}}$ = 5.44 TeV, using the AMPT model. An overview of the main components of the AMPT model namely the HIJING initial conditions, the ZPC parton evolution, the hadronization processes, and the extended ART model is presented below.

5.2 A brief introduction of the AMPT

The A Multi-Phase Transport (AMPT) model [8] is a hybrid framework that uses microscopic and macroscopic methods to simulate the different phases of a heavy-ion collision. It applies the kinetic theory approach to describe the evolution of heavy-ion collisions, from the initial stage through the intermediate stages to the final hadronic state. The model operates through two distinct configurations–the default (DF) mode and the string-melting (SM) mode Each of these modes proceeds through four essential subprocesses: phase-space ini-

tialization, parton scattering, hadronization, and hadronic rescattering. The initialization uses the HIJING model as an event generator, which includes minijet production and soft string excitations. Parton scattering is governed by Zhang's Parton Cascade model, which involves simple two-body scattering processes. The cross-sections of partons are calculated using perturbative Quantum Chromodynamics.

Figure 5.1 shows the schematic layouts of the default AMPT model [8, 9, 10, 11, 12] and the string-melting version AMPT model [11, 13, 14]. The various components and their integration within the AMPT in the two modes of operation are depicted in the figure and a brief overview is given below.

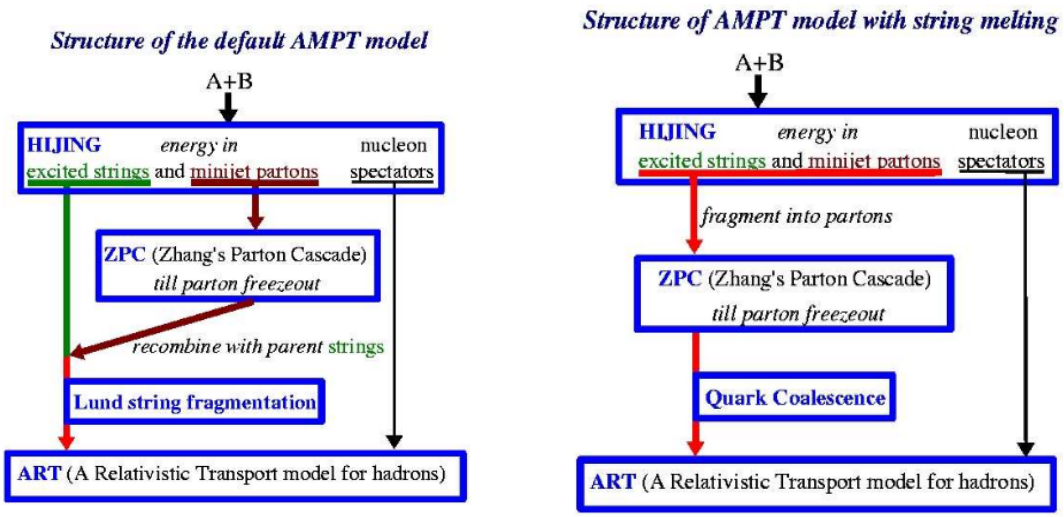

(a) (b)

Figure 5.1: Schematic overview of the two primary AMPT configurations: the default (DF) mode (left) and the string-melting (SM) mode (right).

5.2.1 HIJING initial conditions

The initial conditions for heavy-ion collisions in the default AMPT are derived from the HIJING model [15, 16, 17, 18], which serves as a Monte Carlo event generator capable of simulating numerous collision types, including hadron-hadron, hadron-nucleus, and nucleus-nucleus collisions. When simulating nucleus-nucleus collisions, it relies on the binary approximation method, decomposing such collisions into individual binary nucleon-nucleon

interactions. To characterize the colliding nuclei, the model employs WoodsâĂŞSaxon distributions for their radial density profiles, while multiple scatterings of the incoming nucleons are treated through the EIKONAL formalism [8]. Particle production resulting from these collisions is in general viewed in two components, the hard and the soft component. The hard component involves processes with momentum transfers exceeding a cutoff value p_0 and is computed using perturbative QCD along with the parton distribution functions of the nucleus. This leads to the production of high-energy minijet partons, which are processed using the PYTHIA [19]. The soft component, conversely, deals with non-perturbative processes with momentum transfers below p_0 and is modelled by the formation of strings. These excited strings decay independently according to the Lund fragmentation model [20, 21].

The String Melting mode of the AMPT model includes a mechanism where all excited strings, except for those representing projectile and target nucleons, that do not interact, are converted into partons based on the flavor and spin structures of their valence quarks. Specifically, mesons are transformed into a quark and an antiquark, while baryons are first converted into a quark and a diquark according to SU(6) quark model relations, with the diquark subsequently decomposed into two quarks. The two-body decomposition is assumed to be isotropic in the rest frame of the parent hadron or diquark, and the resulting partons do not scatter until after a formation time $t_f = \frac{E_H}{m_{T,H}^2}$, where E_H and $m_{T,H}$ denote the energy and transverse mass of the parent hadron. Similar to the minijet partons in the default AMPT, the initial positions of partons from melted strings are determined from the positions of their parent hadrons using straight-line trajectories [8]. The formation time for partons refers to the time needed for their production from strong color fields. For convenience, hadrons are introduced prior to the string-melting stage in the model; by assigning their formation time as a function of the parent hadronâĂŹs momentum, it is ensured that the resulting partons share a common formation time. This choice benefits the AMPT model with string melting, as it aligns with HIJING results in the absence of partonic and hadronic interactions. These partons would combine with closest partners at the same freeze-out time, sometimes recombining in such a way to form the original hadron.

5.2.2 ZPC parton evolution

Following a nucleus-nucleus collision, partons emerge as independent entities and serve as initial condition for the parton cascade. The interactions among these partons are governed by the equations of motion for their Wigner distribution function, which semi-classically represents their density distributions in phase space. The parton cascades are developed using the Zhang's Parton Cascade (ZPC) model [22]. This model employs the elastic parton cascade approach to solve the Boltzmann equations for partons. In this cascade model, parton-parton scattering takes place when their closest approach distance falls below π/σ, where σ represents the parton-parton scattering cross-section. The scattering angle is determined by the differential cross-section of the partons. The simplified relationship between the screening mass (μ) and the total parton elastic scattering cross-section ($\sigma_{\rm p}$) which is used in the ZPC, is [8]

$$\sigma_p \approx \frac{9\pi\alpha_s^2}{2\mu^2} \tag{5.1}$$

Here, α_s refers to the strong coupling constant, and μ is the effective screening mass, whose value is determined by the temperature and density of the partons generated in phase space. To establish the initial phase space distribution, the formation time for each parton is determined based on a Lorentzian distribution with a half-width of $t_{\rm f} = \left(\frac{E}{m_{\rm T}^2}\right)$ [8]. The coordinates of the partons are determined through straight-line propagation from the position of parent nucleon. Throughout the formation period, partons are perceived as constituents of the coherent cloud enveloping their parents, thereby avoiding any rescatterings.

5.2.3 Hadronization

Two distinct hadronization mechanisms based on the initial conditions are used in the AMPT model. In the default AMPT model [10, 12, 23], once the minijet partons cease interacting and stop scattering with other partons, they recombine with their parent strings to form excited strings. These excited strings then undergo hadronization through the Lund string fragmentation formalism [21, 24]. In this model, as implemented in the JETSET/PYTHIA routine [19], strings fragment into quark-antiquark pairs with a Gaussian

distribution in transverse momentum. A suppression factor of 0.30 is applied for the production of strange quark-antiquark pairs compared to light quark-antiquark pairs. Hadrons are then formed from these quarks and antiquarks using a symmetric fragmentation function [21, 24]. Within this framework, the longitudinal momentum fraction of hadrons is determined by the Lund symmetric fragmentation function, whereas their transverse momentum arises from the intrinsic motion of the constituent quarks. At SPS and RHIC energies, the default mode of the AMPT model shows good agreement with experimental data for particle distributions and transverse momentum spectra. It considerably underestimates the elliptic flow (v_2) measured at RHIC [25]. However, In the string-melting mode of AMPT, once the partons stop interacting, hadronization is described using a straightforward quark coalescence mechanism. This process combines the closest parton pairs to produce mesons, and the nearest triplets of quarks (or antiquarks) to produce baryons (or antibaryons). The string-melting version of the AMPT model effectively reproduces the large elliptic flow observed in Au–Au collisions at RHIC energies, even with a relatively small parton cross-section [21]. As partons freeze out dynamically at different times during the parton cascade, hadron formation from their coalescence also occurs at different times, resulting in a phase where partons and hadrons coexist during hadronization.

5.2.4 Hardron cascade

The hadron cascade in the AMPT model is done using A Relativistic Transport (ART) model [26, 27], which is proven to be a highly effective transport model for heavy-ion collisions at the AGS energies. It includes elastic as well as inelastic processes among baryon-baryon, baryon-meson, and meson-meson interactions. The model explicitly includes isospin degrees of freedom for the majority of particle species and their interactions, making it well suited for investigating isospin effects in heavy-ion collisions [28].

5.3 The AMPT event samples

from the string-melting mode of the AMPT model are generated for Xe–Xe collisions at $\sqrt{s_{\rm NN}} = 5.44$ TeV. The AMPT model (version *Ampt-v1.26t9b-v2.26t9b*) with its default settings has been used. An input file "ampt.input" in the AMPT code includes all the parameters that can be modified to generate events with varying characteristics. For Lund string fragmentation, the parameters are are chosen as $a = 0.55$ and $b = 0.15$ GeV^2, while the parton cross-section is calculated using a QCD coupling constant $\alpha_s = 0.33$ together with a gluon screening mass of $\mu = 2.265$ fm in the QGP. Radiations from different states are disabled in HIJING. Radiations from different states are turned off in HIJING. A total of about 500K minimum bias events are generated. The analysis is performed on around 300K events with impact parameter $b \leq 3.5 fm$ corresponding to the most central events.

The pseudorapidity density distributions of the generated charged particles in the pseu-

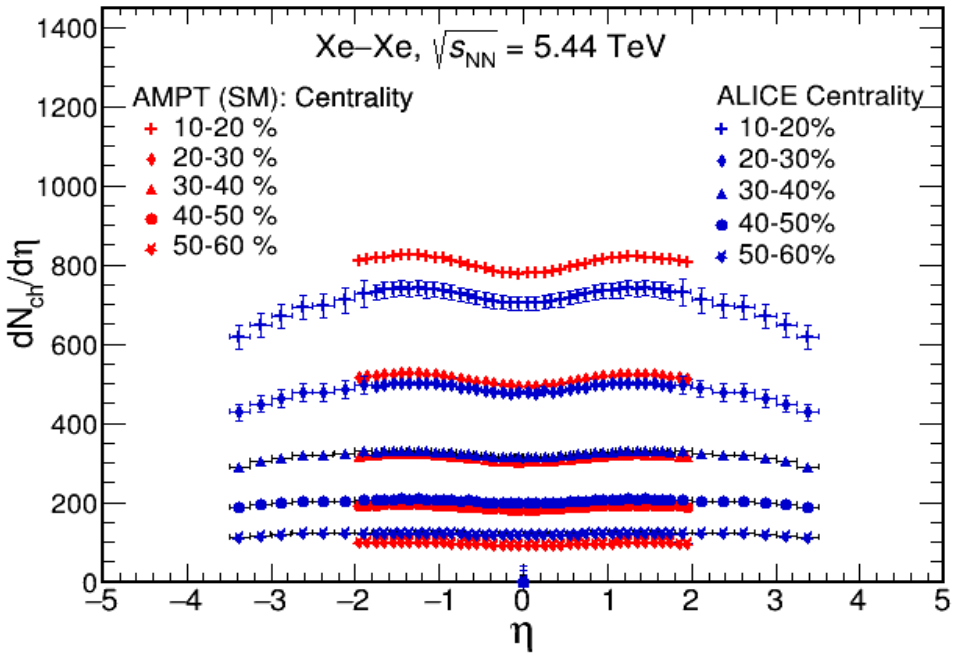

Figure 5.2: Pseudorapidity density distributions of charged particles generated using the SM AMPT at different centrality ranges compared with that of the ALICE data [29].

dorapidity interval $-2 \leq \eta \leq 2$, from events with different collision centrality viz., 10%-20%, 20% - 30%, 30% - 40%, 40% - 50% and 50% - 60% are compared with that from the ALICE [29], (Fig. 5.2). The centrality percentile value for this system are taken from

Ref. [30]. The distributions from SM AMPT event samples across different centrality ranges show consistency with that of the ALICE data. For the sample of events generated

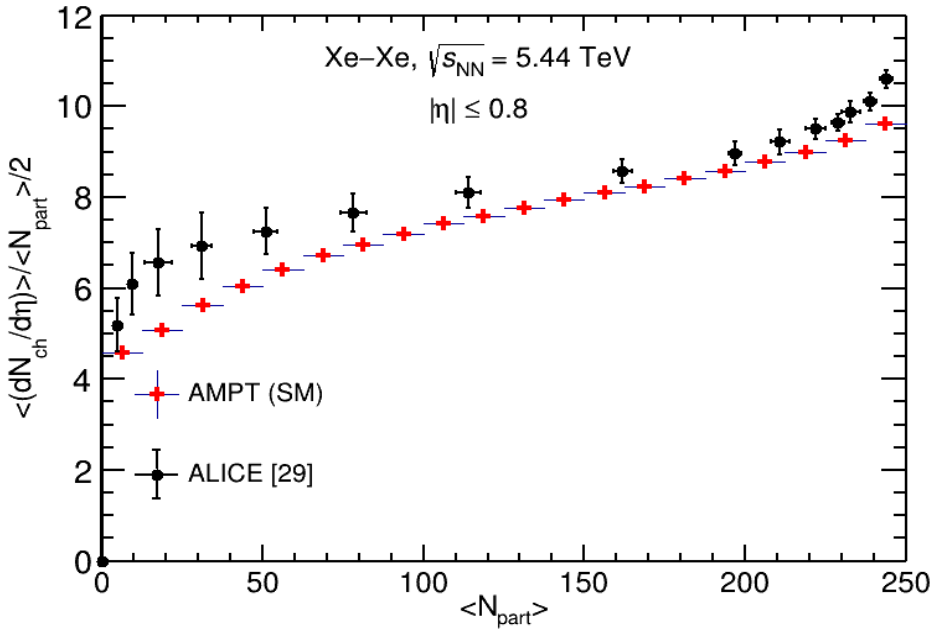

Figure 5.3: Normalized charged-particle density distribution as a function of number of participants from AMPT (SM) events. Data points from ALICE [29] are also shown for comparison.

for studying intermittency, the charged particle density per participant pair as a function of number of participants is shown in Fig. 5.3. Data points from ALICE [29] are also shown. The charged particle density per participant pair from the AMPT increases with the average number of participants in the collision $\left(\langle N_{\text{part}} \rangle\right)$, following a trend that is also observed in the experimental data, however with small quantitative difference at high centrality.

The central events with impact parameter $b \leq 3.5\ fm$ are analyzed to study two dimensiona intermittency and the scaling behaviours in (η, ϕ) phase space, as discussed in chapter 3. Charged particles within $|\eta| \leq 0.8$, covering the full azimuth, and having transverse momentum $p_{\text{T}} \leq 2.0$ GeV/c are considered for analysis. Fig. 5.4 shows the pseudorapidity and azimuthal angle distributions of the charged particles generated in SM AMPT central events for the p_{T} bin $0.4 \leq p_{\text{T}} \leq 0.6$ GeV/c. Similar distributions are observed in other p_{T} bins also. Observations and results from the analysis of data are given in the following sections.

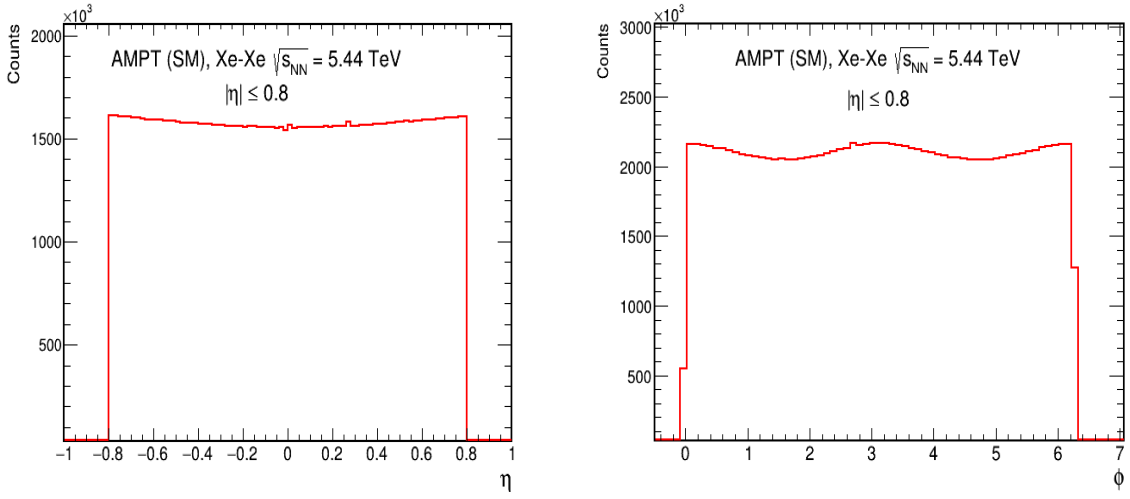

(a) (b)

Figure 5.4: Events from Xe–Xe central collisions at $\sqrt{s_{\rm NN}} = 5.44$ TeV analyzed using the string-melting (SM) AMPT model. Pseudorapidity (η) and azimuthal angle (ϕ) distributions of the generated charged particles (protons, kaons, and pions) within $|\eta| \leq 0.8$ and $0 \leq \phi \leq 2\pi$ for the $p_{\rm T}$ bin are shown.

5.4 Intermittency analysis and observations

Charged particles (protons, pions, and kaons) generated in different $p_{\rm T}$ bins of varying widths are analyzed using intermittency techniques. Scaling behaviour and scaling parameters of the normalized factorial moments along with fractal parameters are studied for $q = 2$, 3, 4 and 5 with varying phase space resolution. The narrow $p_{\rm T}$ intervals analyzed are $0.4 \leq p_{\rm T} \leq 0.6$ GeV/c and $0.6 \leq p_{\rm T} \leq 0.8$ GeV/c, while the wide $p_{\rm T}$ bins studied are $0.4 \leq p_{\rm T} \leq 1.0$ GeV/c, $0.4 \leq p_{\rm T} \leq 2.0$ GeV/c, $0.6 \leq p_{\rm T} \leq 1.0$ c and $0.6 \leq p_{\rm T} \leq 2.0$ GeV/c. Figure 5.5 displays the multiplicity distributions of charged particles in these $p_{\rm T}$ bins for the event sample within the 0–5% centrality range ($0 \leq b \leq 3.5 fm$). For the charged particles, in a $p_{\rm T}$ interval the analysis as described in section 3.1 is performed. The normalized factorial moments $F_{\rm q}(M)$ are calculated for orders $q = 2, 3, 4$, and 5. The number of bins (M) in the phase space is varied, with its maximum value depending on the particle multiplicity within the $\Delta p_{\rm T}$ interval. In this work, the number of bins along each dimension are taken as minimum of 6 to a maximum of 105, varying in the intervals of 3. The charged particles generated in an event within the selected kinematic range are mapped onto the phase space partitioned in M^2 bins. This makes the particles get distributed across the bins depending

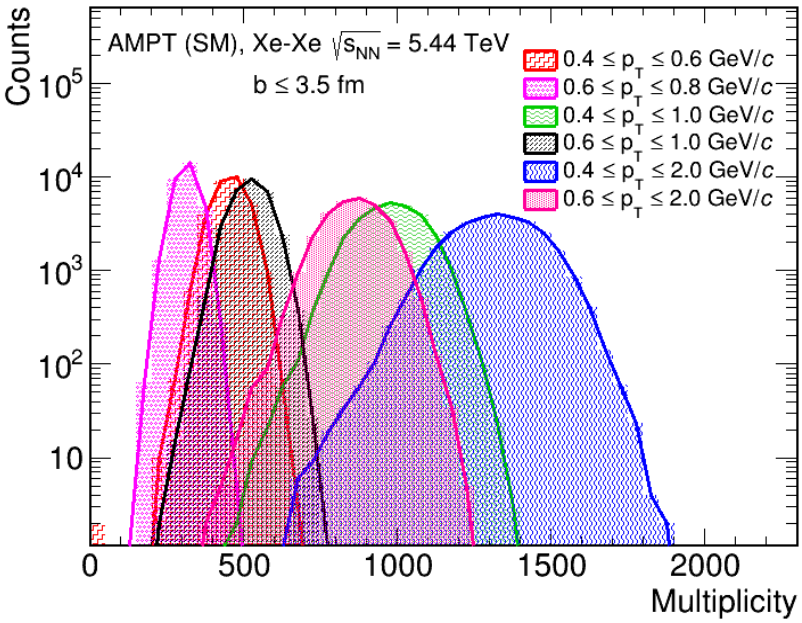

Figure 5.5: Multiplicity distribution plot of charged particles in Xe–Xe collisions at $\sqrt{s_{\rm NN}} = 5.44$ TeV with the SM AMPT model across different $p_{\rm T}$ intervals.

on the η and ϕ values of the tracks.

5.4.1 Average bin content

As the number of bins in the partitioned phase space increases, the number of particles per bin decreases. A quantity called the average bin content ($< n_{\rm i} >$) is obtained by averaging total bin content of all the bins by the total number of bins in the phase-space. Fig. 5.6 shows log-log plot of average bin multiplicity $< n_{\rm i} >$ as function of number of bins M^2 for the $p_{\rm T}$ bins studied. For all cases, it is observed that as M increase, $< n_{\rm i} >$ decreases. Also the average bin content is lower in the narrow transverse momentum intervals compared to the wide onces, demonstrating that most of the bins in the phase space become nearly empty at higher M. This observation is trival but significant as first step to proceed ahead with analysis and to understand the behaviours of NFMs.

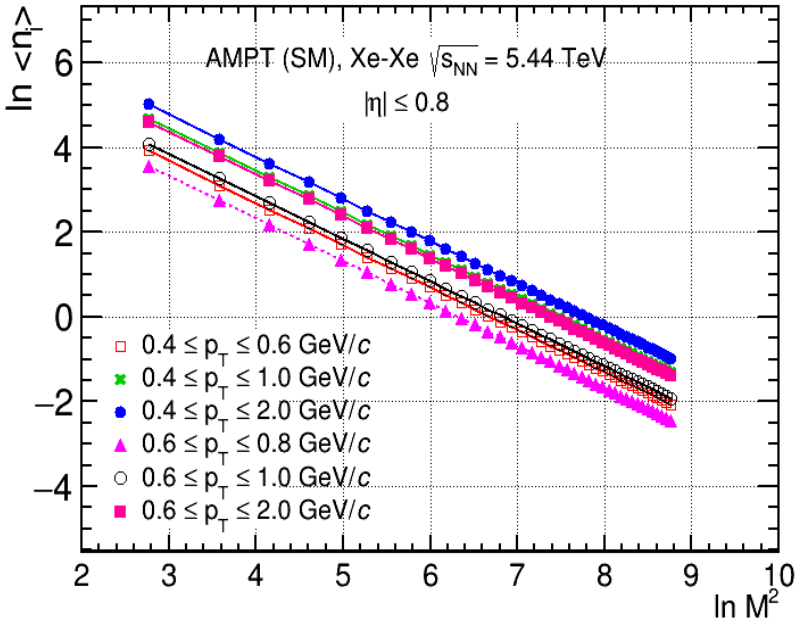

Figure 5.6: log-log plot of the average charged particle bin multiplicity for the p_T bins in the SM AMPT model as a function of number of bins.

5.4.2 *M-scaling*

The normalized factorial moments $F_q(M)$ are computed for orders $q = 2, 3, 4$, and 5. The scaling behaviour of $F_q(M)$ with the number of bins (M), known as *M-scaling*, defined in Eq.(3.9) is investigated. Fig. 5.7 shows the $\ln F_q$ vs $\ln M^2$ plots for q = 2, 3, 4, 5 for p_T bins $0.4 \leq p_T \leq 0.6$ GeV/c, $0.6 \leq p_T \leq 0.8$ GeV/c, $0.4 \leq p_T \leq 1.0$ GeV/c, $0.6 \leq p_T \leq 1.0$ GeV/c, $0.4 \leq p_T \leq 2.0$ GeV/c and $0.6 \leq p_T \leq 2.0$ GeV/c. It is observed that in case of these p_T bins $F_q(M)$ grows with increasing M upto a few values followed by saturation region at higher M. In other words absence of linear growth of $F_q(M)$ with M for the AMPT events is observed. However, $F_{q+1}(M)$ is observed to be greater than $F_q(M)$. Absence of M-scaling and hence the intermittency signal indicates local multiplicity fluctuations are not there in the charged particle generation in the SM AMPT model. Large error bars on $F_q(M)$ at higher M for $q \geq 4$ are because there are not many bins with bin content ≥ 4. As the value of M increases, the average number of tracks per bin decreases and thus the number of tracks within each bin becomes less than the order of the moment and this makes the measured factorial moment values show large statistical fluctuations. The error bars on $F_q(M)$ correspond to the statistical uncertainties estimated

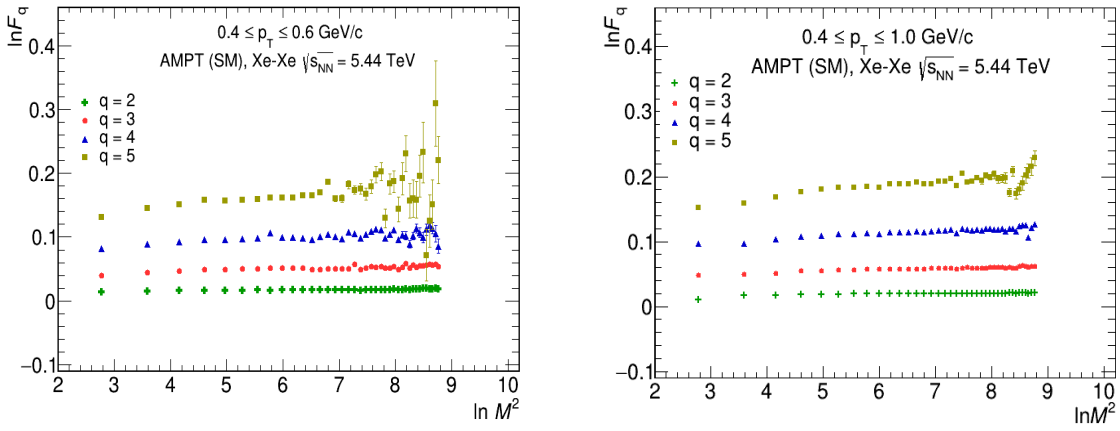

(a)

(b)

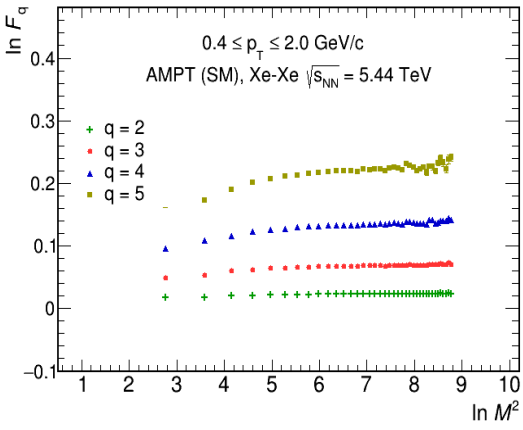

(c)

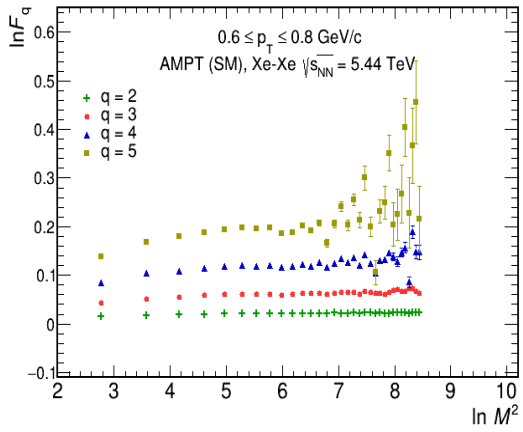

(d)

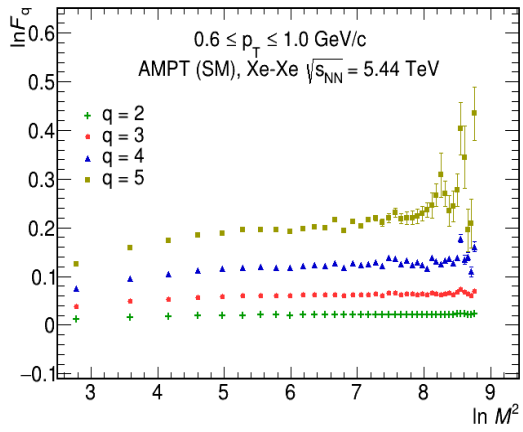

(e)

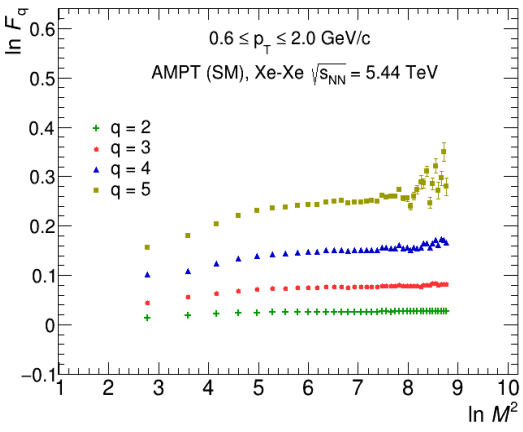

(f)

Figure 5.7: *(M-scaling)* log-log plots of $F_q(M)$, (q = 2, 3, 4 and 5) as a function of the number of cells (M^2) for the p_T bins (a) $0.4 \leq p_T \leq 0.6$ GeV/c, (b) $0.4 \leq p_T \leq 1.0$ GeV/c, (c) $0.4 \leq p_T \leq 2.0$ GeV/c, (d) $0.6 \leq p_T \leq 0.8$ GeV/c, (e) $0.6 \leq p_T \leq 1.0$ GeV/c and (f) $0.6 \leq p_T \leq 2.0$ GeV/c.

Table 5.1: Extracted values of the scaling exponent (ν) for charged particles in different p_{T} intervals.

p_{T} intervals (GeV/c)	Scaling exponent (ν)
$0.4 \leq p_{\mathrm{T}} \leq 0.6$	1.75 ± 0.07
$0.4 \leq p_{\mathrm{T}} \leq 1.0$	1.78 ± 0.30
$0.4 \leq p_{\mathrm{T}} \leq 2.0$	1.63 ± 0.25
$0.6 \leq p_{\mathrm{T}} \leq 0.8$	1.72 ± 0.20
$0.6 \leq p_{\mathrm{T}} \leq 1.0$	1.83 ± 0.09
$0.6 \leq p_{\mathrm{T}} \leq 2.0$	1.81 ± 0.06

using the sub-sampling method.

5.4.3 F-scaling and scaling exponent ν

Although the charged particles produced in Xe–Xe collisions do not show *M-scaling* behaviour, it is still important to examine the *F-scaling* as given in Eq. (3.11). In Fig. 5.8, $\ln F_{\mathrm{q}}(M)$ versus $\ln F_2(M)$ for q = 3, 4 and 5 are shown. Observations from all the p_{T} intervals studied here are shown. It is observed that $\ln F_{\mathrm{q}}(M)$ shows a weak power-law growth with $\ln F_2$ values for both narrow and wide p_{T} bins. The error bars on $F_{\mathrm{q}}(M)$ in Fig. 5.8, depicted as vertical black lines, are smaller in the wide p_{T} bins compared to the narrow p_{T} bins. Line fit is performed to extract the slopes (β_{q}) for these plots. Further the $\ln \beta_{\mathrm{q}}$ versus $\ln(q-1)$ plots are taken (as shown in Fig. 5.9) to determine the scaling exponent. The line fits performed on these plots give scaling exponent (ν), a dimensionless quantity that is independent of M and effectively describes the behaviour of the system. The values of the scaling exponent obtained for the various p_{T} bins are tabulated in Table. 5.1.

5.4.4 Dependence of ν on p_{T}

Plot showing the dependence of scaling exponent ν on the transverse momentum (p_{T}) bins and p_{T} bin width are given in the Fig. 5.10. ν value obtained from the analysis of central Pb–Pb collisions at $\sqrt{s_{\mathrm{NN}}} = 2.76$ TeV using the SM AMPT model [31] for two p_{T} bins are also shown. The scaling exponent ν for all p_{T} bins is found to have average value

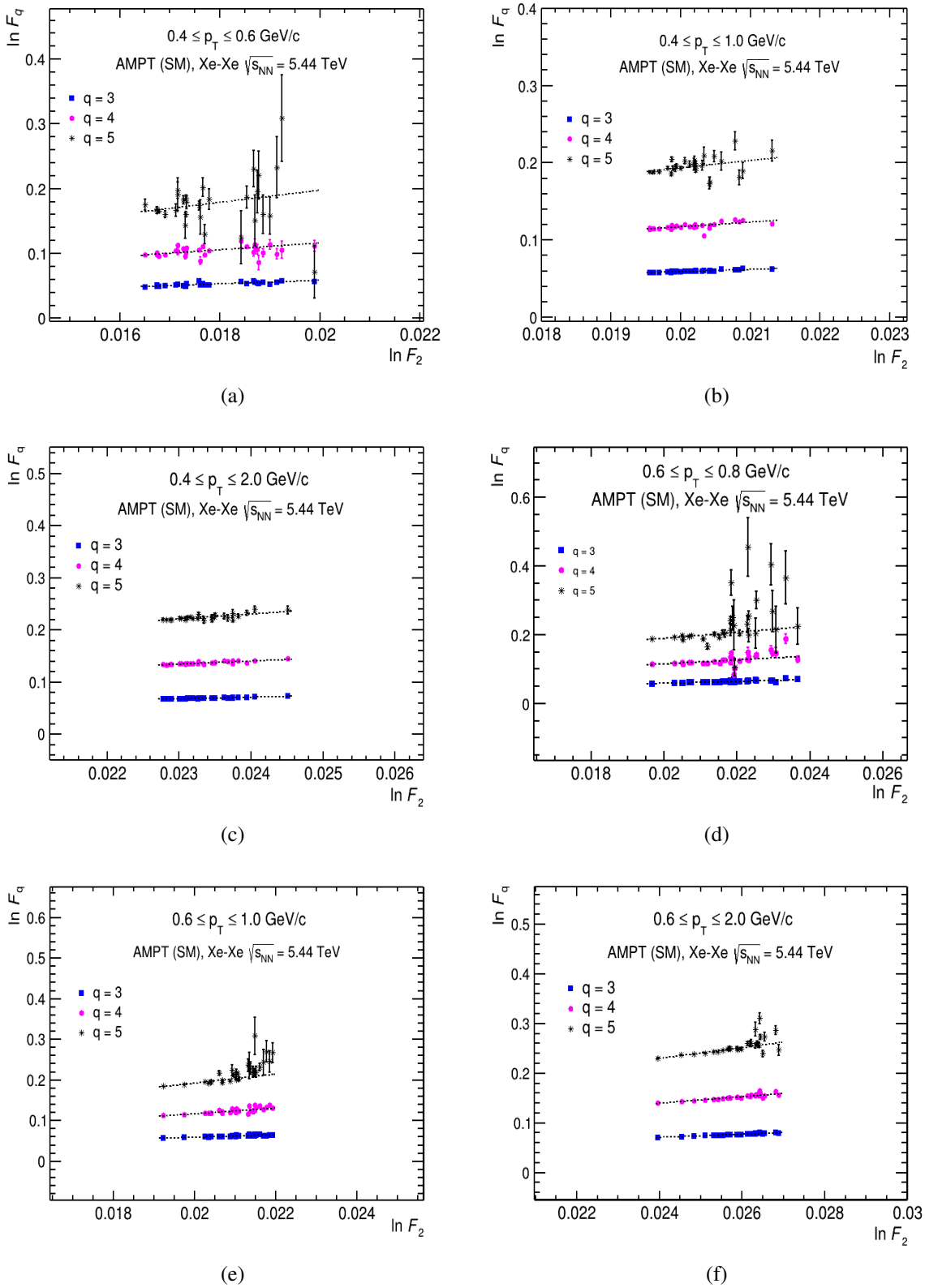

Figure 5.8: *(F-scaling)* log-log plots of (F_q), (q = 3, 4, 5) as a function of F_2 for the p_T bins (a) $0.4 \leq p_T \leq 0.6$ GeV/c, (b) $0.4 \leq p_T \leq 1.0$ GeV/c, (c) $0.4 \leq p_T \leq 2.0$ GeV/c, (d) $0.6 \leq p_T \leq 0.8$ GeV/c, (e) $0.6 \leq p_T \leq 1.0$ GeV/c and (f) $0.6 \leq p_T \leq 2.0$ GeV/c. Lines joining the data points are the straight line fits to obtain β_q (the slope).

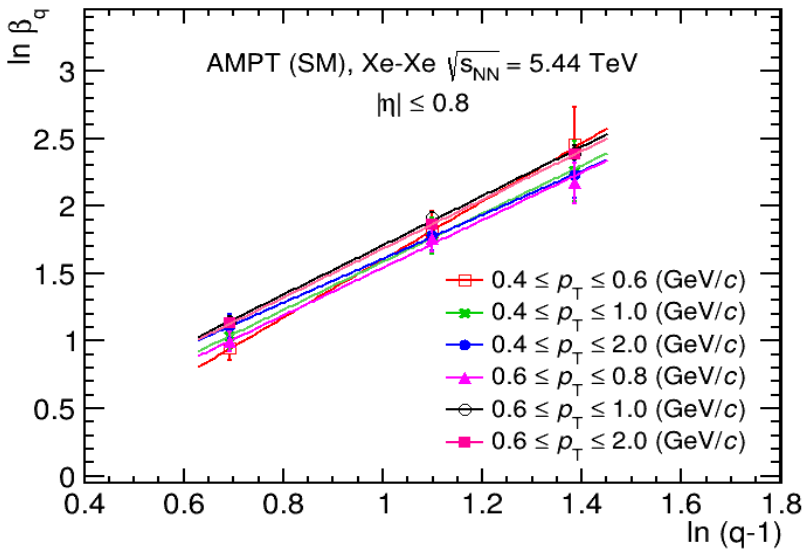

Figure 5.9: Plot for $\ln\beta_q$ vs $\ln(q-1)$ from the various p_T intervals. The lines joining the markers represent the fits used to extract the slope "ν", referred to as the scaling exponent. Error bars denote the fitting uncertainties in the β_q values.

$\approx 1.75 \pm 0.03$ which is quite close to the average value of ν for the Pb–Pb system (1.67 ± 0.12) reported in [31]. Within errors ν is independent of the p_T bin and p_T bin width in the transverse momentum region of $p_T \leq 2.0$ GeV/c. The scaling exponent from the present

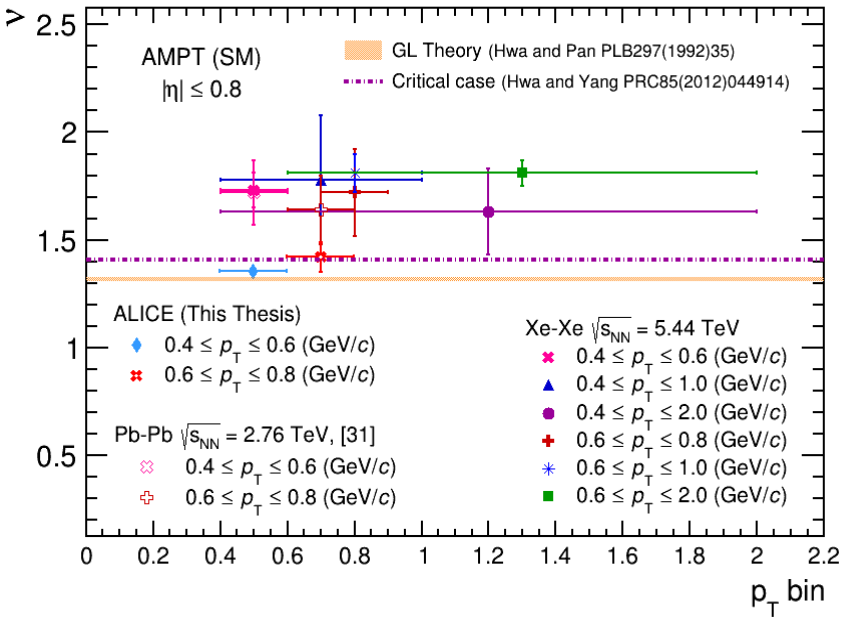

Figure 5.10: Scaling exponent (ν) as a function of p_T intervals and its comparison with the results from Pb-Pb system at $\sqrt{s_{NN}}$ = 2.76 TeV [31] for the same p_T bins. Horizontal bars on both sides of the markers are to show the p_T bins with marker at the center of the bin. Vertical error bars are the fitting errors.

analysis and that from [31] are significantly higher than the value of 1.33, an average value obtained from Ginzburg-Landau theory with formalism for the second-order phase transition. From the Successive Contraction and Randomization (SCR) model [32], where the conditions similar to the critical phenomenon are introduced, the scaling scaling exponent $\nu \approx 1.41$, a value quite different from the ones obtained in the present analysis with the SM AMPT model. Absence of second-order phase transition characteristics similar to those described by the Ginzburg-Landau theory is seen. SM AMPT model has no physics of the phase transition or critical fluctuations and results show the baseline behaviour of particle production in the heavy-ion collisions at high energy.

5.4.5 Fractal dimension D_{q}

The intermittency indices (φ_{q}) as a function of q for the charged particles generated in different transverse momentum ranges are shown in Fig. 5.11. (φ_{q}) are determined using a straight line fit performed at the high M region of the $\ln F_{\mathrm{q}}$ versus $\ln M^2$ plots (Fig. 5.7). For every p_T bin, φ_{q} values are very small and show nearly a flat behaviour with q. From the intermittency indices the fractal dimension D_{q} for q = 2, 3, 4 and 5 are obtained using Eq.(3.15), with $D_{\mathrm{T}} = 2$ for the two dimensional phase space. Fig. 5.12 shows the D_{q} versus q plot for all the p_{T} bins. It is observed that for all the p_{T} bins D_{q} shows no dependence on q for the SM AMPT model. The independence of D_{q} on q for the SM AMPT indicates the *monofractal* nature of particle generation in the model. For two different transverse momentum intervals same plots from ALICE data for same system and energy are also shown which clearly shows a dependence of D_{q} on q and thus a multifractal behaviour.

5.4.6 Coefficient λ_{q}

The coefficient λ_{q} is calculated for q = 2, 3, 4 and 5 as defined in Eq.(3.16). Fig. 5.13 shows λ_{q} versus the order of moments (q) plot. It is observed that for all the p_{T} bins, there is no minimum value of λ_{q} for any q within the range of 2 to 5. λ_{q}'s variation wth q from ALICE data (this thesis) is shown. Qualitatively data and model have similar trends with no minima indicating single phase system formation in both.

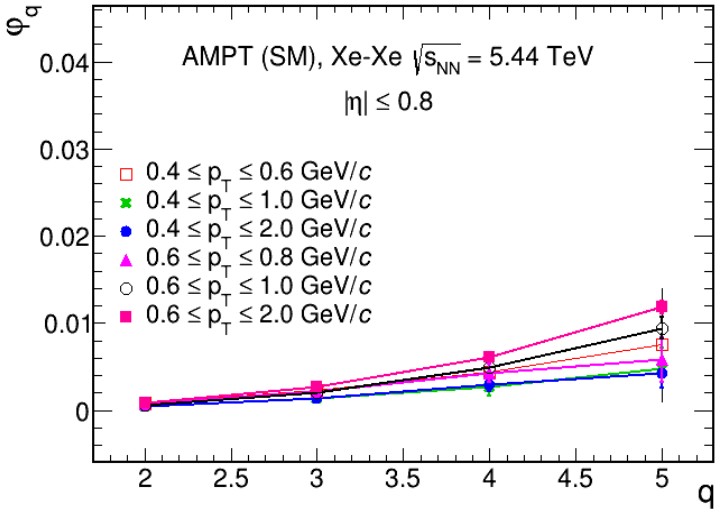

Figure 5.11: Intermittency indices (φ_q) for q = 2, 3, 4 and 5 as a function of q in various p_T bins is shown. Lines joining the data points are to guide the eye.

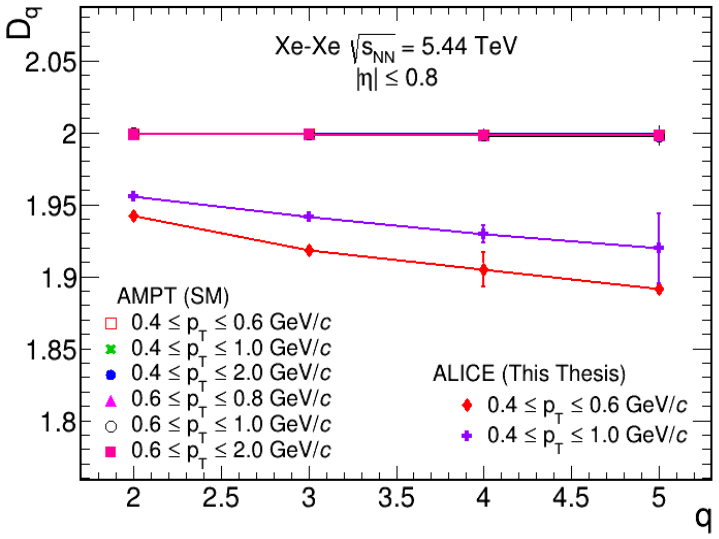

Figure 5.12: D_q as function of q from various p_T intervals are shown. Lines joining the data markers are to guide the eye.

Here intermittency analysis performed for the event samples from the SM AMPT model are presented. The charged particles produced in the Xe–Xe collisions with center of mass energy per nucleon pair of 5.44 TeV are studied. It is observed that there is no strong power-law behaviour of NFM for all M as $M \to \infty$. The NFM show a weak power-law growth with M for very large bins (for all q = 2, 3, 4, 5) but as M goes greater than 16 there is saturation of $F_q(M)$ with M. *F-scaling* is observed with big statistical fluctuations in $F_q(M)$ at high

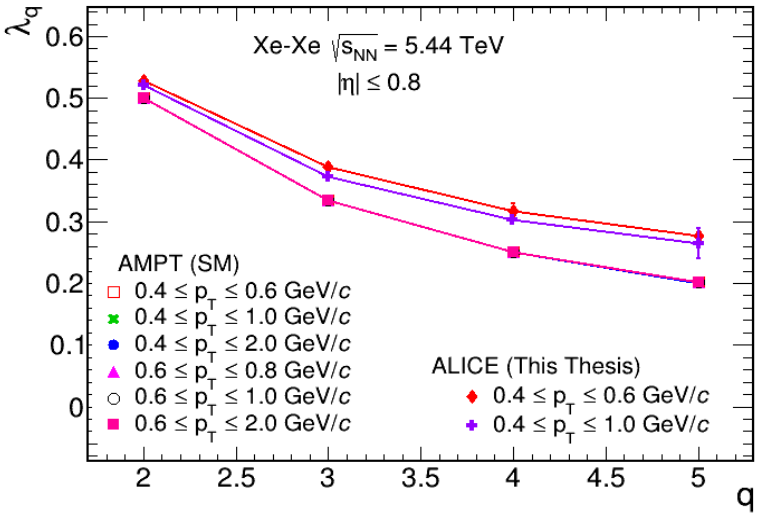

Figure 5.13: λ_q as a function of order of moments (q) for the SM AMPT events for different p_T bins. Experimental value of λ_q from ALICE (This Thesis) are also shown.

values of M in small p_T bins. The scaling exponent (ν) for the symmetric Pb–Pb collision system and asymmetric Xe–Xe collision system has similar values in the soft p_T regions showing no dynamical difference in the behaviour of these two different systems. The SM AMPT shows monofractal nature of multiplicity fluctuations in particles generated from bin-to-bin. The SM AMPT model does not explain the observations from experimental data, with exception to λ_q which is present in chapter 4. Model may be updated accordingly so as to reproduce what is observed in the experimental work. However, the analysis presented suggests that the observables under study are suitable measures with potential to give significant information about the dynamics of multiparticle production.

BIBLIOGRAPHY

[1] G. Torrieri, S. Steinke, W. Broniowski, W. Florkowski, J. Letessier and J. Rafelski, "SHARE: Statistical hadronization with resonances," Comput. Phys. Commun. **167**, (2005) 229-251, [arXiv:nucl-th/0404083 [nucl-th]].

[2] A. Kisiel, T. Taluc, W. Broniowski, W. Florkowski, "THERMINATOR: Thermal heavy-ion generator." Comput. Phys. Commun. **174** (2006) 669.

[3] T. Hirano and K. Tsuda "Collective flow and two-pion correlations from a relativistic hydrodynamic model with early chemical freeze-out," Phys. Rev. C **66** (2002) 054905.

[4] B. A. Li, C. M. Ko,"Formation of superdense hadronic matter in high energy heavy-ion collisions," Phys. Rev. C **52** (1995) 2037.

[5] H. Sorge, H. Stocker, W. Greiner,"Flavor Flow in Ultrarelativistic Nucleus-Nucleus Collisions: The Rqmd Approach," Nucl. Phys. A **498** (1989) 567.

[6] S. A. Bass, M. Belkacem, M. Bleicher, M. Brandstetter, L. Bravina, C. Ernst, L. Gerland, M. Hofmann, S. Hofmann and J. Konopka, *et al.* "Microscopic models for ultrarelativistic heavy ion collisions," Prog. Part. Nucl. Phys. **41**, (1998) 255-369. [arXiv:nucl-th/9803035 [nucl-th]].

[7] B. Zhang, C. M. Ko, B. A. Li and Z. w. Lin, "A multiphase transport model for nuclear collisions at RHIC," Phys. Rev. C **61**, (2000) 067901, [arXiv:nucl-th/9907017 [nucl-th]].

[8] Z. W. Lin, C. M. Ko, B. A. Li, B. Zhang and S. Pal, "A Multi-phase transport model for relativistic heavy ion collisions," Phys. Rev. C **72**, (2005) 064901, [arXiv:nucl-th/0411110 [nucl-th]].

[9] B. Zhang, C. M. Ko, B. A. Li, Z. W. Lin and B. H. Sa,"A Multi-Phase Transport model for nuclear collisions at RHIC," Phys. Rev. C **62**, (2000) 054905.

[10] Z. W. Lin, S. Pal, C. M. Ko, B. A. Li and B. Zhang,"Charged particle rapidity distributions at relativistic energies," Phys. Rev. C **63**, (2001) 011902.

[11] Z. W. Lin and C. M. Ko, "Partonic effects on the elliptic flow at relativistic heavy-ion collisions," Phys. Rev. C **65**, (2002) 034904.

[12] B. Zhang, C. M. Ko, B. A. Li, Z. W. Lin and S. Pal, "Multiphase transport model for heavy-ion collisions at RHIC," Phys. Rev. C **65**, (2002) 054909.

[13] Z. W. Lin, C. M. Ko and S. Pal,"Partonic Effects on Pion Interferometry at the Relativistic Heavy-Ion Collider," Phys. Rev. Lett. **89**, (2002) 152301.

[14] Z. W. Lin and C. M. Ko, "Kaon interferometry at RHIC from the AMPT model," J. Phys. G **30**, (2004) S263.

[15] X. N. Wang, "Role of multiple minijets in high-energy hadronic reactions," Phys. Rev. D **43**, (1991) 104.

[16] X. N. Wang and M. Gyulassy, "HIJING: A Monte Carlo Model for Multiple Jet Production in pp, pA, and AA Collisions," Phys. Rev. D **44**, (1991) 3501.

[17] X. N. Wang and M. Gyulassy, "Systematic Study of Particle Production in p+p (pÌĎ) Collisions via the HIJING Model," Phys. Rev. D **45**, (1992) 844.

[18] M. Gyulassy and X. N. Wang, "HIJING 1.0: A Monte Carlo Program for Parton and Particle Production in High Energy Hadronic and Nuclear Collisions," Comput. Phys. Commun. **83**, (1994) 307.

[19] T. Sjostrand, " High-energy-physics event generation with PYTHIA 5.7 and JETSET 7.4," Comput. Phys. Commun. **82**, (1994) 74.

[20] B. Andersson, G. Gustafson and B. Soderberg, "A general model for jet fragmentation," Z. Phys. C **20**, (1983) 317.

[21] B. Andersson, G. Gustafson, G. Ingelman and T. Sjostrand, "Parton fragmentation and string dynamics," Phys. Rept. **97**, (1983) 31-145.

[22] B. Zhang, "A parton cascade for ultrarelativistic heavy-ion collisions," Comput. Phys. Commun. **109**, (1998) 193.

[23] C. M. Ko, L. W. Chen and B. W. Zhang, "Heavy-Ion Collisions at LHC in a Multi-phase Transport Mode," Braz. J. Phys. **37** 3A, September (2007) 969.

[24] B. Andersson, G. Gustafson and B. Soderberg, "A General Model for Jet Fragmentation," Z. Phys. C **20**, (1983) 319.

[25] Z. W. Lin, L. Zheng, "Further developments of a multi-phase transport model for relativistic nuclear collisions". Nucl Sci Tech 32, (2021) 113.

[26] B. A. Li and C. M. Ko, "Formation of superdense hadronic matter in high energy heavy-ion collisions," Phys. Rev. C **52**, (1995) 2037.

[27] B. Li, A. T. Sustich, B. Zhang and C. M. Ko, "studies of superdense hadronic matter in a relativistic transport model," Int. J. Mod. Phys. E **10**, (2001) 267.

[28] B. A. Li, C. M. Ko and W. Bauer, "Isospin physics in heavy ion collisions at intermediate-energies," Int. J. Mod. Phys. E **7**, (1998) 147-230, [arXiv:nucl-th/9707014 [nucl-th]].

[29] S. Acharya, et al., (ALICE Collaboration), “Centrality and pseudorapidity dependence of the charged-particle multiplicity density in Xe-Xe collisions at = 5.44 TeV,” Phys. Lett. B. **790**, (2019) 35.

[30] C. Loizides, J. Kamin, D. d’Enterria, “Improved Monte Carlo Glauber predictions at present and future nuclear colliders,” Phys. Rev. **C97**, (2018) 054910.

[31] R. Sharma and R. Gupta, "Scaling Properties of Multiplicity Fluctuations in the AMPT Model," Adv. High. Energy. Phys. (2018) 6283801.

[32] R. C. Hwa and C. B. Yang, “Observable Properties of Quark-Hadron Phase Transition at the Large Hadron Collider,” Acta Phys. Polon. B **48**, (2017) 23, [arXiv:1601.04671 [nucl-th]].

CHAPTER 6

SUMMARY AND CONCLUSIONS

In ultra-relativistic heavy-ion collisions, a novel state of strongly interacting matter known as the Quark-Gluon Plasma (QGP) is created under conditions of extremely high energy density. The ALICE experiment at LHC, CERN is specifically designed to study the properties and evolution of this deconfined state of matter. Following its creation, the QGP expands and cools rapidly, eventually transforming back into normal hadronic matter in a process called hadronization. This transition represents a major phase change in the system. Lattice Quantum Chromodynamics (QCD) calculations suggest that the transition boundary between hadronic matter and QGP may include a critical point fluctuations in quantities such as energy density and temperature etc., become very large due to the divergence of the correlation length. This leads to long-range correlations that get reflected as large event-by-event fluctuations in measurable quantities. In statistical systems, this results in the formation of clusters of all sizes, lacking a characteristic scale. In heavy-ion collisions, enhanced multiplicity fluctuations arising from the initial state can evolve into

measurable collective behaviour in the final state. Studying the scaling behaviour of multiplicity fluctuations, therefore, offers critical insights into the nature of the QCD phase transition and the potential existence of a critical point. Collisions at ultra-relativistic energies involving heavy nuclei, such as lead (Pb–Pb) and xenon (Xe–Xe), produce a large number of particles in a single event. This high particle yield makes it possible to analyze event-by-event fluctuations in observables like mean transverse momentum, particle multiplicity particle ratios, etc.

In this work, analysis of data recorded by the ALICE experiment during Run 2 of the LHC's operation to look for local multiplicity fluctuations in charged particles produced in Xe–Xe collisions at $\sqrt{s_{\mathrm{NN}}} = 5.44$ TeV is presented. A two-dimensional intermittency analysis in the angular (η, ϕ) phase space was performed on the charged particles produced in Xe–Xe collisions to study number density fluctuations. Intermittency, characterized by the scaling behaviour of normalized factorial moments ($F_{\mathrm{q}}(M)$), is a powerful technique for identifying non-statistical fluctuations and signatures of critical dynamics in the strongly interacting matter. The analysis was carried out in the midrapidity region ($|\eta| \leq 0.8$) over full azimuthal range ($0 \leq \phi \leq 2\pi$) in various transverse momentum intervals with $p_{\mathrm{T}} \leq 2.0$ GeV/c. Two scaling behaviours of $F_{\mathrm{q}}(M)$ are studied; first the dependence of $F_{\mathrm{q}}(M)$ on the number of bins in the phase space which defines the binning resolution and second the dependence of $F_{\mathrm{q}}(M)$ for $q > 2$ on the $F_2(M)$. In general these scaling behaviours are termed as M-scaling and F-scaling respectively.

The ALICE data analyzed here is observed to show both scaling behaviours. $F_{\mathrm{q}}(M)$ moments for q = 2 to 5 show power-law growth with number of bins (M^2) in log-log plots, indicating the presence of intermittency (non-statistical multiplicity fluctuations) and hence the self-similar nature of the underlying particle production dynamics. However, the HIJING simulations of Xe–Xe collisions at LHC energies, passed through ALICE detector geometry and the events from the String Melting mode of AMPT fails to reproduce this scaling behaviour. Both these Monte Carlo's underestimate the data which reveals that the particle production mechanisms and long-range correlations observed in the experimental data are absent in these model. This emphasizes the need for incorporating the changes in

these models, so as to reproduce the results obtained from experimental data analysis.

The *F-scaling* behaviour, which reveals a linear relationship between $F_{\mathrm{q}}(M)$ and $F_2(M)$ is also observed in the experimental data. A strict linear behaviour of $\ln F_{\mathrm{q}}(M)$ (q > 2) with $\ln F_2(M)$ is seen for all M values. However, a weak F-scaling is observed in case of HIJING and the SM AMPT model. The scaling exponents (ν) are obtained which is a dimensionless quantity that characterizes the critical nature of the system. The average value of ν for the central (0 – 5%) ALICE data for Xe–Xe collisions is 1.41 ± 0.03, a value close to the prediction by the Successive Contraction and Randomization (SCR) model with critical fluctuations ($\nu \approx 1.41$) and a little higher than the one predicted by Ginzburg-Landau theory from the formalism for second-order phase transition ($\nu \approx 1.304$). The String Melting AMPT model fails to reproduce the strict F-scaling and gives scaling exponent value around 1.75 ± 0.03. Similar observations are made from HIJING events passed through detector geometry. Furthermore, experimental data shows that, within the systematic uncertainties, ν is independent of both p_{T}, p_{T} bin width in the soft p_{T} region and of the collision centrality.

Generalized fractal dimension D_{q} and the coefficient λ_{q}, the two fractal parameters give an insight into the self-similar structure of multiparticle systems in the heavy-ion collisions. For ALICE data, D_{q} is observed to decrease with increasing q across all p_{T} bins, which reflects the multifractal nature of the system. In contrast, the SM AMPT model shows no such dependence of D_{q}, indicating a monofractal behaviour of particle generation in the model. A decreasing trend of λ_{q} with q but no minimum up to $q = 5$ is observed for both data and model. This indicates creation of a single phase system. Data shows similar trends of D_{q} and λ_{q} behaviour as function of q across different p_{T} bins which suggest that particle production in the soft p_{T} region follows multifractal dynamics.

A comparison of results from present work with that of ALICE data results from study of charged particle intermittency in Pb–Pb collisions at $\sqrt{s_{\mathrm{NN}}} = 2.76$ TeV, is also done for same centrality classes and kinematic selection. Results from both data sets show a good power-law growth of $\ln F_{\mathrm{q}}$ with $\ln M^2$ for all q, with only a small qualitative difference at lower M values. The scaling exponent (ν) values from the Xe–Xe and Pb–Pb collisions

across different p_{T} intervals are close within uncertainties, indicating that ν is independent of the colliding system. For both systems, D_q shows a decreasing trend with increasing q, indicating the multifractal nature of the particle production process in the experimental data, in contrast to the Toy Model results which has no correlations in the particle generation. This difference demonstrates that the multifractality in the experimental results originates from dynamical correlations, which are absent in uncorrelated particle emission models.

In summary, the scaling behaviour study of the charged particles produced in Xe–Xe collisions at $\sqrt{s_{\mathrm{NN}}} = 5.44$ TeV with ALICE provides important insight into the fluctuation dynamics and multifractal nature of the strongly interacting matter created at LHC energies. The extracted scaling exponent value ($\nu \approx 1.41$) points towards the presence of dynamical critical fluctuations, consistent with theoretical expectations for systems near a QCD critical point. The comparison studies with the Monte Carlo model results highlight the limitations of the models in reproducing the observed scaling features, emphasizing the requirement to improve theoretical descriptions of hadronization and critical phenomena.

Uncertainties on the data values can be improved by increasing the statistics and applying strict track selection cuts. The event-by-event intermittency study performed in this work has potential to add on to our understanding of the underlying particle production dynamics and the critical nature of the system created in the heavy-ion collisions. To get more insights analysis can be extended further to study double moments (erraticity analysis), and to carry identified particle study.

APPENDIX A

DETECTOR EFFECT STUDY

Understanding and accounting for detector effects is essential for accurate data interpretation and analysis in experimental high-energy physics. Detectors are complex instruments that record particles produced in high-energy collisions, such as those observed at the Large Hadron Collider or other particle accelerators. However, no detector used in the experiments is perfect, and a variety of factors can distort measurements, including inefficiencies, resolution limits, noise, and miscalibration. These detector effects can introduce biases or uncertainties into the observed data, affecting particle trajectory reconstruction, energies, and momenta. Due to the random nature of particle interactions with the detector medium, not every particle that passes through the detector will generate a detectable signal. This reduces detector efficiencies, resulting in measurements that do not accurately reflect the true values of the collision. Monte Carlo (MC) simulation studies are conducted to measure these efficiencies accurately. In these simulations, particles generated by an event generator (true particles) move through a detailed model of the detector's geometry

and electronic readout system. This simulation mirrors the response of the actual detector during collisions. The reconstructed events from the Monte Carlo simulation are then compared to the true MC events, representing an ideal scenario with no detector response. By calculating the ratio of reconstructed to true MC events, the tracking efficiencies of the detector can be determined. These tracking efficiencies are then used to correct the observables, allowing a more accurate representation of the true physical values. Therefore, detector effect studies are conducted to quantify and correct for these imperfections. The procedure used for this analysis to correct the normalized factorial moments for efficiencies is discussed below.

A.0.1 Tracking Efficiency Correction

The closure test evaluates the detector effects on the generated normalized factorial moments. Any tracking inefficiencies or detector effects may modify the value of the normalized factorial moments, which may, therefore, impact how strongly the normalized factorial moments $F_{\mathrm{q}}(M)$ depend on bin/cell (M) value. Before drawing any firm conclusions, it is necessary to address track reconstruction inefficiencies that result from other detector effects.

The tracking efficiency is defined as the ratio of physical primary reconstructed tracks to the physical primary generated tracks.

$$\varepsilon = \frac{\text{No. of Reconstructed tracks}}{\text{No. of Generated tracks}} \tag{A.1}$$

The efficiency ε_{q} for the q^{th} order factorial moment of the i^{th} bin and the e_{th} event is written as

$$\varepsilon_{\mathrm{i}}^{\mathrm{q}} = \frac{f_{\mathrm{qi}}^{\mathrm{rec}}(n_{\mathrm{ie}})}{f_{\mathrm{qi}}(n_{\mathrm{ie}})}. \tag{A.2}$$

Thus the true q^{th} factorial moment f_{q} is written as

$$f_{\mathrm{qi}}(n_{\mathrm{ie}}) = \frac{f_{\mathrm{qi}}^{\mathrm{rec}}(n_{\mathrm{ie}})}{\varepsilon_{\mathrm{i}}^{\mathrm{q}}}. \tag{A.3}$$

The corrected factorial moments for an event are thus defined as

$$f_{\mathrm{q}}^{\mathrm{e}}(M) = \frac{1}{M}\sum_{i=1}^{M}\frac{f_{\mathrm{qi}}^{rec}(n_{\mathrm{ie}})}{\varepsilon_{\mathrm{i}}^{\mathrm{q}}} = \left\langle \frac{f_{\mathrm{qi}}(n_{\mathrm{ie}})}{\varepsilon_{\mathrm{i}}^{\mathrm{q}}} \right\rangle. \tag{A.4}$$

Hence, for $q = 1$, we can write the above equation as,

$$f_{1}^{\mathrm{e}}(M) = \frac{1}{M}\sum_{i=1}^{M}\frac{f_{\mathrm{qi}}^{rec}(n_{\mathrm{ie}})}{\varepsilon_{\mathrm{i}}} = \frac{1}{M}\sum_{i=1}^{M}\frac{(n_{\mathrm{ie}})}{\varepsilon_{\mathrm{i}}}. \tag{A.5}$$

As a result of Eq. A.4 and Eq. A.5, we have q^{th} order normalized Factorial moments for N events and M number of bins that have been corrected for efficiency as

$$F_{\mathrm{q}}(M) = \frac{\frac{1}{N}\sum_{e=1}^{N}\left\langle \frac{f_{\mathrm{qi}}^{rec}(n_{\mathrm{ie}})}{\varepsilon_{\mathrm{i}}^{\mathrm{q}}} \right\rangle}{\frac{1}{N}\sum_{e=1}^{N}\left(\left\langle \frac{(n_{\mathrm{ie}})}{\varepsilon_{\mathrm{i}}} \right\rangle_{\mathrm{h}}\right)^{\mathrm{q}}}. \tag{A.6}$$

Where $< \ldots >_h$ represents averaging over the total number of bins M in dimension d. The criterion for closure is that $F_{\mathrm{q}}^{\mathrm{rec}}(M) \approx F_{\mathrm{q}}^{\mathrm{gen}}(M)$. If this is not the case, then efficiency corrections, as discussed above, must be included. However, as previously indicated, for NFM with uniform efficiencies as in Fig.2.5 would result in $F_{\mathrm{q}}^{\mathrm{gen}}(M) \approx F_{\mathrm{q}}^{\mathrm{rec}}(M)$, otherwise $F_{\mathrm{q}}^{gen}(M) \approx F_{\mathrm{q}}^{\mathrm{corrected}}(M)$.

A.0.2 Statistical uncertainty calculation

The statistical uncertainties arise because of the limited number of measurements in an experiment. They show how accurate the measurement is. Statistical uncertainties for fluctuation are typically calculated using either the error propagation technique or the sub-sampling method. Both approaches are widely accepted in statistical analysis. The error propagation technique determines uncertainties by considering how measurement errors affect the final result, where as the subsampling method is a statistical technique used to estimate uncertainties or standard errors within a dataset. The process involves selecting smaller subsets called as subsamples from the original dataset and computing the desired parameter for each. For this analysis, the statistical uncertainty of the observable is calcu-

lated using a subsampling method. In the sub-sampling method, statistical uncertainties are determined by splitting the total events into N independent subsamples of equal size. Each of these subsamples is treated as an individual dataset, and the observable of interest such as a fluctuation measure is calculated for each subsample. The statistical uncertainty is then quantified by calculating the standard deviation of the observable across the N subsamples and is given as

$$\sigma_{\langle F_{\mathrm{q}} \rangle} = \frac{\sigma}{\sqrt{N}}. \tag{A.7}$$

such that,

$$\sigma = \sqrt{\frac{\sum \left((F_{\mathrm{q}})_i - \langle F_{\mathrm{q}} \rangle \right)^2}{N-1}}. \tag{A.8}$$

and

$$\langle F_{\mathrm{q}} \rangle = \frac{1}{N} \sum (F_{\mathrm{q}})_N. \tag{A.9}$$

The sub-sampling method is a widely used approach for determining statistical uncertainty, particularly in scenarios where large datasets are available. The error propagation method, explained in, has been observed to produce the same values for statistical uncertainties. One advantage of the sub-sampling method is that it makes no assumptions about the underlying distribution of the data, allowing for a non-parametric approach to evaluating uncertainty. By dividing the dataset into numerous subsamples, the method captures the range of variation present in the system, resulting in more reliable error estimates. This technique is especially effective in fields like high-energy physics, where large numbers of events are analyzed, and capturing the intrinsic fluctuations is critical to understanding the behaviour of complex systems.

APPENDIX B

SUPPLEMENTARY FIGURES

B.1 Systematic uncertainties plots

In this section, we present the M-scaling ($\ln F_q(M)$ versus $\ln M^2$), F-scaling ($\ln F_q(M)$ versus $\ln F_2(M)$), and scaling exponent ($\ln \beta_q$ versus $\ln(q-1)$)) plots corresponding to the systematic uncertainty cuts described in Section 4.3 for all the p_{T} bins discussed earlier.

B.1.1 Filter-Bit (FB) 32

B.1.1.1 Narrow Over-lapping bins

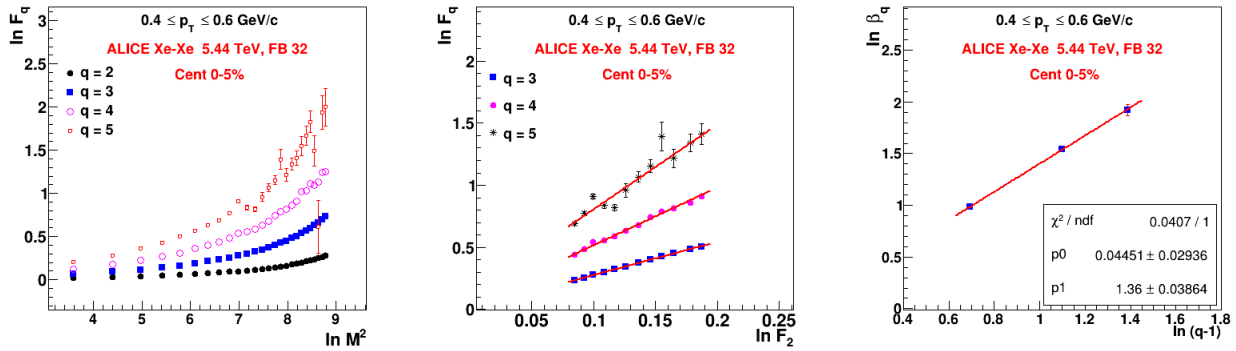

(a) $0.4 \leq p_{\mathrm{T}} \leq 0.6$ GeV/c

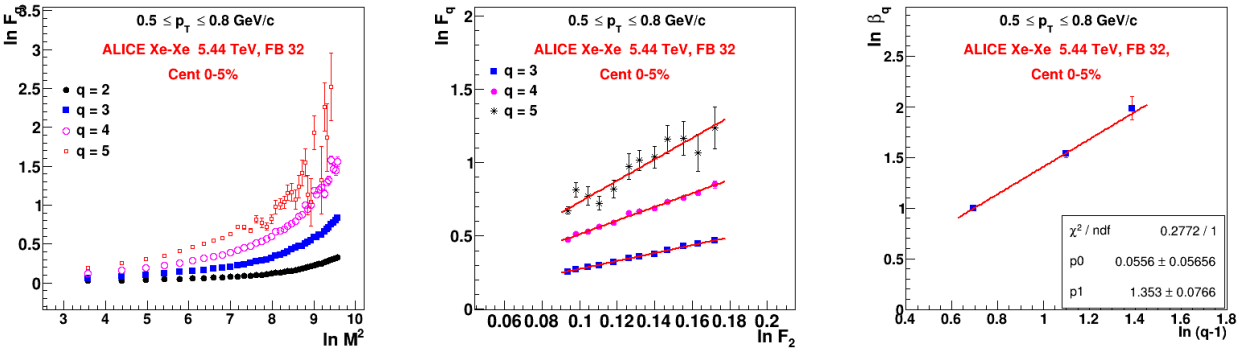

(b) $0.5 \leq p_{\mathrm{T}} \leq 0.8$ GeV/c

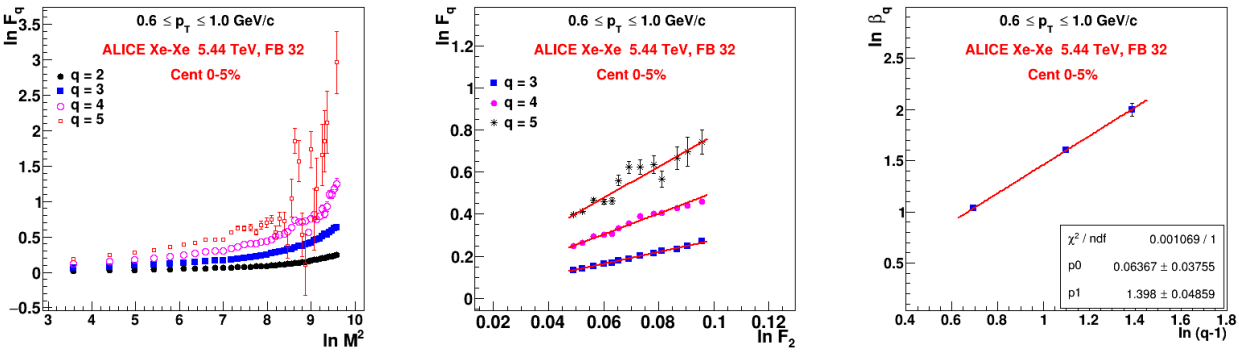

(c) $0.6 \leq p_{\mathrm{T}} \leq 1.0$ GeV/c

Figure B.1: Plots illustrating (left to right): (i) $\ln F_q(M)$ versus $\ln M^2$ (M-scaling), (ii) $\ln F_q(M)$ versus $\ln F_2(M)$ (F-scaling), and (iii) $\ln \beta_q$ versus $\ln(q-1)$ for charged particles in the narrow p_T intervals (a) $0.4 \leq p_T \leq 1.0$ GeV/c, (b) $0.4 \leq p_T \leq 1.5$ GeV/c, and (c) $0.4 \leq p_T \leq 2.0$ GeV/c, using Filter Bit 32.

B.1.1.2 Wider Over-lapping bins

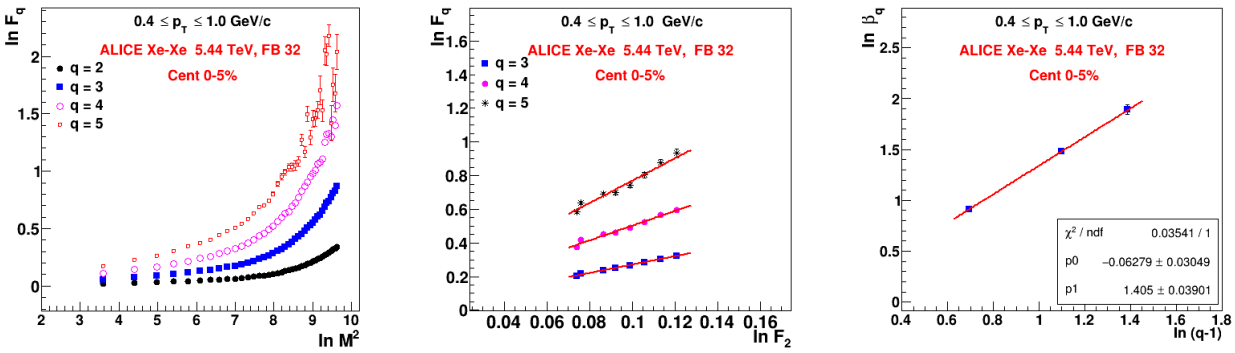

(a) $0.4 \leq p_{\mathrm{T}} \leq 1.0$ GeV/c

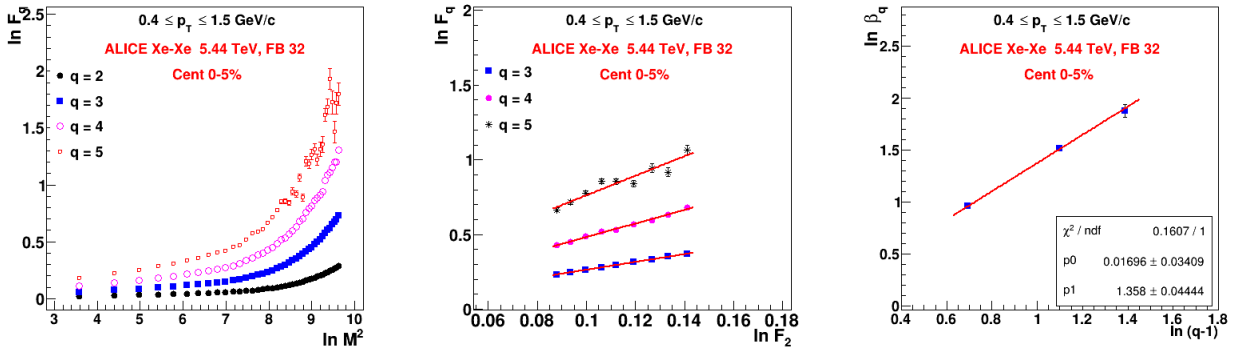

(b) $0.4 \leq p_{\mathrm{T}} \leq 1.5$ GeV/c

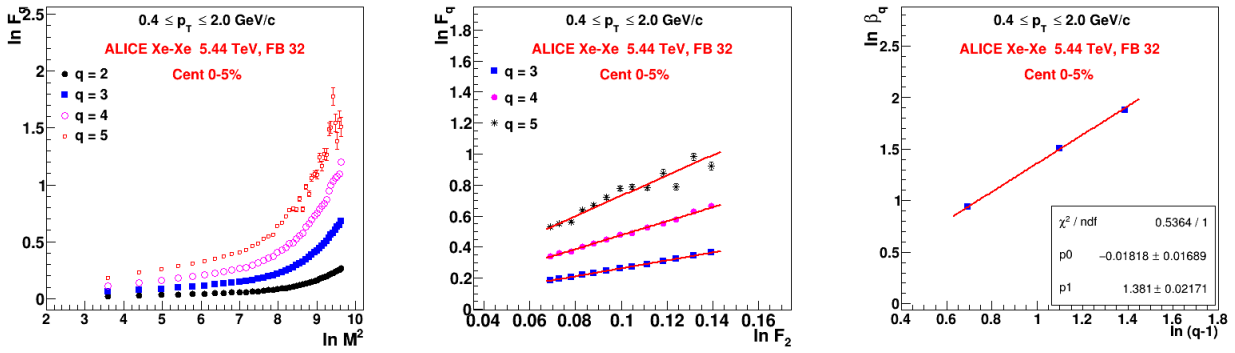

(c) $0.4 \leq p_{\mathrm{T}} \leq 2.0$ GeV/c

Figure B.2: Plots illustrating (left to right): (i) $\ln F_q(M)$ versus $\ln M^2$ (M-scaling), (ii) $\ln F_q(M)$ versus $\ln F_2(M)$ (F-scaling), and (iii) $\ln \beta_q$ versus $\ln(q-1)$ for charged particles in the wide p_T intervals (a) $0.4 \leq p_T \leq 1.0$ GeV/c, (b) $0.4 \leq p_T \leq 1.5$ GeV/c, and (c) $0.4 \leq p_T \leq 2.0$ GeV/c, using filter bit 32.

B.1.2 Centrality Estimation CL0

B.1.2.1 Narrow Over-lapping bins

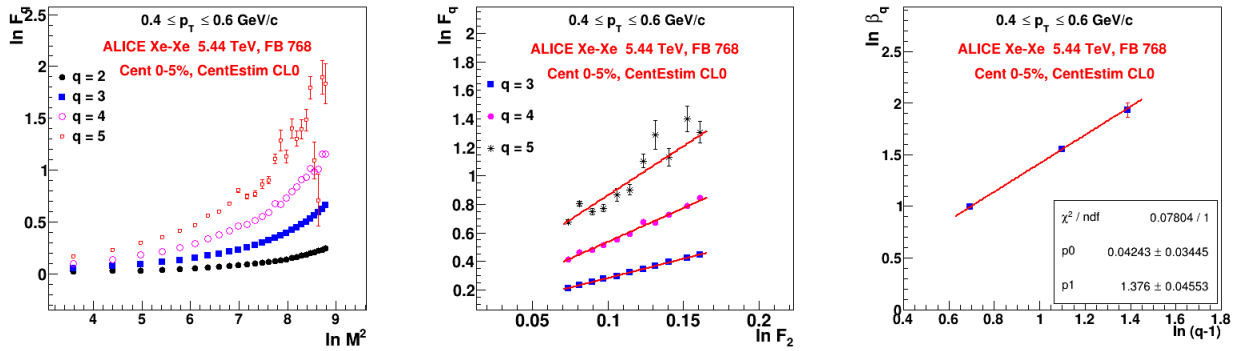

(a) $0.4 \leq p_{\mathrm{T}} \leq 0.6$ GeV/c

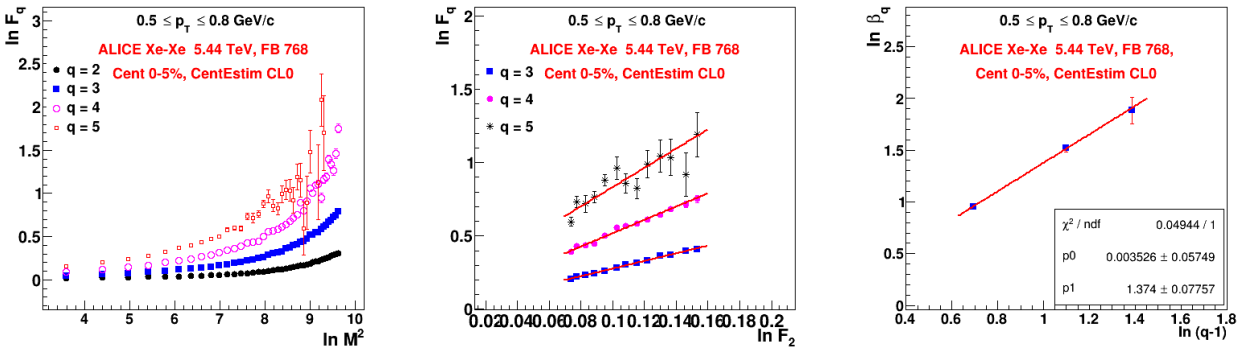

(b) $0.5 \leq p_{\mathrm{T}} \leq 0.8$ GeV/c

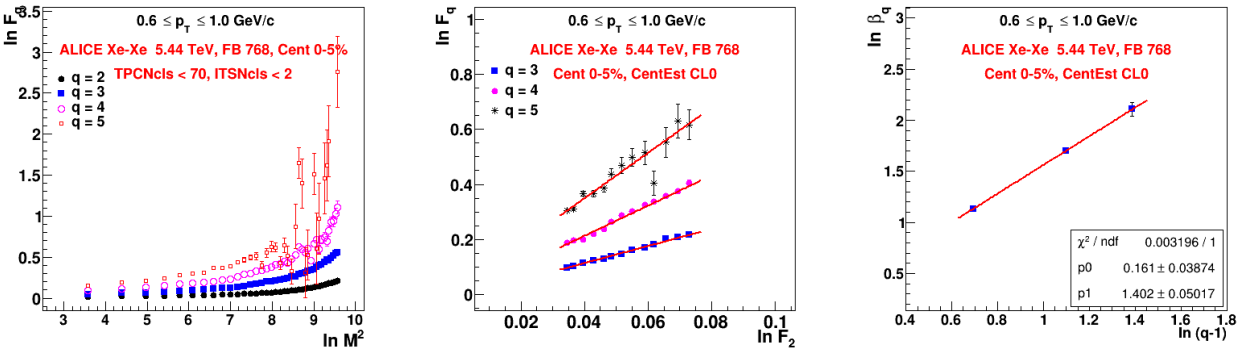

(c) $0.6 \leq p_{\mathrm{T}} \leq 1.0$ GeV/c

Figure B.3: Plots illustrating (left to right): (i) $\ln F_q(M)$ versus $\ln M^2$ (M-scaling), (ii) $\ln F_q(M)$ versus $\ln F_2(M)$ (F-scaling), and (iii) $\ln \beta_q$ versus $\ln(q-1)$ for charged particles in the narrow p_T intervals (a) $0.4 \leq p_T \leq 0.6$ GeV/c, (b) $0.5 \leq p_T \leq 0.8$ GeV/c, and (c) $0.6 \leq p_T \leq 1.0$ GeV/c, with the centrality estimator CL0.

B.1.2.2 Wider Over-lapping bins

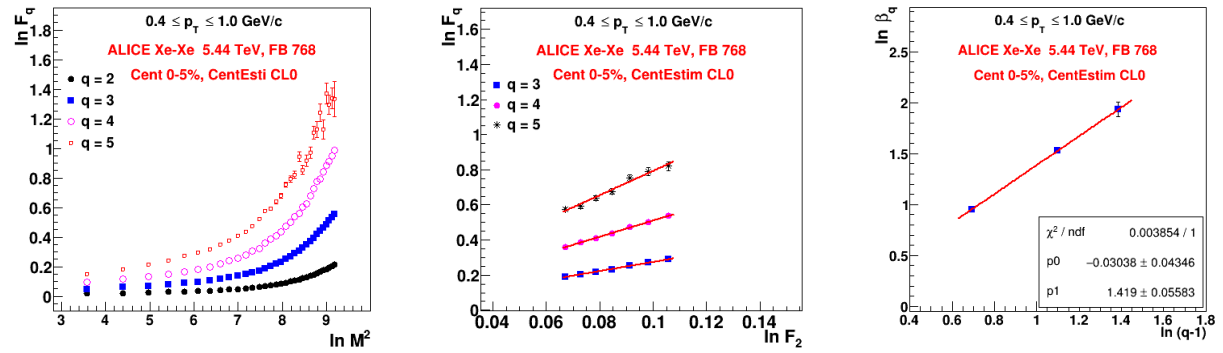

(a) $0.4 \leq p_{\mathrm{T}} \leq 1.0$ GeV/c

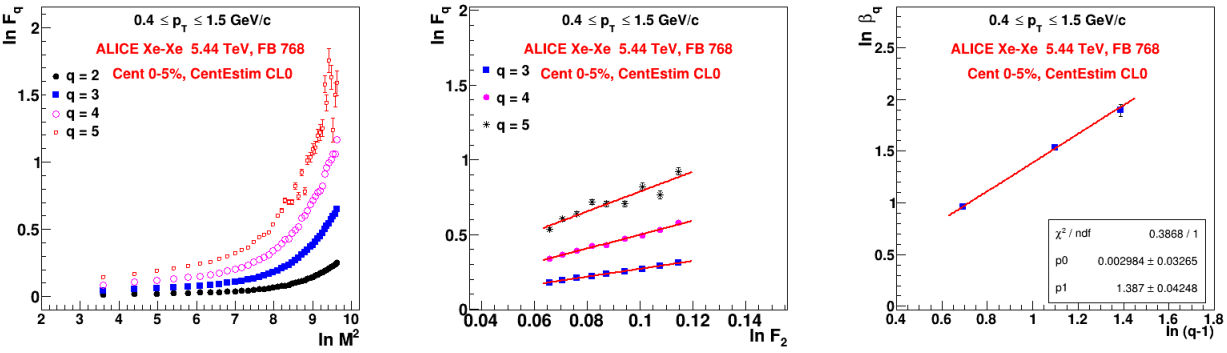

(b) $0.4 \leq p_{\mathrm{T}} \leq 1.5$ GeV/c

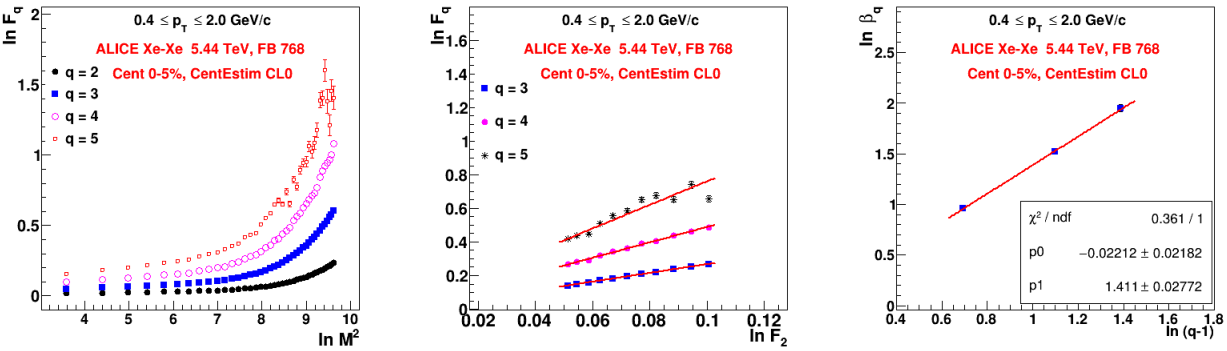

(c) $0.4 \leq p_{\mathrm{T}} \leq 2.0$ GeV/c

Figure B.4: Plots illustrating (left to right): (i) $\ln F_q(M)$ versus $\ln M^2$ (M-scaling), (ii) $\ln F_q(M)$ versus $\ln F_2(M)$ (F-scaling), and (iii) $\ln \beta_q$ versus $\ln(q-1)$ for charged particles in the wide p_T intervals (a) $0.4 \leq p_T \leq 1.0$ GeV/c, (b) $0.4 \leq p_T \leq 1.5$ GeV/c, and (c) $0.4 \leq p_T \leq 2.0$ GeV/c, with the centrality estimator CL0.

B.1.3 Primary Vetex cut $|Vz| \leq 8$ cm

B.1.3.1 Narrow Over-lapping bins

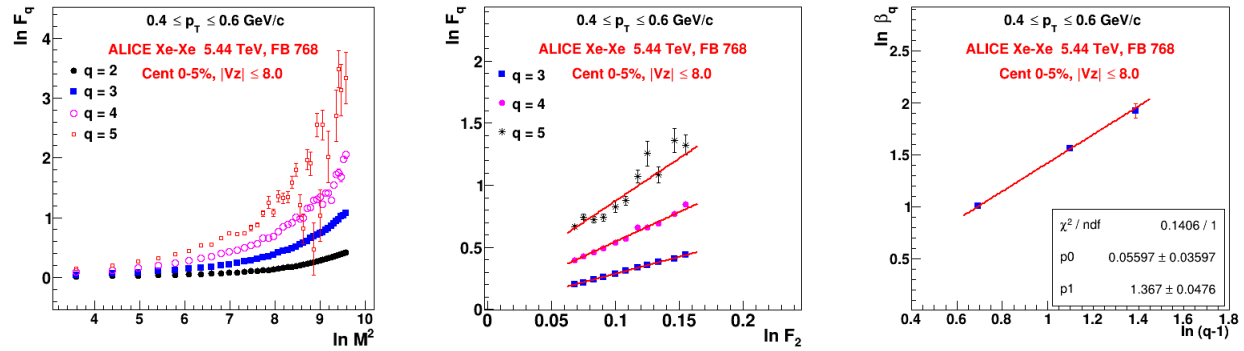

(a) $0.4 \leq p_{\mathrm{T}} \leq 0.6$ GeV/c

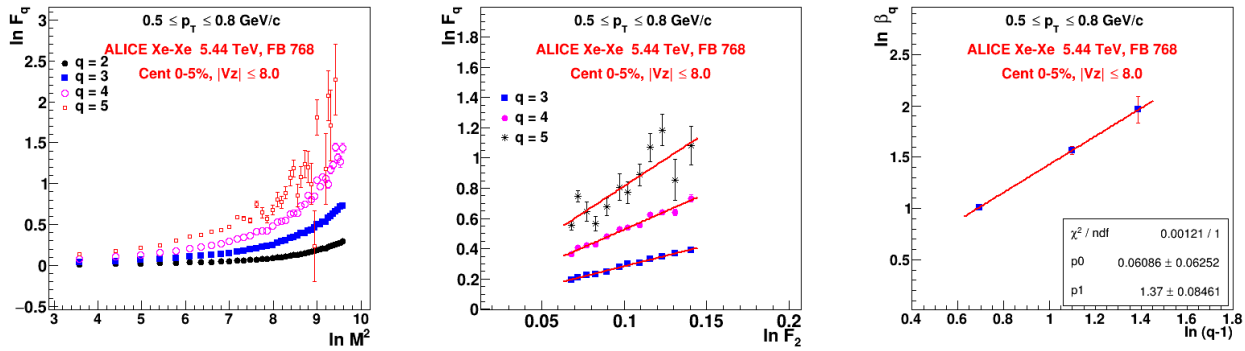

(b) $0.5 \leq p_{\mathrm{T}} \leq 0.8$ GeV/c

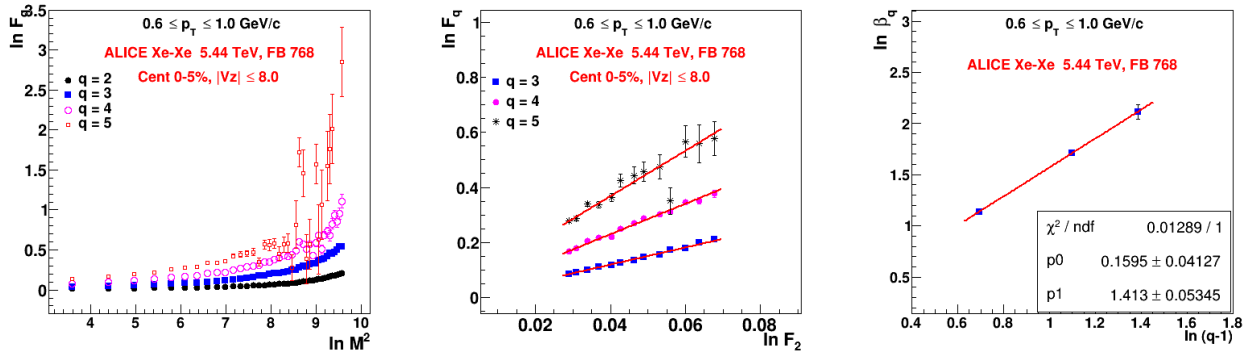

(c) $0.6 \leq p_{\mathrm{T}} \leq 1.0$ GeV/c

Figure B.5: Plots illustrating (left to right): (i) $\ln F_q(M)$ versus $\ln M^2$ (M-scaling), (ii) $\ln F_q(M)$ versus $\ln F_2(M)$ (F-scaling), and (iii) $\ln \beta_q$ versus $\ln(q-1)$ for charged particles in the narrow p_T intervals (a) $0.4 \leq p_T \leq 0.6$ GeV/c, (b) $0.5 \leq p_T \leq 0.8$ GeV/c, and (c) $0.6 \leq p_T \leq 1.0$ GeV/c, with the vertex cut $|V_z| \leq 8$ cm.

B.1.3.2 Wider Over-lapping bins

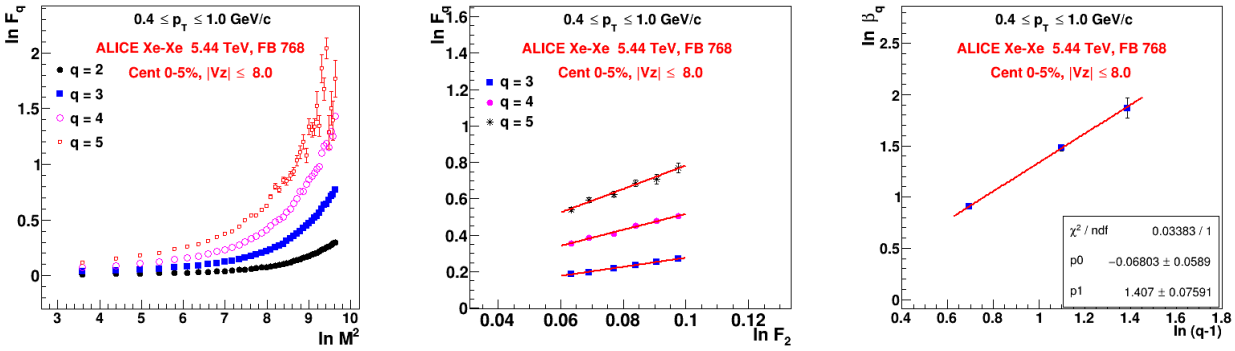

(a) $0.4 \leq p_{\mathrm{T}} \leq 1.0$ GeV/c

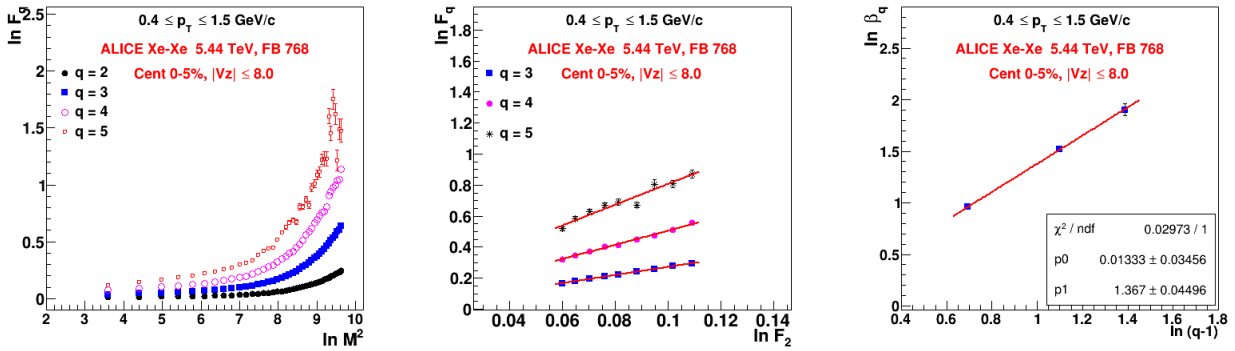

(b) $0.4 \leq p_{\mathrm{T}} \leq 1.5$ GeV/c

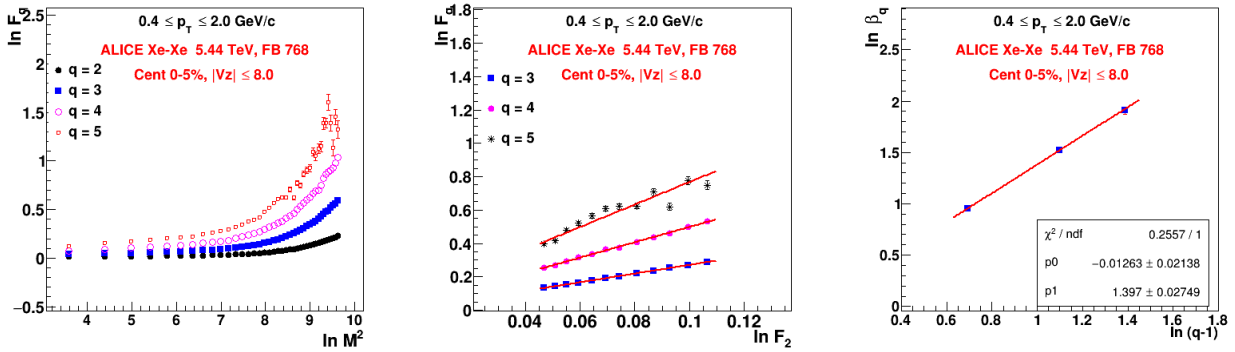

(c) $0.4 \leq p_{\mathrm{T}} \leq 2.0$ GeV/c

Figure B.6: Plots illustrating (left to right): (i) $\ln F_q(M)$ versus $\ln M^2$ (M-scaling), (ii) $\ln F_q(M)$ versus $\ln F_2(M)$ (F-scaling), and (iii) $\ln \beta_q$ versus $\ln(q-1)$ for charged particles in the wide p_T intervals (a) $0.4 \leq p_T \leq 1.0$ GeV/c, (b) $0.4 \leq p_T \leq 1.5$ GeV/c, and (c) $0.4 \leq p_T \leq 2.0$ GeV/c, with the vertex cut $|V_z| \leq 8$ cm.

B.1.4 Primary Vetex cut $|Vz| \leq 12$ cm

B.1.4.1 Narrow Over-lapping bins

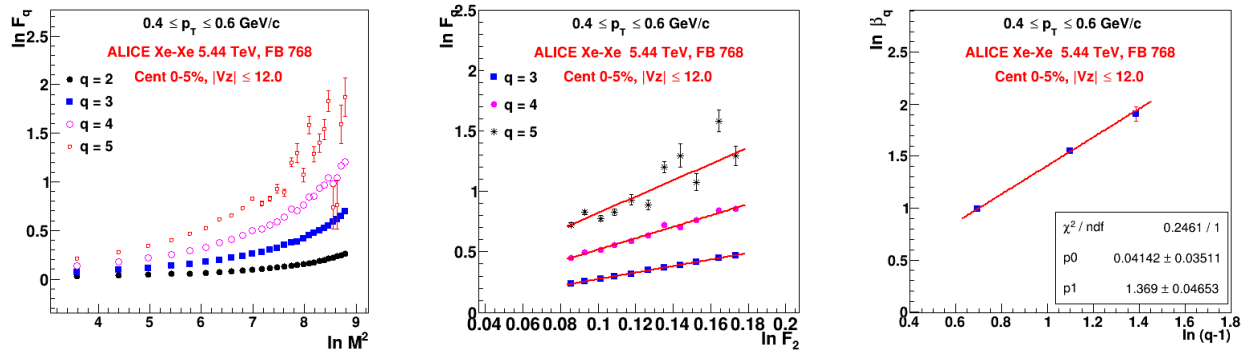

(a) $0.4 \leq p_{\mathrm{T}} \leq 0.6$ GeV/c

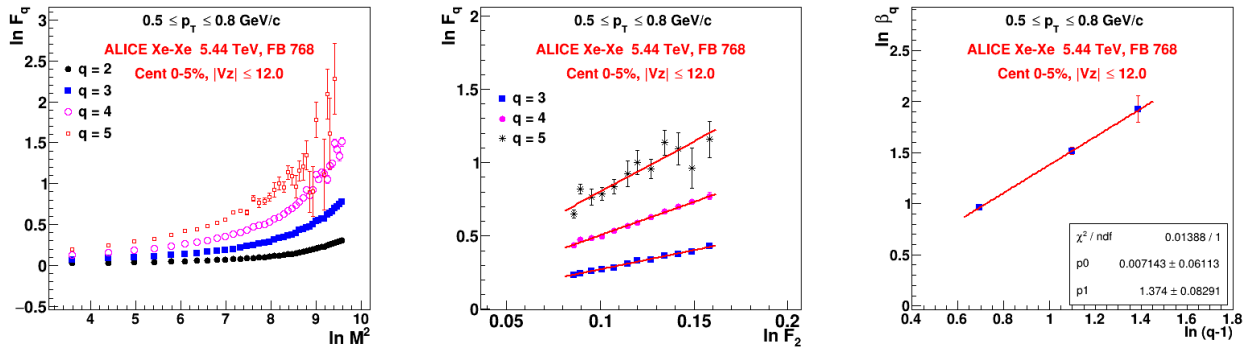

(b) $0.5 \leq p_{\mathrm{T}} \leq 0.8$ GeV/c

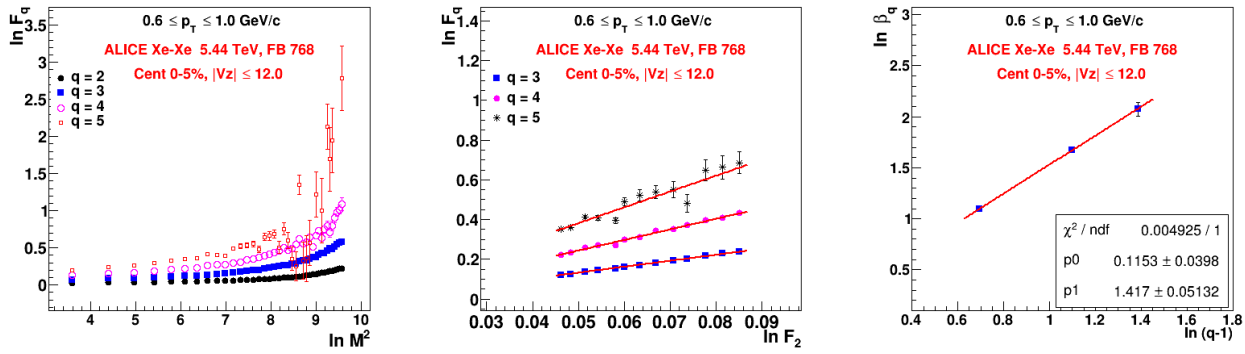

(c) $0.6 \leq p_{\mathrm{T}} \leq 1.0$ GeV/c

Figure B.7: Plots illustrating (left to right): (i) $\ln F_q(M)$ versus $\ln M^2$ (M-scaling), (ii) $\ln F_q(M)$ versus $\ln F_2(M)$ (F-scaling), and (iii) $\ln \beta_q$ versus $\ln(q-1)$ for charged particles in the narrow p_T intervals (a) $0.4 \leq p_T \leq 0.6$ GeV/c, (b) $0.5 \leq p_T \leq 0.8$ GeV/c, and (c) $0.6 \leq p_T \leq 1.0$ GeV/c, with the vertex cut $|V_z| \leq 12$ cm.

B.1.4.2 Wider Over-lapping bins

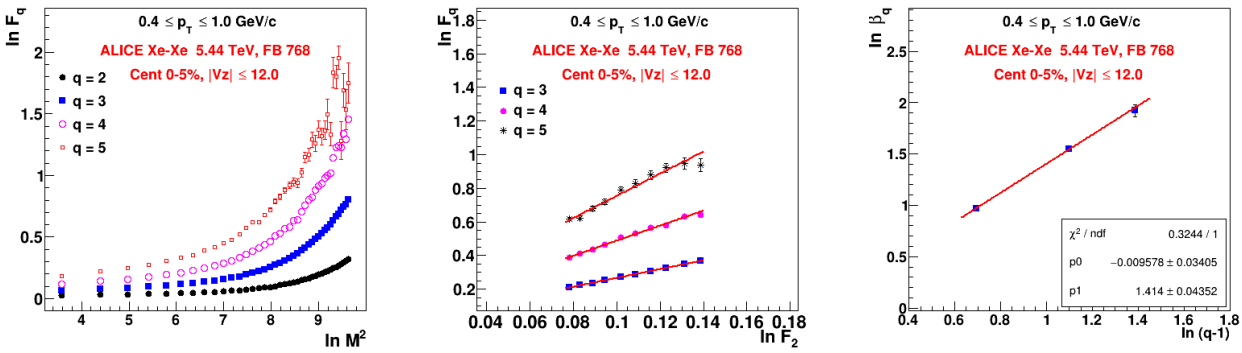

(a) $0.4 \leq p_{\mathrm{T}} \leq 1.0$ GeV/c

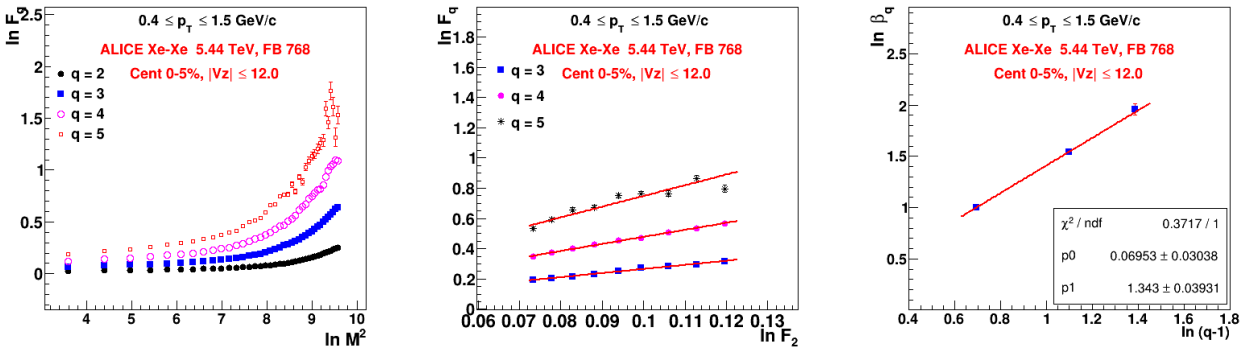

(b) $0.4 \leq p_{\mathrm{T}} \leq 1.5$ GeV/c

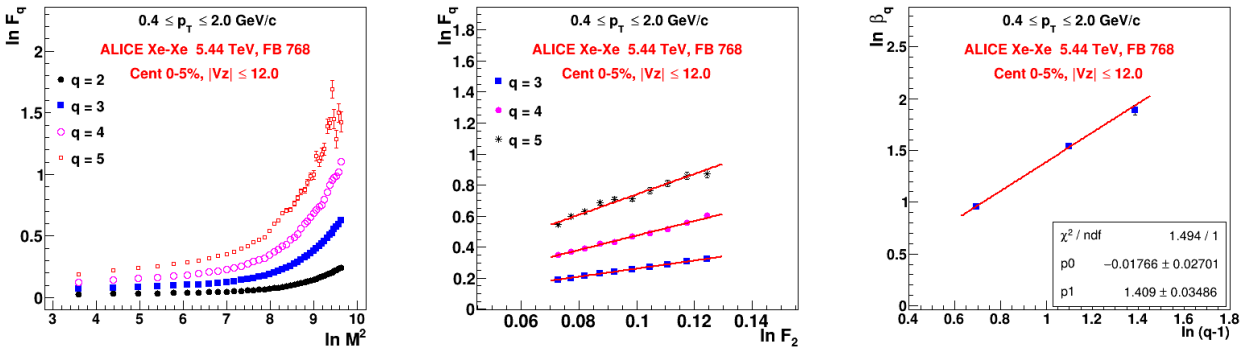

(c) $0.4 \leq p_{\mathrm{T}} \leq 2.0$ GeV/c

Figure B.8: Plots illustrating (left to right): (i) $\ln F_q(M)$ versus $\ln M^2$ (M-scaling), (ii) $\ln F_q(M)$ versus $\ln F_2(M)$ (F-scaling), and (iii) $\ln \beta_q$ versus $\ln(q-1)$ for charged particles in the wide p_T intervals (a) $0.4 \leq p_T \leq 1.0$ GeV/c, (b) $0.4 \leq p_T \leq 1.5$ GeV/c, and (c) $0.4 \leq p_T \leq 2.0$ GeV/c, with the vertex cut $|V_z| \leq 12$ cm.

B.1.5 TPC clusters cut (TPCNcls $\leq$ 80)

B.1.5.1 Narrow Over-lapping bins

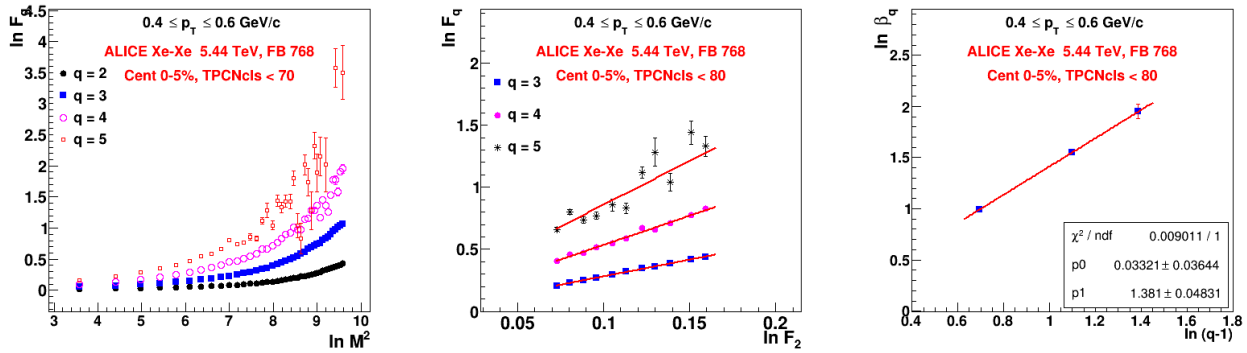

(a) $0.4 \leq p_{\mathrm{T}} \leq 0.6$ GeV/c

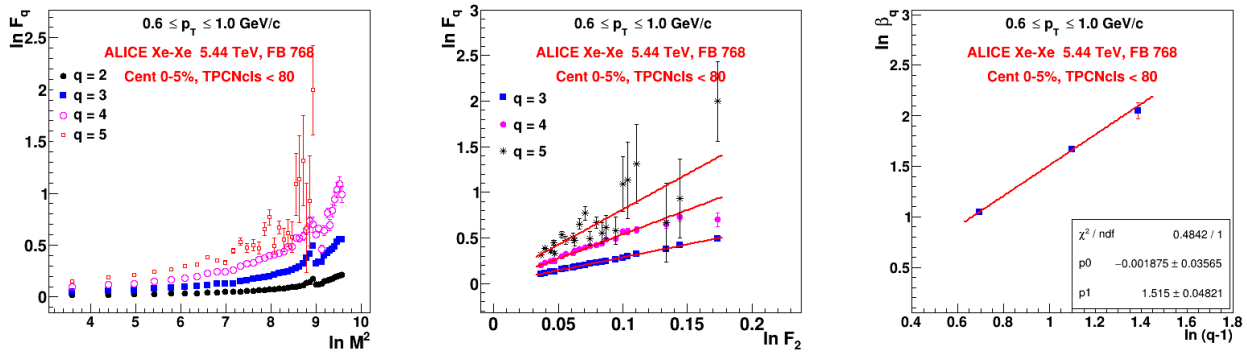

(b) $0.6 \leq p_{\mathrm{T}} \leq 1.0$ GeV/c

Figure B.9: Plots illustrating (left to right): (i) $\ln F_q(M)$ versus $\ln M^2$ (M-scaling), (ii) $\ln F_q(M)$ versus $\ln F_2(M)$ (F-scaling), and (iii) $\ln \beta_q$ versus $\ln(q-1)$ for charged particles in the narrow p_T intervals (a) $0.4 \leq p_T \leq 0.6$ GeV/c and (b) $0.6 \leq p_T \leq 1.0$ GeV/c, with the ITS cluster cut TPCNcls ≤ 80.

B.1.5.2 Wider Over-lapping bins

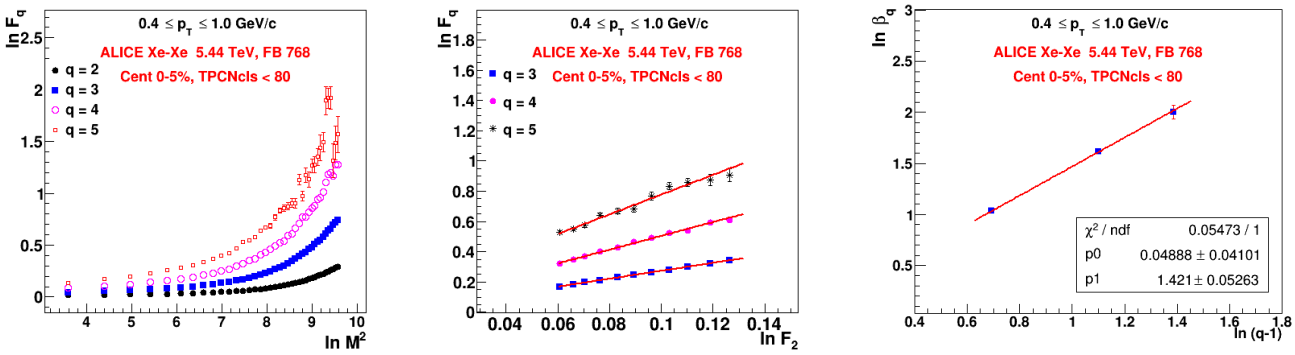

(a) $0.4 \leq p_{\mathrm{T}} \leq 1.0$ GeV/c

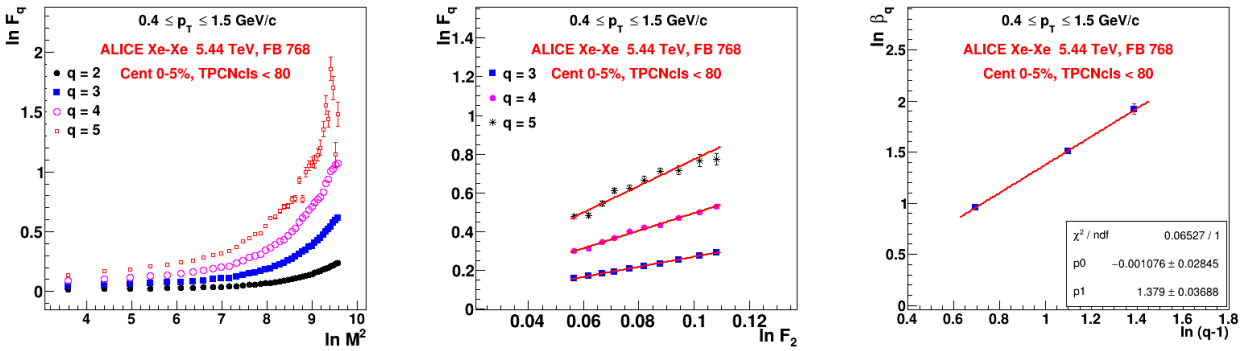

(b) $0.4 \leq p_{\mathrm{T}} \leq 1.5$ GeV/c

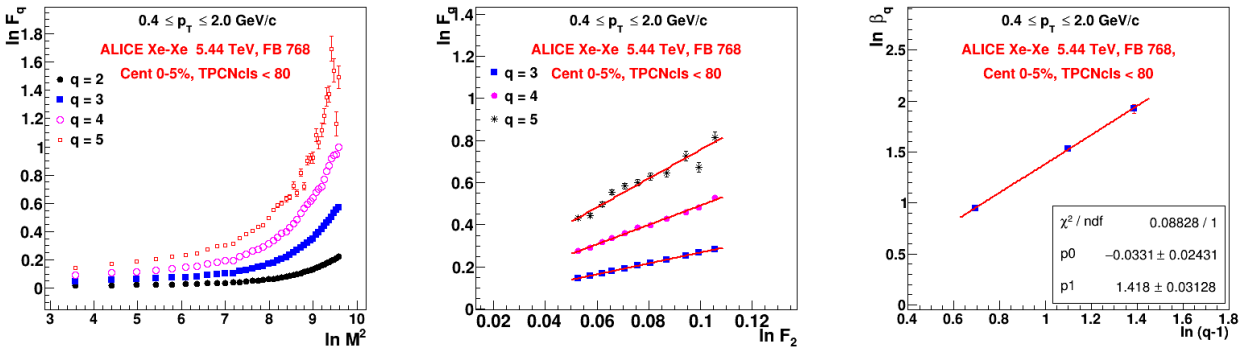

(c) $0.4 \leq p_{\mathrm{T}} \leq 2.0$ GeV/c

Figure B.10: Plots illustrating (left to right): (i) $\ln F_q(M)$ versus $\ln M^2$ (M-scaling), (ii) $\ln F_q(M)$ versus $\ln F_2(M)$ (F-scaling), and (iii) $\ln \beta_q$ versus $\ln(q-1)$ for charged particles in the wide p_T intervals (a) $0.4 \leq p_T \leq 1.0$ GeV/c, (b) $0.4 \leq p_T \leq 1.5$ GeV/c, and (c) $0.4 \leq p_T \leq 2.0$ GeV/c, with the ITS cluster cut TPCNcls ≤ 80.

B.1.6 ITS clusters (ITSNcls ≤ 3)

B.1.6.1 Narrow Over-lapping bins

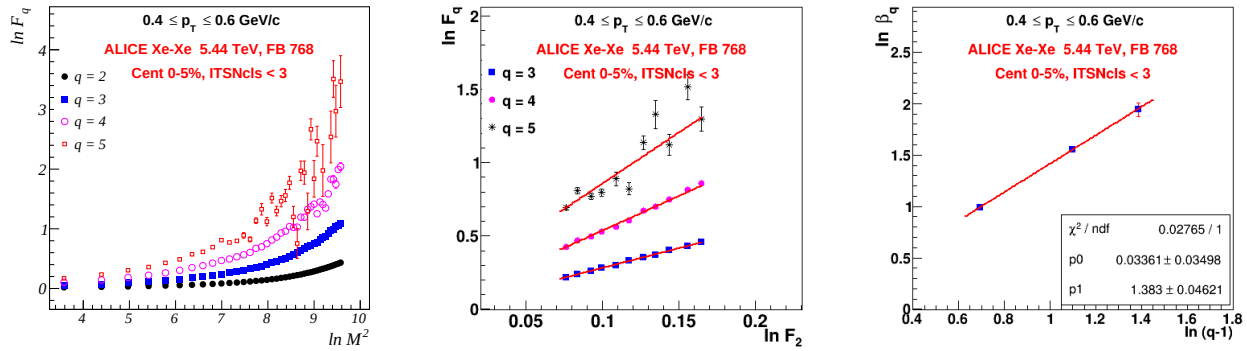

(a) $0.4 \leq p_{\mathrm{T}} \leq 0.6$ GeV/c

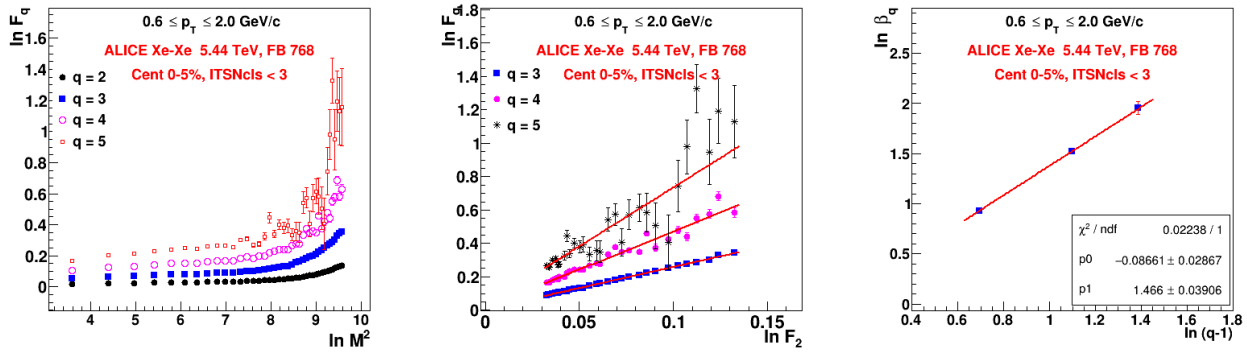

(b) $0.6 \leq p_{\mathrm{T}} \leq 1.0$ GeV/c

Figure B.11: Plots illustrating (left to right): (i) $\ln F_q(M)$ versus $\ln M^2$ (M-scaling), (ii) $\ln F_q(M)$ versus $\ln F_2(M)$ (F-scaling), and (iii) $\ln \beta_q$ versus $\ln(q-1)$ for charged particles in the narrow p_T intervals (a) $0.4 \leq p_T \leq 0.6$ GeV/c and (b) $0.6 \leq p_T \leq 1.0$ GeV/c, with the ITS cluster cut ITSNcls ≤ 3.

B.1.6.2 Wider Over-lapping bins

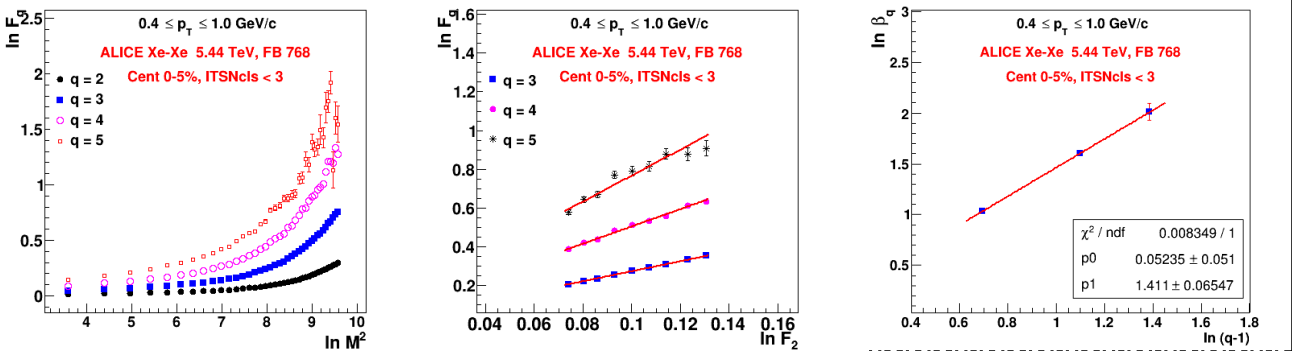

(a) $0.4 \leq p_{\mathrm{T}} \leq 1.0$ GeV/c

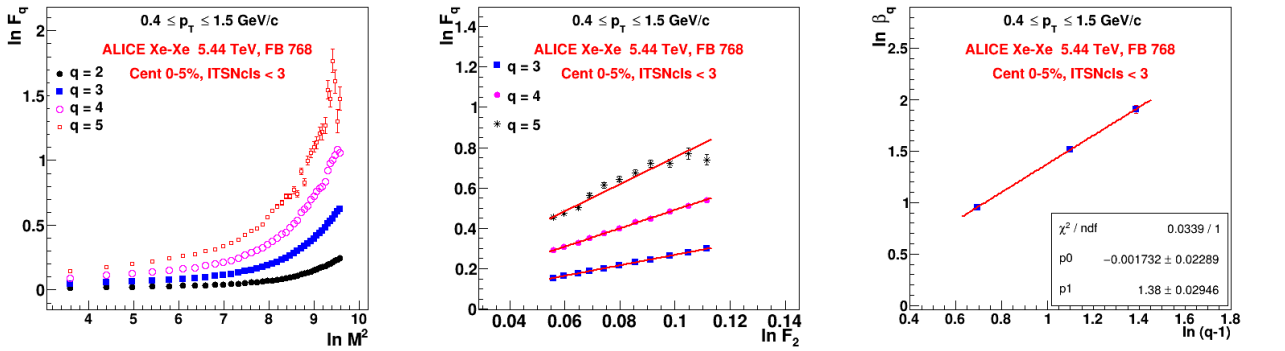

(b) $0.4 \leq p_{\mathrm{T}} \leq 1.5$ GeV/c

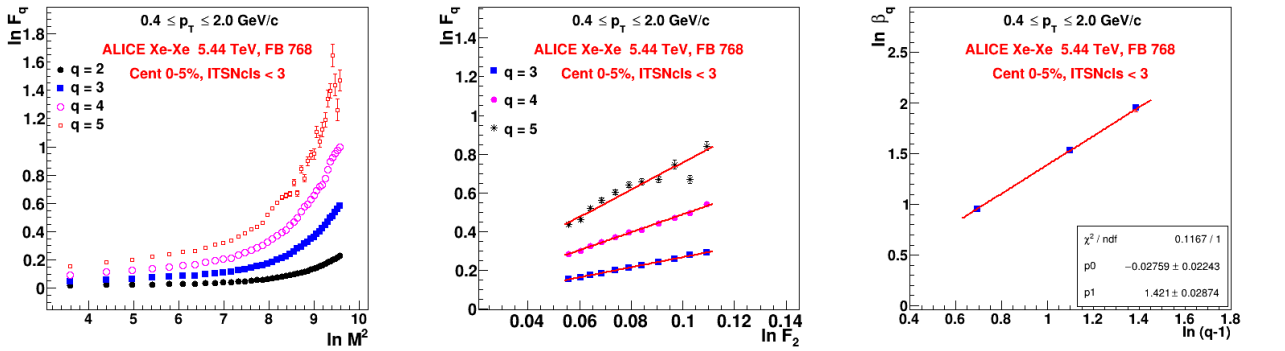

(c) $0.4 \leq p_{\mathrm{T}} \leq 2.0$ GeV/c

Figure B.12: Plots illustrating (left to right): (i) $\ln F_q(M)$ versus $\ln M^2$ (M-scaling), (ii) $\ln F_q(M)$ versus $\ln F_2(M)$ (F-scaling), and (iii) $\ln \beta_q$ versus $\ln(q-1)$ for charged particles in the wide p_T intervals (a) $0.4 \leq p_T \leq 1.0$ GeV/c, (b) $0.4 \leq p_T \leq 1.5$ GeV/c, and (c) $0.4 \leq p_T \leq 2.0$ GeV/c, with the ITS cluster cut TPCNcls ≤ 3.

APPENDIX C

SERVICE WORK

The successful operation of the ALICE experiment during LHC runs depends on well-organized service work carried out by collaboration members. This includes important tasks such as detector maintenance, calibration, data quality monitoring, and support for daily operations. PhD students are expected to actively participate in such service tasks as part of their commitment to the collaboration.

As part of my service work, I contributed to two key areas of the ALICE detector: **Transition Radiation Detector (TRD) tracking Quality Control** and **Global Local Observables (GLO)**

TRD Tracking Quality Control (QC)

My involvement in TRD service work focused on developing and validating the monitoring framework used for tracking performance. Specific tasks included:

- Installation and configuration of the O2 framework and QC environment.

- Preparation of 2D PulseHeight per chamber plots.
- Validation of local test runs using `.tf` and `.ctf` files.
- Execution and successful testing of approximately 900 runs on `lxplus` using `.tf` and `.ctf` data files.
- Merging of updates in `PulseHeight.cxx` and `DigitTask.cxx` for QC development.
- Addition of histograms for PulseHeight per chamber (for all 540 chambers) in `DigitTask.cxx`.
- Projection and verification of 2D PulseHeight plots locally.
- Preparation of layouts (`TRD_PulseHeightPerChamber`) on the QCG monitoring page.
- Implementation of proper detector labelling in the format `SM_S_L`.
- Identification and elimination of duplicate PulseHeight plots.
- Submission of a Pull Request for the new PulseHeight per chamber plots.
- Integration of `checkTracklet.C` for improved analysis of tracking data.

Global Local Observables (GLO)

In addition, I contributed to the GLO module, which is responsible for monitoring the performance of the asynchronous reconstruction. The focus was on evaluating event properties, track properties, and the matching efficiency between the ITS (Inner Tracking System) and TPC (Time Projection Chamber) detectors. This work helped ensure the consistency and accuracy of reconstruction outputs during Run 3 operations.

Data taking shifts for ALICE

During my visit to CERN from **25 September to 10 December 2022** as part of the ALICE Collaboration, I actively participated in data-taking activities for the experiment. One of the primary responsibilities during this period was serving as an **ECS (Experimental Control System) shifter**, ensuring the stable and safe operation of the ALICE detector during active data collection.

Training Shifts: 1 - 3 October 2022.

Main Shifts:

- 12 - 17 October 2022.
- 21 - 26 October 2022.
- 21 - 22 November 2022.

APPENDIX D

LIST OF PUBLICATIONS/ PRESENTATIONS

1. Presentations in conferences

- "Scaling properties of charged particles generated in Xe–Xe collisions at $\sqrt{s_{\mathrm{NN}}} = 5.44$ TeV using the AMPT model"; 10th Edition of the Large Hadron Collider Physics (LHCP) Conference TAIPE, 16th-20th May, 2022.

- "Intermittency Analysis of charged particles generated in Xe–Xe collisions at $\sqrt{s_{\mathrm{NN}}} = 5.44$ TeV using AMPT Model"; 51th International Symposium on Multi-particle Dynamics (ISMD2022), 31st July to 5th August, 2022.

- "A Study of Local Multiplicity Fluctuations in Charged Particle Production in Xe–Xe Collisions at $\sqrt{s_{\mathrm{NN}}} = 5.44$ TeV Using ALICE"; 67th DAE Symposium on Nuclear Physics, 9th-13th December, 2024, IIT Indore, India.

- "Local multiplicity fluctuations in Xe-Xe collision at $\sqrt{s_{\mathrm{NN}}} = 5.44$ TeV with AL-

ICE"; JK-Women Science Congress 2024, 11th-13th February, 2024, University of Jammu, India.

- "Scaling Properties of Charged Particles Generated in Xe–Xe Collision at $\sqrt{s_{\rm NN}}$ = 5.44 TeV with ALICE"; XXVI DAE–BRNS High Energy Physics Symposium, 19th-23rd December, 2024, Banaras Hindu University, Varanasi, India.

2. Workshops/Symposiums attended

- "ALICE QGP school"; 2nd to 8th March 2020, VECC Kolkata, India.
- "Research Methodology and Open Source Softwares workshop"; 24th - 28th June, 2019, Department of Computer Science, University of Jammu, India.
- "Advanced Radiation Detector and Instrumentation in Nuclear and Particle Physics Experiments (RAPID2021) workshop"; 25th - 29th October, 2021, University of Jammu, India.
- "Critical Point and Onset of Deconfinement (CPOD2022) workshop"; 28th November-2nd December, 2022 (online).

3. Publication and conferences proceedings:

1. Zarina Banoo and Ramni Gupta, "Scaling properties of charged particles generated in Xe–Xe collisions at $\sqrt{s_{\rm NN}} = 5.44$ TeV using the AMPT model"; *Proceedings of the* $10^{\rm th}$ *Annual Conference on Large Hadron Collider Physics (LHCP 2022)*; [Link]
2. Zarina Banoo and Ramni Gupta, "Intermittency Analysis of charged particles generated in Xe–Xe collisions at $\sqrt{s_{\rm NN}} = 5.44$ TeV using AMPT Model"; Proceedings of 51st International Symposium on Multiparticle Dynamics (ISMD 2022); [Link]
3. Zarina Banoo and Ramni Gupta, "A Study of Local Multiplicity Fluctuations in Charged Particle Production in Xe–Xe Collisions at $\sqrt{s_{\rm NN}} = 5.44$ TeV Using ALICE"; *DAE Symp.Nucl.Phys. 67 (2024) 1151-1152*; [Link]

4. Sheetal Sharma, Salman Khurshid Malik, Zarina Banoo, Ramni Gupta, "Normalized factorial moments of spatial distributions of particles in high multiplicity events: A Toy model study"; Nucl. Phys. A 1053 122963 (2024); [Link].

4. ALICE internal analysis note

Scaling of charged particles produced in Xe-Xe collision at center of mass energy of 5.44TeV [Analysis note: https://alice-notes.web.cern.ch/node/1423.].

5. ALICE publications co-authored:

1. S. Acharya,...Z. Banoo,...*et al.* [ALICE], "Measurement of anti-^{3}He nuclei absorption in matter and impact on their propagation in the Galaxy," Nature Phys. **19**, no.1, 61-71 (2023).

2. S. Acharya,...Z. Banoo,...*et al.* [ALICE], "Dielectron production in proton-proton and proton-lead collisions at $\sqrt{s_{NN}} = 5.02$ TeV," Phys. Rev. C **102**, no.5, 055204 (2020).

3. S. Acharya,...Z. Banoo,...*et al.* [ALICE], "Proton emission in ultraperipheral Pb-Pb collisions at$\sqrt{s_{\rm NN}}$ = 5.02 TeV," Phys. Rev. C **111**, no.5, 054906 (2025).

4. S. Acharya,...Z. Banoo,...*et al.* [ALICE], "Measurement of ω meson production in pp collisions at $\sqrt{s}$ = 13 TeV," JHEP **04**, 067 (2025).

5. S. Acharya,...Z. Banoo,...*et al.* [ALICE], "Medium-induced modification of groomed and ungroomed jet mass and angularities in Pb–Pb collisions at $\sqrt{s_{\rm NN}}$ = 5.02 TeV," Phys. Lett. B **864**, 139409 (2025).

6. S. Acharya,...Z. Banoo,...*et al.* [ALICE], "Multimuons in cosmic-ray events as seen in ALICE at the LHC," JCAP **04**, 009 (2025).

7. S. Acharya,...Z. Banoo,...*et al.* [ALICE], "First Measurement of A = 4 Hypernuclei and Antihypernuclei at the LH," Phys. Rev. Lett. **134**, no.16, 162301 (2025).

8. S. Acharya,...Z. Banoo,...*et al.* [ALICE], "First observation of strange baryon enhancement with effective energy in pp collisions at the LHC," JHEP **03**, 029 (2025).

9. S. Acharya,...Z. Banoo,...*et al.* [ALICE], "Measurement of the inclusive isolated-photon production cross section in pp and Pb–Pb collisions at $\sqrt{s_{\mathrm{NN}}} = \mathbf{5.02}$ TeV," Eur. Phys. J. C **85**, no.5, 553 (2025).

10. S. Acharya,...Z. Banoo,...*et al.* [ALICE], "Measurement of f1(1285) production in pp collisions at s = 13 TeV," Phys. Lett. B **866**, 139562 (2025).

11. S. Acharya,...Z. Banoo,...*et al.* [ALICE], 'Multiplicity-dependent jet modification from di-hadron correlations in pp collisions at $\sqrt{s}$ = 13 TeV," JHEP **03**, 194 (2025).

12. S. Acharya,...Z. Banoo,...*et al.* [ALICE], "Particle production as a function of charged-particle flattenicity in pp collisions at s = 13 TeV," Phys. Rev. D **111**, no.1, 012010 (2025).

13. S. Acharya,...Z. Banoo,...*et al.* [ALICE], "Rapidity dependence of antideuteron coalescence in pp collisions at $\sqrt{s_{\mathrm{NN}}}$ =13 TeV with ALICE," Phys. Lett. B **860**, 139191 (2025).

14. S. Acharya,...Z. Banoo,...*et al.* [ALICE], "Measurement of beauty production via non-prompt charm hadrons in p–Pb collisions at $\sqrt{s_{\mathrm{NN}}}$ = 5.02 TeV," JHEP **11**, 148 (2024).

15. S. Acharya,...Z. Banoo,...*et al.* [ALICE], "Measurement of the inclusive isolated-photon production cross section in pp collisions at $\sqrt{s} = 13$ TeV," Eur. Phys. J. C **85**, no.1, 98 (2025).

16. S. Acharya,...Z. Banoo,...*et al.* [ALICE], "Measurement of HΛ3 production in Pb–Pb collisions at $\sqrt{s_{\mathrm{NN}}}$ = 5.02 TeV," Phys. Lett. B **860**, 139066 (2025).

17. S. Acharya,...Z. Banoo,...*et al.* [ALICE], "Measurement of the production and elliptic flow of (anti)nuclei in Xe-Xe collisions at $\sqrt{s_{\mathrm{NN}}}$ = 5.44 TeV," Phys. Rev. C **110**, no.6, 064901 (2024).

18. S. Acharya,...Z. Banoo,...*et al.* [ALICE], "Probing Strangeness Hadronization with Event-by-Event Production of Multistrange Hadrons," Phys. Rev. Lett. **134**, no.2, 022303 (2025).

19. S. Acharya,...Z. Banoo,...*et al.* [ALICE], "Investigating Λ baryon production in p-Pb collisions in jets and the underlying event using angular correlations," Phys. Rev. C **111**, no.1, 015201 (2025).

20. S. Acharya,...Z. Banoo,...*et al.* [ALICE], "Measurement of the impact-parameter dependent azimuthal anisotropy in coherent $\rho 0$ photoproduction in Pb–Pb collisions at $\sqrt{s_{\rm NN}}$ = 5.02 TeV," Phys. Lett. B **858**, 139017 (2024).

21. S. Acharya,...Z. Banoo,...*et al.* [ALICE], "Charm fragmentation fractions and $\mathbf{c\bar{c}}$ cross section in p–Pb collisions at $\sqrt{\mathbf{s_{NN}}} = \mathbf{5.02TeV}$," Eur. Phys. J. C **84**, no.12, 1286 (2024).

22. S. Acharya,...Z. Banoo,...*et al.* [ALICE], "Measurement of the production cross section of prompt Ξ_c^0 baryons in p–Pb collisions at $\sqrt{s_{\rm NN}} = 5.02$ TeV," Eur. Phys. J. C **85**, no.1, 86 (2025).

23. S. Acharya,...Z. Banoo,...*et al.* [ALICE], "Investigating strangeness enhancement with multiplicity in pp collisions using angular correlations," JHEP **09**, 204 (2024).

24. S. Acharya,...Z. Banoo,...*et al.* [ALICE], "Investigating strangeness enhancement in jet and medium via $\phi(1020)$ production in p-Pb collisions at $\sqrt{s_{\rm NN}}$ = 5.02 TeV," Phys. Rev. C **110**, no.6, 064912 (2024.

25. S. Acharya,...Z. Banoo,...*et al.* [ALICE], "Measurement of Ω_c^0 baryon production and branching-fraction ratio BR($\Omega_c^0 \to \Omega^- e^+ \nu_e$)/BR($\Omega_c^0 \to \Omega^- \pi^+$) in pp collisions at $\sqrt{s} = 13\,\text{TeV}$," Phys. Rev. D **110**, no.3, 032014 (2024).

26. S. Acharya,...Z. Banoo,...*et al.* [ALICE], "Systematic study of flow vector fluctuations in $\sqrt{s_{\rm NN}}$ = 5.02 TeV TeV Pb-Pb collisions," Phys. Rev. C **109**, no.6, 065202 (2024).

27. S. Acharya,...Z. Banoo,...*et al.* [ALICE], "Studying the interaction between charm and light-flavor mesons," Phys. Rev. D **110**, no.3, 032004 (2024).

28. S. Acharya,...Z. Banoo,...*et al.* [ALICE], "Measurement of beauty-quark production in pp collisions at $\sqrt{s}$ = 13 TeV via non-prompt D mesons," JHEP **10**, 110 (2024).

29. S. Acharya,...Z. Banoo,...*et al.* [ALICE], "Investigating the composition of the K0∗(700) state with $\pi\pm$KS0 correlations at the LHC," Phys. Lett. B **856**, 138915 (2024).

30. S. Acharya,...Z. Banoo,...*et al.* [ALICE], "Emergence of Long-Range Angular Correlations in Low-Multiplicity Proton-Proton Collisions," Phys. Rev. Lett. **132**, no.17, 172302 (2024).

31. S. Acharya,...Z. Banoo,...*et al.* [ALICE], "Common femtoscopic hadron-emission source in pp collisions at the LHC," Eur. Phys. J. C **85**, no.2, 198 (2025).

32. S. Acharya,...Z. Banoo,...*et al.* [ALICE], "Measurements of Chemical Potentials in Pb-Pb Collisions at $\sqrt{s_{\rm NN}} = 5.02\ TeV$," Phys. Rev. Lett. **133**, no.9, 092301 (2024).

33. S. Acharya,...Z. Banoo,...*et al.* [ALICE], "Multiplicity dependence of charged-particle intra-jet properties in pp collisions at $\sqrt{s}$ = 13 TeV," Eur. Phys. J. C **84**, no.10, 1079 (2024).

34. S. Acharya,...Z. Banoo,...*et al.* [ALICE], "Measurement of (anti)alpha production in central Pb–Pb collisions at $\sqrt{s_{\rm NN}}$ = 5.02 TeV," Phys. Lett. B **858**, 138943 (2024).

35. S. Acharya,...Z. Banoo,...*et al.* [ALICE], "Observation of abnormal suppression of f0(980) production in p–Pb collisions at $\sqrt{s_{\rm NN}}$ = 5.02 TeV," Phys. Lett. B **853**, 138665 (2024)

36. S. Acharya,...Z. Banoo,...*et al.* [ALICE], "Photoproduction of K+K- Pairs in Ultra-peripheral Collisions," Phys. Rev. Lett. **132**, no.22, 222303 (2024).

37. S. Acharya,...Z. Banoo,...*et al.* [ALICE], "Light-flavor particle production in high-multiplicity pp collisions at $\sqrt{s}$= 13 TeV as a function of transverse spherocity," JHEP **05**, 184 (2024).

38. S. Acharya,...Z. Banoo,...*et al.* [ALICE], "Charged-particle production as a function of the relative transverse activity classifier in pp, p–Pb, and Pb–Pb collisions at the LHC," JHEP **01**, 056 (2024).

39. S. Acharya,...Z. Banoo,...*et al.* [ALICE], "Multiplicity and event-scale dependent flow and jet fragmentation in pp collisions at $\sqrt{s}$ = 13 TeV and in p–Pb collisions at $\sqrt{s_{\mathrm{NN}}}$ = 5.02 TeV," JHEP **03**, 092 (2024).

40. S. Acharya,...Z. Banoo,...*et al.* [ALICE], "Femtoscopic correlations of identical charged pions and kaons in pp collisions at s = 13 TeV with event-shape selection," Phys. Rev. C **109**, no.2, 024915 (2024).

41. S. Acharya,...Z. Banoo,...*et al.* [ALICE], "Studying strangeness and baryon production mechanisms through angular correlations between charged Ξ baryons and identified hadrons in pp collisions at $\sqrt{s}$ = 13 TeV," JHEP **09**, 102 (2024).

42. S. Acharya,...Z. Banoo,...*et al.* [ALICE], "Measurements of long-range two-particle correlation over a wide pseudorapidity range in p−Pb collisions at $\sqrt{s_{\mathrm{NN}}} = 5.0$ TeV," JHEP **01**, 199 (2024).

43. S. Acharya,...Z. Banoo,...*et al.* [ALICE], "Exploring the Strong Interaction of Three-Body Systems at the LHC," Phys. Rev. X **14**, no.3, 031051 (2024).

44. S. Acharya,...Z. Banoo,...*et al.* [ALICE], "Probing the chiral magnetic wave with charge-dependent flow measurements in Pb-Pb collisions at the LHC," JHEP **12**, 067 (2023).

45. S. Acharya,...Z. Banoo,...*et al.* [ALICE], "Prompt and non-prompt J/ψ production at midrapidity in Pb–Pb collisions at $\sqrt{s_{\mathrm{NN}}}$ = 5.02 TeV," JHEP **02**, 066 (2024).

46. S. Acharya,...Z. Banoo,...*et al.* [ALICE], "Charm production and fragmentation fractions at midrapidity in pp collisions at $\sqrt{s}$ = 13 TeV," JHEP **12**, 086 (2023).

47. S. Acharya,...Z. Banoo,...*et al.* [ALICE], "K*(892)$\pm$ resonance production in Pb-Pb collisions at $\sqrt{s_{NN}} = 5.02$ TeV," Phys. Rev. C **109**, no.4, 044902 (2024).

48. S. Acharya,...Z. Banoo,...*et al.* [ALICE], "Multiplicity-dependent production of $\Sigma(1385)$ and $\Xi(1530)^0$ in pp collisions at $\sqrt{s}$ = 13 TeV," JHEP **05**, 317 (2024).

49. S. Acharya,...Z. Banoo,...*et al.* [ALICE], "Skewness and kurtosis of mean transverse momentum fluctuations at the LHC energies," Phys. Lett. B **850**, 138541 (2024).

50. S. Acharya,...Z. Banoo,...*et al.* [ALICE], "Measurements of jet quenching using semi-inclusive hadron+jet distributions in pp and central Pb-Pb collisions at $\sqrt{s_{\rm NN}}$ = 5.02 TeV," Phys. Rev. C **110**, no.1, 014906 (2024).

A study of local multiplicity fluctuations in charged particle production in Xe–Xe collisions at $\sqrt{s_{\rm NN}}$ = 5.44 TeV using ALICE

Zarina Banoo* and Ramni Gupta
(On behalf of ALICE Collaboration)
Department of Physics, University of Jammu, Jammu 180006, INDIA

I. INTRODUCTION

A fundamental characteristic of the critical behaviour of a system undergoing phase transition is that it exhibits fluctuations of all scales [1]. The most efficient way to address fluctuations of a system created in a heavy-ion collision is to investigate event-by-event (E-by-E) fluctuations, where a given observable is measured on an event-by-event basis, and the fluctuations are studied over the ensemble of the events. To detect such fluctuations in a system, a study of the scaling behaviour of the normalized factorial moments $F_q(M)$ with the number of bins (M) in (η, φ) space is performed. The normalized factorial moments are defined as

$$F_q(M) = \frac{\frac{1}{N_{evt}} \sum_{e=1}^{N_{evt}} \frac{1}{M} \sum_{m=1}^{M} f_q(n_{me})}{\frac{1}{N_{evt}} \sum_{e=1}^{N_{evt}} \frac{1}{M} \sum_{m=1}^{M} f_1(n_{me})} \quad (1)$$

with $f_{q(nme)}$=$\prod_{j=0}^{q-1}(n_{me} - j)$, where e stands for the event, q $\geq$ 2 is the order of the moments, and $n_{me} \geq$ q is the number of particles in a given phase space bin [2]. A power-law behaviour of $F_q(M) \propto M^{\phi_q}$ is defined as M-scaling, where the scaling index $\phi_q \geq 0$ is a constant for any given q [3]. Observation of this scaling implies the absence of any spatial scale in the system, which has been observed in many collision systems with positive scaling index value [4, 5].
For the second-order phase transition in the Ginzburg-Landau (GL) formalism, F_q satisfies with high accuracy the following power law behavior

$$F_q \propto F_2^{\beta_q}. \quad (2)$$

This scaling, which is referred to as F-scaling, can be valid even if the M-scaling is not valid [6, 7]. The scaling exponent ν, which is a universal quantity characterizing the scaling properties of the system, is derived from

$$\beta_{\rm q} = (q-1)^{\nu}. \quad (3)$$

It is essentially independent of the details of the Ginzburg-Landau parameters, where temperature is not a controlling parameter; therefore, the numerical value of ν can be considered as an average value over all temperatures at which the phase transition occurs.

II. ANALYSIS

The analysis is performed for charged particles produced in central events in the midrapidity region $|\eta| \leq 0.8$ with full azimuthal coverage ($0 \leq \varphi \leq 2\pi$) in the $p_{\rm T}$ intervals $0.4 \leq p_{\rm T} \leq 0.6$ GeV/c and $0.4 \leq p_{\rm T} \leq 1.0$ GeV/c. The factorial moments are calculated using the charged particles mapped into the two-dimensional (η, φ) space, where the total number of bins is M^2.
In this contribution, observations and results from the intermittency study of charged particles produced in Xe–Xe collisions at $\sqrt{s_{\rm NN}}$ = 5.44 TeV, recorded with ALICE detector at LHC.

*Electronic address: zarina.banoo@cern.ch

III. OBSERVATION AND RESULTS

The data from ALICE show the presence of M-scaling behavior for q = 2, 3, 4, and 5, indicating the presence of an intermittency signal in the data. The M- and F-scaling for the p_{T} interval of $0.4 \leq p_{\mathrm{T}} \leq 1.0$ GeV/c are shown in Fig. 1 and Fig. 2, respectively. In addition, the value of the scaling exponent (ν) for two different p_{T} intervals is calculated as a function of collision centrality, as shown in Fig. 3.

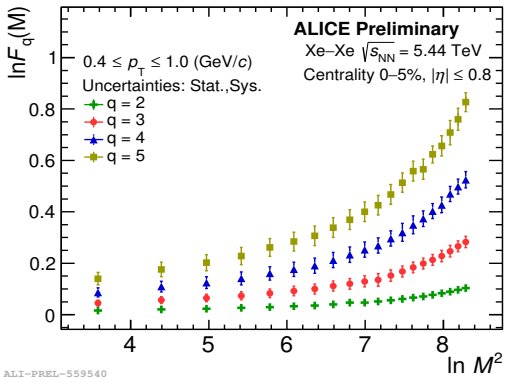

FIG. 1: M-scaling for the p_{T} interval $0.4 \leq p_{\mathrm{T}} \leq 1.0$ GeV/c.

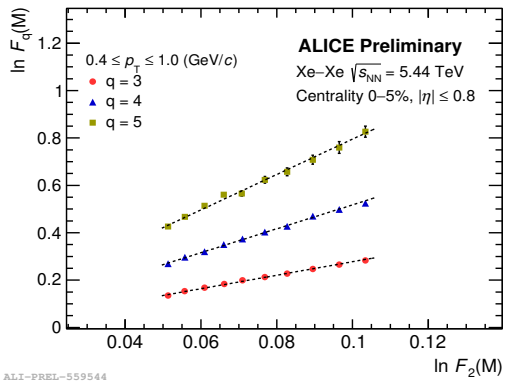

FIG. 2: F-scaling for the p_{T} interval $0.4 \leq p_{\mathrm{T}} \leq 1.0$ GeV/c.

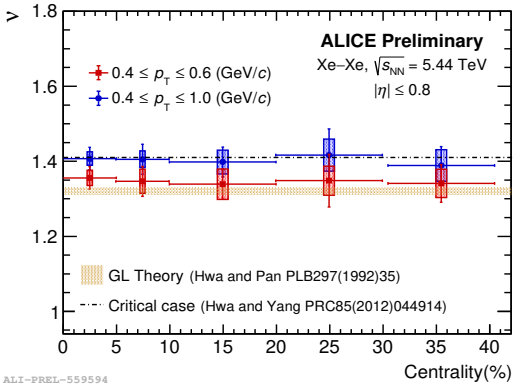

FIG. 3: Centrality dependence of scaling exponent (ν) for the p_{T} intervals $0.4 \leq p_{\mathrm{T}} \leq 0.6$ GeV/c and $0.4 \leq p_{\mathrm{T}} \leq 1.0$ GeV/c.

References

[1] X. Luo, N. Xu, Search for the QCD Critical Point with Fluctuations of Conserved Quantities in Relativistic Heavy-Ion Collisions at RHIC. *Nucl. Sci. Tech.* **28**, 112 (2017).

[2] R. C. Hwa, Recognizing Critical Behavior amidst Minijets at the Large Hadron Collider. *Adv. High Energy Phys.* 526908 (2015).

[3] R. C. Hwa and C. B. Yang, Local Multiplicity Fluctuations as a Signature of Critical Hadronization at LHC. *Phys. Rev. C* **85**, 044914 (2012).

[4] W. Kittel and E. A. De Wolf. *Soft multihadron dynamics.* 2005.

[5] E. A. De. Wolf et al. *Phys. Rep.*, **270**:1−141, (1996).

[6] R. C. Hwa and M. T. Nazirov. Intermittency in second order phase transition. *Phys. Rev. Lett.* **69**:741744, (1992).

[7] A. Bialas and K. Zalewski, Phase Structure of Self-Similar Multiparticle System and Experimental determination of Intermittency Parameters. *Phys. Lett. B.* **238**, (1990) 413-416.

Intermittency analysis of charged particles generated in Xe-Xe collisions at $\sqrt{s_{\rm NN}} = 5.44$ TeV using the AMPT model

Zarina Banoo⋆ and Ramni Gupta

Department of Physics, University of Jammu, India

⋆ zarina.banoo@cern.ch

51st International Symposium on Multiparticle Dynamics (ISMD2022)
Pitlochry, Scottish Highlands, 1-5 August 2022
doi:10.21468/SciPostPhysProc.15

Abstract

The multiplicity fluctuations are sensitive to QCD phase transition and to the presence of critical point in QCD phase diagram. At critical point a system undergoing phase transition is characterized by large fluctuations in the observables which is an important tool to understand the dynamics of particle production in heavy-ion interactions and phase changes. Multiplicity fluctuations of produced particles is an important observable to characterize the evolving system. Using scaling exponent obtained from the normalized factorial moments of the number of charged hadrons in the two dimensional (η, ϕ) phase space, one can learn about the dynamics of system created in these collisions. Events generated using Xe-Xe collisions at $\sqrt{s_{\rm NN}} = 5.44$ TeV with string-melting (SM) version of the AMPT model are analyzed and the scaling exponent (ν) for various p_T intervals is determined. It is observed that the calculated value of ν is larger than the universal value 1.304, as is obtained from Ginzburg-Landau theory for second order phase transition. Here we will also present the results of the dependence of the scaling exponent on the transverse momentum bin width.

Received 19-10-2022
Accepted 06-07-2023
Published 02-04-2024
doi:10.21468/SciPostPhysProc.15.010

1 Introduction

One of the major goals of high-energy heavy ion collision experiments is to understand the particle production mechanism [1]. The spatial fluctuations of the produced particles in the multiparticle production is one of the signatures of criticality and helps to characterize the quark-hadron phase transition [2]. The spatial fluctuations are present at all stages of the collision process, from thermalization, hydrodynamical expansion, hadronization to freeze out. Therefore to collect information about the critical end point and particle production mechanism, it is important to study these types of fluctuations, which are arising out of some dynamical processes [3]. To study the particle density fluctuations, the method of moment was found to be the most suitable one. But in the multiparticle production, the number of hadrons

produced in a single collision is quite small and subject to considerable noise [4]. However the presence of such statistical noise may create problem when the scale dependence of fluctuations is investigated. In that case the use of normalized factorial moments of the multiplicity distribution in a given phase-space volume which filters out the fluctuations of purely statistical origin from the dynamical fluctuations is made [5]. Here we present the results from the study of spatial fluctuations in the charged particles generated in Xe-Xe collisions at $\sqrt{s_{\rm NN}} = 5.44$ TeV using the string melting mode of the AMPT model (version: v1.26t9b-v2.26t9b).

2 The Method

To calculate the particle density fluctuations in spatial distributions, the normalized factorial moments are calculated. For this the angular phase space pseudorapidity and azimuthal angle (η, ϕ) is partitioned into M x M cells. For any value of the number of bins M, let n_i be the number of charged particles in a cell. Then the normalized factorial moments $F_q(M)$ of order q is defined by

$$F_q^e(M) = \frac{\left\langle \frac{1}{M^D} \sum_{e=1}^{M^D} n_i(n_i-1).....(n_i-q+1) \right\rangle}{\left\langle \frac{1}{M^D} \sum_{e=1}^{M^D} n_i \right\rangle^q}. \tag{1}$$

Here, $\langle \ldots \rangle$ represents the averaging over all events [2]. The power law behaviour of F_q with M

$$F_q(M) \propto M^{\phi_q}, \tag{2}$$

is termed as *intermittency*. Eq.(2) is here referred as *M-scaling* and is considered as a signature of self-similar patterns of particle multiplicity and ϕ_q represents the intermittency indices which determines the strength of the intermittency [3]. It has been observed that for the Ginzburg-Landau(GL) formalism, $F_q(M)$ follows power-law [6] as:

$$F_q \propto F_2^{\beta_q}, \beta = (q-1)^{\nu}, \tag{3}$$

this is referred to as *F-scaling*. Here ν is the scaling exponent and $\nu = 1.304$ is the universal value given by GL theory for second order phase transition and is independent of the GL parameters [6].

In the SM version of the AMPT model the excited hadronic strings in the overlap volume are converted into partons along the intervening step of decaying hadrons that would have been produced by the Lund string fragmentation process. A detailed description of the model is available in [7]. In this work a sample of around 300K central SM AMPT events generated with an impact parameter $0 \leq b \leq 3.5$ fm (corresponding to $0-5\%$ centrality) have been analyzed.

3 Observations and Results

Charged particles produced in the kinematic region $|\eta| \leq 0.8$ with full azimuthal coverage and $p_T \leq 2.0$ GeV/c are studied for a range of p_T bins as in [6,8]. Normalized factorial moments F_q's are determined for M = 4 - 82 and q = 2, 3, 4,5 and are studied for their dependence on M (M-scaling). Fig 2(a) shows M-scaling for the p_T bin $0.4 \leq p_T \leq 0.6$ GeV/c. F_q for q =

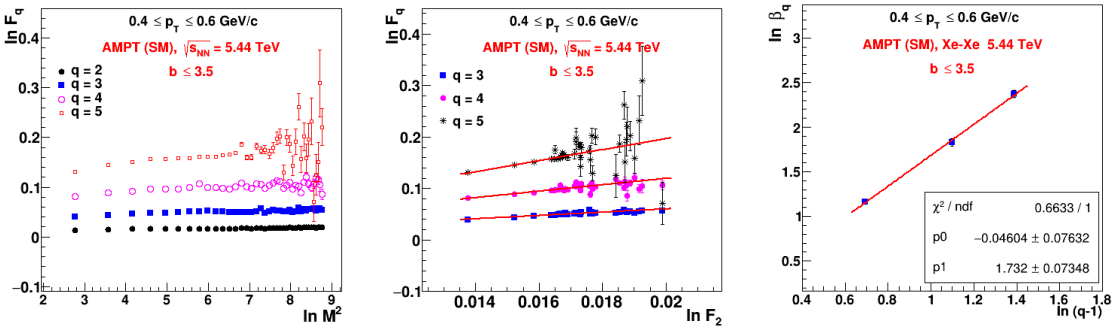

Figure 1: (a) lnF_q(M) vs. ln(M). (b) lnF_q(M) vs. lnF_2(M) (c) lnβ_q vs. ln(q-1), in two dimensional (η, ϕ) phase space ($0.4 \leq p_T \leq 0.6$ GeV/c).

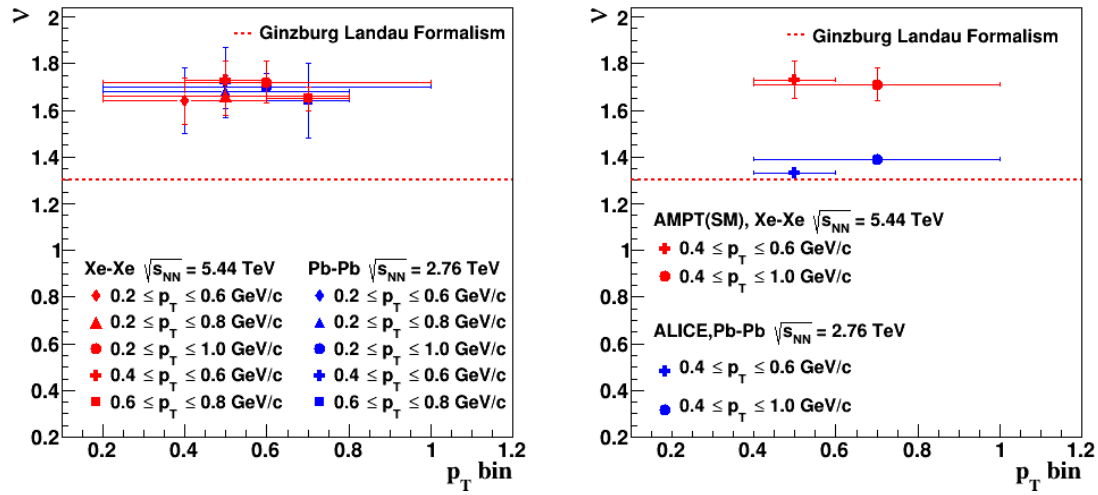

Figure 2: Scaling exponent ν as a function of various p_T bins for Xe-Xe collisions at $\sqrt{s_{\rm NN}} = 5.44$ TeV and its comparision with Pb-Pb (left) AMPT data [8] and (right) ALICE data [9] .

2, 3, 4 are observed to be independent of M, where for q = 5 at high M large fluctuations in the value of F_q are observed. Which are due to statistical effects. Thus the charged particles generated in AMPT for Xe-Xe collisions do not follow self-similar behaviour.
Dependence of $F_q(M)$ for q = 3, 4, 5 on $F_2(M)$ for the same case, given in Fig 2(b), shows linear behaviour. So even though M-scaling is absent, F-scaling is observed to be present. The scaling exponent 'ν' that gives relation between β_q and the order of the moments q as defined in Eq.(3) is determined (Fig 2(c)). For all the p_T bins studied, ν is observed to have average value ≈ 1.7(Fig 2).
The scaling exponent obtained for Xe-Xe collision from the SM AMPT model is much larger than the value predicted by GL theory for second order phase transition. The AMPT model does not have physics of phase transition implemented into it. This study confirms it and gives significance of intermittency studies in characterizing systems created in heavy-ion collisions.

4 Conclusion

Intermittency analysis of Xe-Xe Monte Carlo events at $\sqrt{s_{\rm NN}} = 5.44$ TeV generated with the AMPT model performed to investigate the scaling behaviours and to determine scaling exponent. Whereas M-scaling is absent in charged particles generated in AMPT, F-scaling is observed to be present with scaling exponent (ν) with values different from that for second order phase transition implemented in GL theory and the experimental value from ALICE data. Intermittency methodology is observed to be suitable to characterize various dynamical systems.

Acknowledgements

Funding information Authors are thankful to RUSA 2.0 grant to University of Jammu by the Minisry of Education, Govt. of India for partial support for computing resources.

References

[1] A. Bialas and R. Peschanski, *Moments of rapidity distributions as a measure of short-range fluctuations in high-energy collisions*, Nucl. Phys. B **273**, 703 (1986), doi:10.1016/0550-3213(86)90386-X.

[2] R. C. Hwa and C. B. Yang, *Local multiplicity fluctuations as a signature of critical hadronization at LHC*, Phys. Rev. C **85**, 044914 (2012), doi:10.1103/PhysRevC.85.044914.

[3] R. C. Hwa and M. T. Nazirov, *Intermittency in second-order phase transitions*, Phys. Rev. Lett. **69**, 741 (1992), doi:10.1103/PhysRevLett.69.741.

[4] E. A. De Wolf, I. M. Dremin, W. Kittel, *Scaling laws for density correlations and fluctuations in multiparticle dynamics*, Phys. Rept. **270**, 1 (1996), doi:10.1016/0370-1573(95)00069-0.

[5] S. Bhattacharyya, M. Haiduc, A. T. Neagu and E. Firu, *A study of multifractality and phase transition in heavy-ion collisions — experimental data versus model simulation*, Fractals **26**, 1850015 (2018), doi:10.1142/S0218348X18500159.

[6] R. Gupta, S. K. Malik, *Intermittency study of charged particles generated in Pb-Pb collisions at 2.76 TeV using EPOS3*, Adv. High Energy Phys. **2020**, 5073042 (2020), doi:10.1155/2020/5073042.

[7] Z. W. Lin *Evolution of transverse flow and effective temperatures in the parton phase from a multi-phase transport model*, Phys. Rev. C. **90**, 014904 (2014), doi:10.1103/PhysRevC.90.014904.

[8] R. Sharma and R. Gupta, *Scaling properties of multiplicity fluctuations in the AMPT model*, Adv. High Energy Phys. **2018**, 6283801 (2018), doi:10.1155/2018/6283801.

[9] R. Gupta and R. Sharma, *Local multiplicity fluctuations in Pb-Pb collisions at* $\sqrt{s_{NN}} = 5.44$ *TeV with ALICE data at LHC*, Quark Matter (2022), https://indico.cern.ch/event/895086/contributions/4723639/.

PROCEEDINGS OF SCIENCE

Scaling properties of charged particles generated in Xe-Xe collisions at $\sqrt{s_{\rm NN}}$ = 5.44 TeV using the AMPT model

Zarina Banoo and Ramni Gupta
Department of Physics, University of Jammu, Jammu, J&k, India

E-mail: zarina.banoo@cern.ch, ramni.gupta@cern.ch

At the critical point a system undergoing phase transition is characterized by large fluctuations in the observables. Fluctuations study is thus one of the important techniques to explore phases of the QCD matter and to search for the critical end point of hadron-quark or quark-hadron phase boundary. Scaling properties of the multiplicity fluctuations of charged hadrons produced in the high energy heavy ion collisions may reveal the features of quark-hadron phase transition and also the particle production mechanism. Scaling exponent obtained from the normalized factorial moments of the number of charged hadrons in the two dimensional (η, ϕ) phase space can quantitatively characterize the system created in these collisions. Within the framework of Ginzburg-Landau (GL) formalism for second order phase transition and for the two-dimensional Ising model simulated for quark-hadron phase transition a universal value of scaling exponent (ν) is obtained as 1.316 ± 0.012. Here we will present observations and results from the analysis performed for the charged particle multiplicity distributions obtained from Xe-Xe collisions at $\sqrt{s_{\rm NN}}$ = 5.44 TeV with the string melting mode of the AMPT model. Observations, results on the scaling behaviour of the normalized factorial moments and the dependence of the scaling exponent on the transverse momentum bin width will be presented.

The Tenth Annual Conference on Large Hadron Collider Physics - LHCP2022
16-20 May 2022
online

PoS(LHCP2022)335

1. Introduction

The main purpose of study of the high energy heavy-ion collisions is to understand the Quantum Chromodynamics (QCD) phase transition diagram and the critical point search. In such interactions, under the conditions of high temperature and energy density, conditions similar to those which existed within a few microseconds just after the Big-Bang could be achieved [1]. Lattice QCD calculations provide a quantitative predictions at $\mu_B = 0$ and find that the transition is a rapid crossover [2]. According to the theoretical considerations deconfinement transition at low temperature T and high baryonic chemical potential μ_B is believed to be of the first order. Thus a critical end point (CEP) is supposed to exist at the end of the first-order transition. However, there exists a sign problem at finite μ_B region in the lattice QCD calculations and large statistical uncertainties in the experimental measurements [3]. So it is difficult both theoritically as well as experimentally to determine the exact location of the CP. At critical point the correlation length of the system diverges (known as Critical opalescence) which results in an increase in density fluctuations of multiplicity distribution of the produced particles [4]. This increase of the density fluctuations at the critical point of QCD phase diagram makes the study of fluctuation more intresting and challenging [5]. The most efficient way to address fluctuations of a system created in a heavy ion collision is to study the fluctuation on event-by-event (E-by-E) basis [6]. The objective of this work is to analyze the generated central Xe-Xe collision event at $\sqrt{s_{\rm NN}}$ = 5.44 TeV using the A Multi-Phase Transport (AMPT) model with String Meting (SM) mode by studying the Normalised Factorial Moments (NFM) as function of decreasing phase space bin size.

2. Methodology

In analogy to the turbulence in fluid, the multilicity fluctuations study in the decreasing phase space bins, reffered as Intermittency is studied in multiparticle production in heavy-ion collisions [7]. In this work we study the scaling behaviour of charged particles spacial distributions in angular phase space distribution using normalised factorial moments (NFM) as proposed in [8]. The (η, ϕ) phase space is divided into a square lattice with $M_\eta \times M_\phi$ bins, where M_η and M_ϕ being the number of bins along η and ϕ respectively. Charged particles generated in the selected η, ϕ and p_T cuts are mapped onto the (η, ϕ) matrix [9]. The formula used for calculating the normalized factorial moments F_q as function of number of bins is defined as,

$$F_q^e(M) = \frac{\frac{1}{N}\sum_{e=1}^{M}\frac{1}{M}\sum_{i=1}^{M} f_q(n_{ie})}{(\frac{1}{N}\sum_{e=1}^{M}\frac{1}{M}\sum_{i=1}^{M} f_1(n_{ie}))^q}. \tag{1}$$

where q is the order of the moment, positive integer ≥ 2 and $n_{ie} \geq$ q is the bin multiplicity. If the system exhibits fluctuations, the Normalised Factorial Moment $F_q(M)$ follow a scaling behaviour

$$F_q(M) \propto M^{\phi_q}. \tag{2}$$

refferred to as *intermittency*. Here ϕ_q is called the intermittency index that characterizes the strength of the intermittency behavior. Eq.(2) is referred here as *M-scaling*. Even if the scaling behaviour

in Eq.(2) is not satisfied, to a high degree of accuracy, $F_q(M)$ satisfies the power law behaviour as:

$$F_q(M) \propto F_2(M)^{\beta_q}, \tag{3}$$

such that

$$\beta = (q-1)^{\nu} \tag{4}$$

The Scaling behaviour in Eq.(3) is referred here as *F-scaling* [10]. This behavior has been experimentally verified for optical systems at the threshold of lasing. ν = 1.304 as per GL theory formalism for second order phase transition.

3. A brief introduction of AMPT

A MultiPhase Transport (AMPT) model is a hybrid model based on both the initial partonic and the final hadronic phase. The AMPT model is constructed to describe nuclear collisions with center-of-mass energy ranging from about $\sqrt{s_{\rm NN}}$ = 5 GeV up to 5500 GeV at LHC. This model contains four components namely the initial conditions, parton transport after initialization, hadronization mechanism and hadronic interaction [11]. AMPT exists in two different versions: the AMPT with string melt and the default AMPT version. Around 500K String melting minimum biased Xe-Xe collision events at $\sqrt{s_{\rm NN}}$ = 5.44 TeV are generated. Whereas the analysis is performed for central events with impact parameter $0 \leq b \leq 3.5$ fm. Fig 1(left) shows the pseudorapidity density distribution of the charged particles generated with the AMPT model and are compared with ALICE data points for various centralities and (right) shows the dependence of normalized charged particles density on the number of participants and compared with ALICE data points [12].

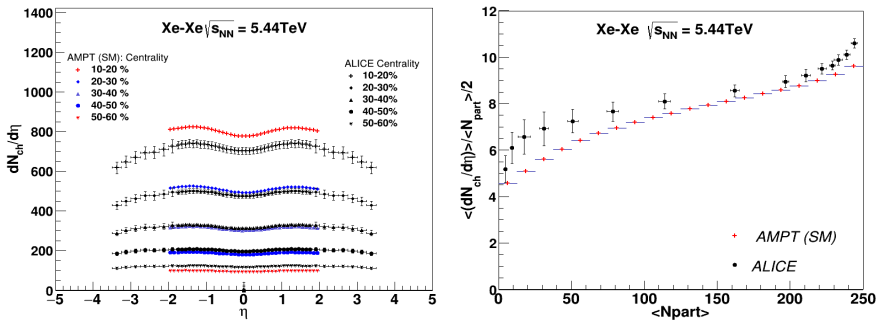

Figure 1: (left) Pseudorapidity density distribution of charged particles for various centralities and (right) charged particle density vs number of participants from the generated events is given and compared with the ALICE data [12] for Xe-Xe collision at $\sqrt{s_{\rm NN}}$ = 5.44 TeV.

4. Observations and Results

The behaviour of the factorial moments $F_q(M)$ are studied for their dependence on M (number of bins) and second order factorial moments $F_2(M)$ in the transverse momentum range of $0.4 \leq$

$p_T \leq 1.0$ GeV/c. From this study, it is observed that $F_q(M)$ is independent of M for q = 2, 3, 4, 5 in the SM mode of the AMPT model. But $F_q(M)$ is observed to show a linear dependence on F_2 for q = 3, 4, 5. Scaling index, ν is determined from the slope for ln β_q against ln(q-1). Fig 2(a) and 2(b) show the *M-scaling* and *F-scaling* behaviour of $F_q(M)$ along with the scaling index value in (c).

Also analysis of the scaling behaviour of F_q is carried in various other p_T bins of various width to

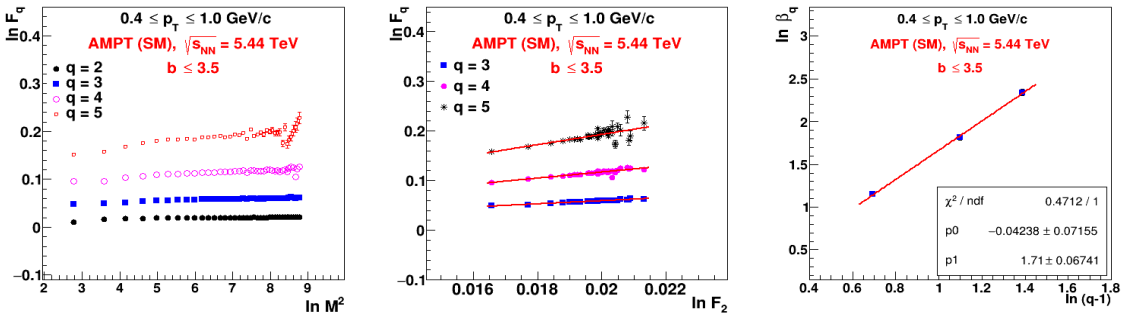

Figure 2: (a) M-scaling behavior of F_q . (b) F-scaling behavior of F_q (c) Log-log plot of β_q versus (q-1), in two dimensional (η, ϕ) phase space in $0.4 \leq p_T \leq 1.0$ GeV/c bin.

study the dependence of scaling exponent on p_T bins and p_T binwidth as studied in [10] . Results from similar analysis from ALICE are also shown for Pb-Pb collision of 2.76 TeV which is close to the theoritically predicted line.

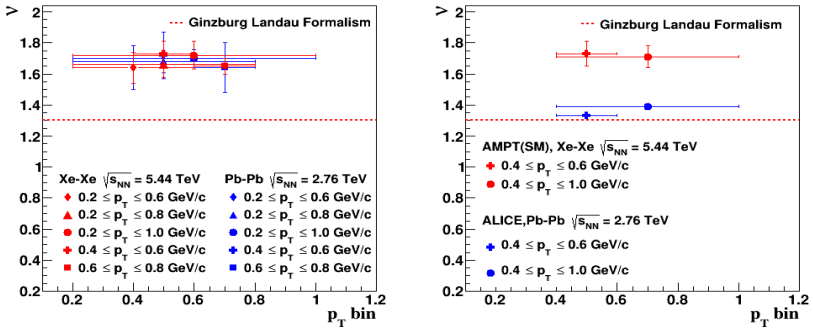

Figure 3: Shows scaling exponent (ν) vs p_T for Xe-Xe at $\sqrt{s_{\rm NN}}$ = 5.44 TeV. ν value obtained for Pb-Pb collision at $\sqrt{s_{\rm NN}}$ = 5.44 TeV from AMPT (SM) model [10] (left panel) and ALICE experiment [13] (right panel) are also given.

5. Summary

Scaling properties of the charged particles generated in the mid rapidity region in Xe-Xe collisions at $\sqrt{s_{\rm NN}}$ = 5.44 TeV have been studied in the framework of intermittency analysis. A power-law growth of NFM (F_q) with M is observed to be absent at high M values in all the p_T bins. However F-scaling is observed to exist in almost all p_T bin. With no phase transition physics implemented in (SM) AMPT model: Scaling behaviour in line with intermittency is absent and the Scaling exponent is different from value predicted by theory for second order phase transition.

References

[1] T. Csorgo, "Search for the Critical Point of Strongly Interacting Matter in Heavy-Ion Collisions", SQM 2015,

[2] G. Stefanek,"Recent results from the search for the critical point of strongly interacting matter at the CERN SPS", Nucl. Part. Phys. Proc. 273-275 (2016) 2596-2598, ICHEP 2014.

[3] J. Wu, Y. Lin, Y. Wu and Z. Li, "Probing QCD critical fluctuations from intermittency analysis in relativistic heavy-ion collisions", Phys. Lett. B **801**, (2020) 135186 .

[4] X. Luo, N. Xu, "Search for the QCD Critical Point with Fluctuations of Conserved Quantities in Relativistic Heavy-Ion Collisions at RHIC," Nucl. Sci. Tech. **28**, (2017) 112 .

[5] J. D. Bjorken " Asymptotic Sum Rules at Infinite Momentum ", Phys. Rev. **169**, (1969) 1547.

[6] M. Mukherjee, S. Basu, S. Choudhury,and T. K. Nayak "Fluctuations in Charged Particle Multiplicities in Relativistic Heavy-Ion Collisions", J. Phys. G:Nucl. Part. Phys. **43**, (2016) 085102.

[7] P. Li, Y. Wang, J. Steinheimer, Q. Li and H. Zhang "Proton correlations and apparent intermittency in the UrQMD model with hadronic potentials", Phys. Lett. B. **818**, (2021) 136393.

[8] R. C. Hwa and C. B. Yang, "Local Multiplicity Fluctuations as a Signature of Critical Hadronization at LHC", Phys. Rev. C **85**, (2012) 044914.

[9] R. C. Hwa and C. B. Yang, "Observable Properties of Quark-Hadron Phase Transition at the Large Hadron Collider", Acta Phys. Polon B **48**, (2017) 23 .

[10] R. Sharma and R. Gupta, "Scaling Properties of Multiplicity Fluctuations in the AMPT Model", Adv. in High Energy Physics.

[11] Z. W. Lin, C. M. Ko, B. A. Li, B. Zhang and S. Pal, "A Multi-Phase Transport Model for Relativistic Heavy Ion Collisions", Phys. Rev. C. **72**, (2005) 064901.

[12] S. Acharya, et al., (ALICE Collaboration), "Centrality and pseudorapidity dependence of the charged-particle multiplicity density in Xe-Xe collisions at = 5.44 TeV", Phys. Lett. B. **790**, (2019) 35.

[13] R. Gupta and R. Sharma, "Local multiplicity fluctuations in Pb-Pb collisions at $\sqrt{s_{NN}}$ = 5.44 TeV with ALICE data at LHC", Quark Matter 2022.

XXVI DAE-BRNS High Energy Physics Symposium 2024

December 19 -23, 2024

Institute of Science, Banaras Hindu University
Varanasi-221005, India

Certificate of Presentation

On behalf of the local organizing committee, this is to certify that,

Zarina Banoo (University of Jammu)

has presented a **Poster Presentation** titled:

Scaling Properties of Charged Particles generated in Xe-Xe Collisions at 5.44 TeV with ALICE

during the XXVI DAE-BRNS High Energy Physics Symposium - 2024, held from December 19-23, 2024, at Banaras Hindu University, Varanasi.

The symposium was held from **December 19 to 23, 2024**, at Banaras Hindu University (BHU), Varanasi, India. This biennial event is a significant platform for the exchange of ideas and scientific collaboration within the high-energy physics community. It is supported by the Board of Research in Nuclear Sciences (BRNS), Department of Atomic Energy (DAE), India.

The symposium will feature deliberations from both experimental and theoretical perspectives, covering a wide range of topics, including: Astroparticle Physics, Cosmology, Flavor physics, Higgs, Heavy-ion, LHC physics, Neutrino, Future experiments and detector development, Formal theory, Beyond the Standard Model and Societal applications, and related areas.

We acknowledge and appreciate the effort and dedication put into this work, which has greatly enriched the symposium.

Dr. Avijit Kumar Ganguly, Convener,
XXVI DAE-BRNS HEP Symposium-2024,
Banaras Hindu University,
Varanasi-221005, India
https://indico.cern.ch/event/1426931/

Prof Andy Buckley
School of Physics & Astronomy
University of Glasgow
Glasgow, G12 8QQ, UK
andy.buckley@cern.ch

February 1, 2023

Contribution to ISMD2022

I confirm that Ms Zarina Banoo of the University of Jammu is an author of the poster "Intermittency analysis of charged particles generated in Xe-Xe collisions at $\sqrt{s_{\mathrm{NN}}}$ = 5.44 TeV using the AMPT model" shown at the ISMD2022 conference in Pitlochry, Scotland from 31 July to 5 August 2022. Ms Banoo was registered to attend the conference virtual sessions held on Zoom and Gather.

Best regards,

Prof Andy Buckley
Co-chair, ISMD2022

2022 LHCP TAIPEI

This is to certify that

zarina banoo

University of Jammu

participated in the LHCP2022 online conference (16-20 May 2022) and presented a poster entitled

Scaling properties of charged particles generated in Xe-Xe collisions at √s_N N = 5.44 TeV using AMPT Model

The Local Organising Committee